UNIVERSITY OF CALIFORNIA SAN DIEGO

Spintronics and Electronic Transport in Epitaxial Thin Films

A dissertation submitted in partial satisfaction of the
requirements for the degree Doctor of Philosophy

in

Materials Science and Engineering

by

Yuxuan Xiao

Committee in charge:

Professor Eric E. Fullerton, Chair
Professor Alex Frañó
Professor Javier E. Garay
Professor Vitaliy Lomakin
Professor Vlado A. Lubarda
Professor Oleg G. Shpyrko

2022

The Dissertation of Yuxuan Xiao is approved, and it is acceptable in quality and form for publication on microfilm and electronically.

University of California San Diego

2022

DEDICATION

To my parents, my fiancée, and my friends, whose support is never overrated.

EPIGRAPH

I have never failed,
I've just found 10,000 ways that won't work.

—Thomas A. Edison

TABLE OF CONTENTS

LIST OF FIGURES

LIST OF TABLES

ACKNOWLEDGEMENTS

Words cannot express how much I appreciate Prof. Eric E. Fullerton for his solid support, broad knowledge, and phenomenal patience. I couldn't have imagined how valuable my research journey would become, from the moment that I knocked on Fullerton's office at Center of Memory and Magnetic Research on November 22, 2016.

Everyone that I worked with during the past 5 years, including students, postdocs, professors, scientists, and staff, helped me shape the way I think, carve the personality I behave, and enlighten the direction I sail to. I thank the interconnected world that I live in.

A large portion of my doctoral work was performed during the COVID-19 global pandemic. I thank those who devoted themselves to struggling against the crisis and saving lives.

Chapter 3, in part, is a reprint of the material "Y. Xiao, H. Wang, E. E. Fullerton, *Crystalline Orientation Dependent Spin Hall Effect in Epitaxial Platinum,*" Front. Phys. 785, (2022). The dissertation author was the primary investigator and author of these materials.

Chapter 4, in part, is currently being prepared for submission for publication of the material "Y. Xiao, N. Liyanage, D. A. Gilbert, E. E. Fullerton, *Néel vector perturbation in chemically ordered $FePt_3$,*" The dissertation author was one of the primary investigators and author of this material.

Chapter 5, in part, is currently being prepared for submission for publication of the material "Y. Xiao, Y. Kim, R. Medapalli, M. J. Gilbert, E. E. Fullerton, *Evolution of Anisotropic Magnetoresistance in Magnetic Weyl Semimetal,*" The dissertation author was one of the primary investigators and author of this material.

Chapter 6, in part, is currently being prepared for submission for publication of the material "Y. Xiao, Y. Kim, M. J. Gilbert, E. E. Fullerton, *Giant Easy-axis Dependent Transport in Epitaxial hcp Co,*" The dissertation author was one of the primary investigators and author of this material.

VITA

2012-2016 B. S. in Materials Science and Engineering, Iowa State University

2016-2017 M. S. in Materials Science and Engineering, University of California San Diego

2017-2022 Ph. D. in Materials Science and Engineering, University of California San Diego

PUBLICATIONS

1. Y. Xiao, Y. Kim, R. Medapalli, M. J. Gilbert, and E. E. Fullerton, "*Evolution of Anisotropic Magnetoresistance in Magnetic Weyl Semimetal,*" in preparation.
2. Y. Xiao, N. Liyanage, D. A. Gilbert, and E. E. Fullerton, "*Néel vector perturbation in chemically ordered $FePt_3$,*" in preparation.
3. Y. Xiao, Y. Kim, M. J. Gilbert, and E. E. Fullerton, "*Giant easy-axis dependent transport in Epitaxial hcp Co,*" in preparation.
4. V. Petrova, A. A. Corrao, S. Wang, Y. Xiao, K. W. Chapman, E. E. Fullerton, P. G. Khalifah, and P. Liu, "*Synthesis of flexible Co nanowires from bulk precursors,*" RSC advances 12(33), 21153-21159 (2022).
5. S. Yu, Z. Wu, J. Holoubek, H. Liu, E. Hopkins, Y. Xiao, X. Xing, M. H. Lee, and P. Liu, "*A Fiber-Based 3D Lithium Host for Lean Electrolyte Lithium Metal Batteries,*". Advanced Science 9, 2104829 (2022).
6. G. Q, Yan, S. Li, H. Lu, M. Huang, Y. Xiao, L. Wernert, J A. Brock, E E. Fullerton, H. Chen, H. L. Wang, and C. H. Du, "*Quantum sensing and imaging of spin-orbit-torque-driven spin dynamics in noncollinear antiferromagnet Mn3Sn,*" Advanced Materials, 2200327 (2022).
7. H. L. Wang, S. Zhang, N. J. McLaughlin, B. Flebus, M. Huang, Y. Xiao, C. Liu, M. Wu, E E. Fullerton, Y. Tserkowvnyak, and C.H. Du, "*Noninvasive measurements of spin transport properties of an antiferromagnetic insulator,*" Science Advances 8, eabg8562 (2022).
8. Y. Xiao, H. L. Wang, and E. E. Fullerton, "*Crystalline Orientation Dependent Spin Hall Effect in Epitaxial Platinum,*" Frontiers in Physics 785 (2022).
9. H. L. Wang, Y. Xiao, M. Guo, E. Lee-Wong, G. Q. Yan, R. Cheng, and C. H. Du, "*Spin Pumping of an Easy-Plane Antiferromagnet Enhanced by Dzyaloshinskii–Moriya Interaction,*" Physical Review Letters 127, 117202 (2021).
10. M.S. El Hadri, J. Gibbons, Y. Xiao, H. Ren, H. Arava, Y. Liu, Z. Liu, A. Petford-Long, A. F. Hoffmann, E. E. Fullerton. "*Giant spin Hall effect in ultrathin gold-silicon multilayers.*" Physical Review Materials 5, 064410 (2021)
11. M.S. El Hadri, V. Polewczyk, Y. Xiao, S. Mangin, and E E. Fullerton, "*Large anisotropic magnetocaloric effect in all-sputtered epitaxial terbium thin films,*" Physical Review Materials 4, 124404 (2020).
12. X. Wang, Y. Xiao, C. Liu, E. Lee-Wong, N. J. McLaughlin, H. Wang, M. Wu, H.L. Wang, E. E. Fullerton, and C. H. Du, "*Electrical control of coherent spin rotation of a single-spin qubit,*" npj Quantum Information 6, 78 (2020).

13. F. Formisano, R. Medapalli, Y. Xiao, H. Ren, E. E. Fullerton, and A. V. Kimel, *"Femtosecond magneto-optics of EuO,"* Journal of Magnetism and Magnetic Materials, 502, 166479 (2020).

ABSTRACT OF THE DISSERTATION

Spintronics and Electronic Transport in Epitaxial Thin Films

by

Yuxuan Xiao

Doctor of Philosophy in Materials Science and Engineering

University of California San Diego, 2022

Professor Eric E. Fullerton, Chair

The rise of neuromorphic and other non-traditional computing approaches and the emergence of new non-volatile memories call for energy-efficient magnetization manipulation by spin and a better understanding of fundamental magneto-transport properties. Over the past decades, much of the work on the conversion of charge currents to spin currents focused on polycrystalline and amorphous materials. In the first part of this dissertation, we investigate the spin Hall effect in epitaxial Pt (200), (220), and (111). A tunable spin current generation can be achieved in Pt (220). The charge-to-spin conversion efficiency can be significantly enhanced along specific crystallographic orientation by exploiting the anisotropic resistivity. Our work highlights the future work on enhanced charge-to-spin conversion arising from crystalline

orientation dependence which may boost the energy-efficient spintronic devices.

Tunable charge-to-spin conversion can be achieved by utilizing the materials with magnetic phase transition, which motivated us to study the 3d transition metal-Pt_3 alloy (e.g., $FePt_3$ and $CrPt_3$) and the rare earth material (Ho). Prior to further spintronics implementation, the fundamental magneto-transport properties in those materials need to be investigated. We successfully fabricate the chemically ordered epitaxial $CrPt_3$ and $FePt_3$. The large anomalous Hall effect measured on $CrPt_3$ is in good agreement with the theoretical prediction. Moreover, by probing the exchange bias via electrical transport, it helps us quantitatively investigate the stability of antiferromagnetic nature in $FePt_3$ under external perturbations.

Furthermore, there are still intriguing properties remaining in "old" materials which lead to the magneto-transport study on hcp Ho and hcp Co. Our discovery of six-fold angular dependent magnetoresistance and step-like planar Hall effect in Ho gives rise to the strong magnetostriction coupled magnetoresistance. Remarkably, although predicted years ago, the strong c-axis dependent anomalous Hall conductivity in hcp Co lacks experimental support, which is demonstrated in this dissertation. The magneto-transport study on hcp Co offers a comprehensive picture of anisotropic anomalous Hall effect and magnetoresistance in ferromagnets with in-plane uniaxial magnetic anisotropy.

Chapter 1

Introduction

1.1 Orbital and Spin Angular Momentum of Electrons

Although practical approaches to utilizing natural magnets have been adopted intensively by our ancestors dating back thousands of years, a systematic understanding of magnetism emerges with the rise of modern science. Classically, electromagnetism reveals that an electric current passing through a straight wire can generate a magnetic field described by the right-hand rule, in which the thumb indicates the direction of the current I and the fingers indicate the direction of the magnetic field lines B and shows the magnetic field is circular in a plane with its normal along the wire axis. Hereby, B can be calculated by Ampere's law as a function of I and the distance to the wire r:

$$B = \frac{\mu_0 I}{2\pi r}\left(\frac{HA}{m^2}, \frac{Wb}{m^2}, T\right) \tag{1.1}$$

where μ_0 is permeability of vacuum which is a constant of $4\pi \times 10^{-7}$ H/m. Intuitively, B describes the lines of magnetic flux per area, which is also called magnetic flux density. Now, if the current wire becomes a circular loop with diameter R, by utilizing the Biot-Savart law, the B at the center of the loop becomes:

$$B = \frac{\mu_0 I}{2R} \tag{1.2}$$

For such a current loop placed in a magnetic field H, a torque will be exerted on the loop and rotate it until its surface normal aligned with the H. The moment of this torque is called magnetic

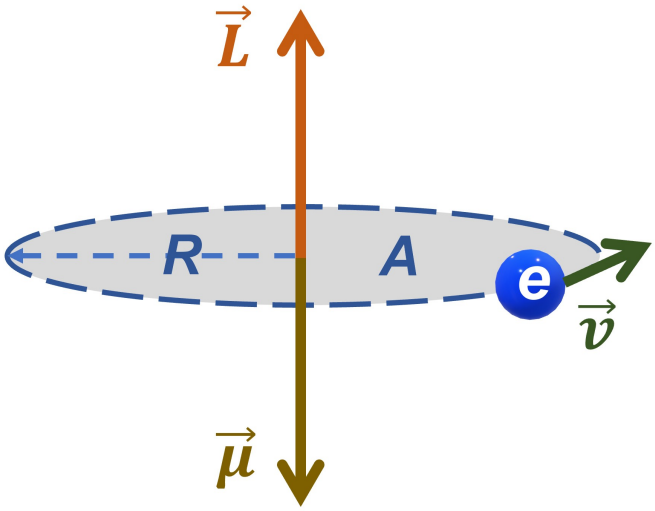

Figure 1.1. Magnetic moment contributed by orbiting electron which forms a current loop.

moment m, which is the product of current and loop area. Denote the angle between the loop surface normal and the H to be θ, then, the potential energy of a magnetised loop with m under H can be quantified by:

$$E = -|\vec{m}||\vec{H}|\cos\theta \tag{1.3}$$

This energy is commonly known as Zeeman energy. Then, as our focal point is shifted microscopically to the atomic level, the magnetic moment of an electron needs to be understood, which can be resulted from the orbital and spin motion of the electron. The orbital motion can be analogous to the aforementioned current loop example. The effective current produced by an electron circling with velocity v is:

$$I = -\frac{ev}{2\pi R} \tag{1.4}$$

Since moment is product of current and loop area, it can be derived into:

$$\mu_m = I\pi r^2 = -\frac{evR}{2} \tag{1.5}$$

Having the magnitude of orbital angular momentum of the moving electron given by $L = m_e$vr

with m_e to be the intrinsic mass of electron, the electron orbit magnetic moment can be written as:

$$\mu_m(orbit) = -g_L \frac{e}{2m_e} L = -g_L \frac{e\hbar}{2m_e} \frac{L}{\hbar} = -g_L \mu_B \frac{L}{\hbar} \tag{1.6}$$

where g_L is the orbital g-factor. Importantly, μ_B is known as the Bohr magneton, which is a fundamental natural unit of magnetic moment. Just as e is the fundamental unit of electric charge.

Similarly, the electron spin magnetic moment can be written as a function of electron spin angular momentum S:

$$\mu_m(spin) = -g_S \mu_B \frac{S}{\hbar} \tag{1.7}$$

The spin-orbit interaction results in the spin and orbital angular momentums being coupled known as spin-orbit coupling (SOC) to create a total electronic angular momentum J. The electron total magnetic moment related to the J is expressed by:

$$\mu_m(total) = -g_J \mu_B \frac{J}{\hbar} \tag{1.8}$$

Thus far, it can be understood that both the electron orbital and spin angular momentum are sources of magnetism in an atom. The combination of a number of atoms with their various atomic moments orientations represents the macroscopic magnetic ordering of real-life materials. For materials where all electron spins and orbital moments are compensated, such as in a full band, these materials are classified as diamagnets (e.g., Si). For uncompensated individual electron moments that are randomly oriented as a result of thermal excitiatons in zero external magnetic field this leads to zero net moment in a material. This class of behavior is classified as paramagnet (Cu). On the other hand, the way that electronic moments are only partially canceled and are ordered by exchange that overcomes thermal energy exhibits atomic net moment, defining ferromagnets (e.g., Co) and ferrimagnets (e.g. Fe_3O_4). Finally, the transitional antiferromagnets are the case when the spins are ordered but exactly cancel (e.g., Cr). We will be covering all these classes or magnet materials in the following content.

1.2 Magnetic Ordering

To quantify the behavior of magnetic ordering, a term called susceptibility χ needs to be introduced, which describes how magnetization M varies with changing H:

$$\chi = \frac{M}{H}\,(dimensionless) \tag{1.9}$$

From this equation, χ is not the slope or gradient of the M vs H curve, instead, it describes the slope of a line connecting the origin to a certain (M, H) on the curve. It should be noted that χ cannot be misunderstood with the term permeability μ:

$$\mu = \frac{B}{H}\,(dimensionless) \tag{1.10}$$

Because (Now use c.g.s but earlier S.I. with μ_0)

$$B = H + 4\pi M \tag{1.11}$$

We have

$$\frac{B}{H} = 1 + 4\pi(\frac{M}{H}) \tag{1.12}$$

Therefore, the μ can be rewritten as a function of χ:

$$\mu = 1 + 4\pi\chi \tag{1.13}$$

As a reference, an empty space has χ value of 0.

1.2.1 Diamagnetism and Paramagnetism

Water, noble gases, and many organic compounds are diamagnetic. In the classical theory of diamagnetism proposed by Langevin, the diamagnet can be considered to own a ”negative”

moment. When a single electron orbit experiences the applied external field, its effective current of the orbit is reduced. As a result, a magnetic moment opposing the applied field is generated [1]. Quantitatively, the χ_m of diamagnetic materials (mass susceptibility, normalized to density) is usually in the order of -10^{-5} [2]. In particular, superconductors in their superconducting state can be considered as diamagnetic because of expelling the external field according to Meissner effect and χ_m approaches 1.

Present in most atoms with incompletely filled atomic orbitals (e.g., oxygen), paramagnetism is due to the presence of unpaired electrons, which contribute to the weak net moment in the material with the absence of strong coupling between the moments. Based on this statement, the χ of paramagnetic materials can be understood to be a positive value with a relatively small magnitude (in the order of 10^4). Distinctive to ferromagnets, paramagnets own zero remanence magnetization under zero external magnetic field because the coupling energy is far less than the k_BT, so the spin orientations are fluctuated by thermal influence. Furthermore, thermal influence plays an important role, especially in the field of magnetic recording, which leads to the stability issue caused by the superparamagnetic effect. In a particle with spontaneous magnetization polarization, its magnetization polarization can be randomized by temperature if the particle size is smaller than a certain scale (typically in the order of 10 nm). That being said, the superparamagnetic effect significantly challenges the bit density in magnetic recording which is limited by thermal stability. Finally, it should be noted that although diamagnet and paramagnet also react to external field and own ”magnetic” behaviour. The term ”magnetic materials” in this dissertation generally excludes diamagnet and paramagnet unless otherwise stated.

1.2.2 Ferromagnetism and Ferrimagnetism

For some paramagnetic materials, it transits to ferromagnets with its saturated magnetization M_S raises from zero as temperature decreases from ordering temperature (so-called Curie temperature T_C) and eventually saturates. Its internal coupling of atomic moments overcomes

the thermal fluctuation and brings about relatively strong magnetization. The self-saturating, spontaneous, long-range magnetization of atomic moments defines a ferromagnet (e.g., Fe, Co and Ni). The χ in ferromagnets can be a billion orders of magnitude higher than that of a paramagnet. But, having such strong magnetization, we need to answer some common phenomenon, such as the reason why a box of iron paper clips do not attract each other. It turns out, in soft ferromagnetic material, such as soft iron, it is divided into magnetic domains at zero external field state. In each domain, it still owns spontaneous magnetization with the magnitude to be saturated magnetization M_S. The various orientations of domains lead to macroscopic zero net moment. When being magnetized, the magnetization tends to rotate and align with the field with its magnitude unchanged.

As a special case of ferromagnetism, ferrimagnets exhibit similar spontaneous magnetization with magnetically saturated domains. As a well-known example, magnetite (Fe_3O_4, or $Fe^{2+}Fe^{3+}{}_2O_4$) is ferrimagnetic. In the crystal structure, O^{2-} ions carry no net moment. The iron ions ($\frac{1}{2}$ of Fe^{3+} and all of Fe^{2+}) in the octahedral site exhibit magnetic moment with different magnitude and opposites to the moment of the iron ions ($\frac{1}{2}$ of Fe^{3+}) in the tetrahedral site, which leads to negative exchange coupling with net spontaneous magnetization.

1.2.3 Antiferromagnetism

Another scenario of negative exchange interaction can be found in antiferromagnets, which also exhibit spontaneous magnetization under ordering temperature (Néel temperature, T_N). In colinear antiferromagnets (e.g., Cr), neighbouring spins are coupled antiparallel to each other with the same magnitude of magnetization, leading to zero total net moment. Exceptionally, neighbouring spins can be asymmetrically exchange coupled due to Dzyaloshinskii–Moriya interaction (DMI). This spin canting phenomenon results in "canted" antiferromagnets with weak net moment (e.g., α-Fe_2O_3). Conclusively, Figure 1.2 summarizes representative relationships between $\frac{1}{\chi}$ and temperature over the aforementioned magnetic ordering configurations.

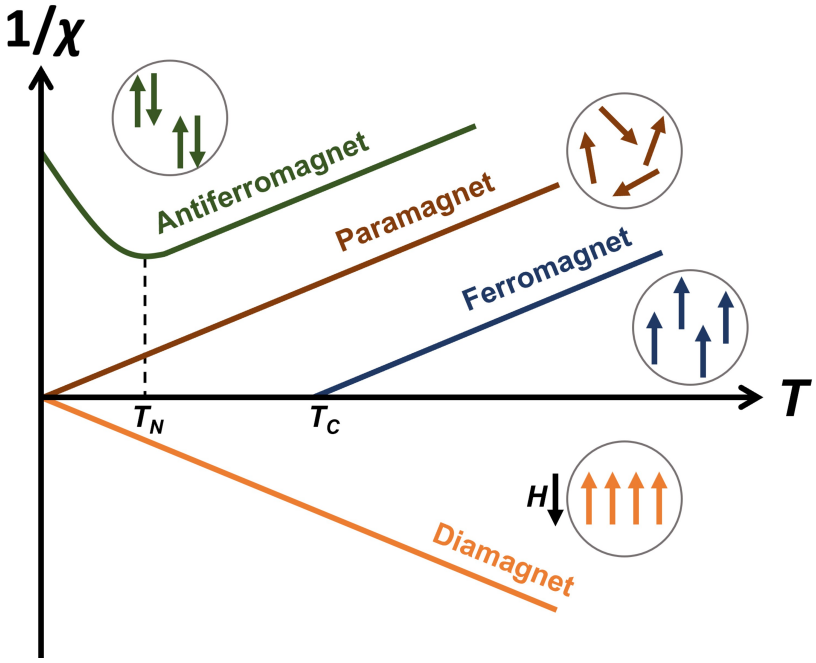

Figure 1.2. General examples of Temperature-dependent $\frac{1}{\chi}$ presented with unspecified values.

1.3 Anisotropic Magnetoresistance and Planar Hall Effect

An external magnetic field can result in a change in resistance of the material because the charge carriers feel the Lorentz force and deflect from the current direction increasing the path length of the carriers. This deflection of the carriers also results in the ordinary Hall effect (OHE) when the field is perpendicular to the sample. This is just one of many types of magnetoresistance (MR) effect (e.g., ordinary MR (OMR), giant MR (GMR), colossal MR(CMR)). Here we emphasize the anisotropic magnetoresistance effect (AMR) in magnetic materials [3, 4, 5]. AMR is not only a fundamental physical property but also critical for magnetic recording as it was the basis of the first MR read head [6]. General examples of room temperature AMR and PHE curves measured on polycrystalline permalloy (Py, $Ni_{81}Fe_{19}$, Ni and Fe in wt%) is shown in Fig. 1.3(a) and (b). We observe that high resistance states can be found when current is colinear with field and low resistance states occur when current is perpendicular to the field. To mathematically describe this behavior, a general angular dependent expression of AMR and

planar Hall effect (PHE) [7, 8] can be written below:

$$\rho_{xx,AMR} = \rho_{\perp} + (\rho_{||} - \rho_{\perp}) \cos^2 \theta \tag{1.14}$$

$$\rho_{xy,PHE} = (\rho_{||} - \rho_{\perp}) \sin \theta \cos \theta \tag{1.15}$$

where $\rho_{xx,AMR}$ is the longitudinal resistivity that probes the AMR, $\rho_{xy,PHE}$ is the transverse resistivity that probes the PHE. θ is the azimuthal angle between the current and the external field. $\rho_{||}$ describes the resistivity when current is colinear with the field (e.g., $\theta = 0^{\circ}$, 180° and 360°). $\rho_{\perp}$ describes the resistivity when current is perpendicular to the field (e.g., $\theta = 90^{\circ}$, 270°). From the above 2 equations, it can be understood that AMR and PHE describe the change of resistance as a function of the change of the angle between current and external magnetic field (magnetization). Also, PHE can be understood as related to AMR but probed by hall resistance. As it can be seen, Eq. 1.15 does not have addition offset compared to that of Eq. 1.14, making PHE a more sensitive probing technique [9]. Now the question is, what can AMR or PHE probe? In industrial applications, a "sensitive" material with large change of AMR can effectively probe the magnetization direction of magnetic medium grains in hard disk drive (HDD), AMR head became a better substitution for inductive head thanks to a much larger readback signal. Furthermore, AMR is the building block for many spintronics techniques, such as ST-FMR, which will be introduced in chapter 2 and chapter 3.

For $3d$ transition metals, the AMR is ascribed to the contribution from both the Coulomb interaction and spin-orbit interaction (SOI) in the event of *s*-*d* scattering. Based on Mott's two-current model, the resistivity of a metal is a sum of spin up and spin down electrons which carry the current in parallel [10]. But the resistivity of spin up channel is unequal to that of spin down channel. When current is colinear with the field, it favors the *s*-*d* scattering because the vacant d states have a component of L orthogonal to M and therefore have classical orbits $(k_x^2 + k_y^2)$ compatible with the conduction electron momentum k_x [2]. Furthermore, the presence

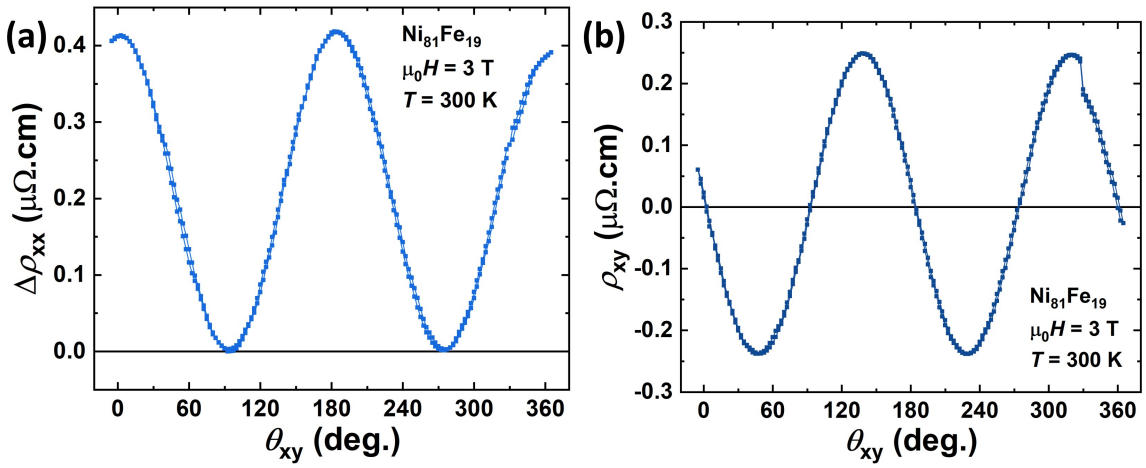

Figure 1.3. General examples of room temperature AMR and PHE curves measured on 8-nm-thick polycrystalline Permalloy. Measurements were probed on 20-μm-wide 4-probe device.

of SOI allows mixing spin-up and spin-down states so that s↑ electrons can be scattered into empty *d* states, which brings additional increase of resistivity [2], that being said, leading to high resistance state.

We also need to note that on polycrystalline or amorphous materials, the magnitude and shape of AMR are usually isotropic regardless of current orientation in the sample plane. The $\rho_{xx,AMR}$ and $\rho_{xy,PHE}$ in such materials solely depend on the angle between current and magnetization. However, for the materials with crystalline symmetry and magnetocrystalline anisotropy, the AMR and PHE can be more complicated, which motivates the investigation of anisotropic AMR and PHE properties of epitaxial materials.

1.4 Spin Hall Effect and Anomalous Hall Effect

From the previous section, we know that both spin-up and spin-down electrons carry the current in parallel. Then some questions arise: can spin-up and spin-down electrons be separated? How can we utilize the information carried by spin? A flow of pure spins with only one polarization is called spin current which carries the flow of angular momentum. Several approaches are applied to generate spin current, for example, Slonczewski *et al.* theoretically predicted the spin transfer torque (STT) mechanism [11]: when a charge current with randomized

spins traverses a ferromagnet, its spins will tend to rotate to follow the local magnetization. Then, the spin-polarized current can transfer spin angular momentum to another ferromagnet where it is absorbed, therefore reorienting its magnetization by this spin transfer torque. STT technique became an efficient measure to generate spin current and manipulate the magnetization, which gives a rise to the spin-transfer torque magnetoresistive random-access memory (STT-MRAM). which is non-volatile in contrast to volatile memory such as dynamic random-access memory (DRAM) and static random-access memory (SRAM).

Alternatively, since the charge current conversion from spin current injection was first proved experimentally by Bakun in 1984 [12], it attracted intensive attraction to generate spin current in nonmagnetic materials. Some theoretical work was done by Hirsch who named this phenomenon spin Hall effect (SHE) [13]. In a nonmagnetic material with its electron spin angular momentum strongly coupled with its orbital momentum (strong SOC), when a charge current flows through, a large effective spin-orbit field will be exerted on randomized electrons. Because of that, a portion of the electrons with the same polarization will be deflected transversely, and the electrons with opposite polarization will be transversely deflected into opposite directions, which yields a flow of spin current perpendicular to the charge current. That is, the spin current direction, charge current direction and the spin polarization of the spin current are orthogonal to each other. A schematic of SHE is in Fig. 1.4 [14].

Anomalous Hall effect (AHE) is another apple that falls out of the SOC tree. After the ordinary Hall effect (OHE) was developed by Edwin Hall, AHE was observed in ferromagnets [15]. Akin to SHE, when charge current pass through a ferromagnet, electrons are deflected transversely into opposite directions for different spin polarizations. If we still remember the STT mechanism, this charge current in ferromagnet will also have polarization following the ferromagnet's magnetization. A net transverse voltage due to this spin-dependent transverse velocity can be measured as Hall voltage [16]. In AHE, the Hall voltage is proportional to the out-of-plane magnetization, while in OHE, the Hall voltage is proportional to the external magnetic field. Moreover, AHE can be observed in the absence of an external field. A single

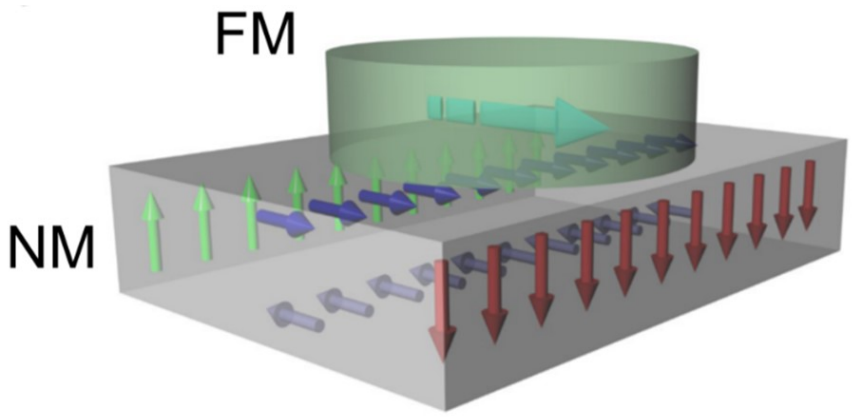

Figure 1.4. Schematic of a heavy metal (HM) and a ferromagnet (FM) heterostructure in which isotropic spin current accumulation is shown. The spin currents carry torque that can manipulate the magnetization in FM. Reproduced from [14] as a fair use. ©Nature Publishing Group

domain can engender a spontaneous Hall current orthogonal to both the magnetization and current, which leads to the terminology of ”anomalous”. The AHE is also called the spontaneous Hall effect and the extraordinary Hall effect, we use AHE throughout the dissertation.

Physically, SHE and AHE share the same origin, both intrinsic and extrinsic mechanisms were proposed [16, 17, 18, 19]. The intrinsic mechanism dominates in the ”relatively dirty” materials with relatively lower mobility. In the intrinsic mechanism, the effective spin-orbit field is ascribed to the momentum-space Berry curvature contribution. In detail, the precession of the spins about the k-dependent magnetic field $B(k)$ characterizes the band structure. We start with a steady non-equilibrium state described as a Fermi distribution displaced along the direction of the charge current. By changing the value of k and of $B(k)$, the electric field forces the electrons titling out of alignment with the effective magnetic field. In the attempt to regain alignment the spins tilt away from the original orientations, and the tilting goes in opposite directions on opposite sides of the Fermi surface, resulting in the generation of spin current [16, 17].

On the other hand, the extrinsic mechanism mainly results from the spin-dependent scatterings (e.g., spin skew scattering and side-jump scattering) which generate the effective spin-orbit field, And spin current is generated between scattering events. The spin skew scattering can be understood that spin-up and spin-down electrons are scattered asymmetrically by a

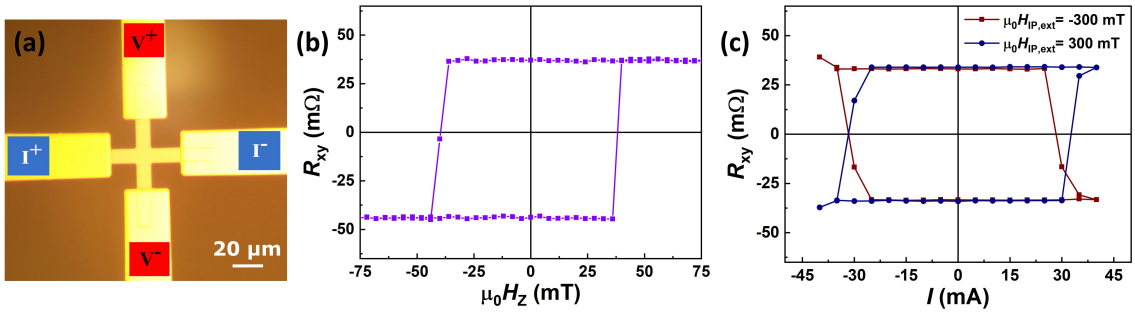

Figure 1.5. SOT switching performed on patterned Hall cross (a). (b) Reference AHE resistance measured as a function of out-of-plane field. (c) AHE resistance as a function of charge current pulse. The current-induced SOT switching was assisted by in-plane symmetry breaking field.

central potential [18]. The side jump scattering is basically due to a spin-dependent difference in acceleration and deceleration during scattering, resulting on repeated scattering a sideway displacement which separates the spin polarization [18] The grain boundaries and impurities induced extrinsic mechanism is prone to dominate in single crystal materials (also called "clean" materials). Now as we introduced intrinsic and extrinsic mechanisms, we need to note that both mechanisms can independently become the source of spin current.

To quantify the SHE efficiency, spin Hall angle (SHA) is introduced to describe the ability of charge-to-spin conversion efficiencies via SHE, which is proportional to the ratio of spin current density J_S and charge current density J_C. Importantly, SHA is usually considered as its absolute value, but SHA still owns sign. However, positive SHA does not mathematically refer to a larger number compared to negative SHA. Instead, positive SHA represents more than half-filling and negative represents less than half-filling of the *d*-bands. Note that charge-to-spin conversion efficiencies can be quantified independently which describes the overall spin current converted from charge current in a spin source material, while SHA only represents the spin current generated by SHE. These two terms cannot be mixed interchangeably.

1.4.1 Magnetization Reversal via SHE

Here, we show an example of using spin current to switch perpendicular magnetization. The specimen was chosen to have a heavy metal(HM)/ferromagnet(FM) heterostructure,

specifically, Co/Ni bilayer grown on Pt (111) epitaxial film. The perpendicular magnetization anisotropy (PMA) in Co/Ni bilayer was confirmed by both the magnetic hysteresis loop and AHE loop. By sending dc charge current pulse into the heterostructure, a portion of current that flows through Pt can be converted into spin current via bulk SHE. The rest of current that flows through Co/Ni bilayer contributes to the AHE signal. As shown in Fig. 1.5, as charge current increases to roughly 30 mA, strong enough spin current switched the Co/Ni magnetization into the opposite direction, leading to an opposite AHE resistance signal, this process can be reversed as changing the current polarity. The AHE resistance difference in switching measurements is close to the magnetic field-induced resistance difference, suggesting full switching. This demonstration is a hint for magnetic recording, as the 2 opposite AHE resistance states can be referred to "0" and "1". By applying this idea, the industry is exploring the spin-orbit torque magnetoresistive random access-memory (SOT-MRAM) as a follow-on technology to STT-MRAM [20, 21].

Some theoretical background on spin dynamics is needed to understand the SOT switching. Understanding the magnetization motion under external influence was unclear until the establishment of Landau-Lifschitz-Gilbert-Slonczewski (LLGS) equation, which combines the early work done by Landau and Lifschitz back to 1930s [22] and later contributions by Gilbert [23]. This equation was extended to included spin-torques by Slonczewski [11] to form the Landau-Lifschitz-Gilbert-Slonczewski (LLGS) equation. The LLGS equation describes the behavior of magnetization subject to external field or spin torques. Among many variations of this equation, here we use the following form:

$$\frac{dm}{dt} = -\gamma[m \times H_{eff}] + \alpha[m \times \frac{dm}{dt}] + \frac{\gamma}{\mu_0 M_S}\tau \tag{1.16}$$

where γ is the gyromagnetic ratio of an electron, α is the Gilbert damping constant, m is the moment, and H_{eff} is the effective magnetic field, τ is the torque, μ_0 is the vacuum permeability, M_S is the saturated magnetization.

The first term on the right represents the total torque exerted by H_{eff}. It describes a

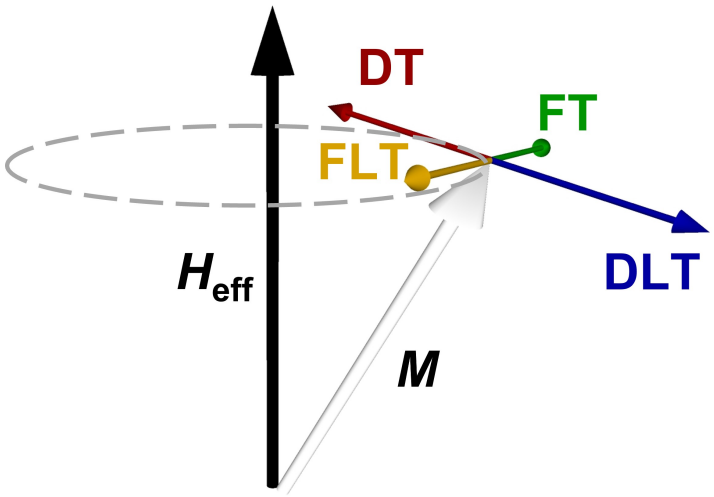

Figure 1.6. Schematic of the torque terms of the Eq. 1.16 and 1.17

precessional motion of magnetization about the effective magnetic field when the magnetization is at a certain angle to the field. In other words, it shows the motion how the magnetization aligns with an external field. In particular, the precession about the external field with an angular frequency are named as Larmor precession and Larmor frequency, respectively. The second term represents the damping during the precession with continuous changing angular momentum. The damping torque tends to make moment in precession and finally align with the local effective field. Then the system will reach an equilibrium state and the changing angular momentum dissipates into heat generated by lattice vibration (phonon). The third term was introduced by Slonczewski in 1996 [11], predicting the spin torque effect on magnetization. The torque can be further understood by the following expression:

$$\tau = \alpha_j[m \times [m \times \sigma]] + b_j[m \times \sigma] \tag{1.17}$$

where the σ is spin polarization. The first term on the right represents the torque which is antiparallel to damping direction, also named as in-plane spin transfer torque, antidamping (damping-like) torque or Slonczewski torque. The second term describes the torque so-called field-like torque. The mutual position of damping torque (DT), damping-like torque (DLT, τ_{DL}),

field torque (FT), and field-like torque (FLT, τ_{DL}) is illustrated in Fig. 1.6, in which DT and DLT, FT and FLT are collinear to each other, DT and FT are orthogonal.

1.5 3d Transition Metal - Platinum Alloys

In the periodic table of elements, the 3d transition metals are referred to the first ten transition metals from group 3 to 12 in period 4. As they intermetallically alloy with Pt, the formed alloy can own distinctive magnetic properties compared to 3d elements themselves. In particular, the chemically ordered XPt_3 alloys (X = V, Cr, Mn, Fe, Co) raised attention in the past two decades and can act as potential novel spin source with the advantages of strong spin-orbit coupling and additional spin polarization manipulation via ASHE when the alloy has net moment. Iwashita *et al.* performed first-principles electronic structure calculations and summarized spin, orbital, and total magnetic moments on both 3d elements sites and Pt site [24], which matched the experimental results that exhibit ferrimagnetic VPt_3 [25] and $CrPt_3$ [26], ferromagnetic $MnPt_3$ [27] and $CoPt_3$ [28], and antiferromagnetic $FePt_3$ [29]. Their magnetic properties are summarized in Table 1.1. In the case of Strukturbericht designation $L1_2$, the lattice is a face center cubic (fcc). When the alloy is chemically disordered, the atoms are arranged randomly in the lattice. When the alloy is chemically ordered, the 3d element atoms occupy the corner sites and Pt atoms occupy the face sites. In the special case of VPt_3 with $D0_{22}$ structure, the V atoms occupy the four corner sites and the geometric center site. Pt occupies all the face sites and four edge sites in the midway of *c*-axis.

This dissertation mainly focused on chemically ordered epitaxial $CrPt_3$ and $FePt_3$. Previous studies on those have unfolded some remarkable magnetic properties. For example, by utilizing the magneto-optic Kerr effect (MOKE), magneto-optical disc drive was commercialized in the 1980s. Serving as potential magneto-optical storage media, $CrPt_3$ (111) with strong perpendicular magnetic anisotropy was predicted to have a large Kerr rotation of 0.2° [30]. Experimentally, Kerr rotation of 0.21° at wavelength = 632.8 nm [31] and 0.65 ° at 1100 nm

Table 1.1. Summary of reported crystal and magnetic properties of chemically ordered XPt_3 alloys. RT represents that the data was obtained at room temperature.

Alloy	Crystal Info	M_S	Curie/Néel Temperature (K)
VPt_3	$L1_2$ (Cu_3Au)	0.89 emu/g (4.2 K)	240
	$D0_{22}$ (Al_3Ti)	0.67 emu/g (4.2 K)	210
$CrPt_3$	$L1_2$ (Cu_3Au)	150 - 300 emu/cc (RT)	450
$MnPt_3$	$L1_2$ (Cu_3Au)	446 emu/cc (RT)	390
$FePt_3$	$L1_2$ (Cu_3Au)	N/A (AFM)	160
$CoPt_3$	$L1_2$ (Cu_3Au)	450 emu/cc (20 K)	210

[32, 33] evidently supported the prediction.

Moreover, in conventional hard disk drives (HDD). One bit of data is statistically averaged over dozens of grains that are magnetized in the same direction. In order to increase storage density, reducing the grain volume needs to be done. However, the energy barrier due to superparamagnetism limits the minimum grain volume, which challenges the improvement of storage density. It was demonstrated that, locally patterned magnetic "islands" with stronger exchange coupling can postpone the superparamagnetism limits with improved storage density and better thermal stability. Rather than pattering the media film by lithography approach, ion-beam irradiation was introduced to locally disrupt the magnetic properties without modify the topography. Especially, ion-beam irradiation was applied to chemically ordered $CrPt_3$ [34] and $FePt_3$ [35] to suppress the local magnetization by driving atom displacement. That is, order-disorder transition can be induced by ion-beam irradiation, which makes XPt_3 a promising system to achieve nondestructive patterned storage media and study the properties of patterned interface. More interestingly, chemically ordered $CrPt_3$ was recently predicted to host the topological Weyl 3D semimetal properties [36], this new prospect rekindles those "old" alloys.

1.6 Topological Semimetal

Building off of the previous section, here we briefly introduce topological semimetal (TSM). Graphene is one of the most well-known 2D materials [37]. A graphene lattice has two

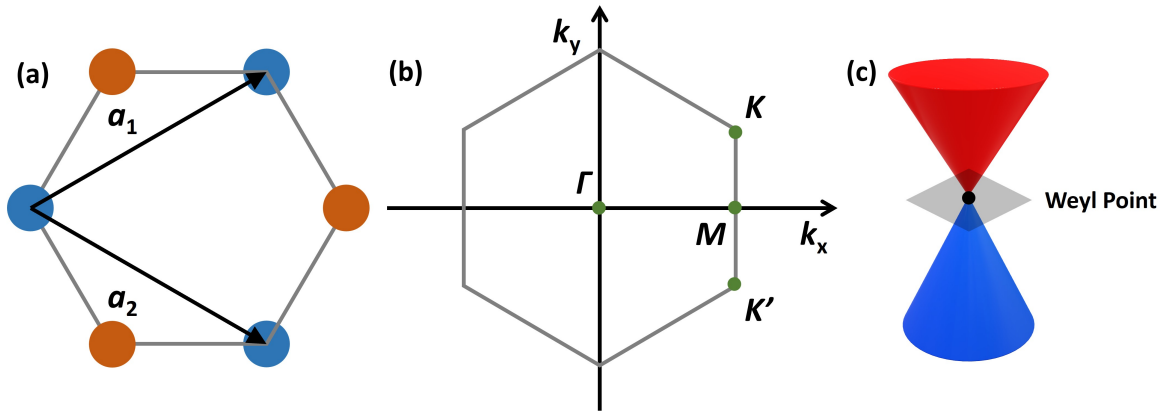

Figure 1.7. Schematic of (a) Graphene lattice. (b) Corresponded first Brillouin zone (BZ). (c) Conventional linear dispersion crosses at Weyl point.

basis atoms in a unit cell. In *k*-space, 2 corners of the first Brillouin zone (BZ) are 2 inequivalent *K* and *K*' points, which are correlated to the primitive vectors, as shown in Fig. [**?**].

By solving tight binding Hamiltonian, the band structure of graphene shows that the conduction bands (CB) and the valence bands (VB) linearly join at *K* and *K*'. Furthermore, without electron doping, the Fermi level lies through these band touching points. Hereby, this band touching behaviour classifies graphene as one kind of semimetal.

Such band touching point is called Weyl point or Weyl node. The combination of the TRS and IS leads to a pair of degenerate Weyl points with opposite chirality, which defines Dirac semimetal (DSM) [38, 39]. The formation of Weyl semimetal requires the breaking of either TRS or lattice IS [40]. Then the question is, can we evaluate the symmetry in pure graphene? For example, graphene doped with magnetic impurities can break the TRS. The IS in graphene can be broken by stacking graphene to certain substrates, e.g., hexagonal boron nitride (h-BN). Obviously, pure undoped graphene itself preserves both TRS and lattice IS. Therefore, graphene is classified as DSM. Furthermore, TSM's Fermi sea is topologically protected. That is, their Fermi surface (FS) shape can be modified, but cannot be gapped [41]. Thus far, the origin of each terminology has been briefly explained when we define graphene as 2D topological Dirac semimetal.

Remember the intrinsic mechanism in the previous SHE and AHE section, the Berry curvature is a gauge field that characterizes the topological entanglement between CB and VB, which is equivalent to an effective magnetic field in the k-space [40, 42]. In particular, the Berry curvature vanishes when both TRS and lattice IS coexist [43]. That is, Berry curvature is absent in topological DSMs. Therefore, engineering the topological WSMs by manipulating the Berry curvature could become promising, which might lead to strong SHE with the aid of strong SOC.

Chapter 2

Experimental Techniques

2.1 Thin film Deposition

The research topics in this dissertation were investigated on multiple materials in thin film form with thickness less than 300 nm. Therefore, a foremost challenge was to fabricate thin films with desirable crystallinity, epitaxy, composition, and surface morphology. Thin film deposition is essentially a long-standing popular coating technique that is applied to every aspect of modern life, such as silvering in mirrors and bottles, optical coating on lenses and screens, and electrical coatings in integrated circuits. The deposition process is either chemical or physical. Electroplating, chemical vapor deposition (CVD), and atomic layer deposition (ALD) are common representations of chemical deposition. On the other hand, classified as one of the physical vapor deposition (PVD) techniques, magnetron sputtering is the sole deposition technique used in this dissertation. The sputtering process can be understood as the following procedure. In an ultrahigh vacuum (UHV) chamber with a partial pressure sputtering gas environment, a high voltage potential is established between a target material and sample holder. By ionizing the Ar in the established electric field and creating a gaseous plasma, the Ar ions accelerate into the negatively charged target material (cathode). When the ion kinetic energy overcomes the target material binding energy, the target material can be ”bombarded” and ”blasted” by the arriving ions, and the sputtered material is ejected in the form of neutral particles. The sputtered materials travel across the chamber and are eventually coated on whatever stops

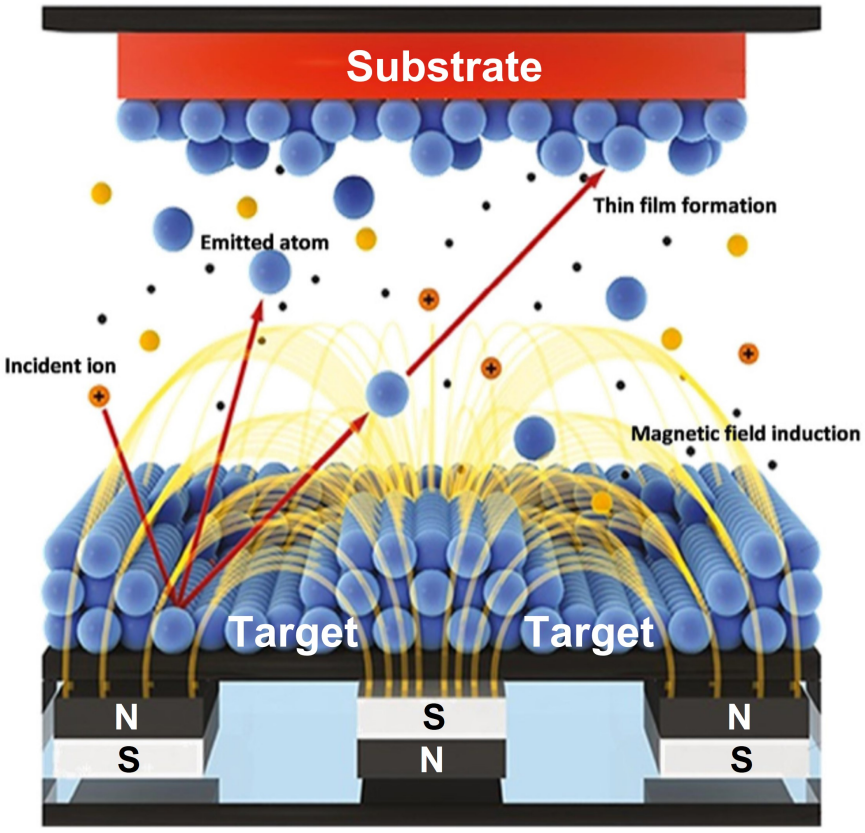

Figure 2.1. Example of a sputtering process. Reproduced from [44] as a fair use. ©2019 Acta Materialia Inc.

them, typically a sample holder with substrates mounted on it.

The basic sputtering process in the previous paragraph is the fundamental building block of various sputtering techniques. However, there are two major problems that need to be addressed. Firstly, the plasma is not ”dense”, resulting in a slow deposition rate. Secondly, as the substrate is positively charged (anode), the unwanted electron bombardment causes structural damage to the substrate.

Remarkably, magnetron sputtering was invented to solve those issues. By creating a strong magnetic field close to the target surface using permanent magnets in the cathode, the free electrons can be ”trapped” in the magnetic field and prevented from bombarding the substrate. Moreover, the magnetic field enhances their probability of ionizing the sputter gas molecule, further significantly raising the sputtering rate. The magnetron sputtering process is illustrated in

figure Fig. 2.1 [44].

DC magnetron sputtering can be applied on conductive target materials, while radio frequency (rf) magnetron sputtering is designed for insulating target materials. In the case of rf sputtering, AC power source ionizes the sputter gas by electromagnetic wave at 13.56 MHz. This frequency is chosen to prevent the interference with common telecommunication frequencies. In the first cycle, target material is negatively charged. The polarized sputter gas ions accumulate towards target and bombard it. Then in the second cycle, target is positively charged. The ejected sputter gas ions and target atoms accelerate toward substrate and finish the deposition.

In Fullerton lab, AJA International ATC Orion sputtering system is operated with the capability of hosting 8 target materials in the chamber, co-sputtering, and high temperature growth. The sputter guns are arranged in a confocal configuration with deposition uniformity of better than $\pm$ 2.5% over a 4" diameter wafer. For epitaxial films, high temperature growth and annealing are critical parameters that need to be optimized. Detailed growth conditions of different epitaxial materials synthesized and studied will be discussed in the following chapters.

2.2 X-ray Reflectivity and X-ray Diffraction

The thickness calibration is critical in thin film deposition. Several calibration methods were applied by the dissertation author, for example, measuring step height using surface profiler or atomic force microscopy (AFM). Although this method is limited by accuracy, it is very practical on rough films with thicknesses above 50 nm. To gain better accuracy, low-angle θ-2θ X-ray Diffraction (XRD), more commonly called X-ray Reflectivity (XRR) specializes in statistically-averaged measurements over the area of X-ray beam. The typical XRR scanning range is from 0° to 10° When X-rays get in contact with specimen under grazing incidence, they will be completely reflected by total external reflection (TER) if the incident angle is below a critical angle. The critical angle is material dependent and related to material's electron density. As the incident angle increases above the critical angle, X-rays start to penetrate into the

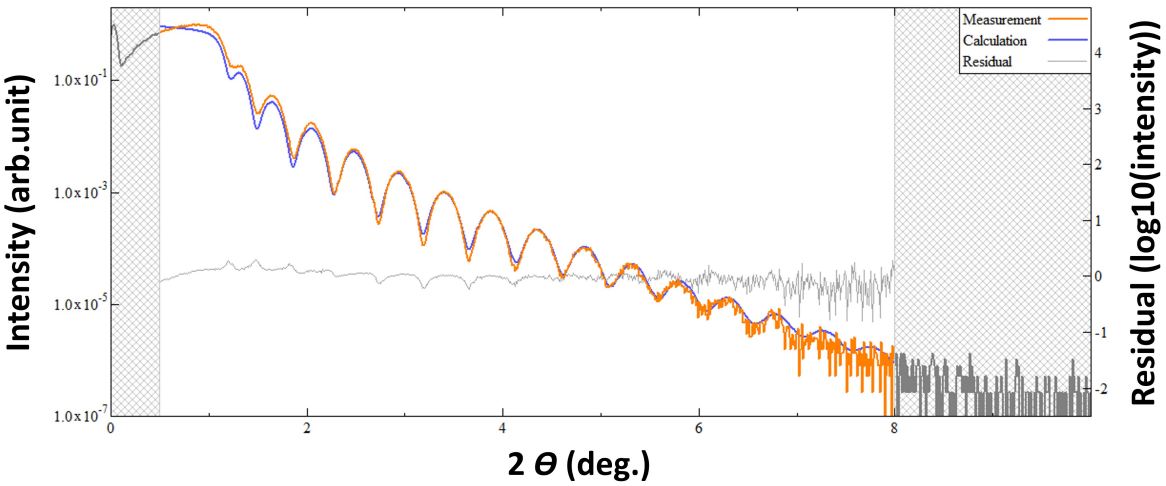

Figure 2.2. A example of XRR fringes on 17.8 nm Au deposited on glass substrate.

specimen. Then, at every interface, a portion of X-rays is reflected. The interference of these partially reflected X-rays results in a series of oscillation patterns (also known as Keissig fringes). Figure 2.2 presents an exemplar of Keissig fringes on pure Au thin film. On the fringes, the position of each valley after the critical angle is extracted at 2θ, its order is denoted as integer n (n = 1, 2, 3, ...). By linear fitting of $\sin^2\theta$ as a function of n^2, the interception of the linear fitting equation is commonly around 3×10^{-5} [45], given the wavelength of Cu $K\alpha$ radiation is 0.154 nm, the film thickness can be calculated using the following equation [46, 45]:

$$(\frac{\lambda}{2t})^2 = \frac{\sin^2\theta}{n^2} \tag{2.1}$$

Furthermore, by using fitting software GenX and Rigaku Globalfit, other important parameters such as the surface roughness and sample density can be obtained. Examples of GenX fitted XRR fringes can be found in the following chapters.

The θ-2θ XRD (Fig. 2.3) in high-angle regime ($2\theta > 15°$) brings more crystallography information, such as crystalline orientations, grain size, epitaxy nature, and internal stress. As X-rays penetrate through the specimen, they are diffracted by the atoms in the specimen structure. The diffracted beams interfere with each other when they leave the specimen. As the out-of-phase

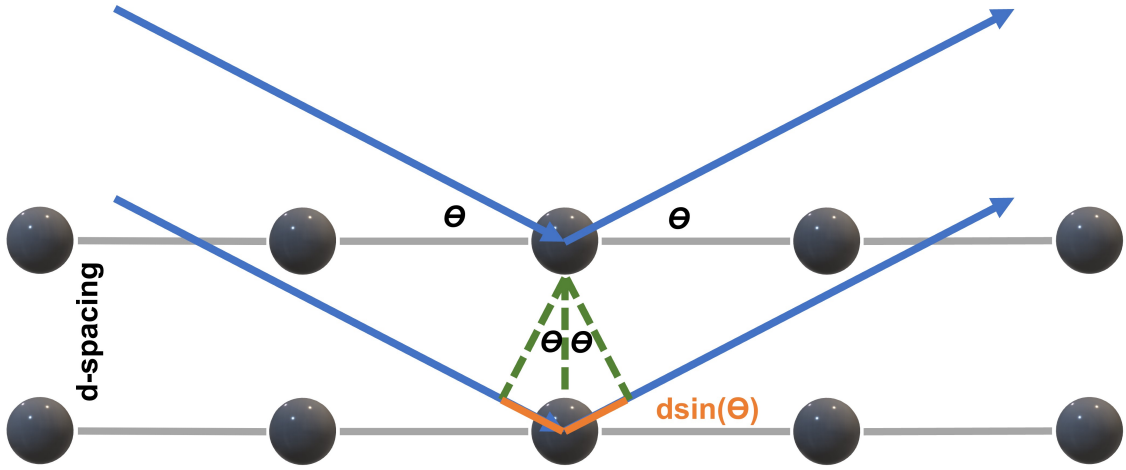

Figure 2.3. A schematic of Bragg's law of XRD

destructive interference cancels out some beams, the in-phase constructive interference results in a greater signal at a certain diffraction angle, where a diffraction peak takes place. The diffraction angle is directly linked to the d-spacing by Bragg's law:

$$n\lambda = 2d\sin\theta \tag{2.2}$$

The epitaxial thin film studied here usually exhibits only single family of peaks in the XRD spectrum, which is governed by the phase purity. Sometimes, additional textured peaks can be observable, but its corresponding grain size is small compared to far larger grain size of the epitaxial crystal. The mosiac spread (i.e. the distribution of out-of-plane grain orientations) can be characterized by a transverse diffusive scan, also known as ω scan, or rocking curve. Mathematically, ω value is equal to θ, but their physical meanings differ. As 2θ is fixed at a diffraction angle, the initial position of the absolute ω is half of 2θ. Then, specimen is "rocked" in a $\pm\ \omega$ range relative to the initial position. The full width at half maximum (FWHM) of the rocking curve can be obtained by fitting with standard Gaussian equation:

$$f(x) = \frac{1}{\sigma\sqrt{2\pi}}\exp -\frac{(x-\mu)^2}{2\sigma^2} \tag{2.3}$$

where σ is the standard derivation and μ is the mean. Note that the fitting should be performed with intensity in linear scale. Then the FWHM is calculated by:

$$FWHM = 2\sigma\sqrt{2\ln 2} \tag{2.4}$$

An example of ω scan in Fig. 2.4 presents a sharp peak with narrow FWHM, indicating a great epitaxy of Co $(10\bar{1}0)$ film. Moreover, the crystalline domain size, τ, which could be smaller or equal to the grain size, can be calculated by Scherrer equation:

$$\tau = \frac{K\lambda}{FWHM\cos\theta} \tag{2.5}$$

where the FWHM in Scherrer equation is the FWHM of θ-2θ diffraction peak. The rocking curve is also used to align the specimen tilting offset before performing XRD measurement. The θ-2θ XRD in this dissertation is specular, in other words, the specimen surface normal is the angle bisector of the incident beam and diffracted beam. However, in real life measurements, the specimen surface normal is always not aligned with the specular beams due to the crystal miscut and sample holder flatness. In general, a rocking curve is measured across a theoretical substrate peak position (e.g. Si (004) at 69.1°), the measured ω peak has an offset to the theoretical peak position, then this offset will be included during the following θ-2θ scan, this type of scan is alternatively called $2\theta/\omega$ scan. Intuitively, when θ-2θ scan is aligned to the substrate offset, then it will assume the thin film on the substrate has the same surface normal as that of substrate. It should be noted that all XRD data shown in this dissertation were aligned to the single crystal substrate.

Moreover, the in-plane XRD should be introduced to further characterize the epitaxial films. The in-plane XRD measures the side facelets of crystal and provides symmetry information. In a simplest scenario, on an epitaxial (100) film, the crystal builds like a cube since (100) is a square plane. When fixing the in-plane Bragg condition (named as $2\theta\chi$) to be the (100) peak

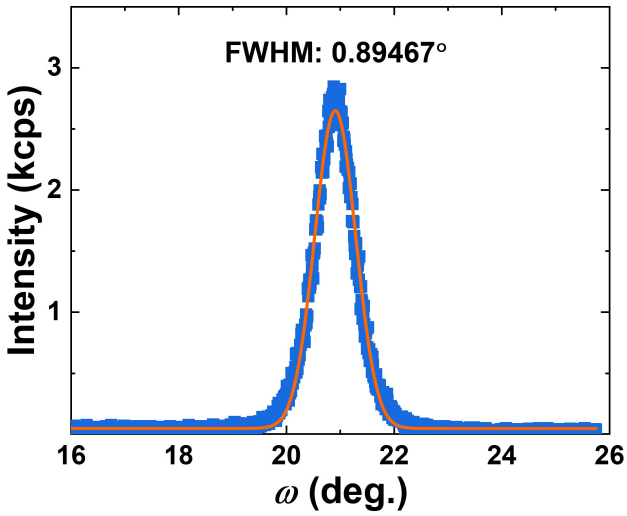

Figure 2.4. An example of ω scan which "rocks" across the Bragg condition of a 30-nm-thick Co $(10\bar{1}0)$ epitaxial film. The blue dots are data points which are Gaussian fitted as shown in the red solid line.

position, it should measure 4 diffraction peaks from the $\{100\}$ family when rotating the sample about its surface normal for 360° because there are 4 sides of a cube. This scan is called ϕ scan, which ϕ corresponds to the sample rotation angle. Furthermore, the in-plane XRD can also provide specular scan, which gives the diffraction peaks from the side facelets as a function of $2\theta\chi$, the procedure is similar to out-of-plane θ-2θ scan, which is not repeatedly described herein. A good epitaxial film should have correct amount of facelet diffraction peaks with a similar amplitude of each peak, making in-plane ϕ scan an important characterization approach.

Last but not least, to further assess the crystal structure, strain, and epitaxial relations, semi-sphere pole figures (Atlas mapping) provides a comprehensive mapping in a 3-dimensional space. In pole figure measurement, the Bragg condition is also fixed to the plane of interest. Again, in the simplest cube example, when Bragg condition is set to be (100). Pole figure essentially presents how many observable (100) facelets on the cube surface and inside the cube. If the cube levitates in the 3D space, there are total of 6 $\{100\}$ facelets. When the cube sits on sample holder, only 5 of $\{100\}$ facelets should be observable, as shown in the example of MgO (200) single crystal (Fig. 2.5). Similar to the ϕ rotation, the specimen rotation in pole figure is

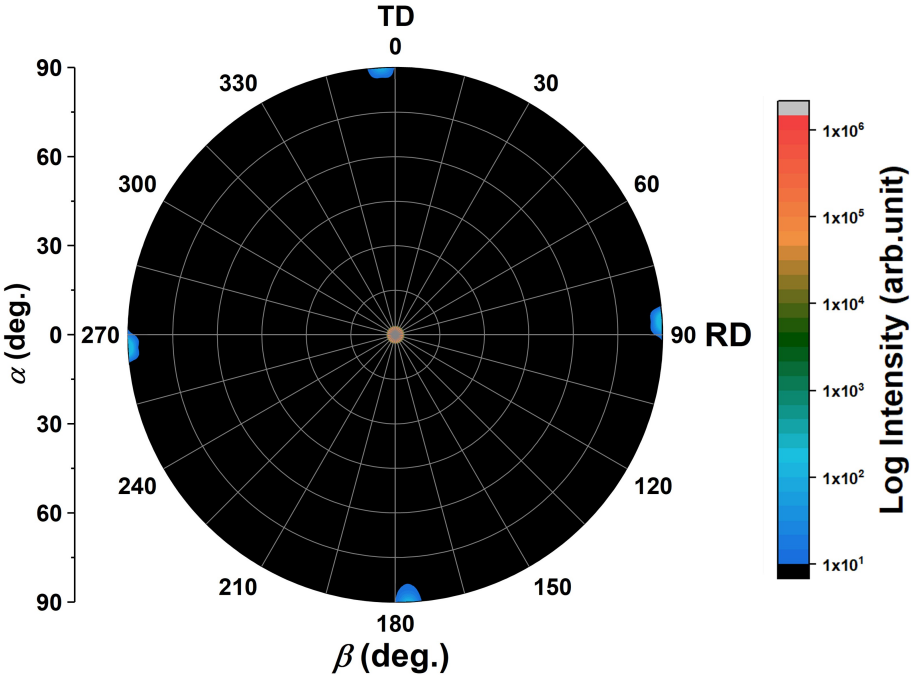

Figure 2.5. An example of pole figure measured on MgO (200) single crystal with Bragg condition fixed to be (200). The data gather into 5 points indicating the 5 side face of a cube. RD refers to "rolling direction". TD refers to "transverse direction".

denoted as β. Another important axis is α, when α equals to 0°, the incident beam and diffracted beam are in the sample plane. As α moves towards 90°, the incident beam and diffracted beam move to general out-of-plane θ-2θ configuration. Generally speaking, the measurement condition in Fig. 2.5 can be denoted as MgO $\{200\} < 002 >$, where $\{200\}$ means the specimen's surface normal aligned with 200 family plane, $< 002 >$ means the Bragg condition is fixed to be $< 002 >$ family direction. This denotation is adopted throughout the whole dissertation. In conclusion, the semi-sphere pole figure directly maps out the crystal structure in a spatial manner. More pole figures on differently oriented crystals can be found in the following chapters.

To summarize this section, XRR and XRD are non-destructive analytical techniques that are essential to characterize the thickness, roughness, and crystallinity in epitaxial thin film. XRR and XRD were performed using Rigaku Smartlab Diffractometor at CMRR Materials Characterization Facility. The power of the primary beam used in this dissertation was fixed to be 1.76 kW. The primary beam area is approximately 0.4 mm by 12 mm.

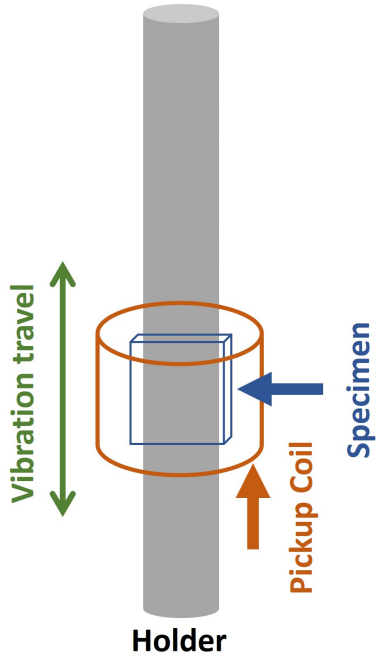

Figure 2.6. Schematic of the VSM operation principle.

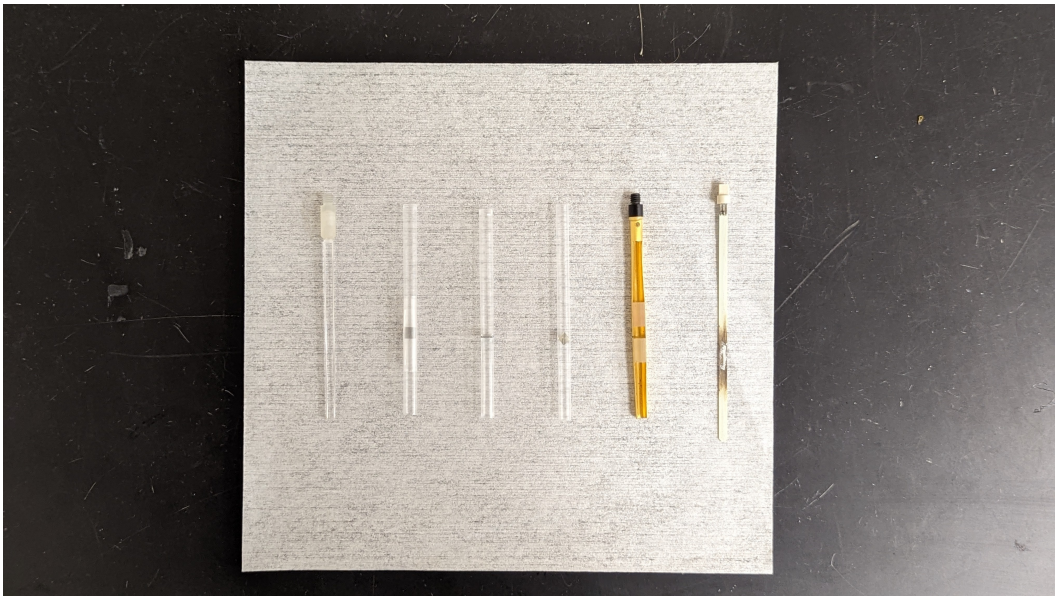

Figure 2.7. Exemplars of VSM sample holders. From left to right: quartz rod, straw with wrapped in-plane specimen, straw with side wall openings to fit out-of-plane specimen, straw with 4.1 mm by 4 mm specimen held diagonally, Cu holder with sliders, and oven option alumina holder.

2.3 Vibrating Sample Magnetometry

For magnetic materials, magnetic moment m, coercivity field H_C, and the shape of hysteresis loop are the key properties to be characterized. Apart from superconducting quantum interference device (SQUID), vibrating sample magnetometry (VSM) is another technique which probes the magnetic moment based on the fundamental Faraday's law of electromagnetic induction. As the specimen vibrates, the changing of magnetic flux results in an induction voltage V in the pickup coil:

$$V = \frac{d\Phi}{dt} = (\frac{d\Phi}{dz})(\frac{dz}{dt}) \tag{2.6}$$

where z represents the vertical travel of the specimen with respect to the pickup coil. t indicates the time-varying V. The V in the pickup coil is amplified by a pre-amplifier and detected by lock-in. The VSM operation can be better understood by Fig. 2.6. The dc magnetic moment m can be calculated from the induction voltage V using the following equation:

$$m = \frac{V}{2\pi f C A \sin(2\pi f t)} \tag{2.7}$$

where C is a coupling constant. A is the amplitude of the sinusoidal oscillation. f is the specimen vibration frequency, and the default f of Quantum Design Versalab VSM linear motor is 40 Hz. Dissertation author used 39 Hz and 40 Hz interchangeably. It should be noted that the difference of 1 Hz has no impact on m, H_C and the shape of hysteresis loop in this dissertation.

The specimen must be attached to a sample holder. The center of the specimen is positioned at the vertical center of the pickup coil, which is fixed at 35 mm from the bottom of the pickup coil. There are multiple ways of mounting the specimen on sample holder, as illustrated in Fig. 2.7. Note that users should secure the specimen to prevent shifting during vibrating measurements at various temperature conditions and be aware of the paramagnetic or diamagnetic background from the both sample holder and any potential impurities introduced

during mounting.

2.4 Microfabrication & Nanofabrication

As a part of the third industrial revolution, microfabrication is at the heart of integrated circuit industry. Microfabrication techniques bridge the full film samples to various devices that make numerous experiments possible. The major processes of microfabrication used in this dissertation are lithography, etching, and bonding. Figure 2.8 exhibits 3 examples of devices that were commonly fabricated by the dissertation author. Each kind consists of 2 layers: a sample layer (typically microstrips or nanowires) and an electrode layer. A general fabrication procedure is illustrated in Fig. 2.9, the first lithography is employed on the spin-coated full film to define the shape of the wire. Then, ion milling is performed to remove the rest of the material around the wire. This is followed by the second lithography process that aligns the electrode pattern on the wire, a layer of Au is deposited on the electrode pattern area which can be wire-bonded to the printed circuit board (PCB) for future measurements. Some key fabrication methods will be further discussed in the coming subsections.

2.4.1 UV Photolithography Patterning

To define the size, shape and the orientation of the wires that are patterned on the film, a mask with ”blocked area” and ”openings” is essential to be designed in the first place. Masks can be in the form of physical masks and digital masks. The physical mask is a fused quartz plate with pattern areas as openings or blocked by chromium. Thanks to computer-aided design (CAD) software, the mask design can be efficiently performed and modified. A physical mask is applied on Karl Suss MA6 mask aligner, while Heidelberg MLA150 has its own digital mask capability. Mask determines the pathway of the light, and photoresist determines the pattern polarity. In principle, photoresist is light-sensitive polymer solution. The positive (negative) photoresist breaks down (hardens) when exposed. Hardening refers to either polymerized or cross-linked, *vice versa*. Afterward, the developer dissolve away only the regions that were not

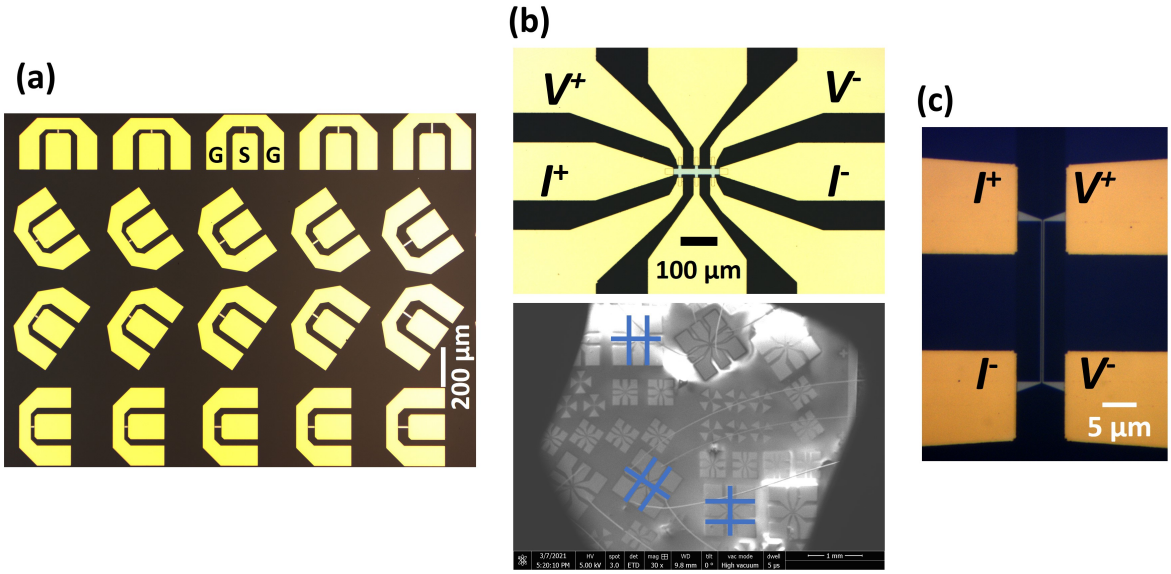

Figure 2.8. (a) 2-probe devices patterned in different orientations. (b) 4-probe devices. The scanning electron microscopy (SEM) picture shows an Au wire-bonded sample. The diameter of the Au wire is 25 μm. (c) 350 nm-wide Pt nanowires with nonlocal configuration of 300 nm separation.

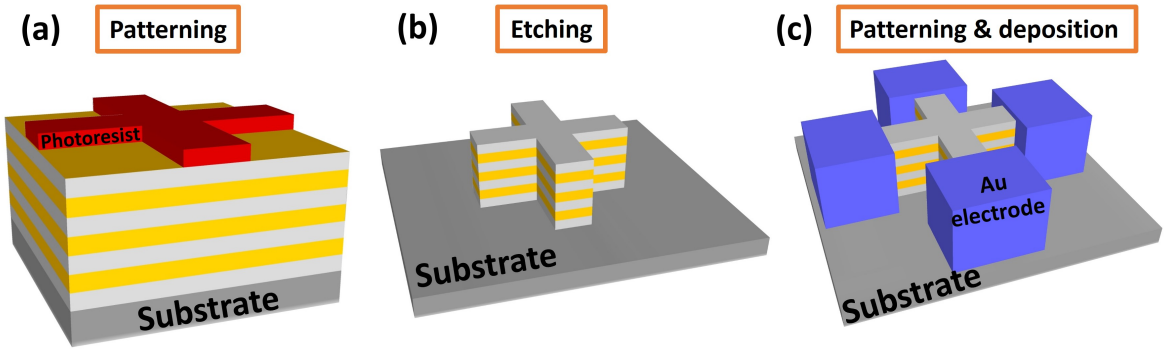

Figure 2.9. Schematic of a general 2-layer device fabrication process.

hardened. In MA6 mask aligner, the ultraviolet (UV) exposure duration was around 8 s (positive photoresist AZ-1512) and 15 s (negative photoresist NR9-1500PY) with light source intensity of 9 mW/cm^2. In MLA150 laser writer, the exposure dose was 130 mJ/cm^2 (positive photoresist AZ-1512) and 1200 mJ/cm^2 (negative photoresist NR9-1500PY). The wavelength used in both tools is 375 nm.

2.4.2 Ebeam Lithography Patterning

For advanced resolution that overcomes the wavelength and diffraction limit of the mask aligner and laser writer, Ebeam lithography is employed to be capable of direct writer (digital mask) with sub-10 nm resolution. Similarly, ebeam resist is ebeam-sensitive polymer solution with positive and negative tone. Ebeam lithography is performed by using a state-of-the-art Vistec EBPG5200 system with capability of a minimum beam diameter 2.2 nm at 100 pA. As shown in Fig. 2.8(c), for the non-local device patterned on surface of yttrium iron garnet (YIG), ebeam dose of 850 μC/cm^2 was applied polymethyl methacrylate (PMMA) A4 positive ebeam resist.

2.4.3 Ion Milling

Ion milling is a dry etching measure that is usually performed after defining the wire by lithography and developing. Compared to isotropic wet etching, dry etching is more anisotropic with fewer undercutting issues. Ion milling is mainly done in the aforementioned sputtering chamber or Oxford P80 system. The sample holder is negatively charged so that the sputter gas ions accelerate toward the sample and blast the material that is not protected by the photoresist. To mitigate the impact of ”burnt” photoresist after etching and the following lift-off issue, the common etching sequence for the devices in this dissertation was performed in repetition of 60 s etching with 60 s cooling using rf power of 50 W and 5 mTorr of Ar. Also, it is worth noting that the Ar etches the photoresist as well, the photoresist thickness should be considered by optimizing the spin-coating speed if the film to be etched is very thick.

2.5 Physical Properties Measurement System

Most of the work in this dissertation relies on a wide temperature range platform (1.8 K - 400 K) with high magnetic field capability (-9 T to 9 T), which is the keystone of a Quantum Design Physical Properties Measurement System (PPMS). Its temperature and magnetic field functionality is achieved by Nb_3Sn superconducting magnet with liquid helium environment. The PPMS is capable of a large variety of physical properties measurements, its standard options include electrical resistivity, *I-V* curve, Hall effect, magnetoresistance with 370° rotation capability, heat capacity, VSM, susceptibility, and torque magnetometry. Moreover, its programmable temperature and magnetic field control make PPMS a superb platform for customized experiments on any specimen that is operational in the PPMS chamber.

2.6 Spin-Torque Ferromagnetic Resonance (ST-FMR) Measurement Setup

To quantify the charge-to-spin current conversion efficiency in spin source material, a spin-torque ferromagnetic resonance (ST-FMR) setup was built in the Fullerton lab. First of all, it should be noted that ST-FMR is sometimes mistakenly referred to spin pumping technique. Both measurements are performed on spin source(detector)/magnet heterostructure shared with similar hardware setup. In spin pumping technique, the FMR excited spin accumulation is detected by large SOC material and converted to measurable charge current via inverse spin Hall effect (ISHE). On the other hand, in ST-FMR, an in-plane rf charge current is injected into spin source. An oscillating spin current can be generated and diffuse into the adjacent magnet. The magnet local magnetization is subsequentially manipulated by both out-of-plane Oersted field torque and in-plane SOT. These oscillating torques initiates the precession of magnetization around the in-plane effective magnetic field, which brings oscillatory change in resistance arising from the anisotropic magnetoresistance (AMR) of magnet layer. The highest precession amplitude is found to occur at FMR frequency. Resulted of mixing the oscillatory resistance and rf current, a

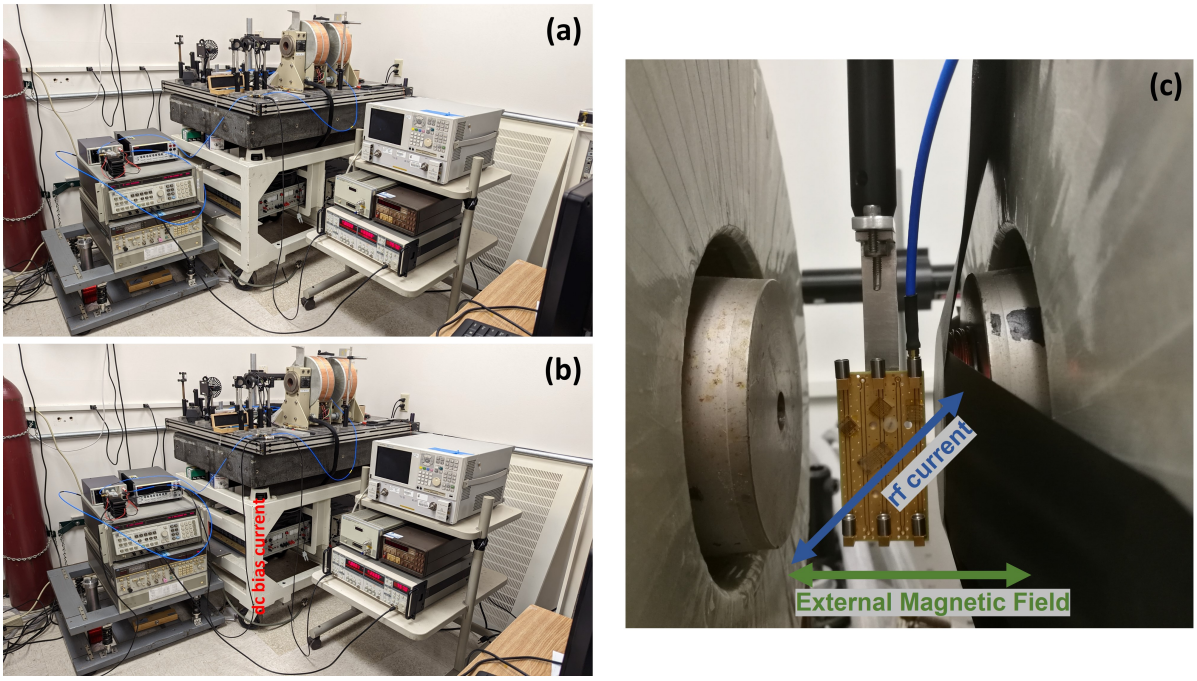

Figure 2.10. (a) Setup of ST-FMR for lineshape method. (b) Same setup with additional dc bias current. (c) Specimen mounted on CBCPW PCB with external magnetic field in the plane with coax rf cable connected to the right channel. A customized coil is attached to the right pole, serving as field modulation.

dc voltage V_{mix} can be measured.

To execute the aforementioned procedure, an ST-FMR hardware setup was built up, as shown in Fig. 2.10. The rf current is supplied by HP 8340B signal generator with power fixed to be 0 dBm (decibel-milliwatts). The rf current is also amplitude-modulated by a carrier wave generated by SR830 lock-in. The carrier wave was optimized to have an amplitude of 0.5 - 0.7 V and frequency of 757 Hz. The frequency is chosen to be a prime number. Then, the rf current will be amplified by a Mini-Circuit ZVE-3W-183+ amplifier to gain a total output power of roughly 30 dBm. The amplifier is powered by an EVENTEK KPS305D dc power source with a constant voltage of 15 V. The amplified rf current is connected to a bias tee and further connected to a customized PCB. The PCB is a conductor-backed coplanar waveguide (CBCPW) which is designed to have ground-signal-ground (GSG) configuration. The specimen is mounted on PCB as presented in Fig. 2.10(c), the signal channel is wire-bonded to one terminal of the microstrip,

and ground panel is wire-bonded to the other terminal which corresponds to the GSG devices shown in Fig. 2.8. The loss on the PCB transmission was calibrated by Vector Network Analyzer (VNA) , which was measured to be negligible below 10 GHz. Therefore, we assume most of the loss originated from the wire bond.

As rf current flow through the microstrip, the in-phase reflected signal passes through the dc channel on bias tee and is detected as a dc voltage by the lock-in. Simultaneously, the horizontal dc magnetic field is controlled by lock-in voltage output. Moreover, as shown in Fig. 2.10(c), some specimens are askew at angle θ, which is denoted as the angle between the microstrip and the magnetic field. The detected V_{mix} is is proportional to $\cos^2\theta \sin\theta$. It can be understood that the V_{mix} has a maximum value when $\cos\theta^2 \sin\theta$ has the largest amplitude at θ = 35°. Therefore, the microstrip should be oriented to be 35° to the external magnetic field for the optimal V_{mix} detection. In reality, $\theta = 45°$ is a commonly accepted configuration.

According to the above procedure, it is a 2-probe transport configuration. Therefore, the device fabrication is critical for a well-controlled contact resistance, because both the microstrip resistance and the contact resistance need to be taken into account for impedance (Z_m) matching. Furthermore, since it is only a 2-probe configuration, why are there 2 grounding electrodes in the aforementioned GSG devices? The symmetric GSG design is chosen over asymmetric GS design for balancing the current-induced out-of-plane Oersted field [47].

The setup in Fig. 2.10(a) is a general configuration for lineshape measurements only. In Fig. 2.10(b), a different configuration is used for tuning the linewidth by dc current-induced SOT, which will be discussed in detail in chapter 3. Technically, an additional dc bias current is applied onto the bias tee by Keithley 2400 or Keithley 220 sourcemeter. Note that unlike the dc current pulse mentioned in the SOT switching example in chapter 1, the current in this measurement was supplied continuously, which can cause significant Joule heating because the power of heating is proportional to the square of current. Therefore, the current used in experiment was kept below 10 mA.

To date, most of ST-FMR measurements are performed at ambient temperature, which

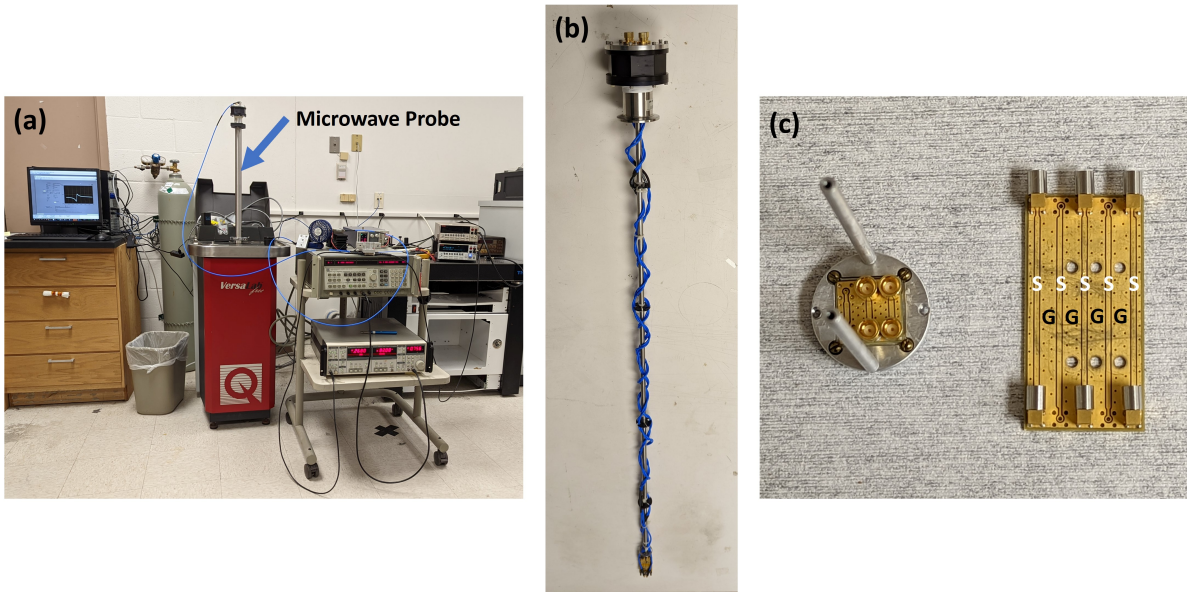

Figure 2.11. (a) Hardware setup of temperature-dependent ST-FMR utilizing QD Versalab platform (50 K - 400 K, up to 3 T). (b) Customized probe platform with 4 rf high frequency channels. (c) Customized in-plane and out-of-plane CBCPWs.

limits its perspectives of temperature-dependent applications, for example, materials with magnetic phase transition are especially intriguing due to the potential of becoming tunable SOT sources. The dissertation author set up a temperature ST-FMR based on a Quantum Design probe assembly with customized in-plane and out-of-plane CBCPW. The temperature-dependent ST-FMR can be operational in Quantum Design Versalab and PPMS, as shown in Fig. 2.11. Materials with magnetic phase transition can be good candidates for temperature-dependent SHE measurement, such as FeRh, $FePt_3$ and rare earth materials.

Chapter 3

Crystalline Orientation Dependent Spin Hall Effect in Epitaxial Platinum

3.1 Introduction

Over the past decade, significant research efforts have been devoted to investigating magnetization manipulation in heavy metal (HM)/ferromagnetic material (FM) heterostructure via spin-orbit torque (SOT) [48, 49, 20, 50, 51, 52]. By engineering the bulk spin Hall effect (SHE) in HMs [13, 53] and interfacial Rashba-Edelstein effect (REE) [54, 55, 56], enhanced SOT values can be achieved that have the potential for developing novel energy-efficient magnetic memory [57], logic [58], and neuromorphic computing devices [59]. Conventional SOT studies mainly focus on textured HMs such as Pt [60], Au [61, 62], β-W [63, 64], and β-Ta [65], and transition metal alloys e.g., Cu-Ta [66] and Fe-Pt [67]. More recently, epitaxial materials with tunable crystalline anisotropy and well-defined orientations have been recognized as promising candidates for SOT studies [68, 69, 70, 71, 72, 73, 74, 75]. Fruitful research highlights crystalline dependent anisotropic properties, for example, crystalline-orientation dependent spin relaxation mechanism in Pt (111) [76] and enhanced SHE in epitaxial metal (Ta (111) [77]), magnetic alloys (Mn_3Ge (0002) [78]), and topological insulators (BiSb (012) [79], Bi_2Se_3 [80]). Particularly, the facet-orientation-dependent SOT in epitaxial antiferromagnetic $IrMn_3$ is contributed by orientation-dependent intrinsic SHE [81]. Likewise, crystallographic-dependent SOT could present in epitaxial HMs when spin current is generated in different crystalline orientations.

In this chapter, we detail the growth of epitaxial Pt thin films and Pt/FM heterostructures with (200), (220), and (111) crystalline orientations. In epitaxial films, symmetries of the magnetic interactions will reflect the underlying crystal and interface symmetries where the three orientations studied have four-fold, two-fold, and three-fold surface symmetries, respectively. The symmetries should be reflected in fundamental properties such as interfacial anisotropy (both in-plane and out-of-plane) [82] and Dzyaloshinskii-Moriya interaction (DMI) [83, 84]. For low symmetry systems such as Pt (220) with C_{2v}, the strength of the DMI may vary in magnitude or sign along different directions [85, 86, 87, 88, 89]. Such anisotropic DMI and anisotropy can stabilize novel phases such as antiskyrmions [86].

In this study, we focus on the SHE with the current flowing in various symmetry directions in Pt. By quantitatively evaluating the SOT along in-plane crystalline orientations via spin torque-FMR (ST-FMR) measurements, isotropic and anisotropic SHE has been observed and the role of the crystal symmetry is enumerated. Moreover, by performing temperature-dependent harmonic measurements, we further reveal the intrinsic and extrinsic mechanisms underlying the SHE in epitaxial and polycrystalline Pt films. By combining directional-dependent SOT and anisotropic magnetic properties, we anticipate energy-efficient magnetization manipulation in novel spin structures.

3.2 Sample Growth and Characterization

Epitaxial Pt films were grown onto single-crystalline MgO (200), MgO (220), and Al_2O_3 $(11\bar{2}0)$ substrates by dc magnetron sputtering. Here, we note that, $(11\bar{2}0)$ is a forbidden peak in Al_2O_3. Instead, the corresponding allowed peak is $(2\bar{1}\bar{1}0)$. But we chose $(11\bar{2}0)$ over $(2\bar{1}\bar{1}0)$ as a widely-accepted prescriptive denotation in academia and industry. Substrates are commercially purchased from MTI corporation. Substrates dimensions are 5 mm by 5 mm by 0.5 mm and 10 mm by 10 mm by 0.5 mm. The sputtering chamber had a base pressure of 8×10^{-8} Torr and a growth Ar pressure of 2.7 mTorr. Pt (200) was grown on Cr (200)-buffered MgO (200) substrates.

The 5-nm-thick Cr (200) seed layers were deposited at 450°C to initiate the epitaxy, followed by Pt (200) deposition at 200°C. Pt (220) and Pt (111) films were grown directly on MgO (220) and Al_2O_3 $(11\bar{2}0)$ substrates, respectively, at 300°C. The growth procedures have been optimized for both epitaxy and desirable smooth surface condition. After the Pt growth, the substrate was naturally cooled to room temperature *in situ* which takes roughly 180 minutes. Subsequential FM layers were grown *in situ* at room temperature to minimize the interfacial mixing effect and magnetic dead layers. All samples were capped with a 2-nm-thick amorphous Al_2O_3 layer to prevent surface oxidation. Following the above procedure, we prepared a series of epitaxial Pt(10)/Py(8) samples for ST-FMR measurements, and both epitaxial Pt (111)(5)/Co(0.8)/Ni(1) and polycrystalline Pt(15)/Co(0.8)/Ni(1) samples with perpendicular magnetic anisotropy for harmonic measurements (thickness in nanometer throughout the chapter unless otherwise stated). Note that the choice of Py as the FM layer is motivated by its wide application as an efficient spin detector [60, 90, 91, 92, 93, 94, 95] and the usage of Co/Ni is due to its spontaneous perpendicular magnetic anisotropy, a prerequisite for harmonic measurements [96, 97].

3.2.1 XRD Characterization

The crystallographic properties of as-deposited Pt films were evaluated by X-ray diffraction (XRD) measurements. The out-of-plane symmetric θ-2θ scans of Pt (200), Pt (220), and Pt (111) films are presented in Figs. 3.1(a)-(c), demonstrating the single phase epitaxy growth along the substrates or the seed layers. The clear Laue oscillations of the Pt (111) peak indicate excellent lattice matching and a sharp Al_2O_3/Pt interface. Figs. 3.1(d)-1(f) show the in-plane XRD ϕ scan, confirming the characteristic four-fold symmetry of Pt (200) film and two-fold symmetry of Pt (220) film. Note that the Pt (111) sample exhibits a six-fold symmetry, which is attributed to crystal twinning.

Moreover, the relative orientation between the crystalline axis of the Pt thin films and substrates has been verified by both ϕ scans and semi-sphere pole figures, as shown in Figs. 3.2, 3.3 and 3.4. Specifically, for the Pt (200) sample, the in-plane Pt $< 002 >$ aligns with

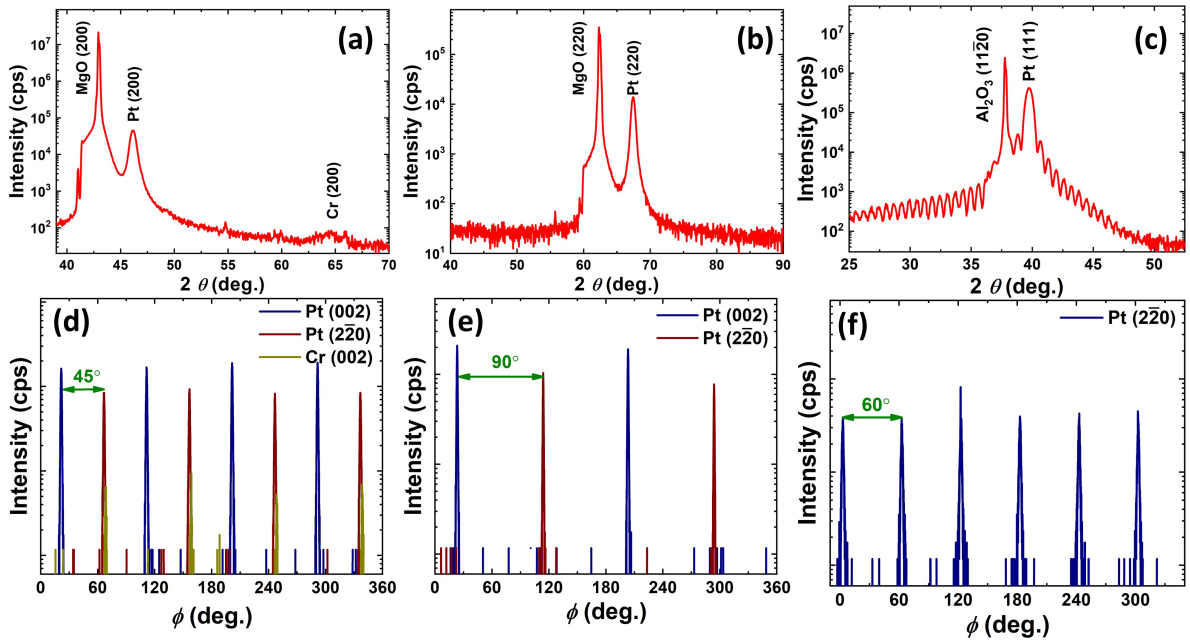

Figure 3.1. Out-of-plane XRD scan of epitaxial Pt films: (a) MgO (200)/Cr (200)/Pt (200). (b) MgO (220)/Pt (220). (c) Al_2O_3 (11$\bar{2}$0)/Pt (111). (d)-(f) In-plane ϕ scans showing epitaxial growth and the four-fold, two-fold, and six-fold symmetry of Pt (200), Pt (220), and Pt (111), respectively.

MgO $<002>$ and is 45° to in-plane Cr $<002>$ and Pt $<2\bar{2}0>$. For the Pt (220) sample, the in-plane Pt $<002>$ // MgO $<002>$ and Pt $<2\bar{2}0>$ // MgO $<2\bar{2}0>$. For the Pt (111) sample, the in-plane Pt $<2\bar{2}0>$ is perpendicular to in-plane Al_2O_3 $<0001>$.

3.2.2 XRR Characterization

By fitting the low-angle X-ray reflectivity (XRR) data using GenX software, the surface roughness of the deposited Pt (111), Pt (220), and Pt (200) films are obtained to be 0.085 nm, 0.25 nm, and 0.37 nm (Fig. 3.5), respectively. The remarkably smooth surface condition of the prepared epitaxial Pt thin films contributes to a sharp HM/FM interface, which is the key to reducing inhomogeneous linewidth broadening [98] and improved spin current conductance [99]. We highlight that some previous studies of Pt (220) films observed significant surface roughness [100] which we have ameliorated.

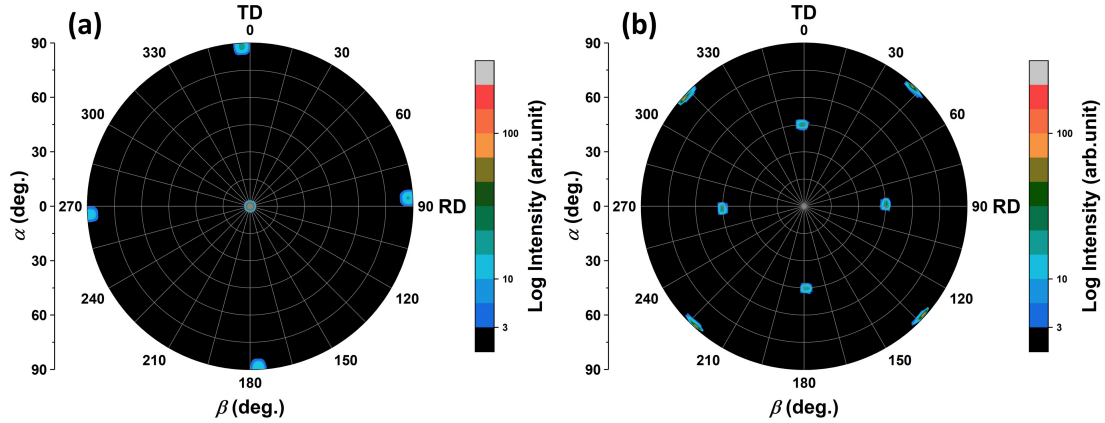

Figure 3.2. (a) and (b) Pole figures Pt $\{200\}<002>$ and Pt $\{200\}<2\bar{2}0>$.

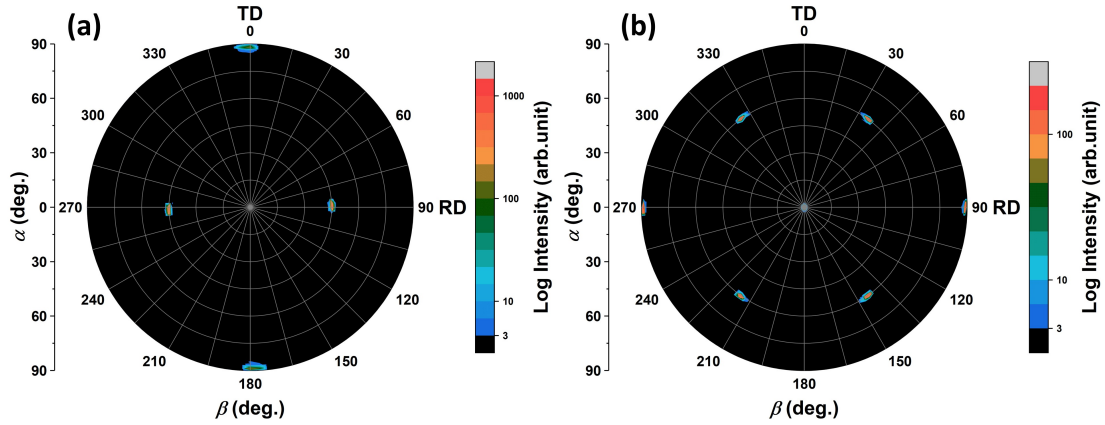

Figure 3.3. (a) and (b) Pole figures of Pt $\{220\}<002>$ and Pt $\{220\}<2\bar{2}0>$.

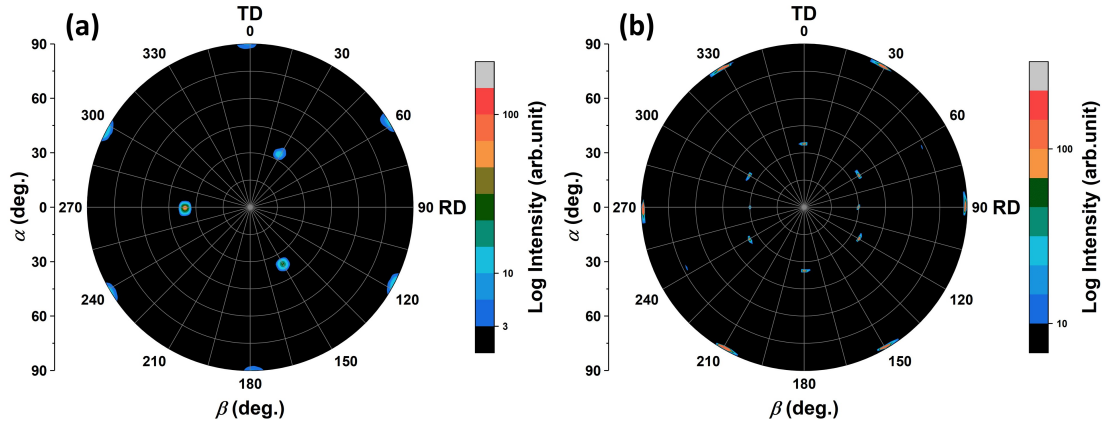

Figure 3.4. (a) and (b) Pole figures of MgO $\{111\}<2\bar{2}0>$ and (b) Pt $\{111\}<2\bar{2}0>$.

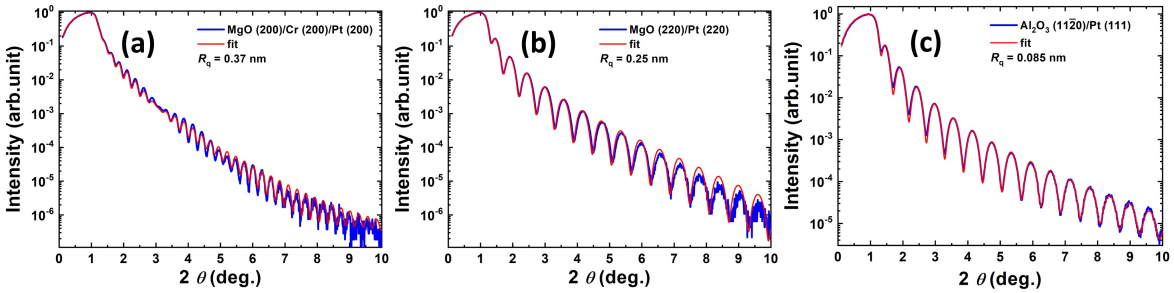

Figure 3.5. (a)-(c) Fitting of X-ray reflectometry data shows smooth surface on Pt (200), (220) and (111) films.

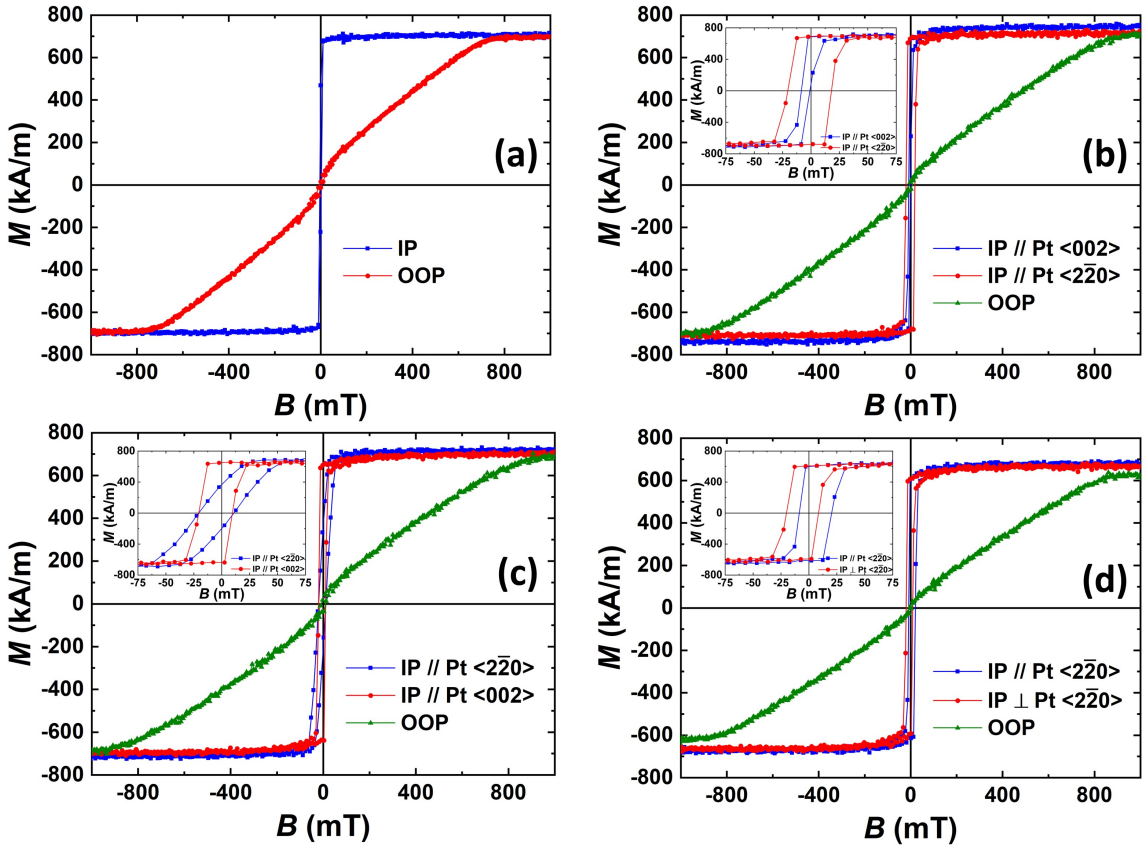

Figure 3.6. (a)-(d) *M* vs *B* curves on reference sample Py(8), Pt (200)(10)/Py(8), Pt (220)(10)/Py(8) and Pt (111)(10)/Py(8) films. Insert: zoom-in view of *M* vs *B* curves shows the in-plane anisotropy of Py induced by Pt.

3.2.3 Magnetometry Characterization

The magnetic hysteresis loop of Py was characterized by VSM on full film samples (Fig. 3.6). By normalizing the M to the volume of Py film, the saturated magnetization M_S is around 698 kA/m. Here it should be noted that Py exhibits isotropic in-plane behavior in a bare polycrystalline Py(8) film and Pt/Py(8) with high symmetries. However, on Pt (220)/Py(8) sample, the in-plane anisotropy is clearly observed with easy axis along Pt (002). The in-plane anisotropic Py induced by low symmetry Pt will also play a role in affecting the FMR resonance field of Py, which can be seen in the next section.

3.3 Experimental Transport Results

3.3.1 ST-FMR Measurements via Lineshape Analysis

Here we introduce our ST-FMR measurement technique to characterize the charge-to-spin conversion efficiency J_S/J_C of the deposited epitaxial Pt films. Figure 3.7(a) illustrates the schematic of our ST-FMR measurement setup. A microwave current is applied along specific in-plane crystalline directions in the Pt layer determined by lithography. Due to the combination of the SHE and spin diffusion effects, oscillating spin currents can be generated in the Pt films and transport across the Pt/Py interface and are absorbed by the adjacent Py layer. The out-of-plane Oersted field torque and the in-plane SOT will drive precessional motion of the Py magnetization around the direction of the in-plane effective magnetic field, leading to an oscillatory change in resistance arising from the anisotropic magnetoresistance (AMR) of Py. The largest precession amplitude is found to occur at the ferromagnetic resonance (FMR) frequency of the Py layer. Mixing the oscillatory resistance and the applied rf current will give rise to a dc voltage, which can be detected by a lock-in amplifier with a modulated rf current.

Figure 3.7(b) shows the optical image of the photolithographically patterned microstrips with varied aspect ratios for impendence matching and different orientations of the current which is designed to align with the crystalline orientations in the prepared Pt/Py films. Ti(6)/Au(200)

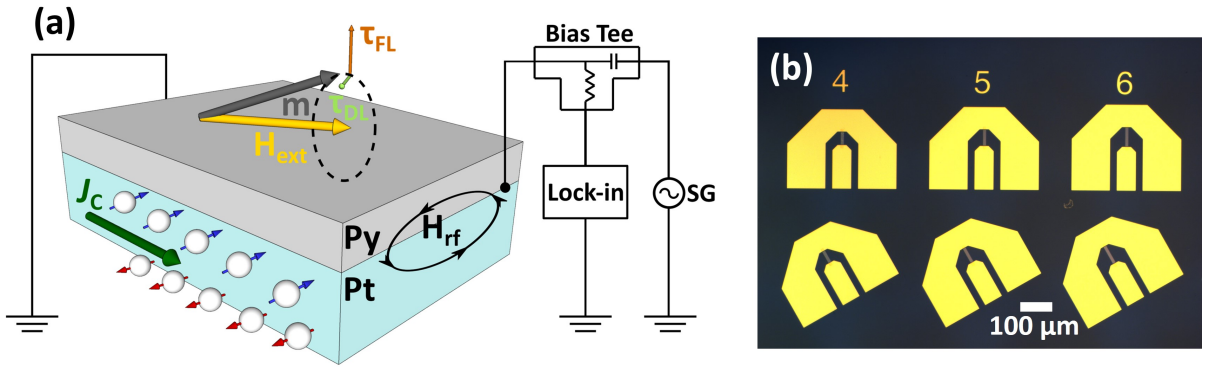

Figure 3.7. (a) Schematic diagram of ST-FMR measurement setup. (b) Optical microscope image of patterned Pt/Py CPWs with ground-signal-ground electrodes.

electrode pads are fabricated for symmetric GSG contact electrodes by sputtering and lift-off technique. For rf measurements, the Au thickness of 200 nm is chosen for less loss. The rf current is applied to the CPW channels via wire bonding from the ground-signal-ground electrodes to the microstrip. The in-plane external magnetic field is oriented 45° relative to the CPWs to improve the magnitude of the measured ST-FMR signals [91]. Measurement of the induced dc voltages takes advantage of a bias tee which separates the input rf microwave currents and the ST-FMR signals. All the ST-FMR measurements presented in this work were performed at room temperature. Although the amplified rf power is relatively high (30 dBm). The measured dc voltage follows a linear dependence on the applied microwave power, as shown in Fig. 3.8(d), suggesting the marginal role of the Joule heating effect in our measurements.

The ST-FMR technique provides a quantitative measurement of the J_S/J_C of the prepared epitaxial Pt films. The lineshape of the measured dc voltage can be expressed as a combination of symmetric Lorentzian and antisymmetric Lorentzian [11, 101, 102]:

$$V_{mix} = S\frac{(\Delta/2)^2}{(B-B_0)^2+(\Delta/2)^2} + A\frac{(\Delta/2)(B-B_0)}{(B-B_0)^2+(\Delta/2)^2} + background \tag{3.1}$$

where the parameter S is the amplitude of symmetric Lorentzian arising from the spin Hall induced anti-damping SOT exerted on Py, A is the amplitude of antisymmetric Lorentzian resulted from the sum of field-like SOT and Oersted field torque, B_0 is the resonance field of

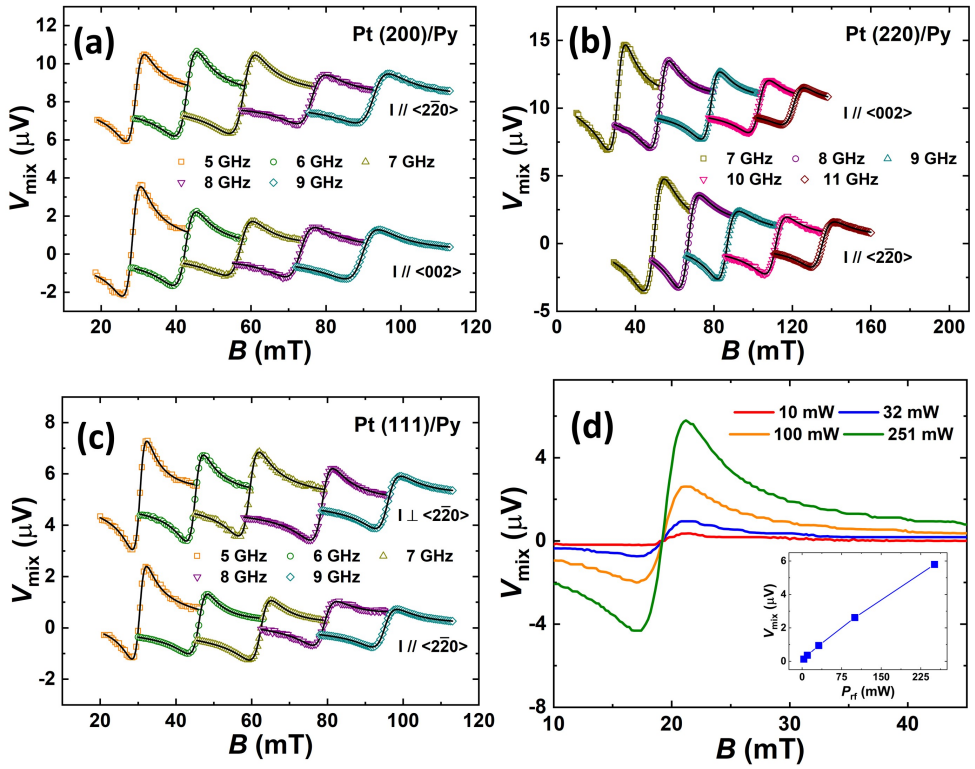

Figure 3.8. (a)-(c) The measured ST-FMR spectra (open dots) with fitting curves (solid lines) on Pt/Py. The curves are offset for visual clarity. (d) rf power-dependent ST-FMR spectra. Insert: the V_{mix} with a linear dependence on the input microwave power. Power in dBm was converted to mW.

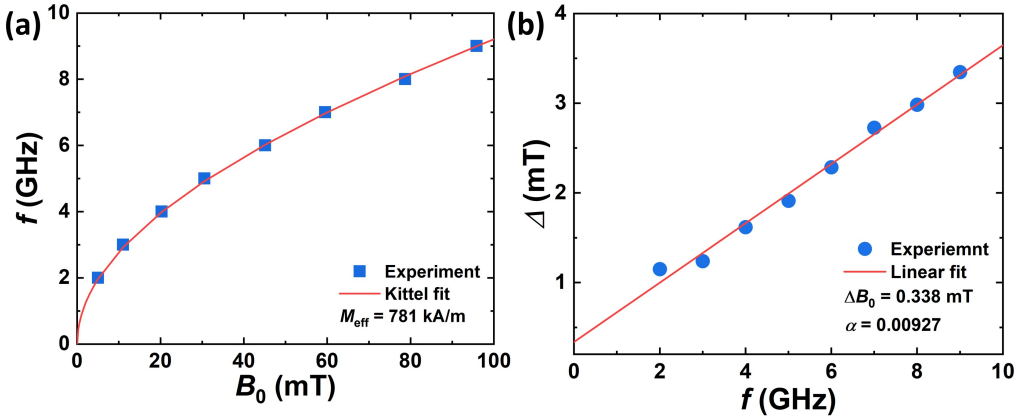

Figure 3.9. (a) An example of Kittel fitting on Pt (111)/Py(8) sample. (b) The fitted inhomogeneity supports a marginal linewidth broadening and sharp interface.

each frequency, and Δ is the fitted full-width-half-maximum (FWHM) linewidth of resonance spectrum resulted from the Py layer. The ratio between S and A is directly proportional to the dimensionless J_S/J_C, which can be further expressed by the following equation [60]. Pay attention to the confusion between SI system of units and cgs system of units in magnetic terms, all the calculation in this chapter was executed using SI.

$$\frac{J_S}{J_C} = \frac{S}{A}\frac{e\mu_0 M_S t d}{\hbar}\sqrt{1+\frac{4\pi M_{eff}}{B_0}} \tag{3.2}$$

where μ_0 is the permeability in vacuum, $\hbar$ is the reduced Planck constant, e is elementary charge, M_S is the saturated magnetization of Py. t and d represent the thickness of Py and Pt layers, respectively. M_{eff} is the effective magnetization of Py which can be obtained from fitting the frequency dependent resonance field by Kittel formula [103]:

$$f = \frac{\gamma}{2\pi}\sqrt{B_0(B_0+4\pi M_{eff})} \tag{3.3}$$

Intuitively, the resonance frequency of a sphere needs to exclude the shape anisotropy term, therefore $f_{sphere} = \gamma B_0$. Additionally, the frequency-dependent linewidth Δ can be expressed as a combination of inhomogeneity and Landau-Lifshitz or Gilbert damping [104]:

$$B_0 = \Delta B_0 + \frac{4\pi\alpha}{\gamma} f \tag{3.4}$$

Examples of Kittel fitting and linewidth broadening can be found in Fig. 3.9, indicating highly consistent ST-FMR spectrum, minimal linewidth broadening and low loss damping in Py.

Figure 3.8(a)-(c) show the experimental ST-FMR resonance spectrum measured on Pt (200)/Py, Pt (220)/Py, and Pt (111)/Py samples with microwave frequencies varying from 5 to 11 GHz. Due to the larger saturation field of Py resulted from the in-plane anisotropy, measurements of the Pt (220)/Py sample are mainly focused in the high-frequency regime. For Pt (220)/Py, the shift of the resonance fields when the rf current applied along different crystalline directions is

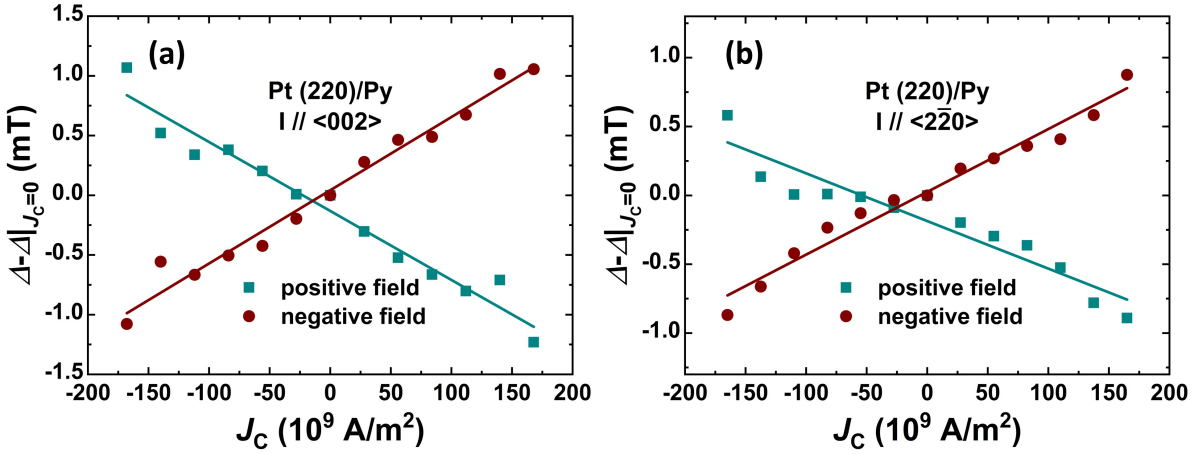

Figure 3.10. FMR linewidth as a function of applied dc current at a microwave frequency f = 7 GHz for current along (a) $< 002 >$ and (b) $< 2\bar{2}0 >$ on Pt (220)/Py, respectively. Solid lines are linear fitting. The linear linewidth vs current density behavior is evidence of limited Joule heating.

attributed to the in-plane anisotropy of Py induced by Pt (220) with low symmetry (C_{2v}). While in high symmetry systems (C_{4v} and C_{3v}) of Pt (200) and Pt (111) samples, nearly isotropic Py magnetic property makes the resonance fields independent of the in-plane direction. The experimental results (open dots) were well-fitted with Eq.3.1 (solid lines) with coefficient of determination R^2 above 0.99. It is worth mentioning that the line-shape method based on Eq. 3.2 only provides an estimation of the upper limit of J_S/J_C due to resonance-driven spin pumping effect from Py back to Pt as reported in the previous work [91, 94].

3.3.2 ST-FMR measurements via Linewidth Modulation

To independently verify the results obtained from the lineshape method, we also performed linewidth modulation measurements. By applying a dc current to the patterned Pt/Py microstrip, a static anti-damping torque effectively modulates the Gilbert damping of Py, resulting in a systematic current-dependent variation of the linewidth of the obtained ST-FMR spectra.

Based on the spin-transfer torque (STT) model [11], the injected dc spin currents effectively increase (decrease) the damping of Py layer when the spin polarization is parallel

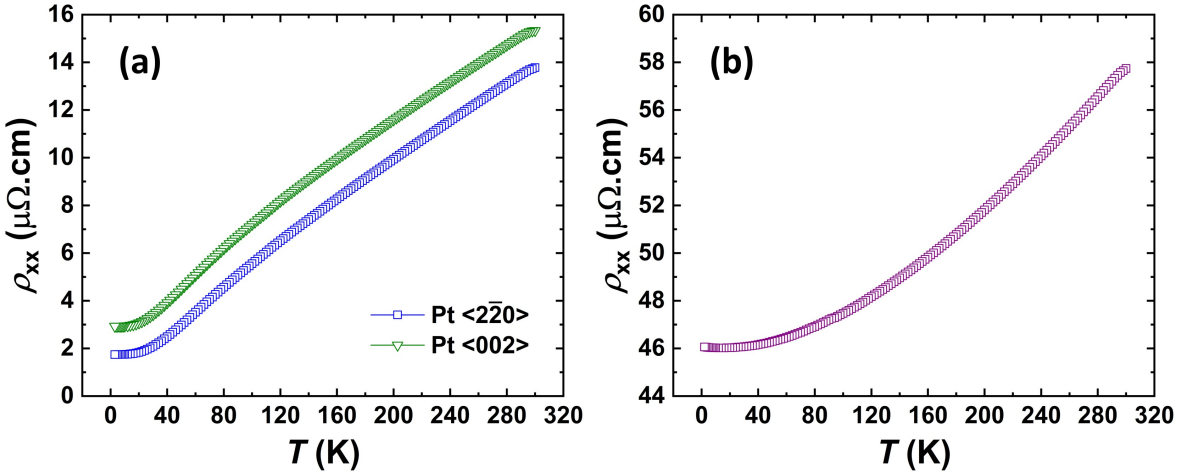

Figure 3.11. 4-probe longitudinal resistivity measurements on patterned (a) Pt (220)(10) and (b) Py (8) control samples. Note that Pt $< 2\bar{2}0 >$ has much lower resistivity than Pt $< 002 >$.

(antiparallel) to the Py magnetization, leading to a broadened (reduced) ST-FMR linewidth [60, 105]. Furthermore, reversing the polarity of the external magnetic field that saturates Py magnetization will also lead to the sign change of the observed signals, as illustrated in Fig. 3.10. Quantitatively, J_S/J_C can be obtained from the slope of the dc current dependent resonance linewidth of Py [60, 68, 94]:

$$\frac{J_S}{J_C} = \frac{\gamma e(B_0 + \mu_0 M_{eff}/2)M_S t}{2\pi f \hbar \sin\varphi} \frac{d\Delta}{dJ_C} \tag{3.5}$$

where φ is the angle between dc current and external magnetic field, f is the FMR frequency, γ is the gyromagnetic ratio, and J_C is the electric current density in the epitaxial Pt layer.

Figure 3.10 presents the results of modulated linewidth as a function of J_C in Pt (220)/Py(8) sample. The y-axis represents the change of linewidth normalized to the reference linewidth when dc current is not present. The x-axis represents the dc current density in Pt. It can be understood that only the charge current in Pt layer is assumed to be the source of spin current. Therefore, it is required to characterize the resistivity of each layer. Individual films of Cr(200)(5), Pt(200)(10), Pt(220)(10), Pt(111)(10), and Py (8) were deposited and patterned into 4-probe configuration, and the longitudinal resistivity ρ_{xx} along various crystalline orientations

of Pt has been characterized independently, example ρ_{xx} vs temperature T curves are presented in Fig. 3.11. Only in this way can J_C be quantitatively calculated from the portion of current distribution based on the parallel resistor model. As shown in Figs. 3.10(a) and (b), when the electric current is along the $< 002 >$, the slope is approximately 54% larger than that when the current is along $< 2\bar{2}0 >$. We note that such distinct crystalline orientation-dependent SHE is absent in higher symmetry Pt (200)/Py and Pt (111)/Py samples.

3.3.3 ST-FMR Results Discussion

To summarize our ST-FMR results, Table 3.1 shows the obtained J_S/J_C of Pt along different crystalline orientations of the prepared epitaxial Pt films. In general, a larger value of J_S/J_C is observed in the sample with a higher ρ_{xx}. In the high symmetry systems such as square Pt (200) and hexagonal Pt (111) lattice with C_{4v} and C_{3v} symmetry, the difference between ρ_{xx} along different in-plane crystalline orientations is less than 5%, within the experimental error. Notably, the isotropic ρ_{xx} yields isotropic J_S/J_C in Pt (220) and Pt (111) samples. Isotropic J_S/J_C has been observed in other high symmetry epitaxial materials, such as $SrIrO_3$ (0001) [70] and Fe (001)/Pt [106]. In contrast, in the low symmetry system (C_{2v}) of Pt (220), the $\rho_{xx}^{<002>}$ is 11% larger than $\rho_{xx}^{<2\bar{2}0>}$. The obtained value of J_S/J_C along $< 002 >$ direction is significantly larger than that along $< 2\bar{2}0 >$ direction via both line-shape and linewidth methods. We remark that the obtained anisotropic J_S/J_C on Pt (220) agrees with the results recently reported [75], where enhancement of the J_S/J_C was also observed in Pt when current along $< 002 >$ direction.

The role of spin diffusion length λ_S in Pt needs to be addressed, if measuring the ST-FMR with varying thickness of Pt, the calculated J_S/J_C can be fitted as a function of Pt thickness d and the spin diffusion length of Pt λ_S by using the equation:

$$\frac{J_S}{J_C} \propto (1 - \mathrm{sech}(\frac{d}{\lambda_S})) \tag{3.6}$$

J_S/J_C hereby tends to saturate when d is larger than λ_S. According to Ref. [75], λ_S of epitaxial

Table 3.1. Crystalline orientation dependent longitudinal resistivity values and charge-to-spin conversion efficiencies of epitaxial Pt films and Pt/FM structures.

Sample	Current Direction	ρ_{xx}^{Pt} ($\mu\Omega$.cm)	J_S/J_C at 300 K (Lineshape method)	J_S/J_C at 300 K (Linewidth method)
Pt (200)(10)/Py(8)	$<002>$	17.3	0.055	–
	$<2\bar{2}0>$	16.6	0.053	–
Pt (220)(10)/Py(8)	$<002>$	15.3	0.05	0.028
	$<2\bar{2}0>$	13.8	0.039	0.018
Pt (111)(10)/Py(8)	$<2\bar{2}0>$	11.7	0.034	–
	$\perp<2\bar{2}0>$	11.8	0.032	–

Pt (220) along $<002>$ and along $<2\bar{2}0>$ are 1.17 nm and 0.98 nm, respectively. Also, Wang *et al* reported the ρ_{xx} dependent λ_S [91]. Therefore, we also anticipate that the λ_S in Pt (200), (220) and (111) samples is anisotropic as the ρ_{xx} varies among in-plane crystalline orientations. However, the Pt thickness in this work is much greater than the reported λ_S. Hence, the crystalline orientation-dependent λ_S is unlikely to play a major role in probing the J_S/J_C.

Following the prerequisite in the previous paragraph, as the thickness of the measured Pt films is greater than the spin diffusion length λ_S, the measured J_S/J_C is mainly contributed by bulk SHE, bulk REE, and interfacial REE [107]. The bulk SHE consists of intrinsic and extrinsic mechanisms, in which orientational dependent anisotropic ρ_{xx} can be contributed by the intrinsic SOC and intrinsic SHE. On the other hand, different extrinsic scattering events can give a rise to anisotropic SHE, however, extrinsic impurity scattering is minor in the undoped, highly-crystalline epitaxial Pt. Therefore, we believe that the anisotropic bulk SHE in Pt is mainly driven by the orientation-dependent intrinsic mechanism. This is supported by the fact that since broken space-inversion symmetry is absent in Pt crystals, the bulk REE contribution can be ruled out [108]. Lastly, the interfacial REE is expected to be anisotropic in Pt (220)/Py interface. Simon *et al*. demonstrated, for reduced symmetry surfaces such as Au (110), the anisotropic REE dominates due to the mixing of the surface state with the bulk state [109]. Conclusively, the anisotropy in both intrinsic SHE and interfacial REE could result in the anisotropic J_S/J_C.

3.3.4 Thoughts of Future Study on Thickness Dependent ST-FMR

Although it is beyond the scope of this work, we acknowledge that the interfacial spin-mixing conductance $G_{(\uparrow\downarrow)}$ also plays a role in the spin current detection and further attribute to the J_S/J_C [91]. To study the anisotropy of $G_{(\uparrow\downarrow)}$, serials of samples with various Pt thicknesses should be prepared: Pt (200)(t)/Py (8), Pt (220)(t)/Py (8), Pt (111)(t)/Py (8), where Pt thickness t varies from sub-spin diffusion length of Pt to thickness higher than spin diffusion length. By analyzing the Pt thickness-dependent Gilbert damping of Py by either broadband FMR or ST-FMR on the aforementioned samples, the $G_{(\uparrow\downarrow)}$ along different in-plane crystalline orientations can be obtained. Then, the spin current transmittivity T can be calculated as a function of longitudinal conductivity σ:

$$T = \frac{2G_{(\uparrow\downarrow)}}{2G_{(\uparrow\downarrow)} + \frac{\sigma}{\lambda_S}} \tag{3.7}$$

Thereafter, J_S/J_C can be expressed as a function of T and intrinsic J_S/J_C:

$$\frac{J_S}{J_C} = T(\frac{J_S}{J_C})_{in} \tag{3.8}$$

Accordingly, anisotropic T can result in anisotropic J_S/J_C, with anisotropic $G_{(\uparrow\downarrow)}$ and anisotropic σ independently attribute to anisotropic T. In this manuscript, only the anisotropic σ is taken into consideration. In addition, this thickness-dependent Gilbert damping study assumes conformal roughness over thickness range, otherwise, variable roughness and interface condition will lead to inconsistent $G_{(\uparrow\downarrow)}$.

3.3.5 Temperature Dependent Harmonic Measurements

To further understand the resistivity-dependent SHE of the epitaxial Pt films, we performed temperature-dependent harmonics measurements on patterned Pt/Co(0.8)/Ni(1) Hall devices, as illustrated in Fig. 3.12(a). Harmonics measurements are based on the anomalous Hall signal measured from the Co/Ni, therefore, the devices are fundamental Hall crosses with

an aspect ratio of 1:3 for reduced Joule heating effect. Figure 3.12(b) shows the characteristic first and second harmonics Hall results measured on the prepared device. For bulk SHE, when a charge current J_C flows through the Pt along the x-axis, spin current J_S is generated along the z-axis with spin polarization σ along the y-axis. A damping-like SOT $\tau_{DL} \sim m \times (\sigma \times m)$ and a field-like SOT $\tau_{FL} \sim \sigma \times m$ produced by the generated spin currents are exerted on the magnetization m of Co/Ni [48, 50]. When m reaches an equilibrium position, the effects of these two SOTs can be described equivalently as the damping-like ($\Delta H_{DL} \sim m \times \sigma$ and field-like effective fields ($\Delta H_{FL} \sim \sigma$), respectively [48, 50]. By applying a 5 mA ac current at a frequency of 161 Hz using SR830 lock-in, the generated $\Delta H_{DL(FL)}$ causes an oscillation of m around the equilibrium position. By sweeping an in-plane external magnetic field along the current direction, the field dependence of the first harmonic signal V_ω and the 90° out-of-phased second-harmonic signal $V_{2\omega}$ can be measured by probing the difference of V^+ and V^- by channel A - channel B on the lock-in amplifier. Then, the derivatives of the harmonics signal are introduced to calculate the ratio coefficient $B_{x(y)}$ [65, 110, 111]:

$$B_{x(y)} = \left(\frac{\partial V_{2\omega}}{\partial H_{x(y)}}\right)\left(\frac{\partial^2 V_\omega}{\partial H_{x(y)}^2}\right)^{-1} \tag{3.9}$$

and the $\Delta H_{DL(FL)}$ can be extracted as follows [65, 110, 111]:

$$\Delta H_{DL(FL)} = -2\frac{B_{x(y)} \pm 2\xi B_{x(y)}}{1 - 4\xi^2} \tag{3.10}$$

where ξ is the ratio of the planar Hall resistance R_{PHE} and AHE resistance R_{AHE}. Note that the reported R_{PHE} is typically much smaller than R_{AHE} [111], giving rise the following approximation: $\Delta H_{DL(FL)} \approx$ -$2B_{(x(y))}$ [70, 111, 112]. Notably, the slope of $V_{2\omega x}$ versus the field along the x-axis is much larger than the slope of $V_{2\omega y}$ versus field along the y-axis, indicating a negligible contribution from field-like SOT. Hence, we only consider the damping-like SOT in this work. From ΔH_{DL}, the J_S/J_C can be calculated based on the following equation [113, 114]:

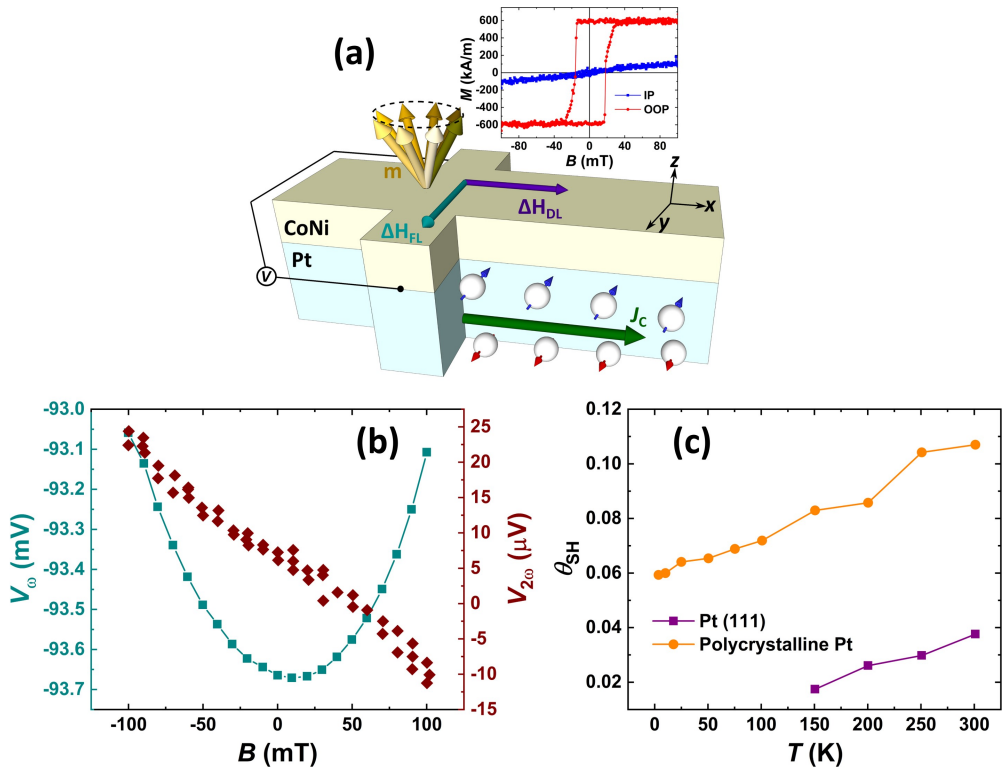

Figure 3.12. (a) Schematic of harmonic measurements of Pt/Co(0.8)/Ni(1) patterned into Hall crosses with Ti(6)/Au(80) electrodes. Insert: M vs B of Pt (111)/Co(0.8)/Ni(1). (b) In-plane longitudinal field dependence of first-and second-harmonic Hall signal. (c) Temperature dependence of the J_C/J_S.

$$\frac{J_S}{J_C} = \frac{2eM_S\Delta H_{DL}t_{CoNi}}{J_C\hbar} \tag{3.11}$$

Figure 3.12(c) presents the obtained temperature dependent J_S/J_C of epitaxial and polycrystalline Pt films. Aforementioned, the growth condition of Co/Ni on Pt (111) is consistent with the growth condition of Co/Ni on polycrystalline Pt. Furthermore, the saturated magnetization M_S of Pt/Co/Ni for both polycrystalline Pt and Pt (111) sample is nearly the same (600 kA/m), suggesting similar surface conditions and negligible interfacial mixing on Pt (111)/Py. We can observe that J_S/J_C measured on Pt (111) at room temperature agrees well with the value obtained from ST-FMR measurements. Also, J_S/J_C of polycrystalline Pt is about 3 times larger than that of the epitaxial Pt (111), which is comparable with the values reported in other studies

[68]. In the temperature range of our measurements, J_S/J_C of both polycrystalline and epitaxial Pt films decreases monotonically with temperature. Due to the high residual-resistance ratio (RRR) in high quality Pt (111), the shunting effect in Pt became significantly pronounced in the low-temperature regime, thus, the measured anomalous Hall signals coming from Co/Ni became negligibly small below 150 K. This issue persisted when reducing the Pt thickness by 20% and 40%. No detectable anomalous Hall and harmonic signals were probed on Pt(4)/Co/Ni and Pt(3)/Co/Ni samples. Therefore, the data points in the case of epitaxial Pt ended at 150 K.

In metals with spin-orbit coupling, spin Hall conductivity is predicted to scale with ρ_{xx} linearly or quadratically [16]. The former contribution results from the extrinsic scattering in "clean metals", and the latter one is driven by the intrinsic mechanism in "dirty metals" [16]. Isasa *et al*. reported that the intrinsic mechanism dominates the SHE in polycrystalline Pt [115] while for the case of epitaxial Pt (111) with significantly reduced resistivity, the weight of extrinsic mechanism is reasonably raised in "cleaner" epitaxial Pt (111). Our results support the above picture.

3.4 Conclusion

In summary, we have prepared high-quality epitaxial Pt thin films on a series of substrates. Systematic ST-FMR measurements demonstrate the isotropic nature of SHE in the high symmetry Pt (200) and Pt (111) films. In contrast, the low-symmetry system such as (220) orientated Pt exhibits the anisotropic SHE behavior that is correlated to the anisotropic resistivity. This work contributes to the development of energy-efficient spintronic devices by engineering the crystalline anisotropy of nonmagnetic metals.

The temperature-dependent harmonic measurements further suggest that SOT can be a hint for "cleaner" metals with more extrinsic contribution to SHE. The observed crystalline-orientation dependent J_S/J_C of epitaxial Pt could be readily extended to other Pt/FM heterostructures with a broad range selection of FMs. Our work reveals the underlying mechanism of

SHE in crystalline textured metals and broadens the material scope available for developing energy-favorable spintronic devices for next-generation information technologies.

3.5 Thoughts of Future Study on Epitaxial β-W

Among the intensive studies on employing polycrystalline heavy metals as spin source, β-W has exceptionally strong charge-to-spin conversion efficiency of 30% [63]. One of the challenges for growing the β-W is due to its metastable phase compared to traditional α-W configuration. β-W has A15 cubic crystal structure, distinctive to bcc α-W. It has been contentious regarding the role of thickness in stabilization of β-W phase in the field of spintronics. Thickness dependent β to α-W transition can be found. It was reported to be challenging to obtain β-W when the film thickness was above 10 - 20 nm [63, 116]. Although β-W with much higher thickness can be achieved with the aid of high deposition pressure, e.g., 3.33 Pa (24.9 mTorr) [117], significant surface roughness will be induced. Here, it was successful to obtain 35-nm β-W with decent surface roughness (roughly 0.84 nm). β-W was dc-sputtered directly on thermally oxidized Si(100) wafer in the aforementioned chamber without the aid of high deposition pressure. The sputtering pressure used was 2.7 mTorr (0.359 Pa). The sputtering power is critical for the formation of β phase because the film heating during fast deposition by high power undermines the stabilization of the metastable phase. Here, 10 W sputtering power was used, which was close to the minimum operational power that can sustain the plasma. The sputtering rate was kept to be around 0.00678 nm/s. From x-ray characterization, our polycrystalline β-W film exhibits 3 diffraction peaks. Note that the Bragg condition of α-W (110) almost overlaps with β-W (211), hence, we do not claim the purity of β phase. Moreover, β-W owns distinctive resistivity, which is higher than that of α-W by an order of magnitude due to higher density of grain boundaries, dislocation, and stacking fault [116]. Experimentally, by applying Van der Pauw resistivity configuration on full film, the resistivity of β-W was characterized to be roughly 140 $\mu\Omega$.cm, while the resistivity of α-W was measured to be around

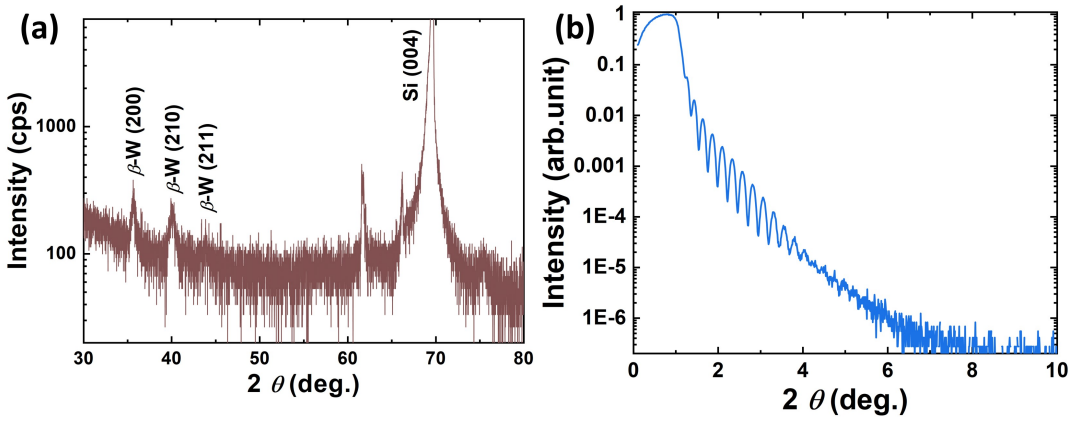

Figure 3.13. (a) XRD spectrum shows 3 peaks on polycrystalline β-W. (b) XRR oscillations support the targeted thickness and desirable surface roughness

20 $\mu\Omega$.cm. The high resistivity supports the existence of β phase.

In the future, studying the SHE in epitaxial metastable film could be attractive, which might exhibit both enhanced and tunable anisotropic charge-to-spin conversion efficiency. Epitaxial growth typically requires raised growth temperature, which is limited by the metastable-to-stable phase transition temperature. Alternatively, interfacial strain energy could favor the stabilization of metastable film, with desirable substrate orientation, growth of epitaxial metastable film can be feasible.

3.6 Acknowledgement

Chapter 3, in part, is a reprint of the material "Y. Xiao, H. Wang, E. E. Fullerton, *Crystalline Orientation Dependent Spin Hall Effect in Epitaxial Platinum,*" Front. Phys. 785, (2022). The dissertation author was the primary investigator and author of these materials.

Chapter 4

Néel Vector Perturbation in Chemically Ordered $FePt_3$

The antiferromagnetic nature and phase transition of chemically ordered $FePt_3$ were investigated independently by electrical transport, magnetometry, and neutron scattering. As a fundamental characterization, negative magnetoresistance and pronounced MR ratio were explored under various temperatures and fields. Next, by utilizing the strong chemical ordering and smooth surface of 20-nm-thick $FePt_3$. We successfully probed the exchange bias via electrical transport, which further helped us quantitatively investigate the stability of AFM nature under external perturbations. Our findings revealed the insensitivity of static field perturbation and proposed an energy-efficient approach to erase the antiferromagnetic memory by field rotation.

4.1 Introduction

The field of magnetic memory has extended to antiferromagnets (AFM) as a promising candidate to replace traditional ferromagnets (FM) [118, 119, 120, 121, 122, 123, 124]. Like the magnetization orientation in FM that represents zero or one, the writability in AFM is imperative to achieve the memory functionality [125]. Since the demonstration of spin-valve-like magnetoresistance in AFM [126], extensive work has followed to delve in the control of Néel vector, which is mainly achieved by the following approaches: magnetic control such as exchange bias control [126, 127], optical control by THz excitation [128, 129], electrical control

[130, 131] and strain control [132, 133, 134]. On the other hand, the stability of AFM memory also needs to be addressed [135]. For example, the FM used in exchange bias control is more sensitive to external perturbation, which is brought to our attention.

We chose to study chemically ordered $FePt_3$ [136, 137]. It exhibits paramagnetic to antiferromagnetic phase transition at 160 K, while chemically disordered $FePt_3$ is ferromagnetic. Early studies on bulk $FePt_3$ mainly focused on full films, Bacon and Palaith performed pioneer analysis on the structural and magnetic behavior with varying stoichiometry near $Fe_{25}Pt_{75}$ [29, 138]. Thereafter, more attraction has been raised on the exchange bias properties on $FePt_3$/FM interface [139], as the growing interest to use AFM for pinning the unidirectional anisotropy of FM in magnetic read head [140, 141, 142]. Furthermore, $FePt_3$ is not only applicable in the pining layer but also has shown potential in storage media. Apart from the aforementioned Néel vector control methods, N^+ ion-beam irradiation has been practical to suppress the chemical ordering in $FePt_3$, making it a candidate for artificial patterned magnetic recording media [35]. Presently, chemically ordered $CrPt_3$ alloy is predicted to potentially host the topological Weyl semimetal quantum properties [36], which could lead to exotic electrical transport properties. It is worth noting that electrical transport is yet to be studied in $FePt_3$. In particular, the anisotropic magnetoresistance (AMR) in AFM starts to attract more attention recently [135, 143, 144, 145, 146, 147, 148, 149, 150, 151], as an important characteristic of AFM memory electrical read-out signal [119, 152, 153].

In this study, the magnetic phase transition in chemically ordered $FePt_3$ was examined from various viewing angles by utilizing the transport, magnetometry and neutron scattering technique. In particular, taking the advantage of strong chemical ordering and smooth interface, we successfully probed exchange bias on transport devices via field dependent magnetoresistance (FDMR), which can become an alternative to mainstream magnetometry method. The field-and temperature-dependent AMR helped understand the role of Néel vector canting and reorientation in response of external field. Our findings support the robustness of antiferromagnetic memory and provide an approach to erase the memory states with a relatively low magnetic field below

the spin-flop field, which could potentially benefit the antiferromagnetic memory in low energy consumption applications.

4.2 Sample Growth and Characterization

4.2.1 Co-sputtering of Epitaxial Chemically Ordered $FePt_3$

The growth of alloy and oxides typically requires using a compound target material with prerequisite compound stoichiometry or using co-sputtering technique. The key to co-sputtering technique is tuning the power of each gun for the desirable stoichiometry. In the case of $FePt_3$ alloying, the final alloy depends on the volume fraction *vol%* of Fe and Pt, which can be calculated using the following equations:

$$vol\%_{Fe} = \frac{at\%_{Fe} \times V_{m(Fe)}}{at\%_{Fe} \times V_{m(Fe)} + at\%_{Pt} \times V_{m(Pt)}} \tag{4.1}$$

$$vol\%_{Pt} = \frac{at\%_{Pt} \times V_{m(Pt)}}{at\%_{Fe} \times V_{m(Fe)} + at\%_{Pt} \times V_{m(Pt)}} \tag{4.2}$$

where at% is the atomic fraction of Fe and Pt in the alloy, V_m is the molar volume of each element which is the division of molar mass M and mass density ρ. Theoretically, $at\%_{Fe} : at\%_{Pt}$ in $FePt_3$ is 0.25 : 0.75, which yields the $vol\%_{Fe} : vol\%_{Pt}$ is 0.206 : 0.794 from Eq. 4.1 and 4.2. Then, setting the value for alloy deposition rate R_{alloy}, an example of R can be 0.15 nm/s, the calculated co-sputtering rates of Fe and Pt becomes:

$$R_{Fe\,or\,Pt} = R_{alloy} \times vol\%_{Fe\,or\,Pt} \tag{4.3}$$

then, given the individually calibrated sputtering rates of Fe r_{Fe} and Pt r_{Pt} which are calibrated under individual power of p_{Fe} and p_{Pt}. The co-sputtering power for Fe and Pt can be calculated by:

$$P_{Fe\,or\,Pt} = p_{Fe\,or\,Pt} \times \frac{R_{Fe\,or\,Pt}}{r_{Fe\,or\,Pt}} \tag{4.4}$$

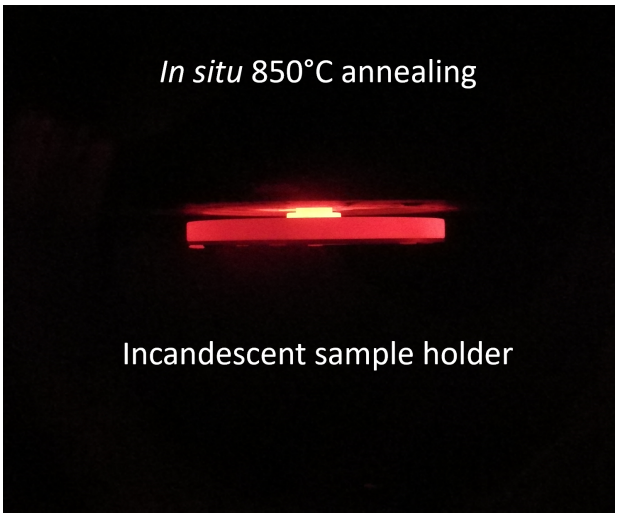

Figure 4.1. A incandescent sample holder picture that was taken right after finishing annealing at 850° for 40 minutes.

given the calculated sputtering power of Fe and Pt in Eq. 4.4 with targeted sputtering time, the co-sputtering process can be executed to achieve the alloy with targeted stoichiometry and thickness.

Epitaxial $FePt_3$ films were grown directly onto single-crystalline MgO (220) and Al_2O_3 (0006) substrates using a dc magnetron sputtering system with a base pressure of 5×10^{-8} Torr. The Fe and Pt targets are co-sputtered in a confocal geometry in Ar ambient of 2.7 mTorr. The co-sputtering rate was calibrated to be 0.15 nm/s. The growth temperature is 500°C to build epitaxy and control the surface roughness. To obtain desirable chemical ordering, samples were post-annealed *in situ* at 850°C for 40 minutes. The chemical ordering is highly sensitive to the annealing temperature, which can be significantly undermined by a 20 K temperature offset. Therefore, the annealing performance needs to be intensively monitored because the actual temperature on the substrate might differ every time. Here, 850° is only a reference set point. The chemical ordering assessment solely depends on the following characterization techniques instead of the annealing performance. An example of annealed sample holder is shown in Fig. 4.1, where an incandescent sample holder can be seen.

After annealing, samples were cooled below 100°C, followed by a 2-nm-thick Al_2O_3

grown *in situ* to prevent surface oxidation. On the other hand, samples for the exchange bias measurements have a bilayer structure of $FePt_3$(20)/Fe(4) (thickness in nm throughout the text unless otherwise stated). In order to limit the interfacial intermixing, $FePt_3$ were cooled completely from 850°C to room temperature, which could take roughly 240 minutes. Then, a subsequential 4-nm-thick Fe layer and a 2-nm-thick Al_2O_3 capping layer were deposited *in situ*.

4.2.2 X-ray Characterization

Figures 4.2(a)-(d) present X-ray diffraction (XRD) measurements on $FePt_3$ (110)(20) and $FePt_3$ (111)(20). The $at\%_{Fe} : at\%_{Pt}$ was optimized to be 0.27 : 0.73 based on the highest relative intensity ratio of (110) and (220) peaks. (110) is forbidden in chemically disordered $FePt_3$ and allowed in chemically disordered $FePt_3$, as confirmed in Fig. 4.2(a). The Laue oscillation on $FePt_3$ (111) peak suggests excellent lattice matching and epitaxy. The full-width-at-half-maximum (FWHM) of the ω curve across $FePt_3$ (110) and (111) are 1.550° and 0.0417°, respectively, supporting good crystalline quality. Furthermore, the in-plane ϕ scan confirmed the C_{2v} symmetry of $FePt_3$ $\{110\}<002>$ respect to MgO $\{220\}<002>$, and C_{6v} symmetry of $FePt_3$ $\{111\}<2\bar{2}0>$ respect to Al_2O_3 $\{0006\}<11\bar{2}0>$, as shown in Figs 4.2(c) and (d). The alloy thickness was calibrated using XRR, which also supports the correct stoichiometry because the calibrated alloy thickness matches the targeted thickness based on calculated co-sputtering power and targeted sputtering time. Moreover, the surface smoothness is not only important for a sharp exchange coupling interface in $FePt_3$/Fe bilayer, but also critical for spin current conductance in $FePt_3$/Cu/Py heterostructure. Therefore, the surface roughness of chemically ordered $FePt_3$ (110) and (111) films were calibrated from fitting XRR data, which are approximately 0.589 nm and 0.126 nm, respectively. As a comparison, the chemically disordered $FePt_3$ (110) and (111) films exhibit improved smoothness with fitted roughness of approximately 0.156 nm and 0.0967 nm, respectively. Remember no post-annealing was applied to the disordered film. Significantly enlarged surface roughness by annealing is what we can learn from the roughness comparison. The XRR calibration can be found in Fig. 4.3.

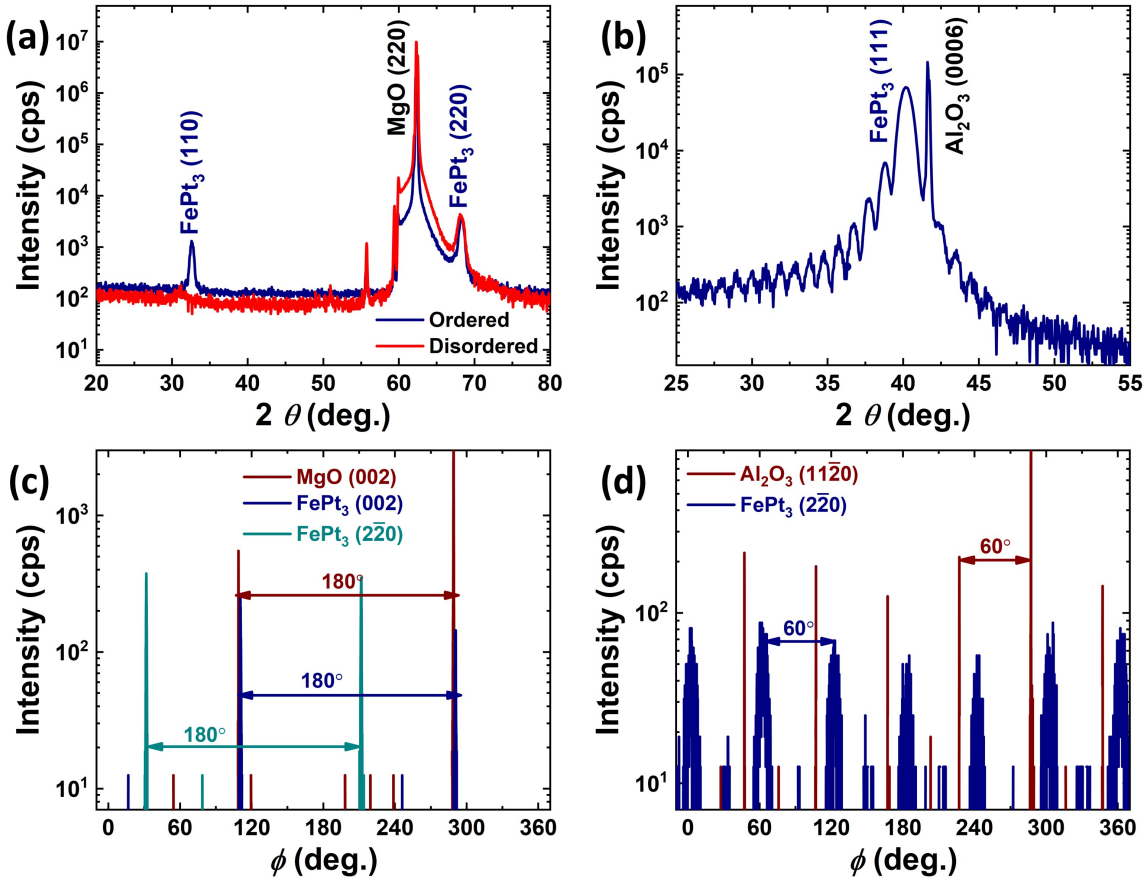

Figure 4.2. Specular XRD on (a) $FePt_3$ (110) and (b) $FePt_3$ (111). In-plane ϕ scans evidently support the 2-fold and 6-fold symmetry of $FePt_3$ (110) and $FePt_3$ (111), respectively.

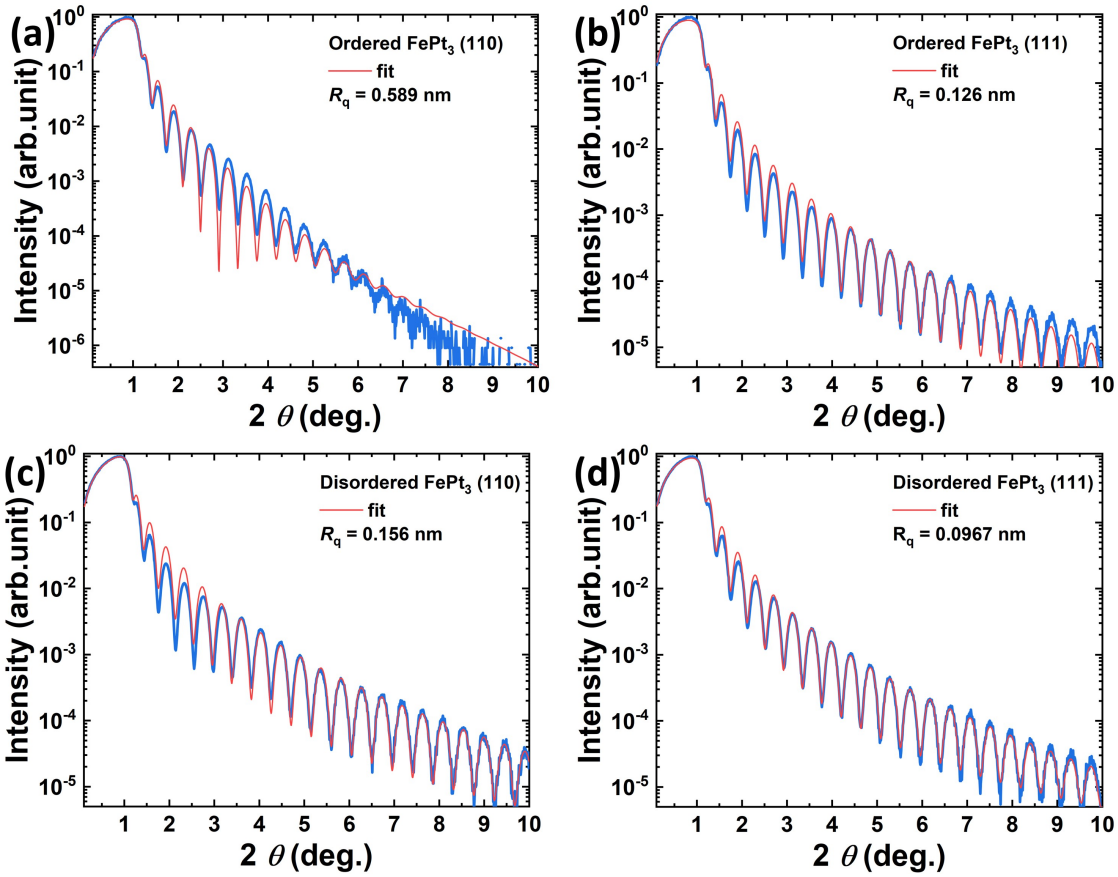

Figure 4.3. XRR on (a) ordered $FePt_3$ (110)(20), (b) ordered $FePt_3$ (111)(20), (c) disordered $FePt_3$ (110)(20), (d) disordered $FePt_3$ (111)(20). Red solid lines are fitting curves by GenX software.

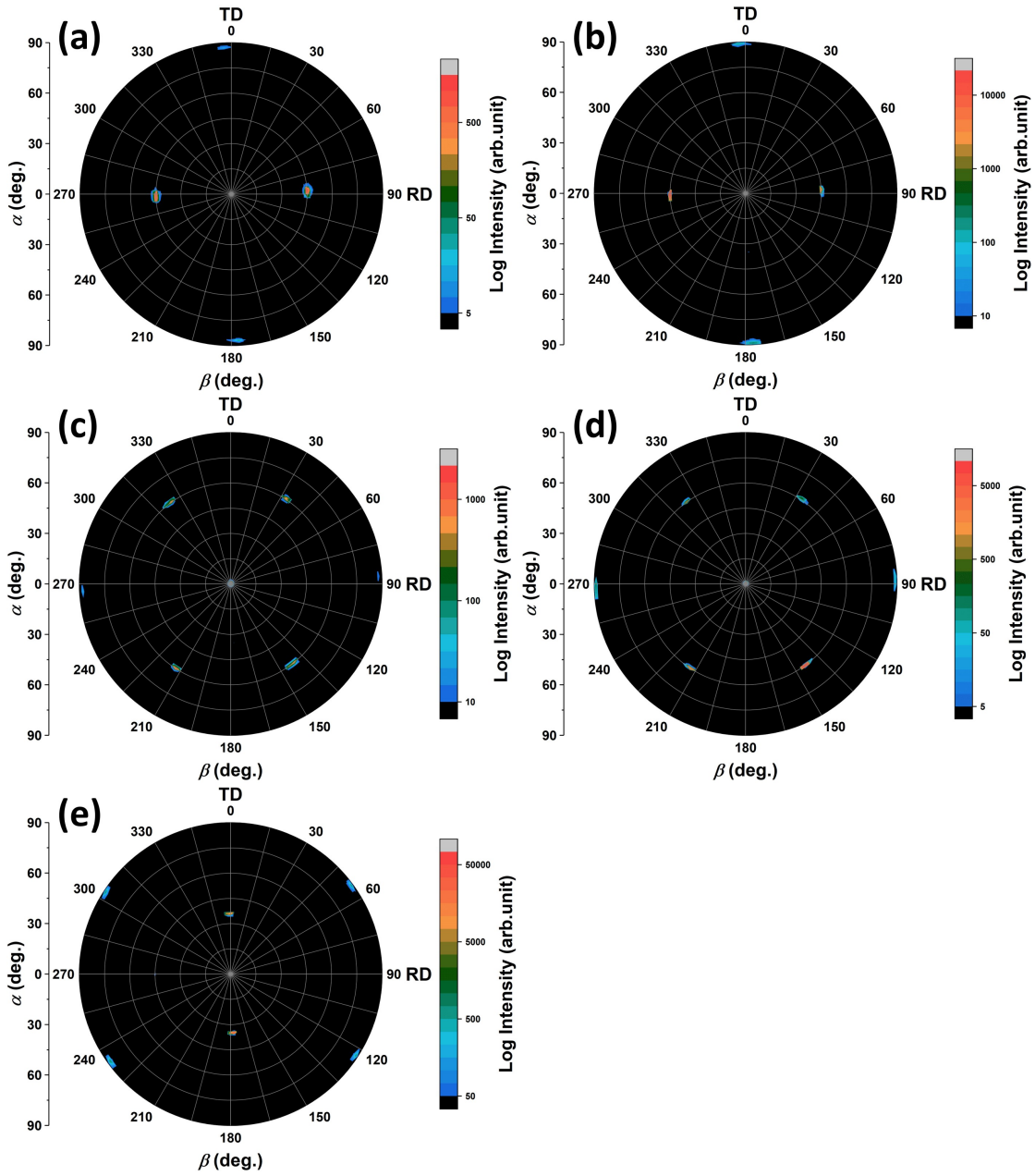

Figure 4.4. (a)-(e) Pole figure of $FePt_3$ $\{110\} < 001 >$, $\{110\} < 002 >$, $\{110\} < 1\bar{1}0 >$, $\{110\} < 2\bar{2}0 >$, $\{110\} < \bar{1}11 >$, respectively.

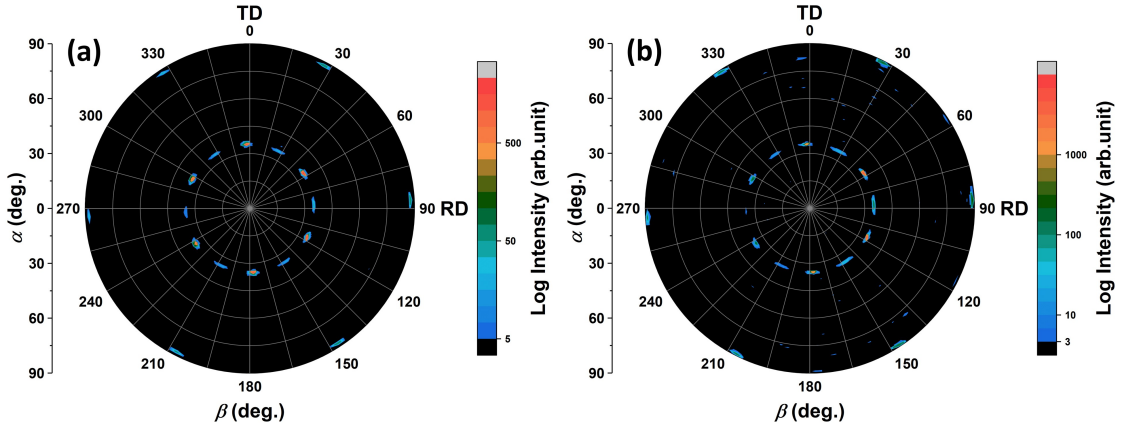

Figure 4.5. (a) and (b) Pole figure of $FePt_3$ $\{111\} < 1\bar{1}0 >$, and $\{111\} < 2\bar{2}0 >$.

Pole figures were measured on 250-nm-thick $FePt_3$ (110) and (111) samples. In Fig. 4.4, it presents excellent "single crystal" symmetries without any twining. When Bragg conditions are fixed to be $< 002 >$ and $< 2\bar{2}0 >$, their pole figures are consistent with the pole figures with Bragg condition of $< 001 >$ and $< 1\bar{1}0 >$, which is positive evidence for correct chemical ordering, otherwise, in chemically disordered $FePt_3$, the forbidden $< 1\bar{1}0 >$ does not lead to any symmetry, whose pole figure should only be background signal. Furthermore, as shown previously, out-of-plane XRD data on $FePt_3$ (111) only present the (111) peak, which is insufficient to examine the chemical ordering. From Fig. 4.5 which shows the pole figures on $FePt_3$ (111) with Bragg condition fixed to be $< 1\bar{1}0 >$ and $< 2\bar{2}0 >$, we can learn several aspects, firstly, pole figure maps out all 110 and 220 planes existing in (111) crystal, which clearly indicates the twining structure. Secondly, having the fact that the $[111]$ is calculated to be 35.3° from $[110]$, this calculation can be supported by observing the diffraction peaks of $[110]$ and $[220]$ locating evenly on a ring where $\alpha = 54.7^\circ$, which is 35.3° to the surface normal (111). This is evident for a correct cube structure minimal distortion. Thirdly, the consistent symmetry in both pole figures supports the picture of good chemical ordering.

4.2.3 Chemical Ordering Parameter

The chemical ordering parameter S needs to be calculated on prepared $FePt_3$ (110) film to assess the degree of ordering, which is quantified by the following equation:

$$S = (\frac{F_{220}}{F_{110}})^2 \sqrt{[(\frac{I_{110}}{I_{220}})(\frac{L_{220}}{L_{110}})(\frac{A_{220}}{A_{110}})]} \tag{4.5}$$

where F_{hkl} is the structure factor of $FePt_3$ including the Debye-Weller factor. F_{110} and F_{220} were calculated using the Visualization for Electronic and Structural Analysis software (VESTA). I_{hkl} is the integrated diffraction peak intensity, which can be obtained from the XRD data. L_{hkl} is the Lorentzian polarization factor, which can be estimated by:

$$L_{hkl} \approx \frac{1+\cos^2 2\theta}{2\sin^2\theta\cos\theta} \tag{4.6}$$

where θ is half of 2θ. A_{hkl} is the absorption factor, which can be estimated by:

$$A_{hkl} \approx 1 - \exp\frac{-2t\mu_{FePt_3}}{\sin\theta} \tag{4.7}$$

where t is the sample thickness. μ_{FePt_3} is the linear absorption factor which is deducted by:

$$\mu_{FePt_3} = \mu_{m(FePt_3)}\rho_{FePt_3} \tag{4.8}$$

where ρ_{FePt_3} is the mass density of $FePt_3$. $\mu_{m(FePt_3)}$ is the mass attenuation coefficient of $FePt_3$, which needs to be calculated from the mass attenuation coefficient of Fe and Pt:

$$\mu_{m(FePt_3)} = \mu_{m(Fe)} \times wt\%_{Fe} + \mu_{m(Pt)} \times wt\%_{Pt} \tag{4.9}$$

note that the $\mu_{m(Fe)}$ and $\mu_{m(Pt)}$ need to be obtained from the literature, or referring to the NIST Standard Reference Database 126 [154] (retrieved from https://dx.doi.org/10.18434/T4D01F). Similar to the previous calculation on $vol\%_{Fe}$ and $vol\%_{Pt}$, the $wt\%_{Fe}$ and $wt\%_{Pt}$ can be calculated

as a function of the molar weight M of Fe and Pt:

$$wt\%_{Fe} = \frac{at\%_{Fe} \times M_{Fe}}{at\%_{Fe} \times M_{Fe} + at\%_{Pt} \times M_{Pt}} \tag{4.10}$$

$$wt\%_{Pt} = \frac{at\%_{Pt} \times M_{Pt}}{at\%_{Fe} \times M_{Fe} + at\%_{Pt} \times M_{Pt}} \tag{4.11}$$

From the rough estimation above, the ordering parameter of $Fe_{27}Pt_{73}$ (110)(20) film shown in the previous XRD spectrum is roughly 60.8%, given the fact that $\frac{I_{110}}{I_{220}}$ is around 33.1% compared to the theoretically calculated ratio of 45.2%.

4.2.4 Magnetometry Characterization

Ideally, neither paramagnetic nor antiferromagnetic $FePt_3$ exhibits magnetic moment due to the collinear Néel vectors configuration. However, the ferromagnetic disordered $FePt_3$ impurity in ordered $FePt_3$ film is inevitable and reported in previous study [136]. The magnetization of disordered $FePt_3$ impurity in ordered $FePt_3$ (110)(20) film was characterized to be approximately 44 kA/m^2. Note that this manuscript only focuses on the chemically ordered $FePt_3$, henceforth referred to $FePt_3$ unless otherwise stated.

4.3 Results

4.3.1 $FePt_3$ Phase Transition

Phase Transition Probed by R vs T

We explore the nature of secondary phase transition in $FePt_3$ by both electrical transport and magnetometry measurements. The longitudinal resistivity ρ_{xx} of 20-nm-thick $FePt_3$ was measured on photolithographically patterned 4-probe devices along different in-plane crystalline orientations. Figure 4.6(b) shows temperature-dependent ρ_{xx} under zero field cooling (ZFC). Pronounced slope change and characteristic ”kink” can be observed on all in-plane crystalline orientations which suggest the secondary phase transition around 160 K. The residual-resistance-

ratio (RRR) along $< 1\bar{1}0 >$, $< \bar{1}11 >$ and $< 001 >$ are 1.44, 1.37 and 1.34, respectively. The discrepancy in ρ_{xx} along different crystalline orientations is commonly seen in single crystals [155, 156, 157, 158, 159] and previous Pt (220) films [160]. It could be attributed by the anisotropy in both the intrinsic mobility and extrinsic scattering events. In particular, the anisotropic mean-free path along different crystalline directions leads to the discrepancy in intrinsic mobility, which can be quantified by the anisotropy in Fermi surface projections on sample surface [161]. Additionally, the temperature-dependent ρ_{xx} under 9 T-field cooling was compared to ZFC ρ_{xx} in Fig. 4.7. The phase transition temperature on the FC curve is marginally shifted to a lower temperature compared to the ZFC curve due to the fluctuated AFM spins by strong field [162]. More pronounced shifting can be observed by FC above the spin-flop field $\mu_0 H_{sf}$. Moreover, given the fact that the "kink" can be completely suppressed if the field can saturate the AFM spins to FM state [148], we consider the saturation field $\mu_0 H_{sf}$ of $FePt_3$ is above 9 T. We shall return to this point in the ADMR section.

Phase Transition Probed by Exchange Bias

Exchange coupling on AFM/FM interface leads to a biased magnetic hysteresis loop which helps confirm the phase transition and AFM nature of $FePt_3$ [139, 141, 142]. Most previous work studied on full films. Here, exchange bias was measured separately on patterned $FePt_3$(20)/Fe(4) transport devices by FDMR technique, as a comparison to the hysteresis loops measured on $FePt_3$(20)/Fe(4) full film using magnetometry. In this chapter, the exchange bias measurements mainly focus on the $FePt_3$ (110)/Fe samples, because the exchange bias strength on $FePt_3$ (111)/Fe was measured to be weaker for an order of magnitude. The magnetometry collects the statistical magnetic moment signal from the full film, while FDMR strongly depends on the FDMR signal in Fe, that being said, there should be enough current distribution in Fe because most of current is shunt by $FePt_3$ on a $FePt_3$(20)/Fe(4) bilayer. Therefore, a 200 μA ac current was used on bilayer measurements, as a comparison, only 50 μA ac current was used on $FePt_3$ single layer measurements.

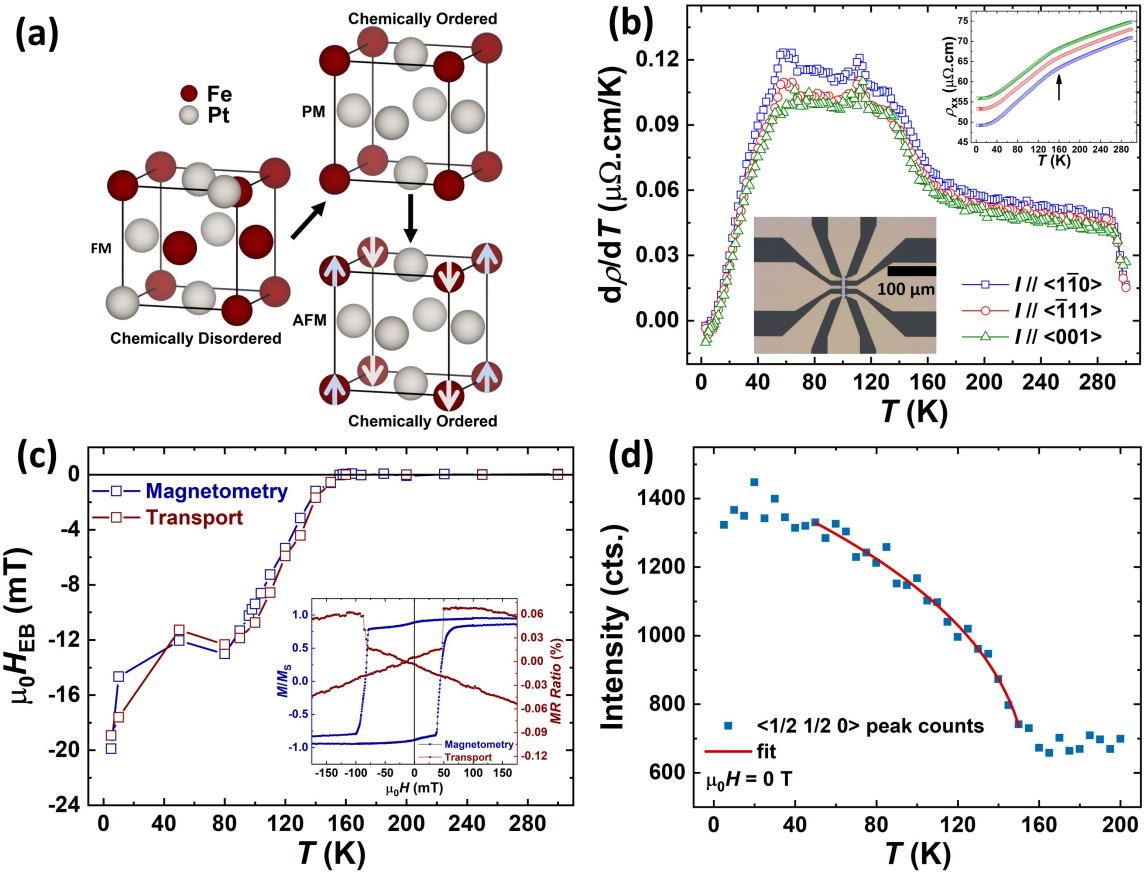

Figure 4.6. (a) $L1_2$ structure of $FePt_3$. (b) Derivative of ρ_{xx} vs T of $FePt_3$ (110). Insert left: Optical microscope image of 4-probe devices. (c) $\mu_0 H_{EB}$ vs T. Insert: biased FDMR and hysteresis loop at 10 K. (d) ZFC neutron scattering intensity vs T on $FePt_3$ (110)(250). Solid line is the fit to power law.

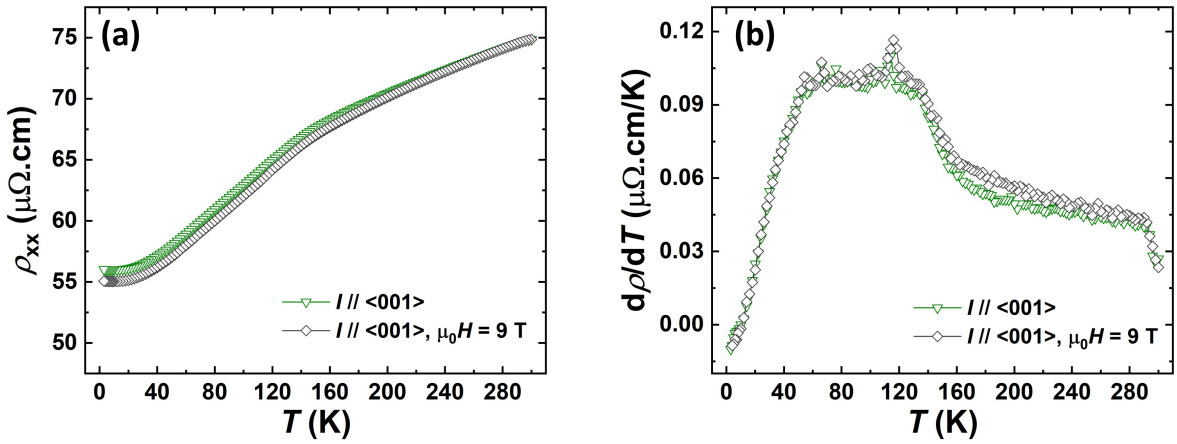

Figure 4.7. Temperature dependent resistivity of $FePt_3$ (110)(20) with current along $< 001 >$. Green curve is the same as the ZFC curve in Fig. 4.6(b). Grey curve is 9 T field cooling along current direction. (b) The first derivative of data in (a).

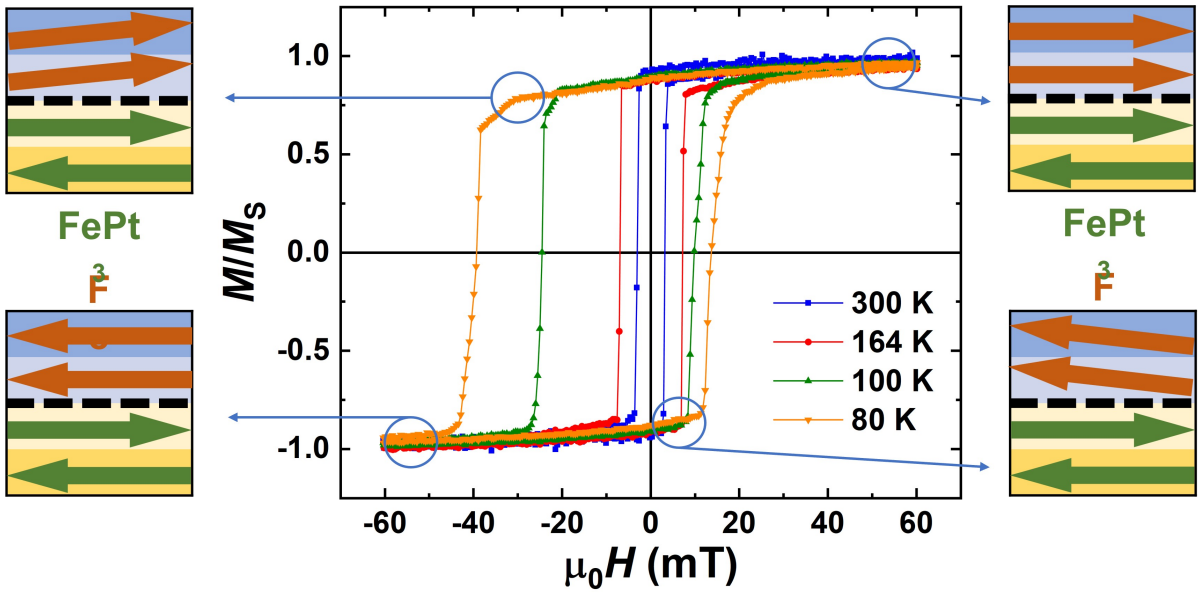

Figure 4.8. Examples of exchange biased magnetic hysteresis loops measured on $FePt_3$/Fe bilayer as temperature passes through the Néel temperature. Sketch describes the changing states of ferromagnetic and antiferromagnetic order under external field.

Samples were cooled to 5 K under a positive 4000 Oe field along the easy axis of Fe to saturate the Fe and define the exchange coupling polarity. In order to reduce training effects and better data accuracy, all hysteresis and FDMR loops in this manuscript were repeated 3 times at each temperature setpoint for averaging $\mu_0 H_{EB}$. The exchange bias field $\mu_0 H_{EB}$ can be calculated as the average of $\mu_0 H_{C1}$ and $\mu_0 H_{C2}$, where $\mu_0 H_{C1}$ and $\mu_0 H_{C2}$ are coercivity fields exacted from the descending and ascending branch of the hysteresis loops and FDMR loops [139]. In Fig. 4.6(c), transport data shows a good agreement with magnetometry data on temperature-dependent $\mu_0 H_{EB}$. Negative $\mu_0 H_{EB}$ starts to be observed when $T < 160$ K, which is consistent with the previously reported T_N of $FePt_3$. The magnitude of $\mu_0 H_{EB}$ increases monotonically above 80 K and decreases slightly around 50 K, then resuming increases monotonically below 50 K. The non-monotonic behavior around 50 K could be a result of spin reorientation [136].

Phase Transition Probed by Neutron Scattering

Elastic Neutron scattering measurements were performed on 250-nm-thick $FePt_3$ (110) full film by using beam-line HB-1A (λ = 0.2357 nm) at the High Flux Isotope Reactor at the

Oakridge National Lab (ORNL). As illustrated in Fig. 4.6(d), we first address the temperature-dependent magnetic scattering respect to surface normal $Q = <\frac{1}{2}\frac{1}{2}0>$ reflection under zero external field. The AFM ordering state gives rise to the increasing scattering intensities below 160 K. In the intermediate temperature regime, the temperature-dependent intensity can be fitted by random-exchange Ising model (REIM) power law [137, 163, 164]:

$$\phi(T)^2 \propto (1 - \frac{T}{T_N})^{2\beta} \tag{4.12}$$

giving the fitted T_N = 155.9 K. The T_N is close to the transport and magnetometry results, possibly due to the broad transition found on $\mathrm{d}\rho/\mathrm{d}T$ vs T curves in Fig. 4.6(b). The fitted β = 0.377, which is in excellent agreement with previously reported values [137]. Moreover, when the temperature is low enough, the AFM domains are thermally stable with a large enough kinetic barrier, leading to saturated scattering intensities below 50 K [165].

4.3.2 Anisotropic Magnetoresistance of $FePt_3$

We then examine the angular dependence magnetoresistance (ADMR) in $FePt_3$. Figure 4.9 presents the field-and temperature-dependent ADMR in $FePt_3$ (110)(20). The ac current was applied along $< 001 >$ which is parallel to the easy axis and Néel vector of $FePt_3$. Note that the ADMR is independent of current polarity, and the difference between using ac and dc current is absent. The external field was rotated within the sample plane. The angle between current and field is denoted as θ_{xy}. Taking into consideration of the potential angle offset that can be introduced during the patterning and the rotator hardware, ADMR was measured from -5° to 365° then reversed to -5° with a fixed step of 2.5°. The measured ρ_{xx} was normalized to magnetoresistance ratio by:

$$MRRatio(\%) = \frac{\rho_{\parallel} - \rho_{\perp}}{\rho_{\perp}} \times 100 \tag{4.13}$$

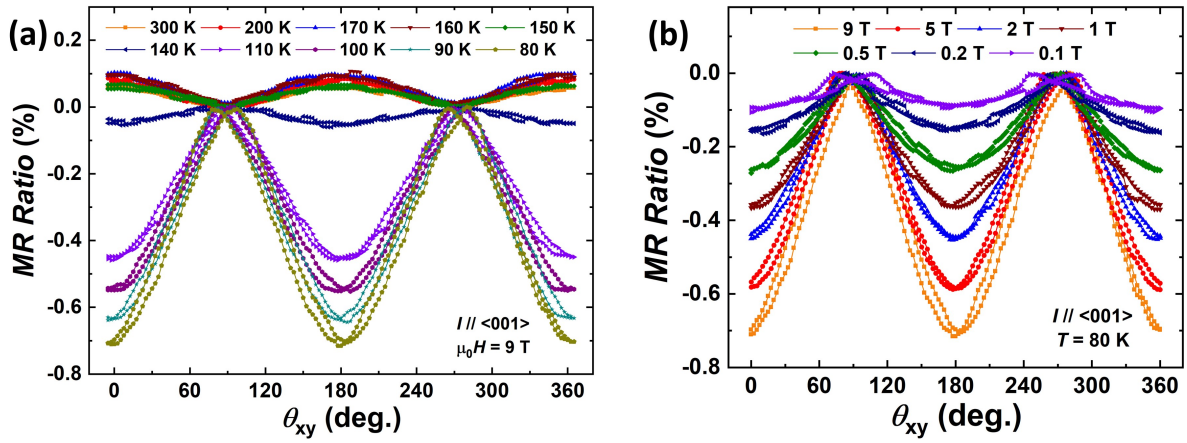

Figure 4.9. (a) Temperature- and (b) field dependent ADMR on $FePt_3$ (110)(20) with current along $< 001 >$. θ was rotated in the sample plane.

where $\rho_{\parallel}$ and $\rho_{\perp}$ are the resistivity when the current is parallel and perpendicular to the field. We recall that in classical ferromagnetic ADMR, the magnetization is expected to align with the external field. The scattering event on electron orbitals yields a high resistance state when the current is collinear with the magnetization. In other words, the local resistance maximum can be detected at $\theta_{xy} = 0°$, 180° and 360°. Fig. 4.9(a) presents the temperature-dependent ADMR under $\mu_0 H$= 9 T with harmonic $\cos 2\theta$ shape. When $T > T_N$, the paramagnetic $FePt_3$ leads to zero MR ratio under current $\mu_0 H$. Thus, the measured positive MR ratio at high temperatures was mainly contributed by the classical ferromagnetic response of disordered $FePt_3$ impurity. When $T < T_N$, the AFM response became dominant in the ADMR signal. MR ratio switched sign from positive to negative. Notably, the MR ratio reaches the value of 0.71% at 80 K. This is a relatively large MR ratio as a collinear undersaturated AFM [144, 150, 151].

Figure 4.9(b) shows the MR ratio in AFM phase under multiple $\mu_0 H$. The hysteresis on ADMR curve from sweeping back and forth can be a result of pining states. Note that the MR ratio gradually increases with $\mu_0 H$ and was not saturated, also indicating the $\mu_0 H_s$ of $FePt_3$ is above 9 T. Furthermore, suppose in spin-flop regime, the significant step-like increase of magnetic susceptibility should lead to a pronounced MR response. The absence of dramatic change in MR ratio hence suggests the $\mu_0 H_{sf}$ of $FePt_3$ is above 9 T. Therefore, we speculate the

ADMR on $FePt_3$ is governed by the canted Néel vectors that are only partially reorientated from the zero-field position.

We discuss, if the Néel vectors are in spin-flop regime, they tend to be perpendicular to the external field. Thus, when current is perpendicular to the field, it leads to a high resistance state at $\theta_{xy} = 90^\circ$ and 270°, which might be a possible explanation for the negative longitudinal magnetoresistance (nLMR) in AFM when $\mu_0 H > \mu_0 H_{sf}$. However, it cannot explain the nLMR in $FePt_3$ since the negative sign is persistent from 0.2 T to 9 T. Indeed, distinctive MR sign and field independent MR sign were observed in other AFM conductors such as $EuTiO_3$ (negative sign) [146], Fe_2As (negative sign) [151], and CuMnAs (positive sign) [166], which could suggest that the MR sign has intrinsic origins in different materials, as the AMR is essentially a result of spin-orbit interaction. Theoretically, the anisotropy of density of states (DOS) and corresponding chemical potential with respect to the magnetization angle was predicted to quantitatively describe the MR [144]. This could build a relation to the anisotropic scattering event which is directly governing the AMR.

Additionally, it was reported that the nLMR can be strongly induced by the nonuniformed current injection arising from the field-induced anisotropy of conductivity, named as current-jetting effect [145]. This effect yields inconsistent local voltage depending on the relative placement of current and voltage electrodes. We note that consistent MR ratio and nLMR was measured on multiple devices patterned on the same sample with different scales, therefore the current-jetting effect cannot be the reason for nLMR in $FePt_3$.

4.3.3 Perturbation of the Néel Vector and AFM Domains

Next, we address the perturbation of the Néel vector and AFM domains. By utilizing the neutron scattering on $FePt_3$ (110)(250), a set of measurements was performed in which the sample was ZFC to 1.5 K, resulting the sample in a multidomain state. Then, in-plane external field was applied along the Néel vector at $\mu_0 H$ = 0 T to 6 T with step of 0.5 T. Figure 4.10 showed the $< \frac{1}{2}\frac{1}{2}0 >$ diffraction peaks under multiple field strength. Suppose that the field is

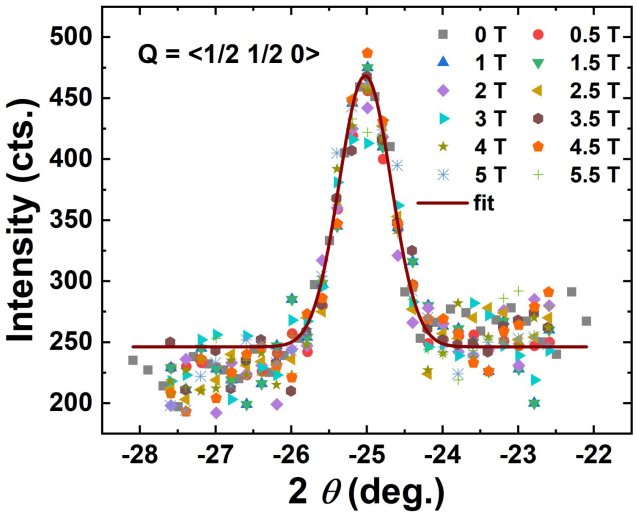

Figure 4.10. Neutron scattering peaks of $< \frac{1}{2}\frac{1}{2}0 >$ under multiple field at 1.5 K on $FePt_3$ (110)(250), solid line is an example of Gaussian fit.

large enough, it will re-orient the domains that are misaligned with the field and eventually turn the sample into a monodomain state. As the domain reorients in response to the field, the change of diffraction peak should be observed. However, the scattering intensity is insensitive to the field up to 6 T. The Gaussian fitted peak area and FWHM in Fig. 4.11 also exhibit the field independence behavior, indicating the stability of Néel vector under external field perturbation.

Furthermore, as a measure of quantifying the influence from external field perturbation, we investigated the change of exchange bias strength by FDMR on $FePt_3$/Fe transport devices. Here, we introduce 5 perturbation measurements that were executed independently at 80 K. Akin to the aforementioned exchange bias measurement, we follow the same FC process with ameliorated training effect. The field cooling direction is parallel to current and easy axis of $FePt_3$ (110). To exclude the history effect, sample was warmed to 300 K at the end of each perturbation measurement. At the beginning of each of the 5 measurements, FDMR was first measured as a reference of exchange bias strength, denoted as $\mu_0 H_{EB}$ (0). Each perturbation measurement was performed with 5 repeats of the following loop: applying perturbation and subsequential FDMR loops were measured to extract $\mu_0 H_{EB}$ (n), where n represents the number of repeats. The 1st perturbation was applying -9 T antiparallel to the cooling field direction, then

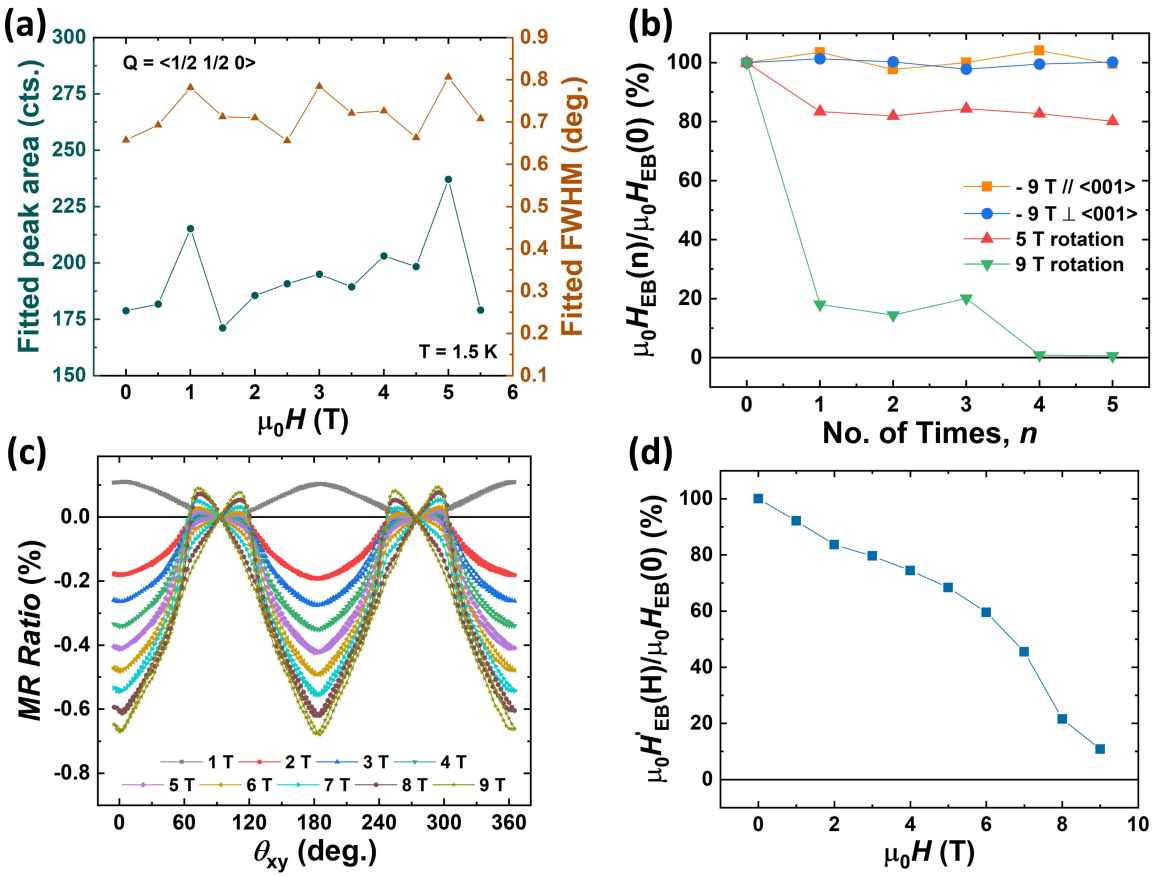

Figure 4.11. (a) Fitted neutron scattering peak and FWHM under multiple fields. (b) Change of exchange bias field after repeating different perturbations for 5 times. (c) ADMR on $FePt_3$ (110)(20)/Fe(4) under 1-9 T. (d) Change of exchange bias field after field rotation perturbation from 1-9 T.

withdrawn to 0 T. The 2nd perturbation was applying –9 T perpendicular to the cooling field direction, then withdrawn to 0 T. For the 3rd and 4th perturbation, 5 T and 9 T field was rotated back and forth in the sample plane with the same procedure as the previous ADMR, respectively.

As shown in Fig. 4.11(b), for the 1st and 2nd perturbation measurements, the magnitude of $\mu_0 H_{EB}$ is considerably persistent, compared to the reference $\mu_0 H_{EB}$ (0) across the 5 repeats. Therefore, according to neutron scattering results and the first two perturbation measurements, we speculate that the unidirectional anisotropy of Néel vector is impervious to the 9 T, irrelevant to the field direction. On the contrary, the rotation perturbation yields distinctive results. After the first 5 T rotation, the $\mu_0 H_{EB}$ (1) declined 17% compared to the $\mu_0 H_{EB}$ (0) and maintained

roughly 80% of the $\mu_0 H_{EB}$ (0) after 5 rotation repeats. More importantly, $\mu_0 H_{EB}$ (0) was significantly suppressed by 82% after the 1st 9 T rotation, suggesting the field dependence of rotation perturbation. Here, we highlight that $\mu_0 H_{EB}$ vanished after 4th 9 T rotation. In other words, the stability of AFM unidirectional anisotropy in $FePt_3$ can be fully suppressed by rotating the sample for 4 times under $\mu_0 H < \mu_0 H_{sf}$.

To further explore the role of perturbation history, the 5th measurement was performed in a continuous sequence and results were plotted in Figs.4.11(c) and (d). After extracting $\mu_0 H_{EB}$ (0), 9 perturbation rotations were carried out in the form of ADMR from 1 T to 9 T with $\mu_0 H_{EB}^{'}$ (H) measured after each rotation, where H is denoted as the field strength of each rotation. As seen in Fig. 4.11(c), the ADMR on $FePt_3$/Fe is positive under 1 T, as it was dominated by the classical ferromagnetic response in undersaturated Fe. The $\mu_0 H_{EB}^{'}$ (1) is roughly 90% of $\mu_0 H_{EB}$ (0). Starting from 2 T rotation, the ADMR switched sign and became AFM response dominant. The hysteresis on ADMR is a joint contribution from the pinned Néel vector and Fe spins due to exchange bias. As the perturbation rotation continues under increasing fields, the $\mu_0 H_{EB}^{'}$ (H) is suppressed monotonically and eventually reached to 10% of $\mu_0 H_{EB}$ (0) after 9 T rotation. Comparing 5 T and 9 T results in Fig. 4.11(b) to Fig. 4.11(d), $\mu_0 H_{EB}$ (1)/$\mu_0 H_{EB}$ (0) for 5 T rotation without history is 83% compared to 68% for 5 T rotation with 1 - 4 T rotation history, which is 18% for 9 T rotation without history compared to 10% for 9 T rotation with 1 - 8 T rotation history.

Moreover, a serial of rotation perturbation measurements was performed with fixed 9 T but different rotation angles, as shown in Fig. 4.12. $FePt_3$ (110)(20)/Fe(4) was rotated in-plane for x° (x = 45°, 90°, 135°, 180°, 270° and 360°) then rotated back to initial position. After each rotation, the FDMR was measured to extract $\mu_0 H_{EB}$ (x) compared to the reference $\mu_0 H_{EB}$ (0) before each rotation. The ADMR amplitude and shape for every rotation angle are highly consistent and reproducible. The more it rotates away from the easy axis of Néel vector, the more change of $\mu_0 H_{EB}$ can be observed. In the case of rotation angle equals or above 90°, $\mu_0 H_{EB}$ exhibits more dramatic decline compared to the 45° rotation, which suggests that it requires to

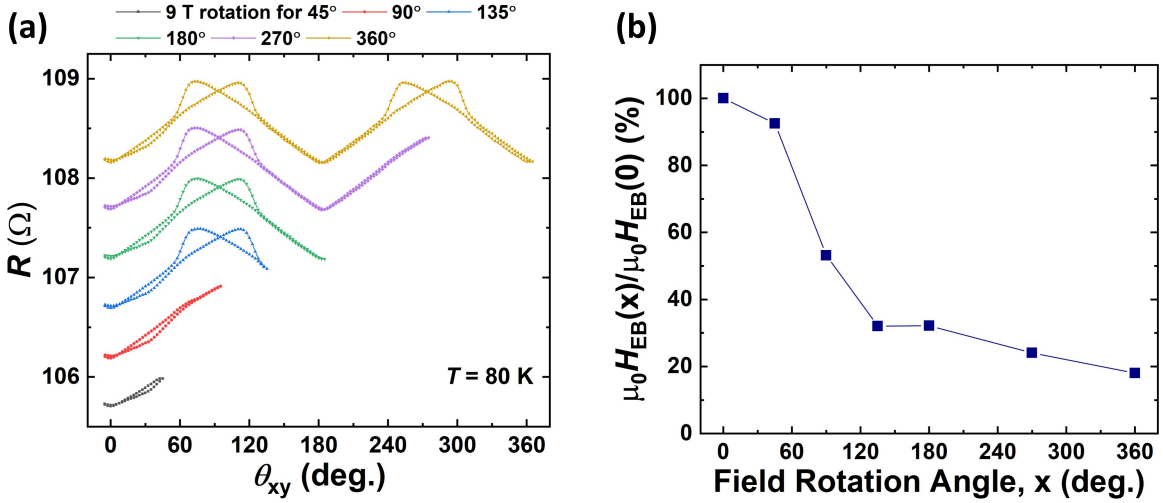

Figure 4.12. (a) ADMR on $FePt_3$ (110)(20)/Fe(4) under 9 T for different rotation angles, data in raw resistance, curves are offset for visual clarity. (b) Change of exchange bias field after 9 T rotation perturbation for different rotation angles.

be rotated beyond its hard axis for efficient suppression of exchange bias.

Now we go back to the results of 1st to 5th measurements, the insensitivity against static field perturbation suggests the same remanence state after the field is removed. To equivalently visualize this statement, FDMR was measured on both $FePt_3$ (110)(20) and $FePt_3$ (111)(20), plotted in Figs. 4.13(a) and (b). The current was fixed with field sweeping in different crystalline directions and returning to zero, yielding similar remanence state by showing very close resistance signal at remanence. If the remanence states differ when field is applied in different crystalline direction, then the remanence resistivity should show distinctive readings because of the anisotropic ρ_{xx} shown in Fig. 4.7. In other words, the multidomain state in $FePt_3$ has strong anisotropic energy, making the Néel vectors recover to the same remanence state independent of the field history. On the other hand, field rotation could increase interface inhomogeneity by breaking the sample into more domains, therefore becoming an effective approach to perturb the AFM domains. We also highlight the important role of the field rotation history in reduction of unidirectional anisotropy of Néel vector.

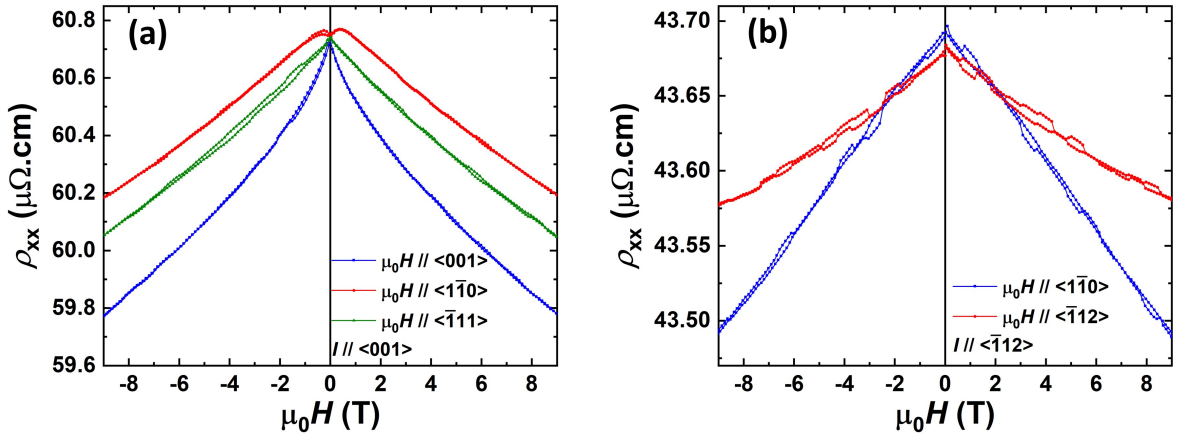

Figure 4.13. FDMR on (a) $FePt_3$(110)(20) and (b) FePt3(111)(20) measured at 80 K.

4.4 Conclusion

Conclusively, we have revisited chemically ordered $FePt_3$ whose AFM nature was investigated in the previous studies [19–23]. The phase transition results on 20-nm $FePt_3$ are in accord with the neutron scattering results on bulk $FePt_3$, indicating the persistence of excellent chemical ordering in thin film down to 20 nm. The nLMR and pronounced 0.7% MR ratio can serve as a characteristic AMR reference for electrical read-out in antiferromagnetic memory. The stability of AFM under static high field is not only essential to memory applications but also calls for insights on spin fluctuation and Fermi liquid theory [167, 168]. The Néel vector perturbation by field rotation may inspire a pathway to energy-efficient memory erasing and spin current reorientations in neuromorphic computing devices.

4.5 Acknowledgement

Chapter 4, in part, is currently being prepared for submission for publication of the material "Y. Xiao, N. Liyanage, D. A. Gilbert, E. E. Fullerton, *Néel vector perturbation in chemically ordered $FePt_3$,*" The dissertation author was one of the primary investigators and author of this material.

Chapter 5

Magnetoresistance in Epitaxial Ho

5.1 Introduction

Different from other lanthanides, Tb, Dy, and Ho have shown second-order phase transition from paramagnetic (PM) to helical antiferromagnetic (HAFM) phase at Néel temperature T_N [169]. The helicity is presented by spiral spins around their hcp c-axis orientation. As further going through a first-order transition at Curie temperature T_C, they transit into ferromagnetic (FM) phase. This transition happens when strain and magnetoelastic energy surpass the isotropic spin exchange energy which contributes to HAFM phase[170]. In particular, Ho's T_C and T_N were reported to be 19 K and 132 K[171]. Below T_C, Ho's FM polarization is conical with spins deflected from hcp basal plane and tilted towards c-axis. Above T_C and below T_N, HAFM configuration displays within the basal plane. In both phases, the moment in each basal plane has certain polarity. The outstanding HAFM and conical FM phases trigger to study the temperature-dependent electronic transport in Ho. The field-and temperature-dependent structure and magnetic properties in bulk Ho single crystal has been widely investigated [172, 173, 174, 175, 176, 177, 178, 179, 180, 181, 182, 183, 184, 171, 185]. Noteworthy, the angular dependent magnetoresistance (ADMR) in the epitaxial Ho thin film yet has been hitherto unexplored.

In this chapter, we chose to investigate epitaxial Ho thin film with hcp $P6_3/mmc$ space group symmetry. The Ho thickness is determined to surpass the length scale of a complete

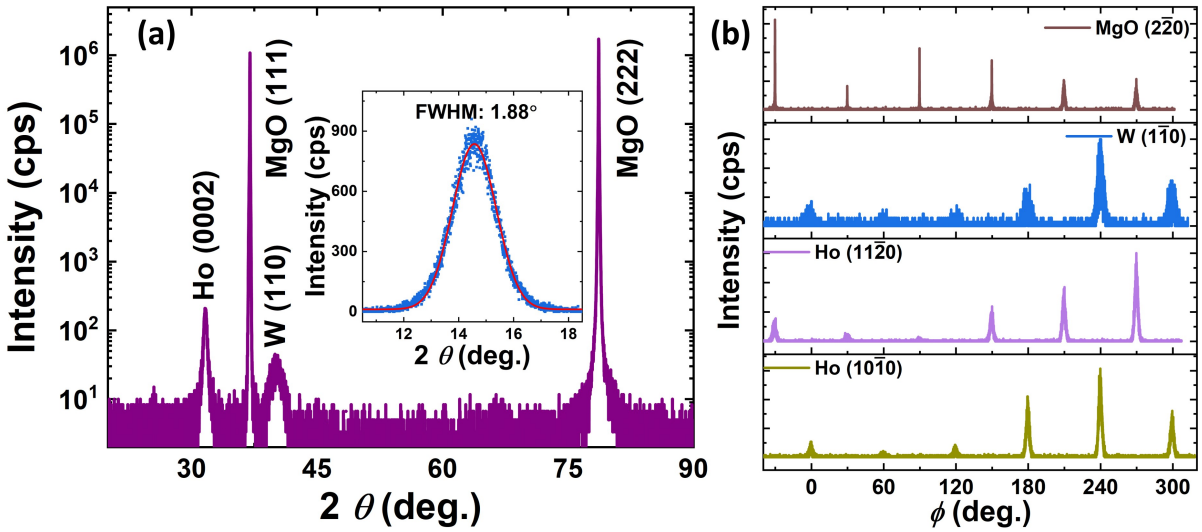

Figure 5.1. (a) Out-of-plane XRD spectrum on MgO (111)/W (110)/Ho (0002)/W sample. Insert: fitted rocking curve aligned to Ho (0002). (b) In-plane ϕ scan with Bragg conditions of W (110), MgO (220), Ho $(11\bar{2}0)$ and Ho $(10\bar{1}0)$, respectively.

helicity in HAFM and FM phases. The sputter-grown Ho samples possessed $<0002>$ orientation (hereinafter *c*-axis) out of plane with in-plane $<11\bar{2}0>$ denoted as *a*-axis and $<10\bar{1}0>$ denoted as *b*-axis. The ADMR displayed distinctively pronounced 6-fold contribution which is yet to be reported in other hcp materials.

5.2 Sample Growth and Characterization

The epitaxial Ho (0002) samples were sputter-grown on single crystal MgO (111) substrates. The sputter chamber had a base pressure of 7×10^{-8} Torr with Ar growth pressure of 2.7 mTorr.The substrate was preheated to 700°C for one hour, followed by 5 nm of W growth at the same temperature to help build epitaxy. Subsequent 40 nm Ho was grown *in situ* at 300°C. Then the sample was naturally cooled and capped with another 5 nm of W to prevent oxidation.

Specular X-ray diffraction (XRD) spectrum on Fig. 5.1 indicates the single-phase nature of Ho (0002) on W (110) buffered MgO (111). The rocking curve on Ho (0002) Bragg condition yields full-width-at-half-maximum (FWHM) of 1.88°, indicating good epitaxial crystallinity. The C_{6v} symmetry of Ho hcp structure is further confirmed by in-plane XRD ϕ scans. The Ho

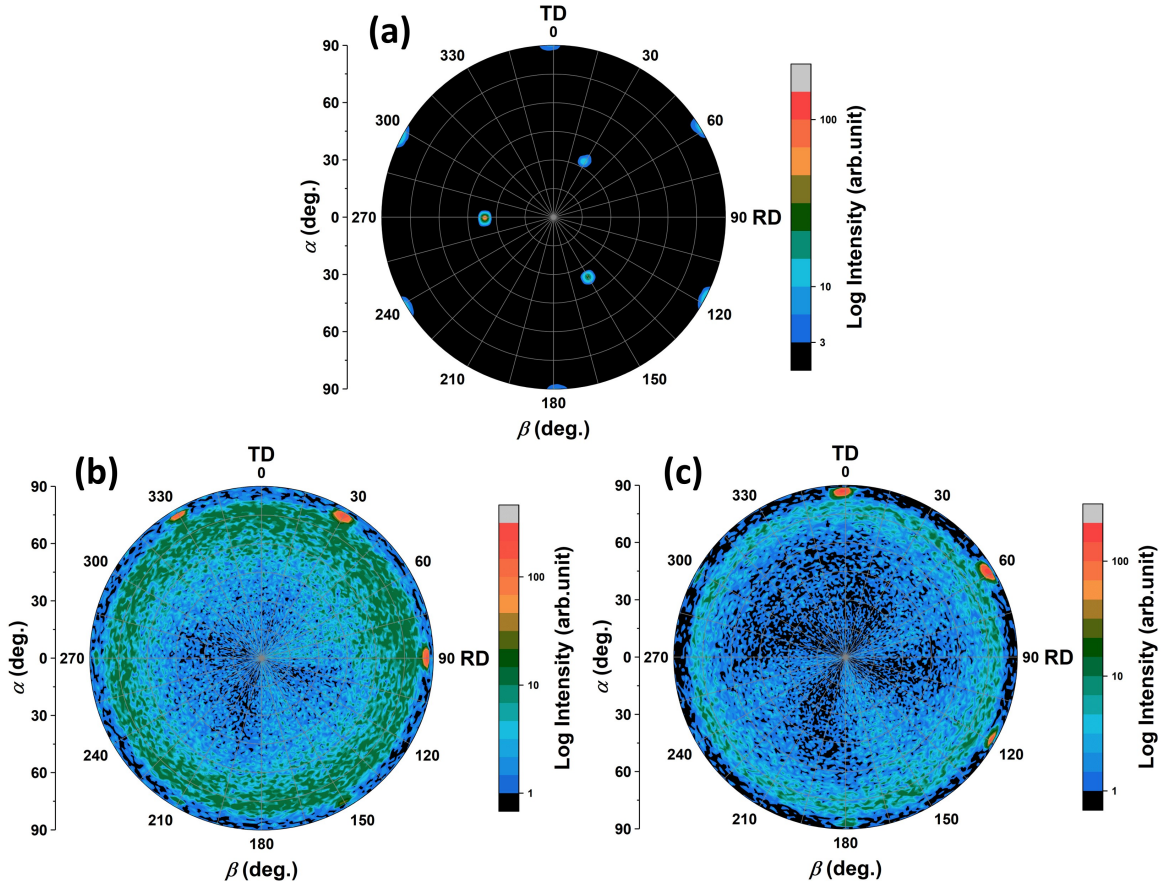

Figure 5.2. Hemisphere X-ray pole figure pattern on Ho (0002) with Bragg condition fixed to be (b) *b*-axis and (c) *a*-axis. A reference single crystal MgO (111) is shown in (a) with Bragg condition of MgO $(2\bar{2}0)$. The scale bar is in the log scale.

a-axis is aligned with MgO $< 2\bar{2}0 >$ and 30° from Ho *b*-axis, see Fig. 5.1. Pole figures in Fig. 5.2 further show the pure phase of Ho (0002) and support the aforementioned symmetry.

The prepared W/Ho (0002)/W samples were patterned into four-probe devices by using e-beam lithography, ion-milling, photolithography, sputtering, and lift-off process. The electrical transport measurements were executed in Quantum Design Physical Properties Measurement System (PPMS).

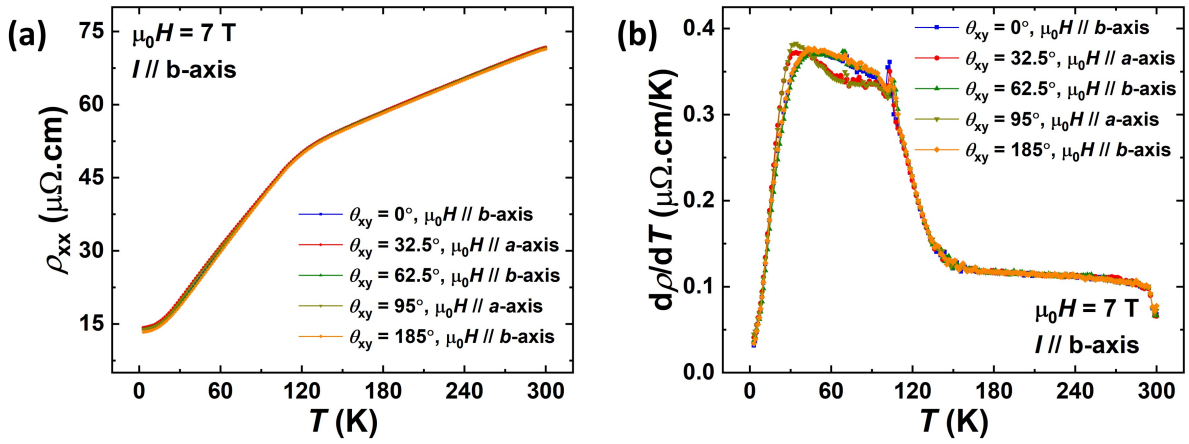

Figure 5.3. Resistivity vs temperature measured on patterned W/Ho (0002)/W under fixed field of 7 T. The derivative of (a) is plotted in (b).

5.3 Electronic Transport Measurements

As measuring the resistivity vs temperature with current along b-axis, the characteristic kink can be observed around 135 K, which is in good match with the T_N.As shown in Fig. 5.3 (a), the resistivity difference when applying external field along multiple a- and b-axes is very marginal. The derivative curves present more anisotropy especially in the regime from 100 K to 30 K. When the field is along a-axis, resistivity declines in a slower rate, indicating more scattering events.

Temperature-dependent longitudinal ADMR and transverse PHE were probed concurrently on the same device with I fixed in b-axis (Figs. 5.4 and 5.5). Sample was 7 T-field cooled to 5 K along b-axis and then warmed to each temperature setpoint. The ADMR and PHE was measured by rotating in the sample plane (xy plane) under external field $\mu_0 H$ of 7 T. The azimuthal angle between I and $\mu_0 H$ is denoted as θ_{xy}, which was scanned from -5 ° to 365 ° then reversed to -5 ° with fixed step of 2.5 °.

In Fig. 5.4(a), the ADMR was observed to have a negative sign with distinctive symmetries in FM and HAFM phases. Above 30 K, the ADMR in HAFM phase was mainly attributed to 6-fold symmetry. In particular, the ADMR at 60 K hosts approximately equal amplitude across the full range. All global maxima can be observed when $\mu_0 H$ is along a-axis. Below

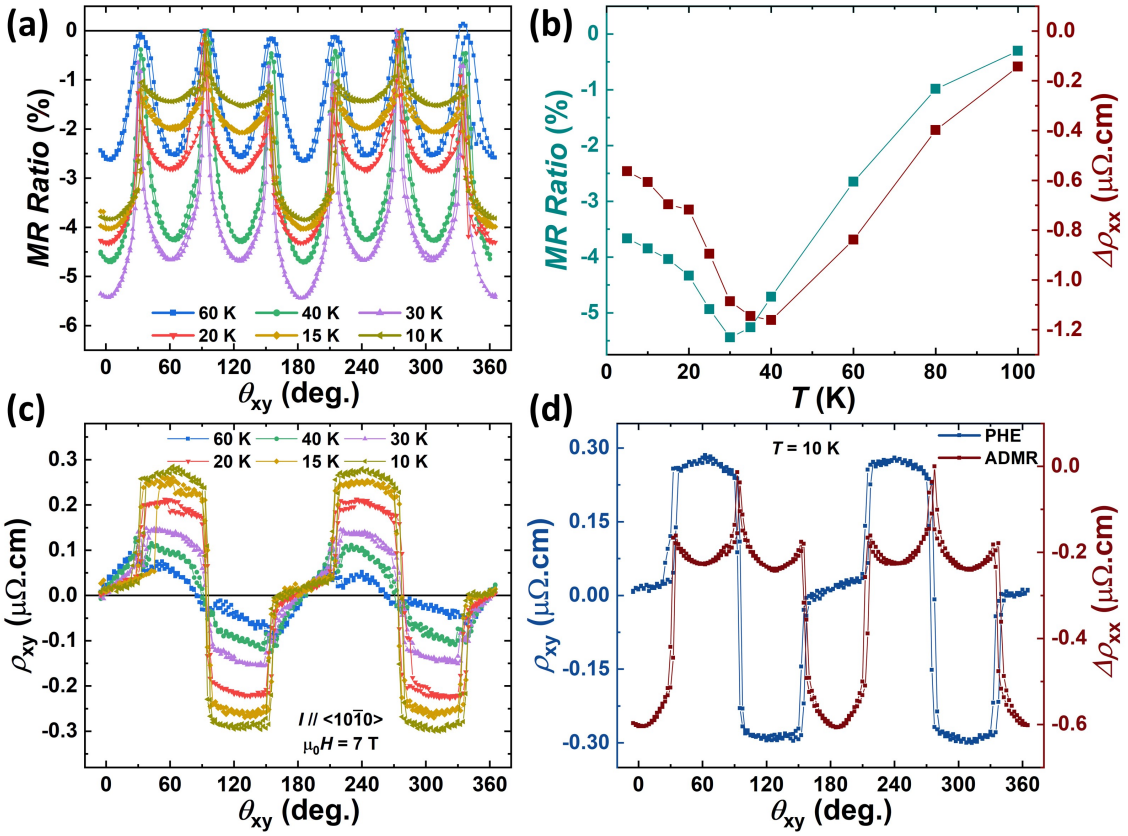

Figure 5.4. (a) Temperature-dependent ADMR at 7 T field. (b) MR Ratio and change of resistivity extracted from ADMR as a function of temperature. (c) Temperature-dependent PHE measured in parallel with ADMR. (d) A comparison of PHE and ADMR at 10 K plotted in resistivity.

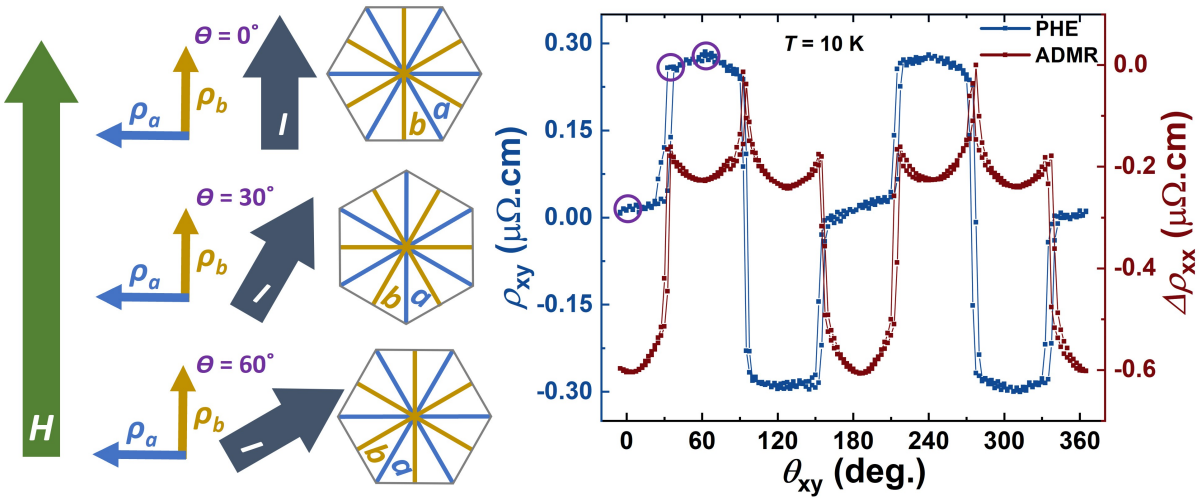

Figure 5.5. Schematically showing the relative position of current, magnetic field and hcp basal plane during ADMR and PHE as θ rotates in the sample plane.

20 K, the interplay between 2-fold and 6-fold contributions tends to be more pronounced. The 2-fold behaviour leads to global maxima when the $\mu_0 H$ is perpendicular to I ($\theta_{xy} = 90°, 270°$). The global minima can be observed when $\mu_0 H$ is colinear with I at $\theta_{xy} = 0°, 180°, 360°$. Local minima at $\theta_{xy} = 60°, 120°, 240°, 300°$ is speculatively ascribed to 6-fold contribution. The magnitude of MR Ratio and $\Delta\rho_{xx}$ ascended dramatically in HAFM phase as temperature decreased, followed by a monotonically decline in the FM phase (Fig. 5.4(b)). The MR ratio was obtained to be roughly 5% at 30 K, which is outstandingly larger compared to Dy [171] and some of topological Weyl antiferromagnets such as Mn_3Pt [186].

As shown in Fig. 5.4(c), the characteristic PHE data exhibit positive sign and monotonic increase of amplitude as temperature decreases. The PHE curves show $\sin(2\theta_{xy})$ symmetry with significantly different shapes. Remarkably, the PHE in FM phase displays a characteristic step-like wave function starting around 30 K. Above 30 K, PHE started to recover the conventional harmonic shape. Note that the amplitude of $\Delta\rho_{xx}$ and ρ_{xx} own similar magnitude as illustrated in Fig. 5.4(d), which is in agreement with the amplitude defined by the previous general mathematical expression in Eq. 1.14 and Eq. 1.15.

Field-dependent magnetoresistance (FDMR) was measured with $\mu_0 H$ sweeping separately along *a*-and *b*-axis, as illustrated in Fig. 5.6. Evident hysteresis can be observed in both FM and HAFM phases. In HAFM phase such as 40 K and 60 K, the *a*-and *b*-axis curves host very close coercivity and similar curve shape. The sign of MR ratio changes to negative in high field regime. At 10 K, the MR ratio mainly host negative sign in the whole field range. Pronounced anisotropic hysteresis loops can be observed. When field is along *b*-axis, MR is saturated at lower field, indicating *b*-axis as the easy axis in FM phase. The sharp peaks near $\mu_0 H$ = 0 T is due to multidomain structure, it is not due to the ballistic magnetoresistance because the MR was probed in a scale which is orders of magnitude larger than the electron mean free path in Ho. Throughout the whole temperature range, the MR does not saturate up to 7 T, which is due to the Lorentz force-induced geometrical magnetoresistance effect.

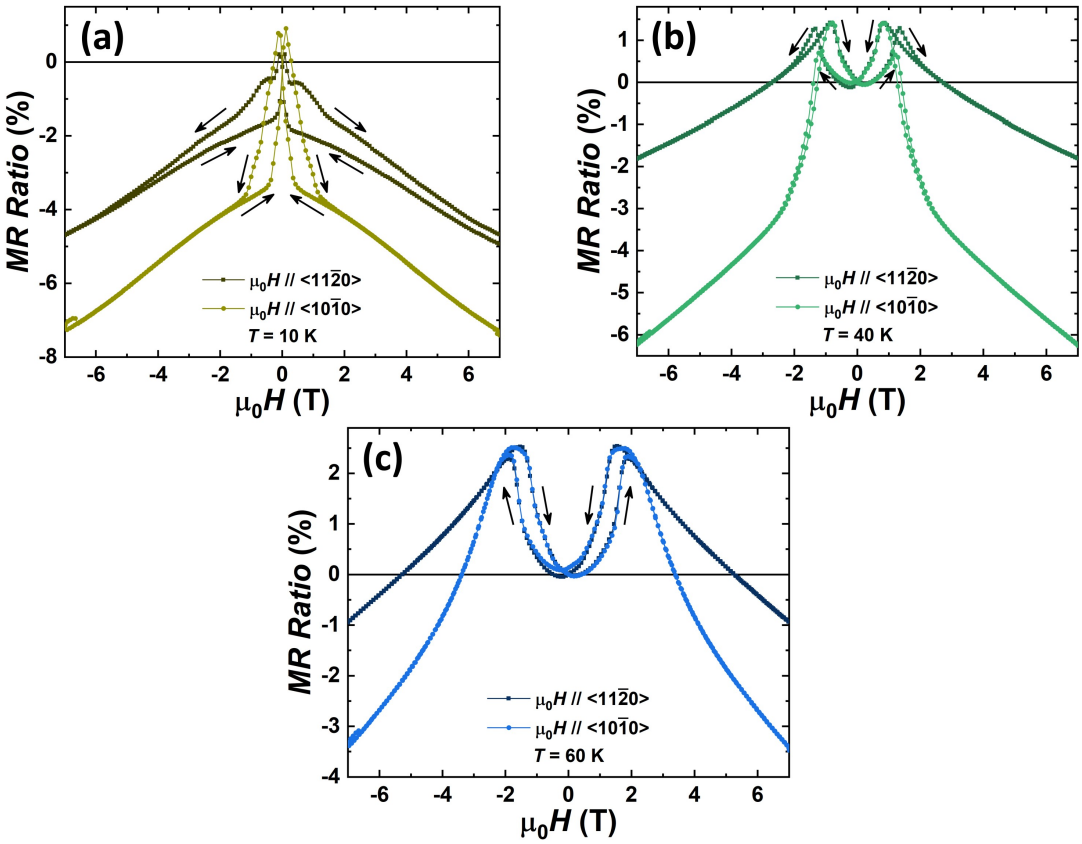

Figure 5.6. FDMR with field applied along *a*-and *b*-axis at (a) 10K, (b) 40 K, (c) 60 K. Arrows represent the direction of the sweeping field.

5.4 Discussion

According to the definition of ADMR, the amplitude of ADMR is governed by the difference between the resistivity when magnetization is along the current and perpendicular to the current, that is, (ρ_b - ρ_a). Therefore, the influence on ρ_b and ρ_a by external magnetic field shall be addressed, which is directly linked to the reported giant magnetostriction effect in Ho [173]. At 77 K, Ho exhibited negative magnetostriction (-λ) along a-and b-axis with the magnitude of $\lambda_a > 1.5\ \lambda_b$ [173]. Such distinctive magnetostriction-induced change of resistivity was absent in the ADMR at 60 K, as the difference of amplitudes is almost diminutive when $\mu_0 H$ // a-axis and b-axis. Hence, the magnetostriction is insufficient to explain the 6-fold dominant behavior of ADMR at 60 K. It is speculative that the overall resistivity in the basal plane was uniformly modified by magnetoelastic distortion on the entire lattice which could possibly result in similar magnitude of ($\rho_b - \rho_a$) that overcomes the magnetostriction contribution. On the other hand, the dominant 2-fold contribution at lower temperatures resulted in different amplitudes when $\mu_0 H$ // a-axis and b-axis, being inconclusive to separate the magnetostriction contribution from the 2-fold contribution at lower temperatures.

Generally, three origins of PHE are reported [187]. The first is the interaction between magnetic orders and spin-orbit interaction in the ferromagnetic material. The second is the time-reversal symmetry (TRS) breaking due to in-plane magnetic field in the topological insulator. The last is the orbital MR that is induced from anisotropic Fermi surface or anisotropic effective mass tensor [170]. PHE in this work could be ascribed to the first and the third origin as Ho is not a topological insulator. The first origin mainly leads to conventional $\sin(2\theta)$ behavior in the high-temperature regime. However, the step-like PHE in low-temperature regime is yet to be experimentally reported, which could be a joint consequence of multiple contributions. Here, we mainly discuss the 10 K data. The PHE curve can be described as a two-stage shape. The two stages in the negative regime are considered to be theoretically equivalent to the two stages in the positive regime, as the positive to negative sign switching is ascribed to the sign-

switching of $\sin(2\theta_{xy})$. In particular, λ_a was reported to ascend steeply at 4.2 K when $\mu_0 H$ was rotating away from b-axis to the adjacent a-axis [173]. Such step-like surge could result in distinctive $\Delta\rho$ in the low-temperature regime. Therefore, the PHE amplitude can be interpreted as $(\rho_b \pm \Delta\rho_b) - (\rho_a \pm \Delta\rho_a)$. The sharp transition between the two stages might be elucidated by the surged magnetostriction induced $\Delta\rho$ as $\mu_0 H$ was rotating away from b-axis. Moreover, the global extrema of standard $\sin(2\theta_{xy})$ can be seen to be 90° apart, which are 60° apart in the step-like PHE which corresponds the uniaxial anisotropy from the 6 easy axes (b-axis) in the basal plane. We argue that this phenomenon could be potentially induced by anisotropic Fermi surface and led to a similar effect as orbital MR. Lastly, it is worth noting that Kriegner *et al*. theoretically modeled PHE curves on antiferromagnetic hcp MnTe. Step-like PHE was predicted at remanence state ($\mu_0 H$ = 0 T) when the domain size is large (30 nm) [135]. Although the domain size is unlikely to be the major contribution in the saturated Ho at 7 T, future work might extend the step-like PHE to other hcp materials with fruitful physics origins.

5.5 Acknowledgement

Chapter 5, in part, is currently being prepared for submission for publication of the material "Y. Xiao, Y. Kim, R. Medapalli, M. J. Gilbert, E. E. Fullerton, *Evolution of Anisotropic Magnetoresistance in Magnetic Weyl Semimetal,*" The dissertation author was one of the primary investigators and author of this material.

Chapter 6

Easy-axis Dependent Electronic Transport, in The Cases of Epitaxial $CrPt_3$ and hcp Co

In this chapter, we investigate the strong anomalous Hall effect (AHE) in chemically ordered $CrPt_3$, which is superior to traditional element ferromagnets. As a comparison, although hcp Co owns lower AHE, its highly *c*-axis dependent anomalous Hall conductivity (AHC) is successfully examined which is in good agreement with theoretical predictions. Moreover, the easy-axis dependent AHE and ADMR in $CrPt_3$ (110) is further understood by a comprehensive magnetotransport study on hcp Co with *c*-axis in the plane. Unusual and exotic anisotropic magnetotransport can be found in engineering the crystalline orientation, which is averaged out in polycrystalline/amorphous materials.

6.1 $CrPt_3$ Growth and Characterization

Akin to the $FePt_3$ growth in chapter 4, $CrPt_3$ was also grown by using co-sputtering technique with similar growth conditions as $FePt_3$. The chemical ordering was also achieved by 40-minute annealing. Differently, $CrPt_3$ sometimes requires higher annealing temperature compared to $FePt_3$, which can vary from 850°C to 885°C. Cr : Pt ratio was varied from 21 : 79 to 35 : 65, and 33 : 67 led to the strongest I_{220}/I_{110} ratio according to XRD characterization. Therefore, the $CrPt_3$ in the following content is $Cr_{33}Pt_{67}$ unless otherwise stated. Similar to what

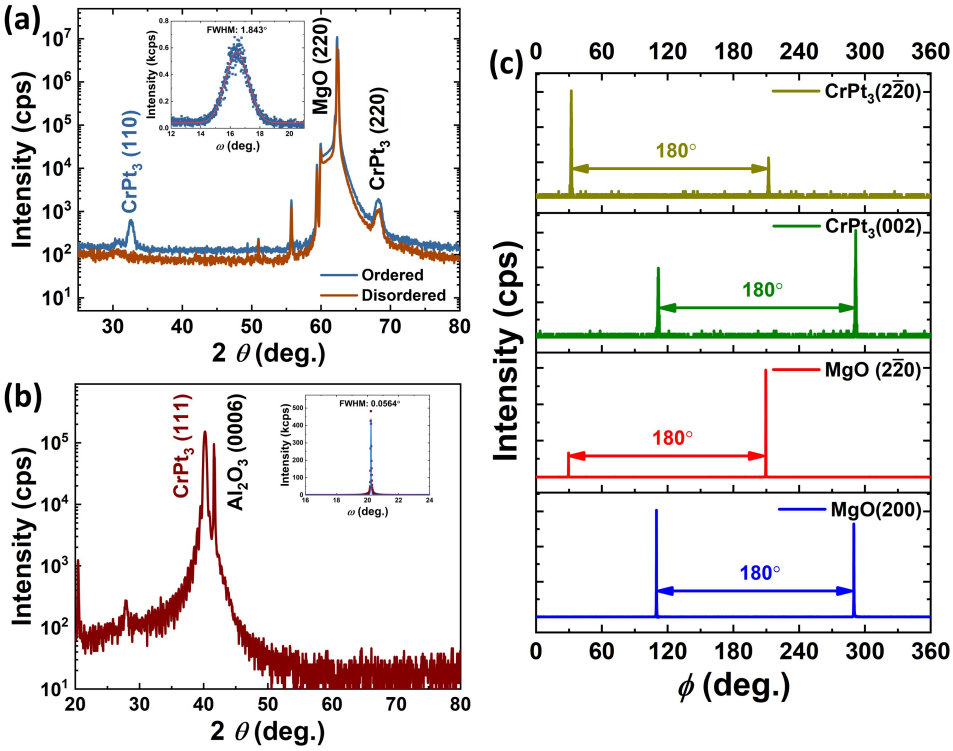

Figure 6.1. Specular XRD on (a) $CrPt_3$ (110) and (b) (111). (c) In-plane ϕ scans show the 2-fold symmetry of $CrPt_3$ (110) and its in-plane orientation with respect to the MgO (220) substrate.

we learnt from $FePt_3$, the chemical ordering nature in $CrPt_3$ was confirmed by out-of-plane XRD and pole figures. Chemically ordered $CrPt_3$ also exhibits a characteristic (110) peak compared to disordered $CrPt_3$ reference. The ordering parameter S of a 15-nm-think $CrPt_3$ (110) was 55.9 % based on a similar calculation in chapter 4 using Eq. 4.5. As shown in Fig. 6.1, the FWHM of ω scan over $CrPt_3$ (110) and (111) is 1.843° and 0.0564°, indicating similar crystalline quality compared to $FePt_3$ in chapter 4. Also, this chapter only focuses on chemically ordered $CrPt_3$, hence, the following $CrPt_3$ represents chemically ordered alloy unless otherwise stated.

In chemically ordered $FePt_3$, only Fe atoms exhibit magnetization. However, both Cr and Pt atoms contributed to the ferrimagnetic property of chemically ordered $CrPt_3$, the opposite moment on Cr and Pt atoms is shown in Fig. 6.4. The moment on Cr atom is calculated to be 2.33 μ_B/atom, while Pt atom has a moment of -0.27 μ_B/atom [24]. In bulk $CrPt_3$, the easy axis is $< 100 >$ due to cubic anisotropy. However, $CrPt_3$ (110) exhibits uniaxial in-plane anisotropy

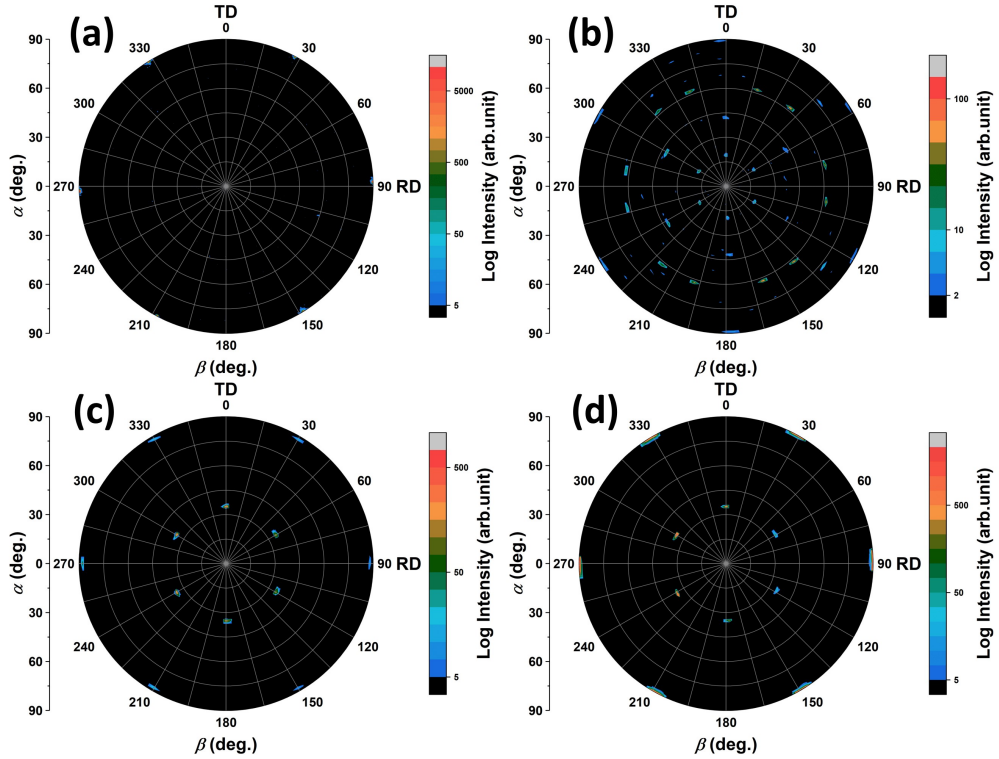

Figure 6.2. (a)-(d) Pole figure of $CrPt_3$ $\{110\} < 001 >$, $\{110\} < 002 >$, $\{110\} < 1\bar{1}0 >$, $\{110\} < 2\bar{2}0 >$, respectively.

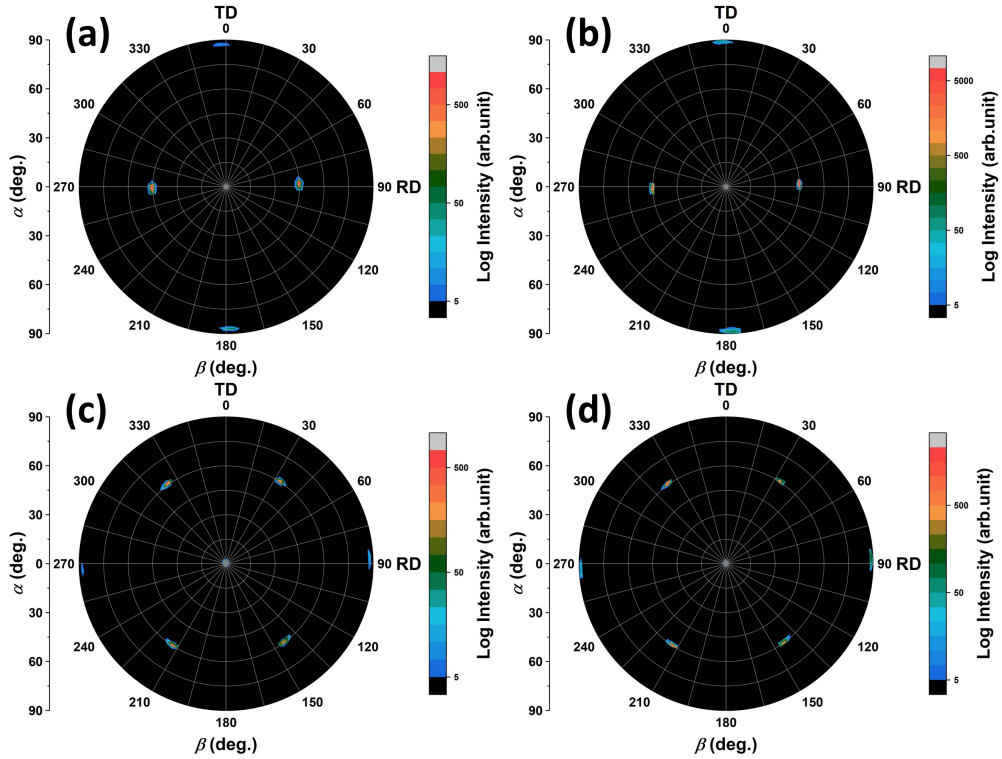

Figure 6.3. Pole figure of (a) Al_2O_3 $\{0006\} < 10\bar{1}0 >$, note the narrow diffraction peaks of Al_2O_3 $< 10\bar{1}0 >$, (b) $CrPt_3$ $\{111\} < \bar{1}12 >$, (c) $CrPt_3$ $\{111\} < 1\bar{1}0 >$, and (d) $CrPt_3$ $\{111\} < 2\bar{2}0 >$. From the pole figures on $CrPt_3$ (110) and (111), the consistent chemical ordering is evident.

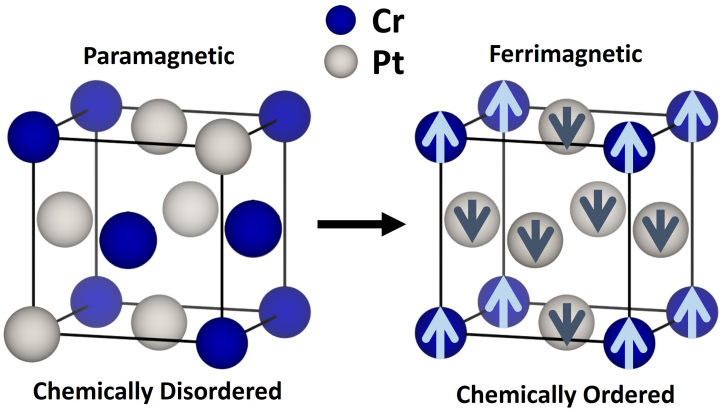

Figure 6.4. Sketch of chemically disordered $CrPt_3$ and ordered crystal structure.

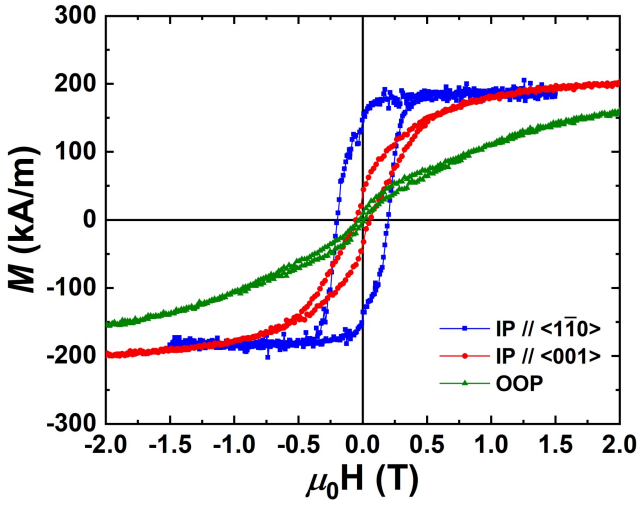

Figure 6.5. Room temperature magnetic hysteresis loop measured on $CrPt_3$ (110) with in-plane and out-of-plane orientations.

with easy axis along $< 1\bar{1}0 >$ due to the substrate-induced strain. The M_S is characterized to be 185 kA/m, which is strongly correlated to the long range ordering.

Classical 4-probe devices were also photolithographically patterned on $CrPt_3$ films (Fig. 6.6). The orientation of patterned wires was determined based on the crystalline orientations relative to the substrate according to pole figures in Figs. 6.2 and 6.3. The longitudinal resistivity ρ_{xx} of $CrPt_3$ (110) and $CrPt_3$ (111) was characterized along different in-plane crystalline orientations (Fig. 6.7). Similar to high symmetry cases shown in the previous chapters, such as Pt (111) and $FePt_3$ (111), isotropic ρ_{xx} can be found in the $CrPt_3$ (111) plane. On the other

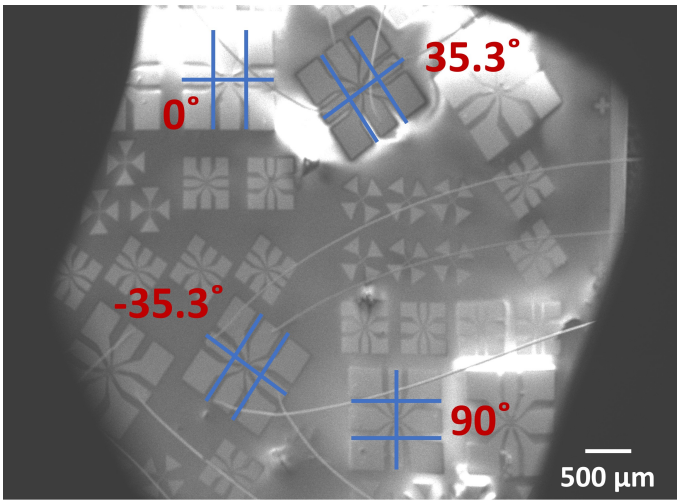

Figure 6.6. An SEM picture of patterned devices on $CrPt_3$ sample with current in angles of easy axis. It is clear to be found many devices with current 0°, 35.°, -35.3°, and 90° to the easy axis.

hand, anisotropic ρ_{xx} is also observed in $CrPt_3$ (110) plane. Notably, ρ_{xx} along $< 001 >$ always exhibits the highest magnitude in the three cases of Pt (220), $FePt_3$ (110), and $CrPt3_3$ (110).

6.2 hcp Co Growth and Characterization

Epitaxial hcp-Co films were grown onto single-crystalline MgO (220) and Al_2O_3 (0006) substrates using a dc magnetron sputtering with a base pressure of 8×10^{-8} Torr and a growth Ar pressure of 2.7 mTorr. Co $(10\bar{1}0)$ was grown on Cr-buffered MgO (220) substrates. The Cr (211) seed layers were deposited at 500°C to initiate a desirable epitaxy, followed by Co $(10\bar{1}0)$ deposition at 200°C [188, 189, 190, 191]. Co (0002) films were grown directly on Al_2O_3 (0006) substrates at 300°C [192]. Before starting high temperature growth, the temperature setpoint was held for 25 minutes to achieve uniform temperature across the sample holder. The first 25-minute baking also helps to remove the moisture on the substrate, this is particularly important when using MgO as it is hydrophilic. Later, the substrate was naturally cooled, and a subsequential 1.5-nm-thick amorphous Cr layer was grown *in situ* to help prevent surface oxidation. Cr(5)/Co $(10\bar{1}0)(60)$ films were also grown as comparison samples using the same growth condition as that of Cr(10)/Co $(10\bar{1}0)(30)$ films. Additionally, polycrystalline Co reference films were

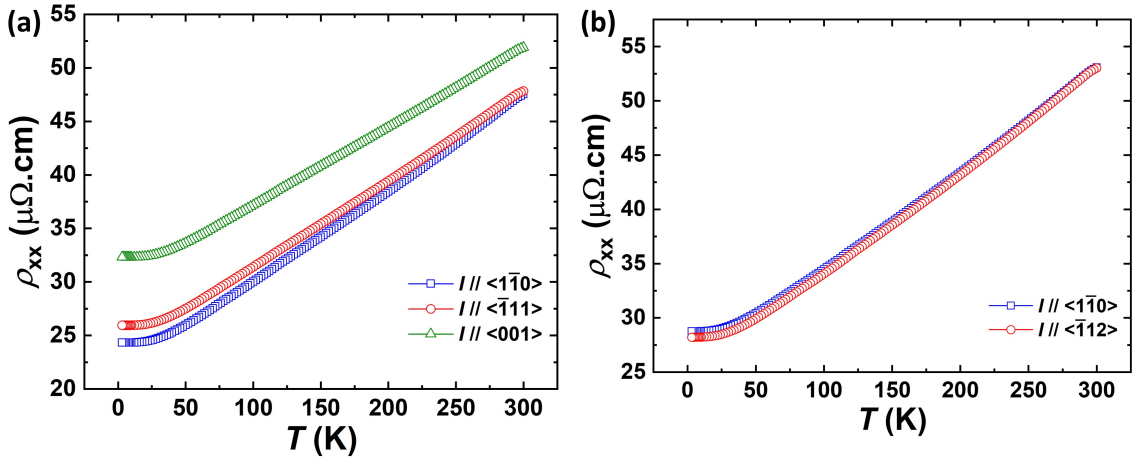

Figure 6.7. Resistivity vs temperature measured on patterned $CrPt_3$ (110) and $CrPt_3$ (111) with zero external magnetic field.

room-temperature grown directly on thermally oxidized Si (004) substrates with the same Cr capping. The thermal oxide is 300-nm-thick SiO_2, thus, the orientation of Si substrate is not considered to play a role in inducing the anisotropy in polycrystalline Co.

To characterize the crystallographic properties of Co films, XRD measurements were performed. Figs. 6.8(a) and (b) present the out-of-plane symmetric θ-2θ scans of Co (0002)(30) and Cr(10)/Co $(10\bar{1}0)$(30) films (thickness in nm throughout the text unless otherwise stated), demonstrating the single-phase epitaxy growth along the substrates or the seed layers. By rocking the Bragg condition, the diffraction peak broadening was evaluated. The Lorentzian fitted full-width-half-maximum (FWHM) of the ω curve across Co (0002) and Co $(10\bar{1}0)$ are 0.0614° and 0.7562°, respectively, indicating excellent crystalline quality and large grain size. Moreover, the in-plane ϕ scan further confirmed the C_{6v} symmetry of Co $\{0002\} < 10\bar{1}0 >$ respect to Al_2O_3 $\{0006\} < 11\bar{2}0 >$, and C_{2v} symmetry of Co $\{10\bar{1}0\} < 0002 >$ film respect to MgO $\{220\} < 002 >$ (see Figs. 6.9).

To investigate the magnetization of Co (0002) and Co $(10\bar{1}0)$, we performed magnetic field- and temperature-dependent magnetization measurements by using VSM module on PPMS. For Co $(10\bar{1}0)$, Fig. 6.10(a) and Figs. 6.11(d)-(f) indicates a strong uniaxial anisotropy with its easy axis along the $< 0002 >$ (henceforth referred as c-axis of hcp structure). For Co

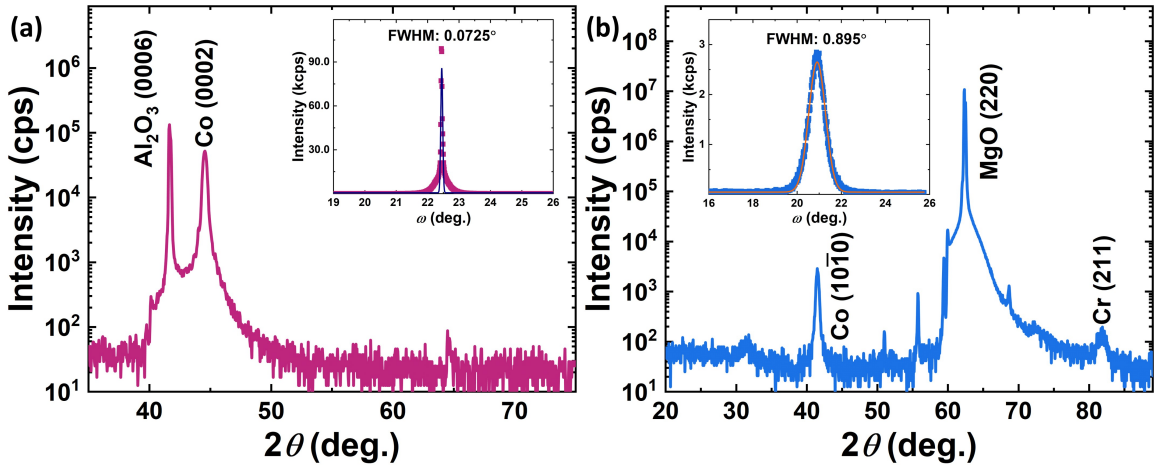

Figure 6.8. Specular XRD on (a) Co (0002) and (b) Co $(10\bar{1}0)$. Insert: ω scan across (a) Co (0002) and (b) Co $(10\bar{1}0)$ diffraction peaks.

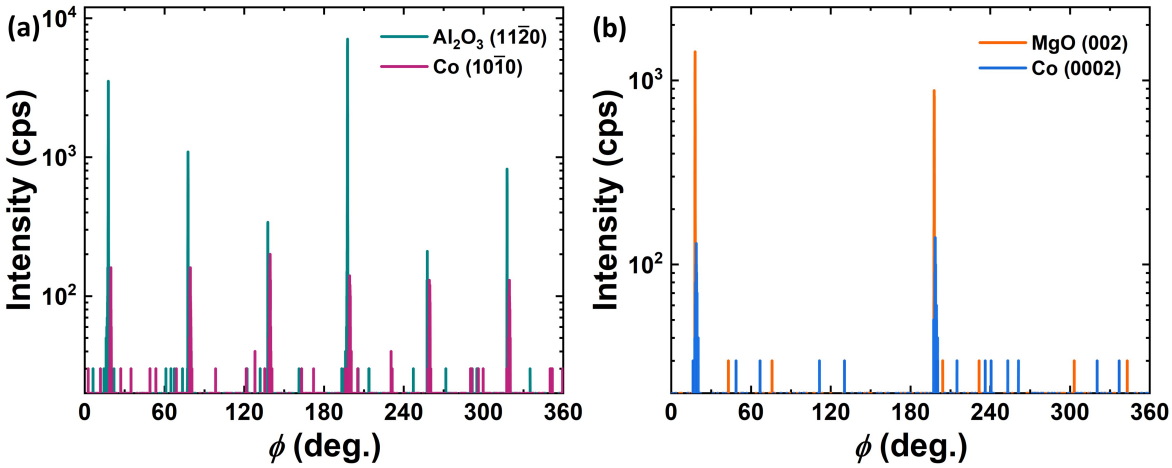

Figure 6.9. In-plane ϕ scans evidently reveal the 6-fold and 2-fold symmetry of (a) Co (0002) and (b) Co $(10\bar{1}0)$.

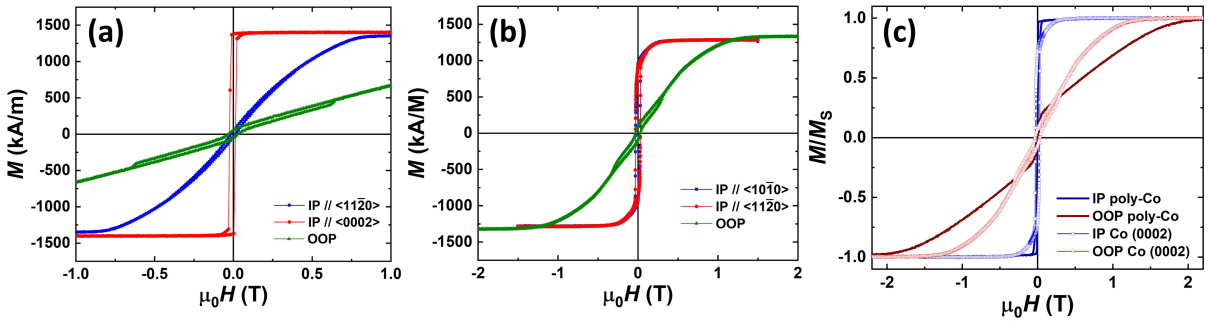

Figure 6.10. (a) Room temperature magnetic hysteresis loops on (a) Co $(10\bar{1}0)$ (b) Co (0002) measured with in-plane and out-of-plane field. (c) Comparison between polycrystalline Co and Co (0002) film.

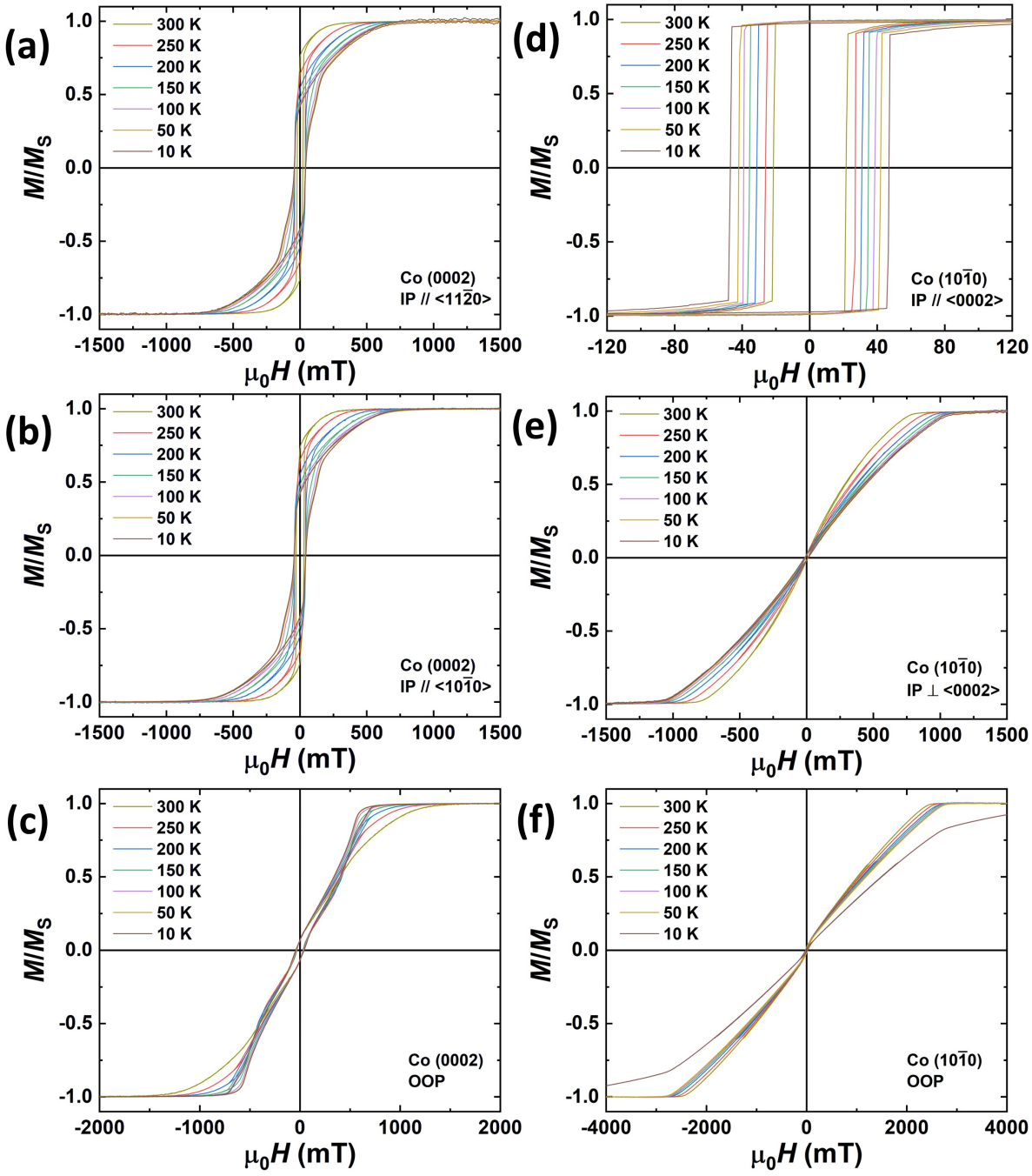

Figure 6.11. (a)-(c) Temperature-dependent magnetic hysteresis loops on Co (0002). (d)-(f) Temperature-dependent magnetic hysteresis loops on Co $(10\bar{1}0)$. M was normalized to the M_S at each temperature setpoint.

(0002), despite its perpendicular uniaxial magnetocrystalline anisotropy along c-axis, the shape anisotropy dominates the overall anisotropy. Fig. 6.10(b) and Fig. 6.11(a)-(b) display isotropic hysteresis loops when field is along both $< 11\bar{2}0 >$ and $< 10\bar{1}0 >$ (henceforth referred as a-axis and b-axis of hcp structure, respectively), suggesting that Co (0002) sample's basal plane is the easy plane. Fig. 6.10 (c) shows the comparison between Co (0002) and polycrystalline Co. The out-of-plane saturation field in Co (0002) is much lower, that is, the in-plane anisotropy of Co (0002) is significantly reduced compared to polycrystalline Co.

Figure 6.11 summarized magnetic hysteresis loops on Co (0002)(30) and Cr(10)/Co $(10\bar{1}0)$(30) samples under various temperature setpoints from 10 K to 300 K. The uniaxial in-plane anisotropy of Co $(10\bar{1}0)$ is consistent throughout the whole temperature range. More importantly, the in-plane hard axis curves (Fig. 6.11(e)) of Co $(10\bar{1}0)$ can be fitted by the following equation [193, 191]:

$$\mu_0 H = (\frac{2K_1}{\mu_0 M_S})(\frac{M}{M_S}) + (\frac{4K_2}{\mu_0 M_S})(\frac{M}{M_S})^3 \tag{6.1}$$

where $\mu_0 H$ is the magnetic field strength, K_1 and K_2 are the first- and second-order anisotropy constant. M_S is the saturated magnetization. μ_0 is the vacuum permeability. Each hard axis curve was well fitted with M_S averaged above saturation at each temperature (see Fig. 6.12(a)). The coefficient of determination R^2 of each curve was above 0.999, indicating excellent fitting. The fitted K_1 and K_2 are 350 kJ/m^3 and 103 kJ/m^3 at 300 K (Fig. 6.12(b)), respectively, in good agreement with the reported those of Co $(10\bar{1}0)$ thin films [194, 191].

The longitudinal resistivity ρ_{xx} of Co (0002) and Co $(10\bar{1}0)$ was characterized on photolithographically patterned 4-probe devices along different in-plane crystalline orientations (Fig. 6.14). Similar to the previous cases on high symmetry plane, the ρ_{xx} in the Co (0002) basal plane is relatively isotropic, while being anisotropic on Co $(10\bar{1}0)$ sample due to the C_{2v} symmetry of $(10\bar{1}0)$ plane. In particular, ρ_{xx} has a higher value when I is along c-axis. The ρ_{xx} when I is 45° to the c-axis is roughly in the middle. The residual resistance ratio (RRR) in Co (0002) is around

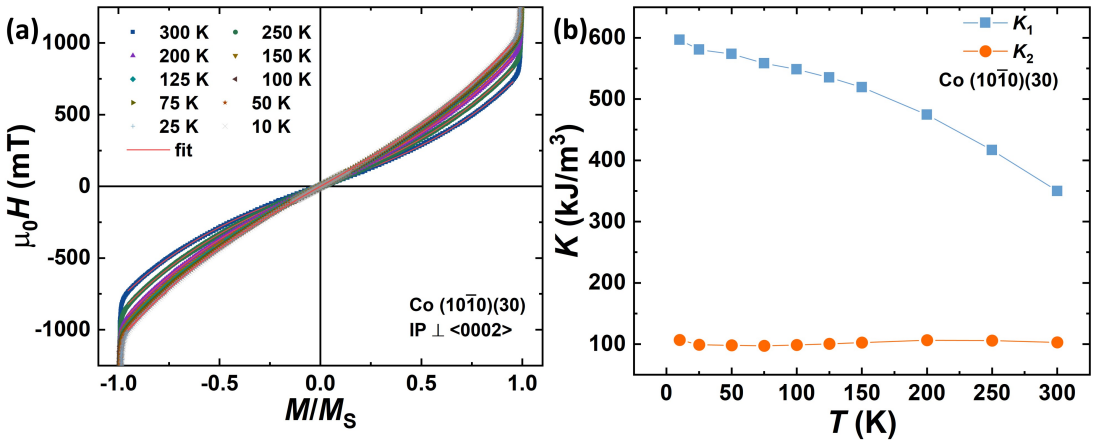

Figure 6.12. (a) Hard axis magnetic hysteresis loops of Co $(10\bar{1}0)$ fitted by Eq. 6.1. Dots are data points. Solid red lines are fitting curves. (b) Fitted anisotropy constant plotted as a function of temperature.

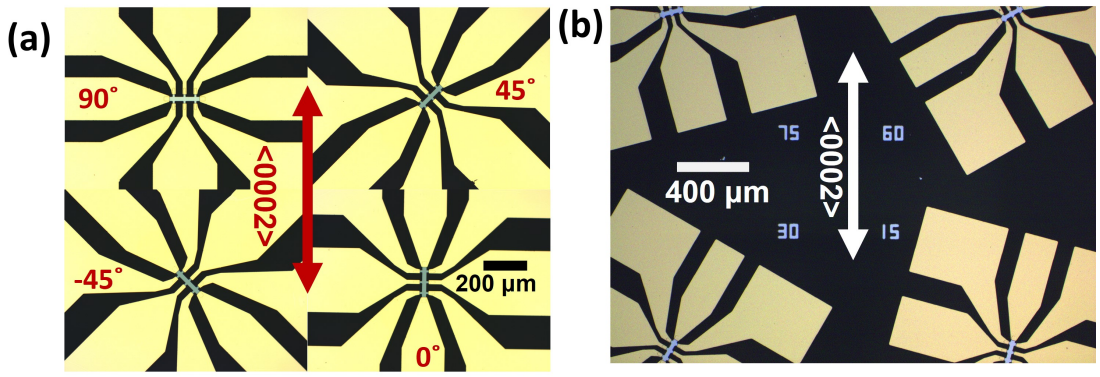

Figure 6.13. Examples of patterned devices on Co $(10\bar{1}0)$ with current in angles of *c*-axis. (a) Zoom-in optical picture shows the 4-probe devices with current 90°, 45°, -45°, and 0° to *c*-axis. (b) The zoom-out optical picture shows the 4-probe devices with current 15°, 30°, 60°, and 75° to *c*-axis.

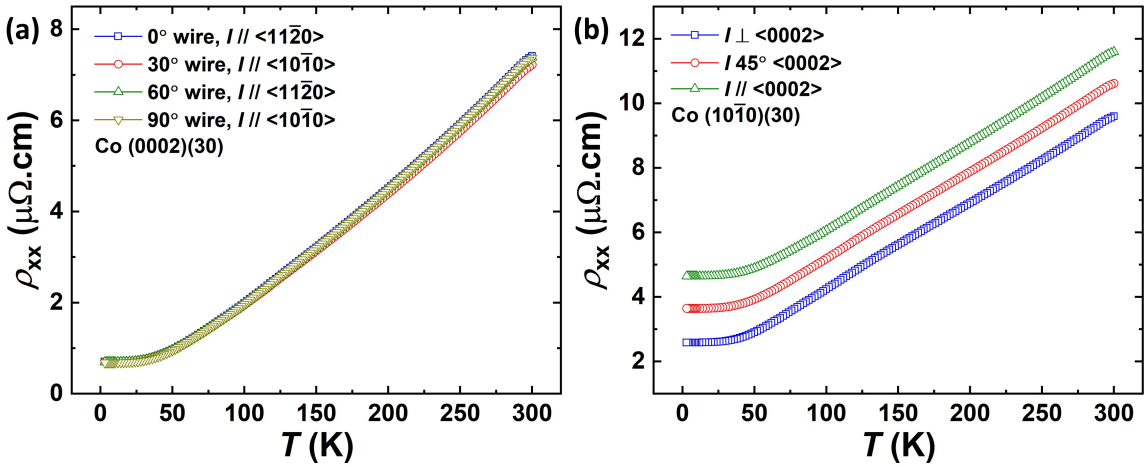

Figure 6.14. Resistivity vs temperature measured on patterned Co (0002) and Co $(10\bar{1}0)$ with zero external magnetic field.

10.56, which is at least 2 times higher than that of in Co $(10\bar{1}0)$. The ρ_{xx} of Cr seed layer was characterized separately by using the same 4-probe device on a MgO (220)/Cr (211)(10) sample. Here, we note that in Cr (211)(10)/ Co $(10\bar{1}0)$(30) bilayer, 94.6% of the current was shunted in Co layer, the current distribution in Cr is hereby negligible in this chapter. Additionally, the 1.5-nm-thick Cr capping layer became highly resistive after being naturally oxidized. Its conductivity is not taken into account in this work. Also, when I is perpendicular to c-axis in Co $(10\bar{1}0)$, it is, in fact, along a-axis, which is crystallographically equivalent to the case when I is along a-axis in Co (0002) sample. However, since Co (0002) and $(10\bar{1}0)$ have different film quality, these two cases are named differently and their results are presented separately.

6.3 Basic Mathematical Background Related to AHE Loops

In this chapter, the temperature-dependent AHE measurements were done with I along various crystalline orientations. The external magnetic field is fixed to be out of the sample plane with sweeping field strength. The AHE resistance R_{xy}^{AHE} is normalized to AHE resistivity ρ_{xy}^{AHE} by sample thickness. The Hall resistivity of magnetic materials can be typically expressed as a

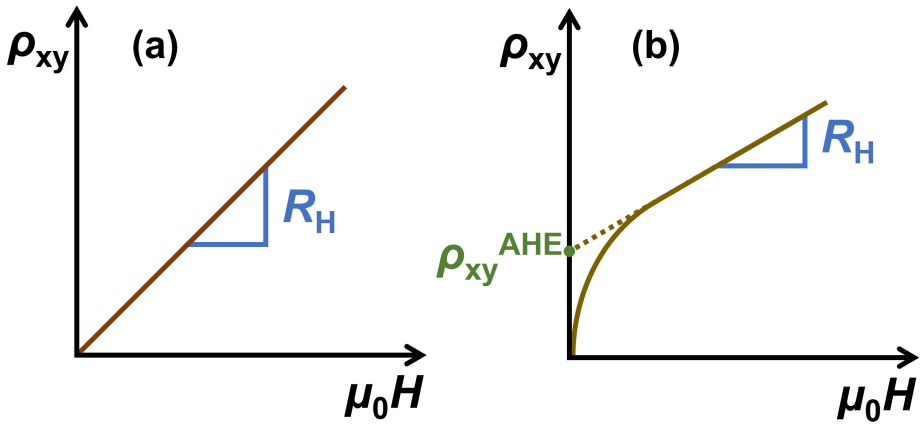

Figure 6.15. Schematic of Hall resistivity vs magnetic field with (a) OHE contribution only and (b) OHE + AHE contribution.

sum of OHE contribution and magnetization contribution:

$$\rho_{xy} = R_H \mu_0 H_z + R_S M_S = R_H \mu_0 H_z + \rho_{xy}^{AHE} \tag{6.2}$$

where R_H and R_S are the OHE and AHE coefficients. As illustrated in Fig. 6.15, the R_H can be achieved from the slope of OHE contribution, and the ρ_{xy}^{AHE} can be obtained as the interception from fitting the linear portion of the Hall loop.

Remember the mechanisms of SHE and AHE in chapter 1, the AHE resistivity can be interpreted as a combination of intrinsic and extrinsic contributions. Mathematically, we have:

$$\rho_{xy}^{AHE} = a(\rho_{xx}) + b(\rho_{xx})^2 + c(\rho_{xx})^2 \tag{6.3}$$

then, this equation can be transformed to a linear equation:

$$\frac{\rho_{xy}^{AHE}}{\rho_{xx}} = a + b\rho_{xx} + c\rho_{xx} \tag{6.4}$$

where a, b, and c represent the contributions from skew scattering, side jump and intrinsic mechanism, respectively. From the above equations, we learn that by investigating ρ_{xy}^{AHE} as a

function of longitudinal resistivity ρ_{xx}, the extrinsic and intrinsic contribution can be unpacked. However, it also can be seen that the side jump contribution cannot be separated from the intrinsic contribution. Furthermore, it needs to be noted that the AHE conductivity σ_{xy}^{AHE} is not a simple reciprocal of the AHE resistivity just as the conversion of longitudinal conductivity σ_{xx}, instead, it is calculated by:

$$\sigma_{xy}^{AHE} = \frac{\rho_{xy}^{AHE}}{\left(\rho_{xy}^{AHE}\right)^2 + \left(\rho_{xx}\right)^2} \tag{6.5}$$

since the $(\rho_{xy}^{AHE})^2$ is far less than the $(\rho_{xx})^2$, the Eq. 6.5 can be commonly simplified to:

$$\sigma_{xy}^{AHE} \approx \frac{\rho_{xy}^{AHE}}{\left(\rho_{xx}\right)^2} \tag{6.6}$$

However, in this dissertation, σ_{xy}^{AHE} was still calculated using the unsimplified Eq. 6.5. Furthermore, similar to the spin Hall angle θ_{SH}, the AHE angle θ_{AH} quantifies the strength of bulk AHE:

$$\theta_{AH} = \frac{\sigma_{xy}^{AHE}}{\sigma_{xx}} \tag{6.7}$$

Experimental AHE results can be found in the following sections.

6.3.1 AHE in $CrPt_3$

We first show the AHE results on $CrPt_3$. In $CrPt_3$ (111), the AHE is isotropic in the sample plane with pronounced hysteresis loops, suggesting strong perpendicular magnetic anisotropy (PMA) of $CrPt_3$ (111). In $CrPt_3$ (110), when I is along easy axis ($< 1\bar{1}0 >$), the AHE curve is more linear above saturation compared to that of I is 90° to easy axis ($< 001 >$), indicating stronger influence from the magnetization contribution ($M(T,H)$) when I // $< 001 >$. More interestingly, the AHE loops are "biased" when I // $< \bar{1}11 >$, as shown in Fig. 6.18, that is, the AHE loops are not centered at remanence. It can be observed that the biasing is dependent to

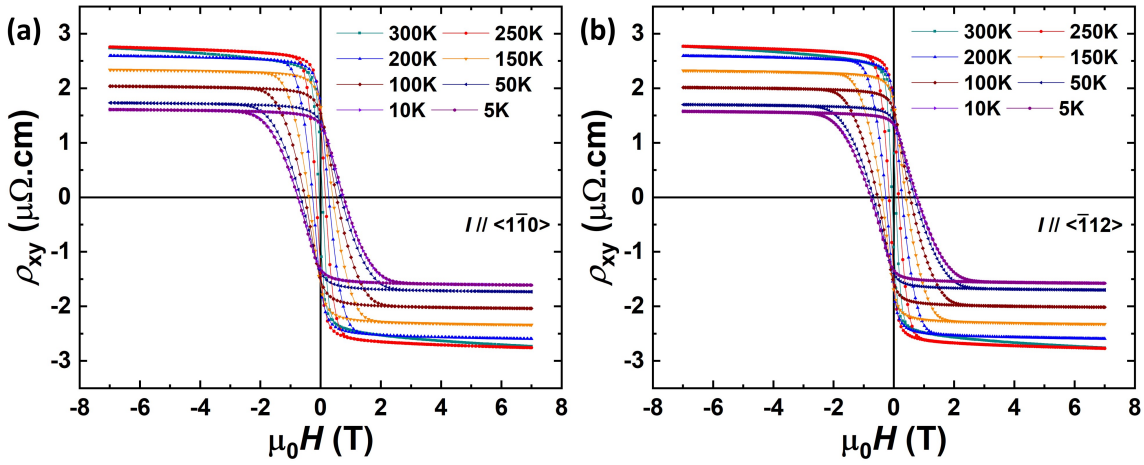

Figure 6.16. Hall resistivity vs temperature measured on patterned $CrPt_3$ (111) with current along (a) $< 1\bar{1}0 >$ and (b) $< \bar{1}12 >$

the relative position between I and the easy axis. When I is 35.3° to the $< 1\bar{1}0 >$, AHE loops have a negative bias, and the raw resistivity has negative offset. On the contrary, when I is -35.3° to the $< 1\bar{1}0 >$, AHE loops have a positive bias, and the raw resistivity has a positive offset. If taking the average values of the AHE loops in Figs. 6.18(a) and (c), the biasing vanishes in the averaged loops Figs. 6.18(d). In order to help understand this bias effect, we performed similar AHE measurements on hcp Co, especially focusing on the Co $(10\bar{1}0)$ because of similar uniaxial in-plane anisotropy.

6.3.2 AHE in hcp Co

As shown in Fig. 6.19 (a) and (b), in Co (0002) samples, the AHE loops exhibit isotropic behavior when I is along a- and b-axis. As the field is above the saturation field, the slope of AHE loop (OHE coefficient) remains quite constant throughout the whole temperature range. Except for the curves below 50 K, the slope is slightly higher. Also, the AHE curves became straight lines below 100 K, suggesting being dominated by the OHE. Such dominant OHE behavior at low temperatures was also reported in bulk hcp Co single crystals [195], which can be the result of the low residual resistance (high RRR) in Co (0002).

However, due to the strong uniaxial in-plane magnetic anisotropy in Co $(10\bar{1}0)$, the AHE

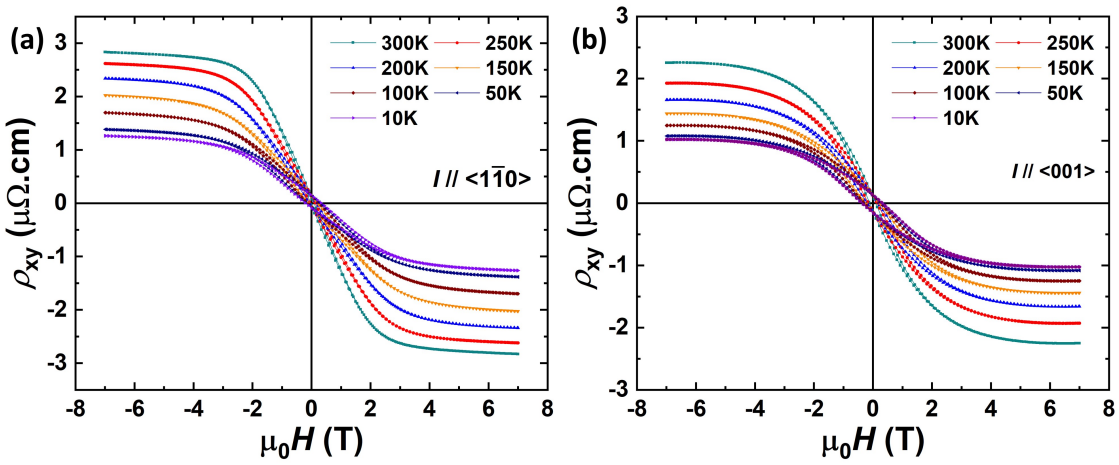

Figure 6.17. Hall resistivity vs temperature measured on patterned $CrPt_3$ (110) with current along (a) $< 1\bar{1}0 >$ and (b) $< 001 >$.

results are highly anisotropic depending on the current orientation relative to the *c*-axis (Figs. 6.20 and 6.21). Similar to Co (0002) sample, the temperature dependence of OHE coefficient of Co $(10\bar{1}0)$ remains weak. However, due to the lower RRR, the OHE does not fully dominate in the low-temperature regime on Co $(10\bar{1}0)$, leading to larger residual ρ_{xy}^{AHE} compared to Co (0002). More interestingly, in Co $(10\bar{1}0)$, in the cases when I is neither 0° nor 90° to the *c*-axis, the AHE exhibits "sinusoidal" curvature, as shown in Fig. 6.21. In particular, when I is 45° to the *c*-axis, it owns the most pronounced "sinusoidal" shape (Fig. 6.21(e)). Moreover, the AHE loops in those cases are not "centered" at the origin, that is, they are biased at the remanence state when field is zero, akin to the biasing effect in the aforementioned $CrPt_3$ (110). In comparison, when I is either 0° or 90° to the *c*-axis, the AHE loops are not biased. This "sinusoidal" shape can also be observed when measuring field-dependent magnetoresistance (FDMR) with external field sweeping out of the sample plane, as shown in Fig. 6.22, pronounced "sinusoidal" FDMR curves can be observed as temperature decreases, which is related to $M\cos$ contribution.

This "sinusoidal" shape can be understood as a result of PHE contribution. Recall the classical PHE expression in Eq. 1.15, which depends on the angle between I and in-plane magnetization $(\sin(\theta)\cos(\theta))$. At high fields above saturation, the Co magnetization M is saturated out of plane, therefore, the projection of Co magnetization in the sample plane is none,

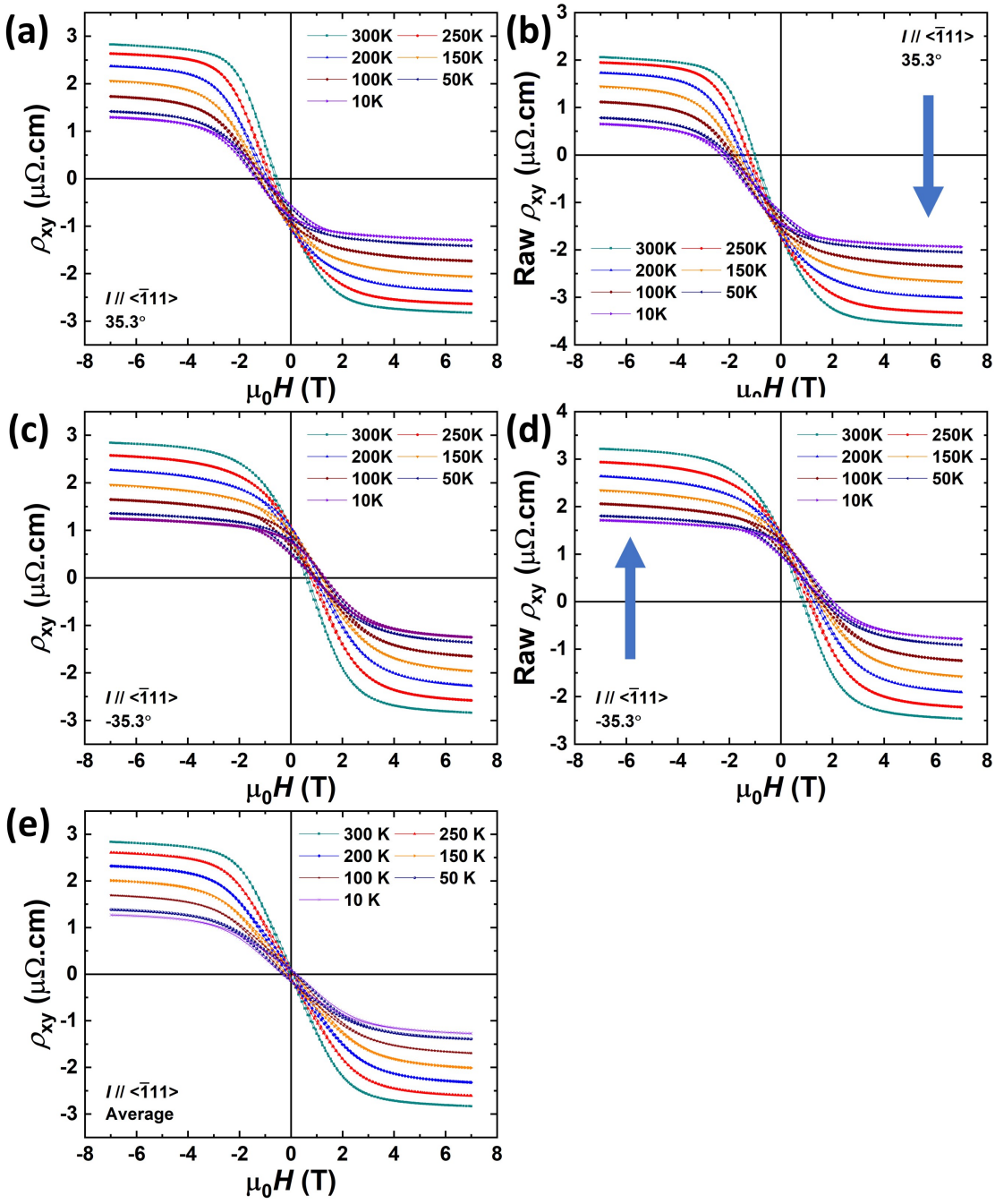

Figure 6.18. Hall resistivity vs T of patterned $CrPt_3$ (110) with current along $< \bar{1}11 >$. Raw resistivity is compared to the resistivity with corrected offset. (a)-(b) Current is along 35.3° orientation. (c)-(d) Current is along -35.3° orientation. (e) Hall Resistivity vs field averaged from (a) and (b).

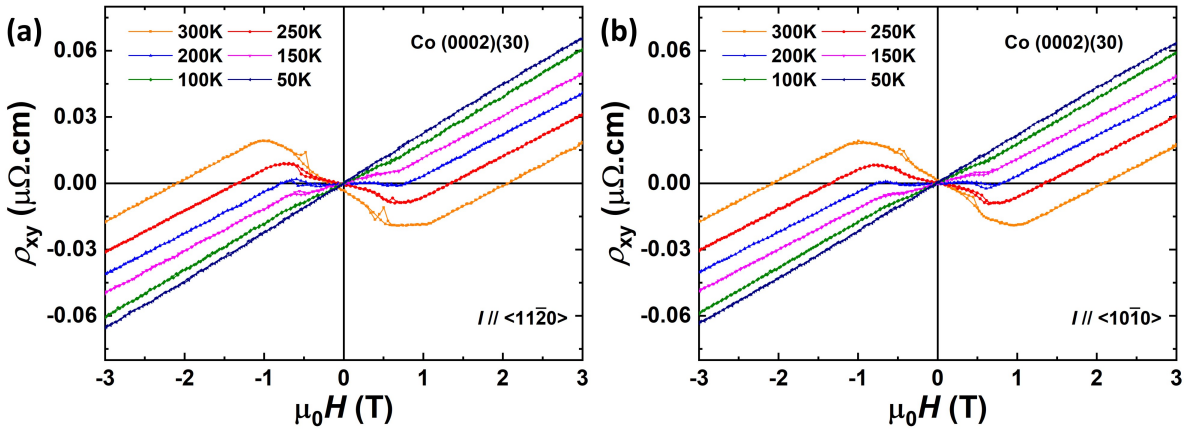

Figure 6.19. Hall resistivity vs temperature measured on patterned Co (0002) with current along (a) *a*-a and (b) *b*-axis.

leading to no PHE contribution because $\theta = 90^\circ$. As field decreases below saturation, M rotates towards in-plane with the orientation along the easy axis (c-axis), which is always in angle of the current direction, resulting in non-zero PHE signal, which is superposed on the AHE loop and makes the AHE loop "biased" at remanence. When I is 45° to the c-axis, the maximum PHE signal results in the largest AHE signal (Fig. 6.21(e)). This also explains the reason that no biasing is observed when I is either 0° or 90° to the c-axis. Because the PHE contribution vanishes if the projection of M is either 0° or 90° to the I. Based on this discussion, the giant resistivity offset is ascribed to the large resistivity difference when I is 0° to the c-axis compared to I is 90° to the c-axis, that is, $(\rho_{c-axis}(\mu_0 H) - \rho_{a-axis})$ plays the role.

6.3.3 AHE Mechanism in Co and $CrPt_3$

In both Co (0002) and Co $(10\bar{1}0)$, ρ_{xy}^{AHE} was extracted from fitting the linear regime on every AHE loop at each temperature. And ρ_{xx} was obtained from R vs T curves in Fig. 6.14. Then, the plotted $\rho_{xy}^{AHE}/\rho_{xx}$ decreases monotonically with decreasing ρ_{xx}, which can be well fitted by the Eq. 6.4. As shown in Fig. 6.23(a), in Co (0002), $\rho_{xy}^{AHE}/\rho_{xx}$ vs ρ_{xx} exhibits isotropically as I is along a- and b-axis. The fitted skew scattering parameter a is much less than the combination of side jump parameter b and intrinsic parameter c. On the other hand, the $\rho_{xy}^{AHE}/\rho_{xx}$ vs ρ_{xx} in Co $(10\bar{1}0)$ owns remarkable anisotropy in skew scatting parameter a, while

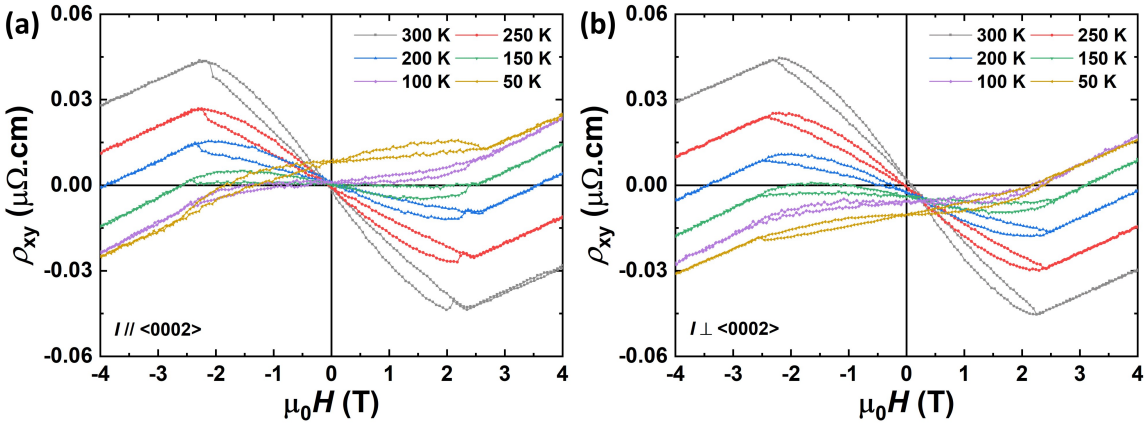

Figure 6.20. Hall resistivity vs temperature measured on patterned Co $(10\bar{1}0)$ with current along (a) c-axis, and (b) 90° to c-axis.

Table 6.1. Summary of fitted AHE mechanisms in hcp Co

Sample	Current Orientation	Fitted a	Fitted (b+c)
Co (0002)	I // a-axis	1.83E-4	4.12E-4
	I // b-axis	1.61E-4	4.19E-4
Co $(10\bar{1}0)$	I // c-axis	-5.83E-5	2.81E-4
	I 45° to c-axis	7.01E-4	2.83E-4
	I 90° to c-axis	1.07E-3	3.03E-4

the slope values are relatively similar. In particular, lowest a can be observed as I is along c-axis, suggesting a minimal skew scattering mechanism in the case of I along c-axis. The highest a can be seen when I is perpendicular to the c-axis. All the fitted a and (b+c) values are summarized in Table 6.1.

Figures 6.23 (b) and (e) present the calculated AHE conductivity σ_{xy}^{AHE} as a function of longitudinal conductivity σ_{xx}. The anisotropy of σ_{xy}^{AHE} is mainly ascribed to the anisotropy σ_{xx} according to the Eq. 6.5. The highest σ_{xy}^{AHE} measured on hcp Co is 936 S/cm at 100 K, which is almost 4 times as high as the value reported on polycrystalline Co at 78 K [196] and also higher than that of fcc Co [197]. More importantly, lower σ_{xy}^{AHE} along c-axis was theoretically predicted [198, 199]. In 2019, by using first-principles calculation to compute the intrinsic spin current conductivity, Amin *et al.* predicted that σ_{xy}^{AHE} in hcp Co along a-axis is roughly 2.88 times of σ_{xy}^{AHE} along c-axis, such anisotropy was absent in cubic Fe and Ni, which was ascribed

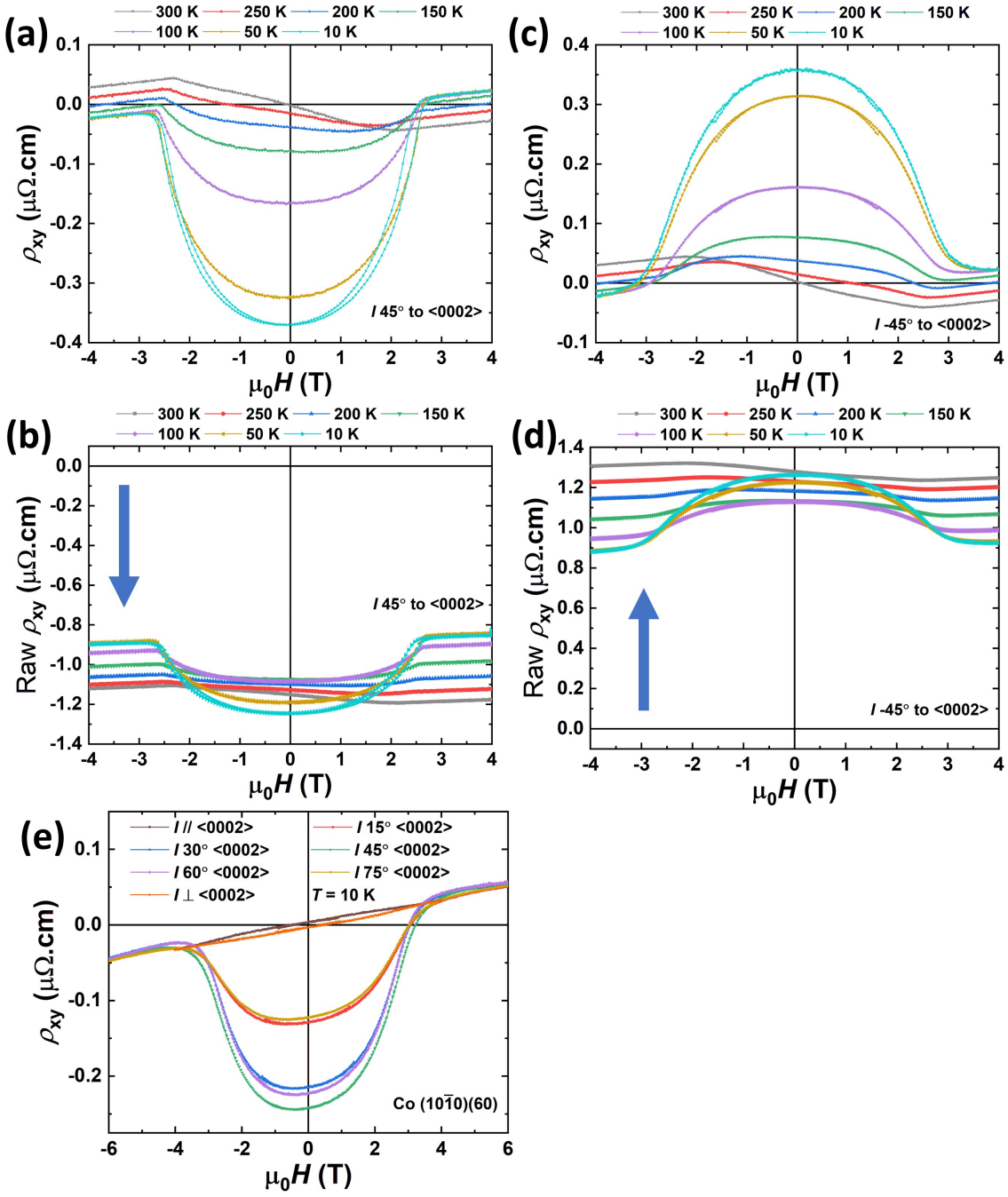

Figure 6.21. Hall resistivity vs temperature measured on patterned Co $(10\bar{1}0)$ with current along (a)-(b) 45° to *c*-axis, and (c)-(d) -45° to *c*-axis. Raw Hall resistivity with uncorrected offset was plotted as a comparison. (e) Compilation of AHE loop with various current orientations at 10 K.

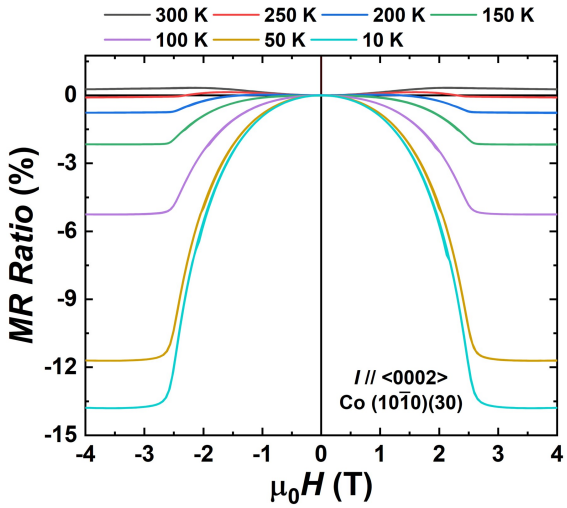

Figure 6.22. Temperature dependent FDMR measured on Co $(10\bar{1}0)$ with current along c-axis, external magnetic field was applied out of sample plane.

to the crystal anisotropy in hcp Co [199]. Our experimental results strongly support this trend.

From Table 6.1 and Figures 6.23 (a)-(e), the σ_{xy}^{AHE} in Co (0002) has marginal change over the whole σ_{xx} range, which suggests that the AHE mechanism in Co (0002) film is independent to scattering event. That is, the intrinsic mechanism dominant. While in Co $(10\bar{1}0)$, when I // c-axis, the σ_{xy}^{AHE} remains insensitive to the the σ_{xx}, the AHE is still intrinsic mechanism dominant. However, in the cases when I is 45° and 90° to c-axis, σ_{xy}^{AHE} is more sensitive to the σ_{xx}, and enhanced skew scattering contribution plays a role.

In $CrPt_3$, the $CrPt_3$ was fitted to have a larger skew scattering contribution compared to that of $CrPt_3$ (110) (Fig. 6.24(a)). The σ_{xy}^{AHE} in $CrPt_3$ is more sensitive to σ_{xx} compared to the hcp Co in Figures 6.23 (b) and (d). The predicted strong intrinsic σ_{xy}^{AHE} is supported by our experimental results, which is comparable to Fe [200] and much higher than that of Ni and Co [200].

The AHE angle θ_{AH} in hcp Co decreases monotonically with temperature. The highest σ_{xy}^{AHE} when I is perpendicular to c-axis yields the enhanced θ_{AH}. The maximum θ_{AH} in Co was measured to be 0.68%. The θ_{AH} value of element metals follows the density of states (DOS) and is typically very low (below 1%) [16] because the energy dependence of the σ_{xy}^{AHE} is constrained

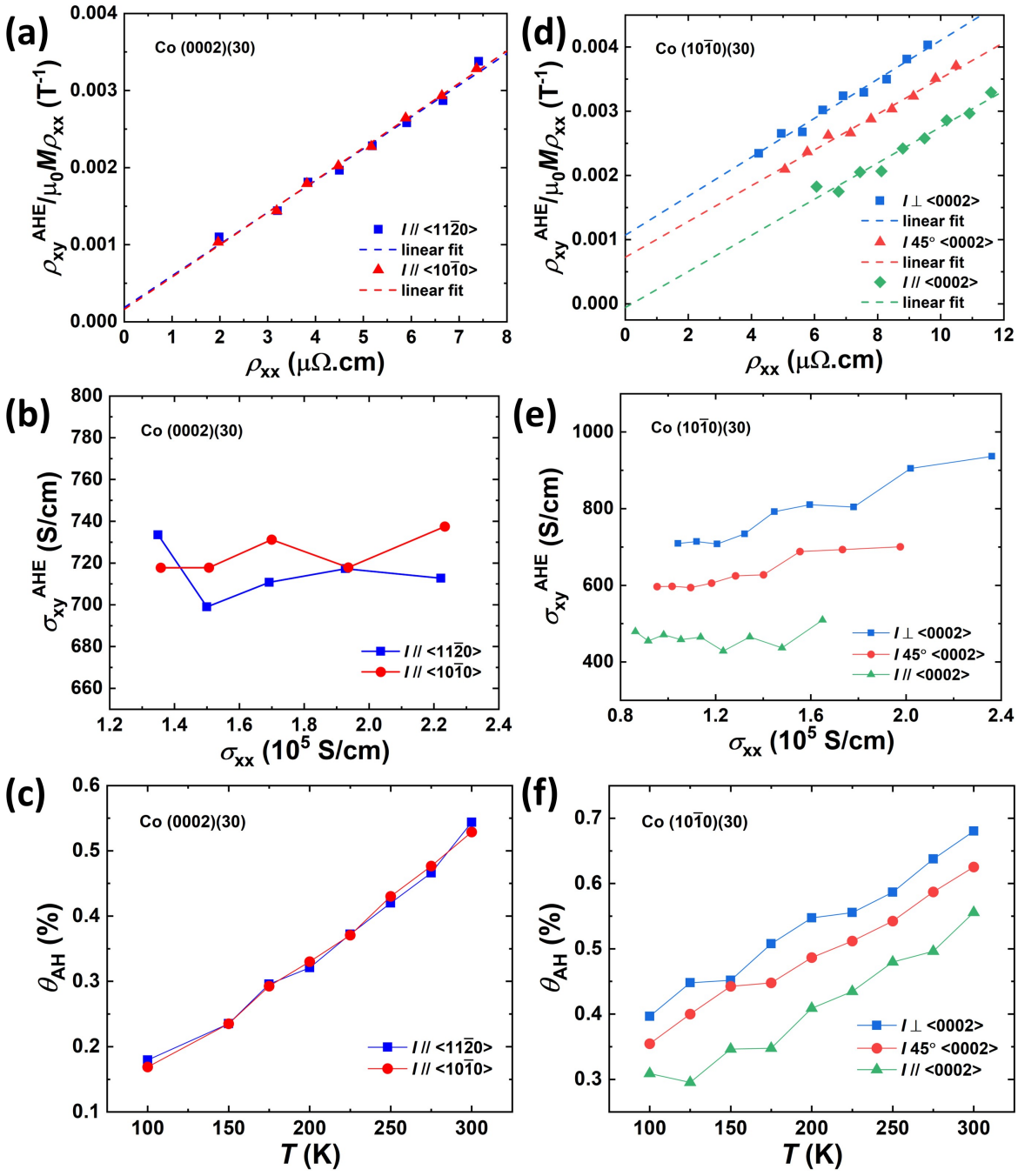

Figure 6.23. (a)-(c) AHE calculation results on Co (0002). (d)-(f) AHE calculation results on Co (10$\bar{1}$0).

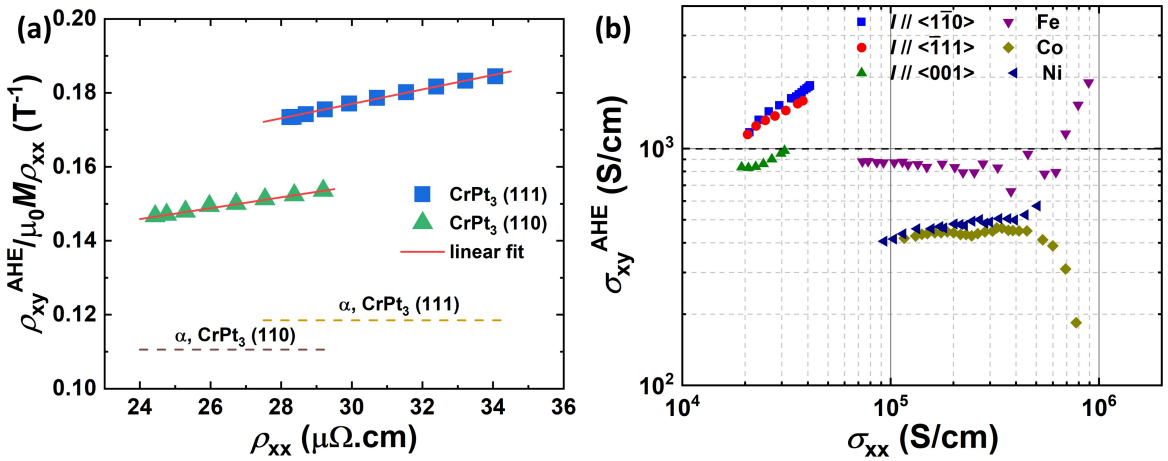

Figure 6.24. (a) AHE results Analysis on $CrPt_3$ (110) and (111). (b) Giant AHE conductivity measured on $CrPt_3$ (110) compared to traditional ferromagnets from literature.

if there is a trivial band gap close in energy, where the σ_{xy}^{AHE} vanishes [201]. On the other hand, the maximum θ_{AH} in $CrPt_3$ (110) is around 5.6%, in a good agreement with previous study on $CrPt_3$ (111) [36]. The θ_{AH} in $CrPt_3$ is much larger compared to traditional 3d ferromagnets because in $CrPt_3$, the connectivity of the occupied bands is nontrivial due to the band crossings. While the Berry curvature exhibits a strong peak close to the crossing points, the DOS vanishes, but the σ_{xy}^{AHE} surges dramatically in energy. The inverse relation between the DOS and σ_{xy}^{AHE} leads to a large θ_{AH} [201].

6.4 ADMR and PHE in $CrPt_3$

Figure 6.25 presents the ADMR and PHE in $CrPt_3$ with external field fixed to be 7 T. Similar to previous ADMR and PHE measurements in chapter 4 and chapter 5, the angle between I and $\mu_0 H$ is denoted as θ, which was scanned from -5 ° to 365 ° then reversed to -5 ° with fixed step of 2.5 °. In general, the MR Ratio is normalized to the $\rho_\perp$. Therefore, in all three current configurations, the ADMR shows a negative sign (also called negative longitudinal magnetoresistance, nLMR) throughout the whole temperature range because the global maximum is found to be around $\rho_\perp$. In particular, When I // $< 1\bar{1}0 >$, it exhibits highest temperature dependence. While I // $< 001 >$, the MR Ratio has marginal change, which remains around

1.25% from 300 K to 10 K. This anisotropy in temperature sensitivity could be ascribed to the temperature-dependent strain. As the Curie temperature, T_C is 450 K, which implies the temperature-dependent magnetization below 300 K is insignificant and minor. Surprisingly, the largest MR Ratio is not observed when I // easy axis ($< 1\bar{1}0 >$), instead, when I // $< \bar{1}11 >$, the MR Ratio exhibits the highest value above 5% at 10 K. Moreover, according to the classical AMR expression Eq. 1.14, $\rho_\perp$ should refer to θ around 90° if considering the inevitable angle offset that arises from lithography and measurement hardware. When I // $< 1\bar{1}0 >$ and $< 001 >$, the global maximum of ADMR curve can be found when θ is near 90°. However, the global maximum when I // $< \bar{1}11 >$ is evidently biased to the higher angle. Such anisotropy in temperature sensitivity, magnitude, and biasing is absent in $CrPt_3$ (111) (Fig. 6.26). As a comparison, the MR Ratio is isotropic when I // $< 1\bar{1}0 >$ and I // $< \bar{1}12 >$. The same MR Ratio and temperate sensitivity are observed.

Remember the classical PHE follows $sin(\theta)cos(\theta)$ symmetry, therefore, the measured PHE has a positive sign in $CrPt_3$ (110). The PHE magnitude when I // $< 1\bar{1}0 >$ and $< 001 >$ are similar, which is higher than the PHE magnitude when I // $< \bar{1}11 >$. That is, when I // $< \bar{1}11 >$, it yields the highest MR Ratio and lowest PHE magnitude.

Furthermore, in classical ferromagnets, when the I // easy axis, the MR tends to saturate with the increasing external magnetic field. However, as shown in Fig. 6.27, the MR Ratio increases monotonically with increasing field and remains unsaturated under 7 T. This unsaturated MR Ratio can be observed in many topological semimetals such as WTe_2 (up to 60 T) [202], NbP (up to 62 T) [203], LuAs (up to 58.5 T) [204], which is ascribed to low carrier density, that is high mobility resulted from low effective mass.

We also investigated the ADMR with other rotation configurations when I was fixed to $< 1\bar{1}0 >$. Fig. 6.28(a) shows three configurations in which θ_{xy}, θ_{xz} and θ_{yz} represent when the θ rotates in xy, xz and yz plane, respectively. Note that in this dissertation, the magnetic field has fixed position, hence the rotation of θ arises from the rotation of sample. Fig. 6.28(a) and (b) present the characteristic compilation of θ_{xy}, θ_{xz} and θ_{yz} rotation. Intuitively, when sample

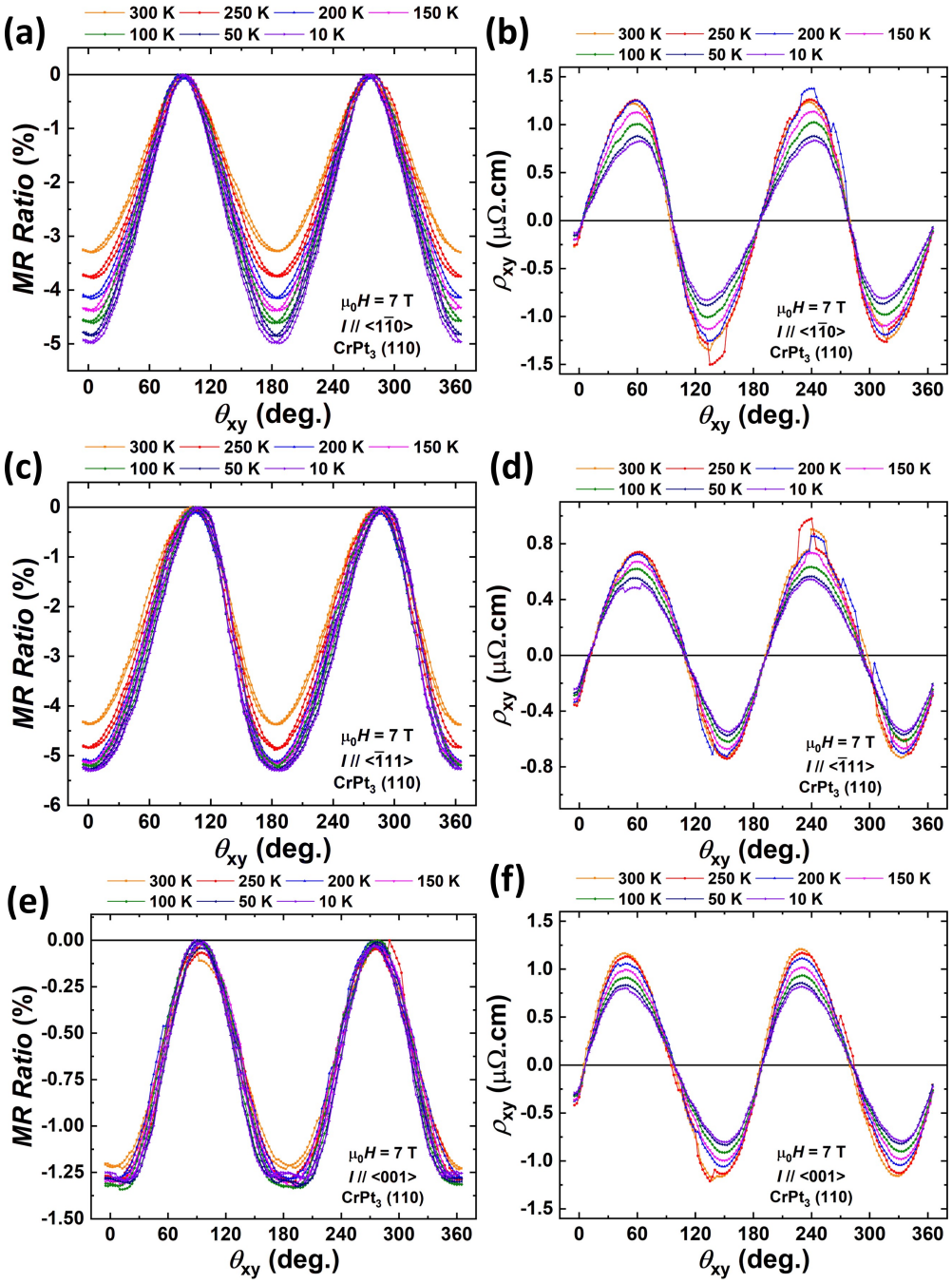

Figure 6.25. Temperature dependent ADMR and PHE on $CrPt_3$ (110) with current along (a)-(b) $< 1\bar{1}0 >$. (c)-(d) $< \bar{1}10 >$ (e)-(f) $< 001 >$. ADMR was plotted in MR Ratio. And PHE was plotted with corrected offset.

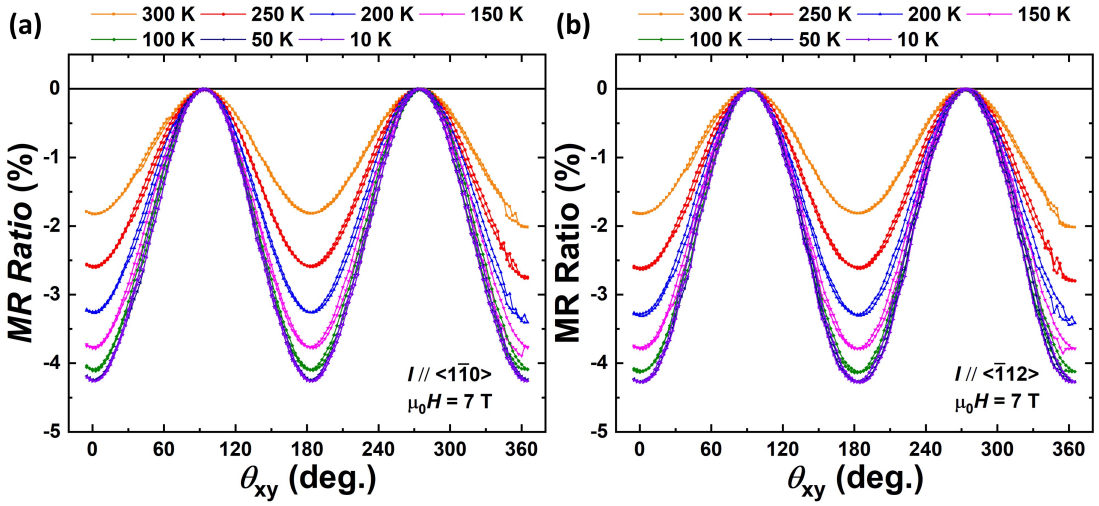

Figure 6.26. Temperature dependent ADMR on $CrPt_3$ (111) with current along (a) $< 1\bar{1}0 >$ and (b) $< \bar{1}12 >$

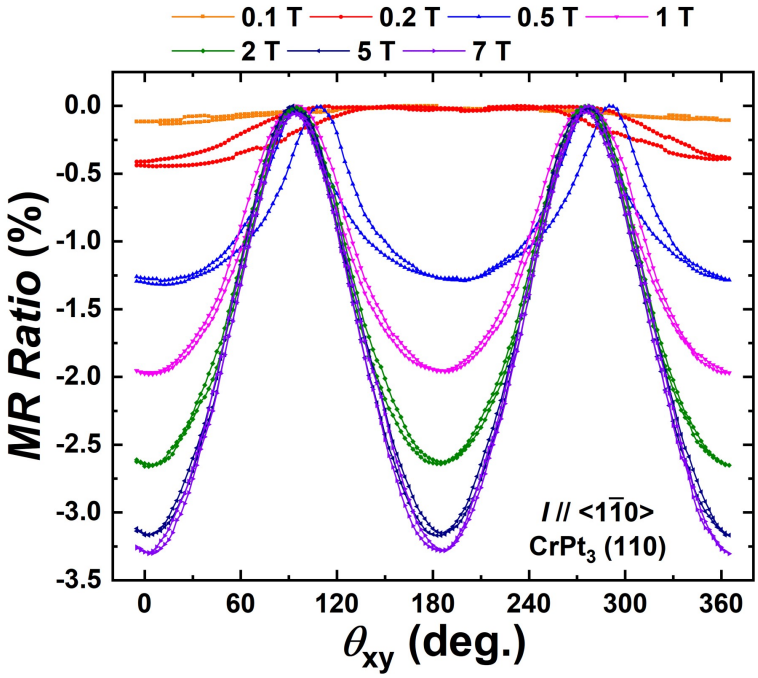

Figure 6.27. Room temperature ADMR on $CrPt_3$ (110) with current along $< 1\bar{1}0 >$ measured with various magnetic field magnitudes.

rotates in xy, xz and yz plane, they should share some common points, in other words, the raw resistance must have a common value when θ is at a certain angle. For example, when θ = 0°, the field in xz and yz plane should be out-of-plane, therefore the green curve (θ_{yz}) and red curve (θ_{xz}) share the same raw resistance value when θ = 0°, 180° and 360°. Similarly, when θ = 90°, the field in xy and yz plane lies on y-axis, thus, the green curve (θ_{yz}) and the blue curve (θ_{xy}) share the same raw resistance when θ = 90° and 270°. This excellent consistency indicates great fabrication consistency that leads to good uniformity over the whole 4-probe device. ADMR consists of a noncrystalline and a crystalline component [144, 205], in which the noncrystalline component describes the interplay between M and I when the angle between them changes. While the crystalline component describes the change of scattering matrix elements for the electrons arising from the M direction-dependent anisotropy of the electronic structure [144, 205]. By measuring the ADMR in yz plane, the M is always perpendicular to I, and the crystalline ADMR component is thereby separated.

6.5 ADMR and PHE in hcp Co

We also investigate the ADMR and PHE in hcp Co to help understand the behavior in $CrPt_3$. The measurement setup remains the same as that of $CrPt_3$, the external field during ADMR and PHE was fixed to be 3 T. According to the previous magnetization characterization, 3 T is enough to saturate both Co (0002) and $(10\bar{1}0)$ in the plane over the whole temperature range.

6.5.1 ADMR and PHE in Co with *c*-axis out of Plane

Firstly, ADMR measured on Co (0002) is shown in Fig. 6.29. The ADMR in Co (0002) experienced positive to negative sign change between 100 K and 75 K. The magnitude of nLMR at low temperatures is significantly larger than the magnitude of positive ADMR. The magnitude of ADMR is almost isotropic when I // a-axis and b-axis. However, the shapes of ADMR curve in Fig. 6.29(a) tend to be more distinctive from that of ADMR curve in Fig. 6.29(b) as temperature

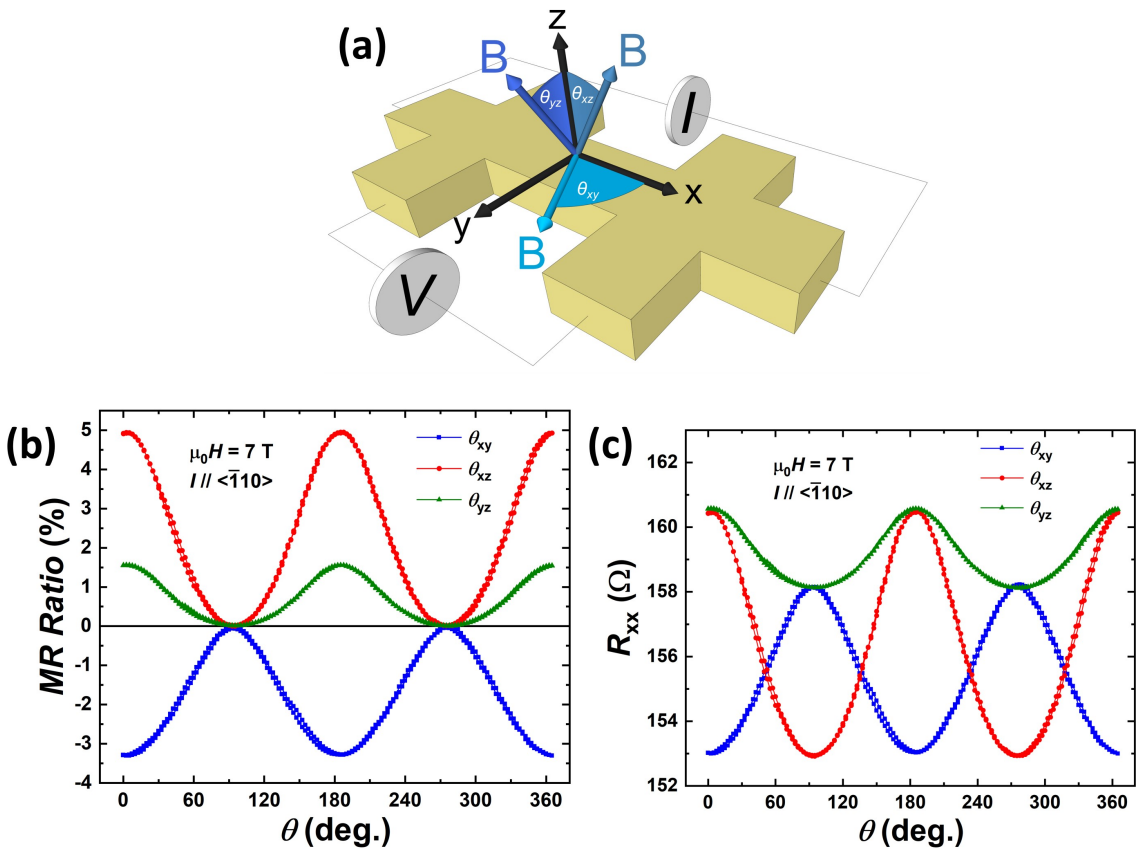

Figure 6.28. (a) Sketch of ADMR in three configurations with θ rotates in xy, xz and yz plane. B is used to represent $\mu_0 H$ for clarity. (b)-(c) Room temperature ADMR on $CrPt_3$ (110) measured with xy, xz and yz configuration. ADMR was plotted in MR Ratio and change of resistivity.

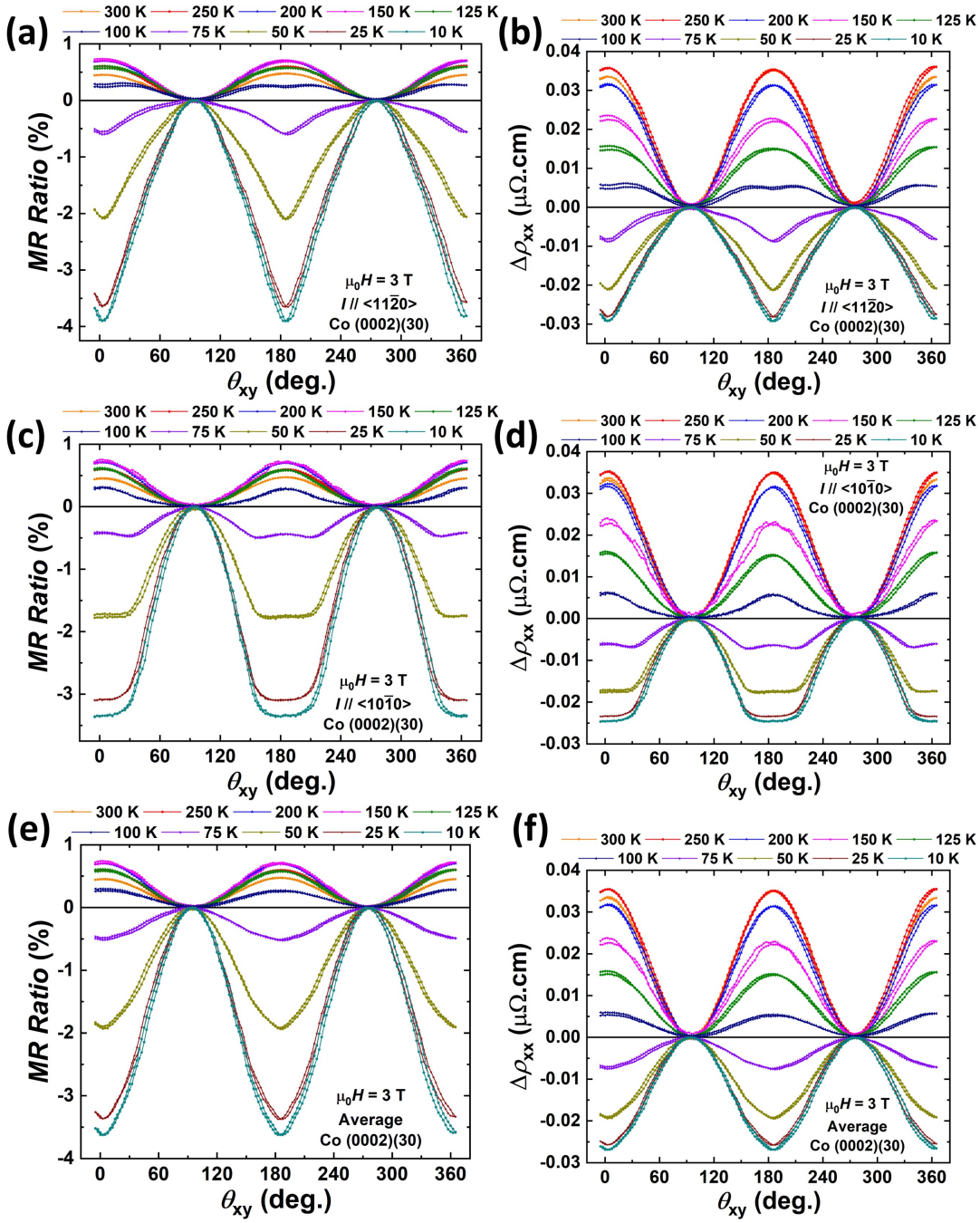

Figure 6.29. (a)-(b) Temperature-dependent ADMR on Co (0002) with current along *a*-axis. (c)-(d) Temperature-dependent ADMR on Co (0002) with current along *b*-axis. (e)-(f) Averaged ADMR data from (a) and (c), (b) and (d). ADMR was plotted in MR Ratio and change of resistivity.

decreases. When I // a-axis, it has sharper evolution as field moves towards to a-axis. On the contrary, the ADMR curve is flatter as field moves towards to b-axis. Interestingly, this behavior vanishes when taking the average of the ADMR in Fig. 6.29(a) and (c), as shown in Fig. 6.29(e), the averaged ADMR shape is close to the classical $cos^2(\theta)$ shape. This shape difference could result from the anisotropy in magnetostriction when the field is along the a- and b-axis.

Remarkably, the sign change is also found in PHE, where the opposite sign was measured (Fig. 6.30). At high temperatures, PHE in Co (0002) owns a negative sign, and the sign change takes place simultaneously when ADMR changes sign. The PHE when I // a- and b-axis has similar magnitude. However, the PHE when I // a-axis is slightly biased to the lower angle, while the PHE when I // b-axis is slightly biased to the higher angle. The averaged PHE becomes centered with classical $sin(\theta)cos(\theta)$ symmetry. The ADMR and PHE on Co (0002) can be well fitted by using the following equation, in which the ADMR is fitted using change of resistivity ρ_{xx} instead of MR Ratio, in order to compare the magnitude of PHE.

$$\Delta\rho_{xx} = C_1 \cos^2(\theta - \theta_I) + offset \tag{6.8}$$

where C_1 is the amplitude fitting parameter of ADMR, θ_I is denoted as the phase correction to the angle of current, which should be close to 0°. Similarly, the PHE fitting equation for Co (0002) results is:

$$\rho_{xy} = C_1^{'} \sin(\theta - \theta_I)\cos(\theta - \theta_I) + offset \tag{6.9}$$

where $C_1^{'}$ is the amplitude fitting parameter of PHE. The temperature-dependent fitting results are shown in Fig. 6.30(d). The magnitude of ADMR and PHE are similar to each other, supporting the classical ADMR and PHE definitions.

6.5.2 ADMR and PHE in Co with *c*-axis in Plane

Remember Co $(10\bar{1}0)$ was grown on Cr (211) seed layer, before showing the ADMR and PHE results in Co $(10\bar{1}0)$, we first exclude the influence from Cr. Reference Cr (211) was

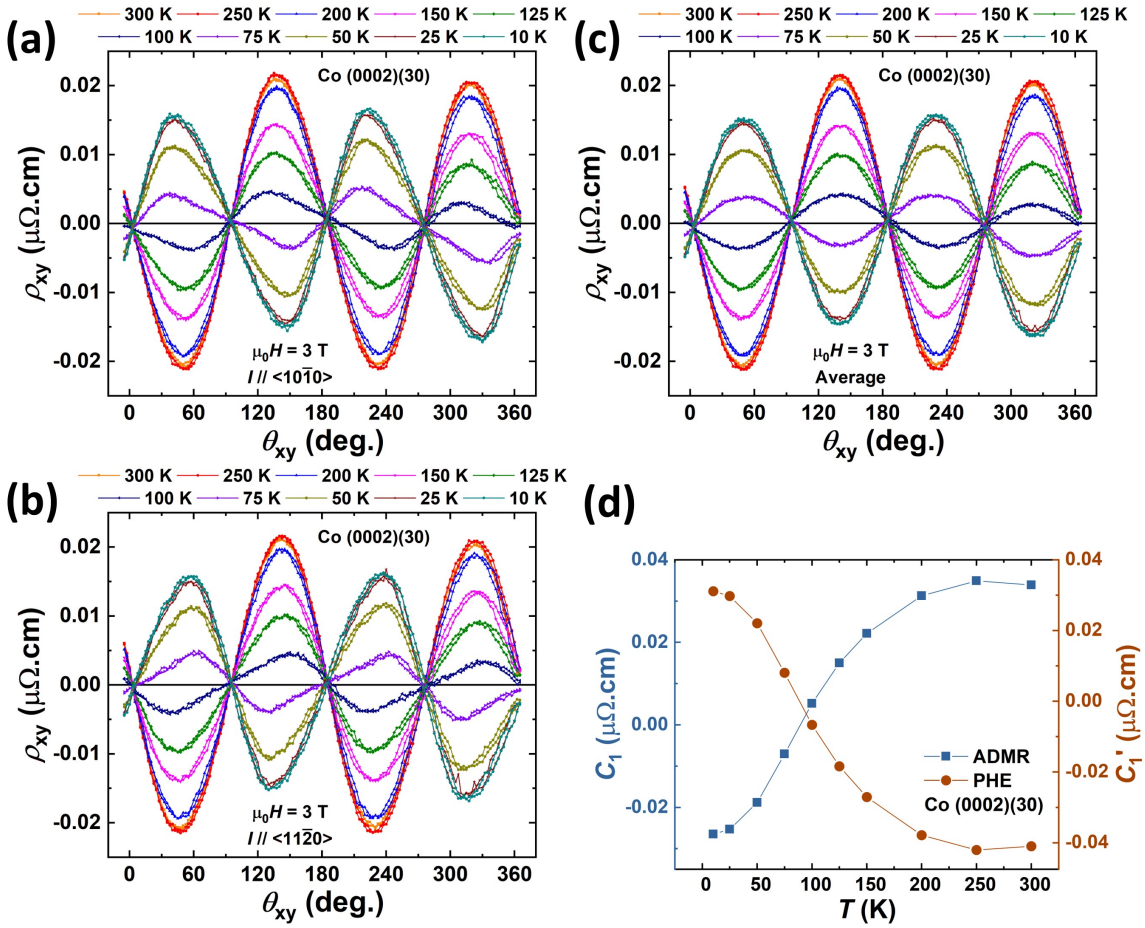

Figure 6.30. (a)-(b) Temperature-dependent PHE on Co (0002) with current along *a*- and *b*-axis. (c) Averaged PHE data from (a) and (b). (d) Fitted parameter plotted as a function of temperature.

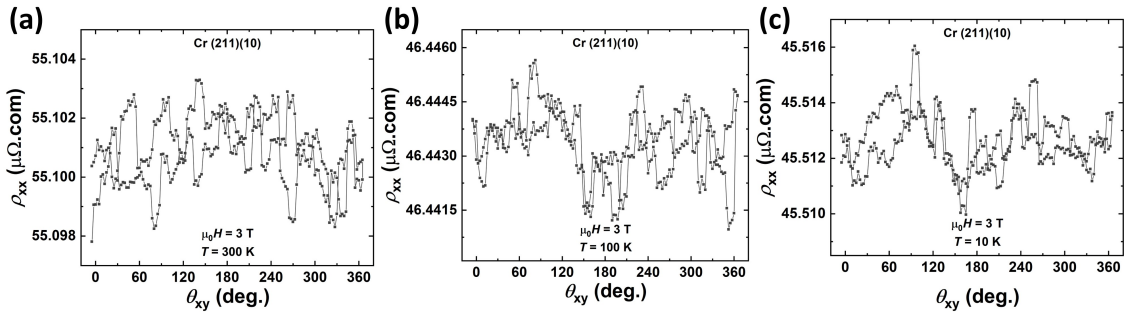

Figure 6.31. Temperature dependent ADMR on patterned Cr (211) film measured from 300 K to 10 K. (a)-(c) shows 3 examples at 300 K, 100 K, and 10 K.

grown on MgO (220). The patterned Cr (211)(10) film was measured for ADMR using the same parameter as what was used on Co. As shown in Fig. 6.31, the resistance was stable with marginal fluctuation which is independent of θ. Thus, MR was absent in Cr (211)(10) in the whole temperature range. Also, although Cr is an antiferromagnetic material, the antiferromagnetic nature of Cr is not considered in this work. The transport properties of both MgO (220)/Cr (211)(10)/Co $(10\bar{1}0)$(30) and MgO (220)/Cr (211)(5)/Co $(10\bar{1}0)$(60) were examined, leading to close results with minimal difference. Therefore, the results are considered to arise from Co$(10\bar{1}0)$ only.

Different from Co (0002) sample, giant anisotropy exists in Co $(10\bar{1})$ when measuring ADMR and PHE with I in various angles of c-axis. Figs. 6.32 and 6.33 indicate the temperature-dependent ADMR with I being 0°, 15°, 30°, 45°, 60°, 75°, and 90° to c-axis. Interestingly, at room temperature, the largest MR Ratio is found when I is 45° to c-axis, which is in good agreement with $CrPt_3$ (110) results. Bozorth reported that in hcp Co, the largest magnetostriction (contraction) can be found when the external magnetic field is applied at about 50° to the c-axis [206], which could cause the largest MR Ratio when I is 45° to c-axis. At low temperature (10 K), the largest MR Ratio is found when I is along c-axis, which is a remarkable value of about 14%. When I is along c-axis, it has nLMR at 300 K and 250 K, and its sign changes to positive between 250 K and 200 K. On the other hand, when I is 90° to c-axis, it owns positive ADMR at high temperatures and the sign change is found between 50 K and 25 K. For the cases when I

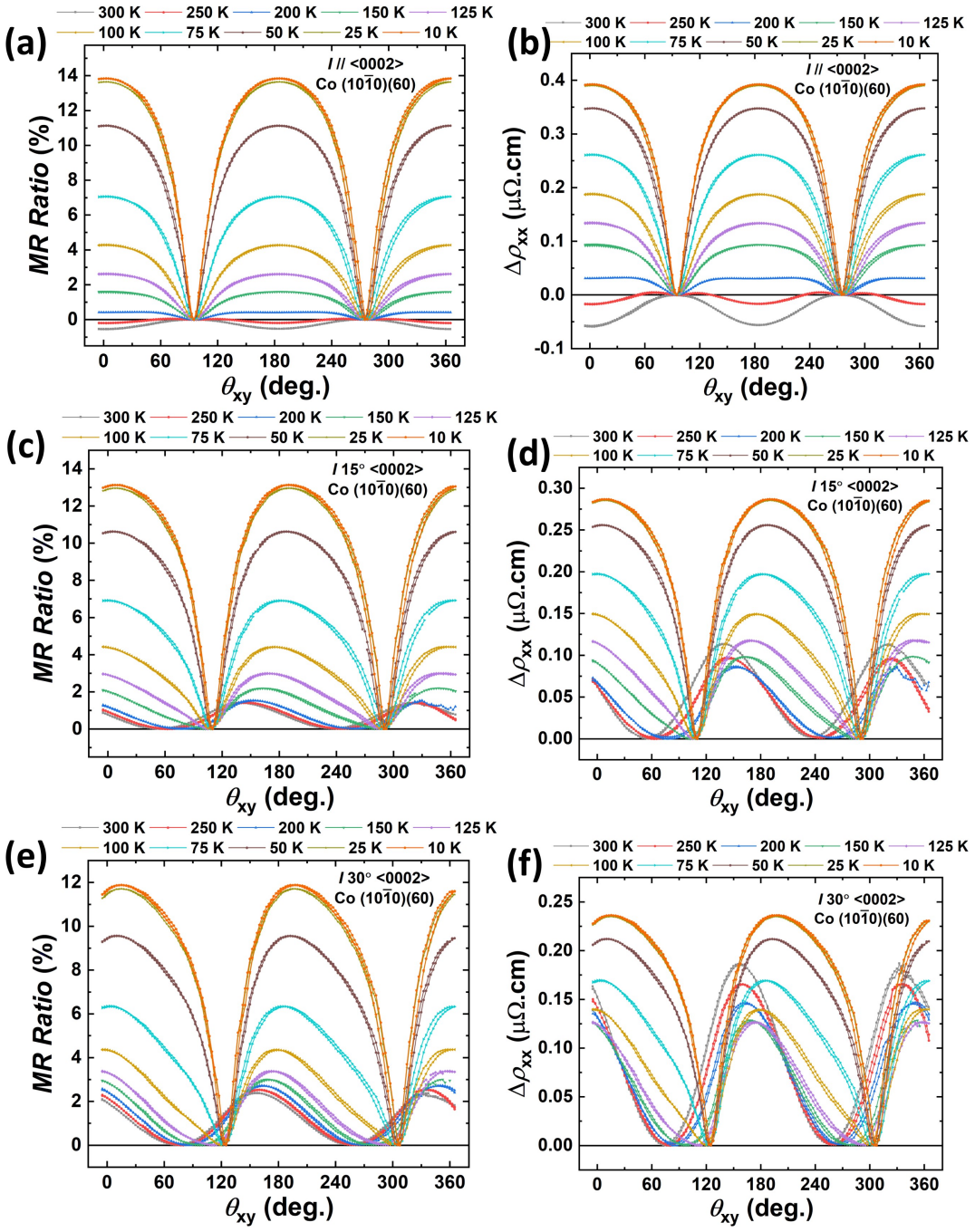

Figure 6.32. Temperature dependent ADMR measured on patterned Co $(10\bar{1}0)$ with current (a)-(b) along *c*-axis, (c)-(d) 15° to *c*-axis, and (e)-(f) 30° to *c*-axis. ADMR was plotted in MR Ratio and change of resistivity.

is in other angles to c-axis, ADMR remains positive throughout the whole temperature range. Moreover, for the cases when I is neither 0° nor 90° to c-axis, the global minimum of ADMR curve shifted away from 90°, remember similar behavior can be observed in $CrPt_3$ when I is 35.3° to the easy axis.

Fig. 6.34 summarizes the PHE with I in various angles to c-axis. When I is either 0° or 90° to c-axis, the PHE has alike behavior of negative sign, similar magnitude. The room temperature PHE has its highest magnitude when I is either 0° or 90° to c-axis, and low temperature (10 K) PHE reaches its highest magnitude when I is 45° to c-axis. The biased PHE behavior can be found dependent on the temperature and angles to c-axis.

To better visualize the biasing effect in ADMR and PHE, Fig. 6.35 plots the curves with various angles to c-axis together. As shown in Fig. 6.35(a) and (b), at 300 K, the biasing is determined by the 45° curve. 30° and 60° curves have the same bias magnitude relative to 45° curve. 15° and 75° curves have a larger bias with the same bias magnitude relative to 45° curve. At 10 K, the 0° curve has a global minimum at $\theta = 90°$. Then, with increasing angle to the c-axis, the global minimum is gradually biased to a higher angle and eventually reaches $\theta = 180°$, that is, the global minimum of 90° curve. Such global minimum takes place when M is perpendicular to c-axis, distinctive to M being perpendicular to I in classical ADMR.

Moreover, for the PHE cases shown in Fig. 6.35(c) and (d), at 300 K, the 0°, 75° and 60° curves are biased to lower angle as a reference to 45° curve. The 90°, 15° and 30° curves are biased to a higher angle. At 10 K, the 45° curve is still unbiased. On the contrary, the 0°, 75° and 60° curves are biased to a higher angle. The 90°, 15° and 30° curves are biased to a lower angle.

Obviously, the ADMR and PHE behavior in Co $(10\bar{1}0)$ cannot be understood by the classical expression, therefore, the ADMR expression is modified to:

$$\Delta\rho_{xx} = C_1|\cos(\theta - \theta_c)| + C_2\cos^2(\theta - \theta_I) + C_3\cos^2(\theta - \theta_c) + offset \tag{6.10}$$

where C_1, C_2, and C_3 are the amplitude fitting parameter of the first term, second term, and third

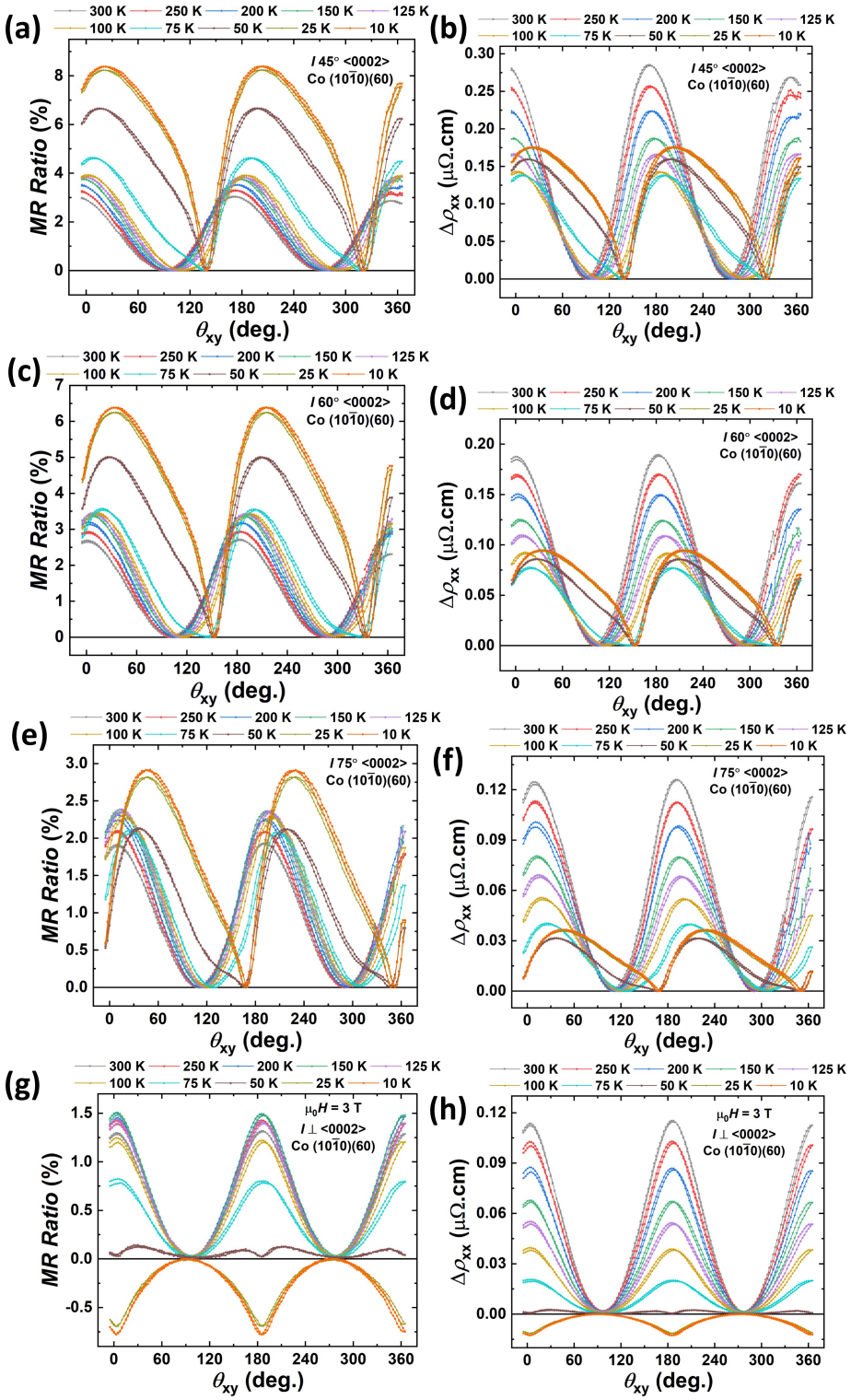

Figure 6.33. Temperature dependent ADMR measured on patterned Co $(10\bar{1}0)$ with current (a)-(b) 45° to *c*-axis, (c)-(d) 60° to *c*-axis, (e)-(f) 75° to *c*-axis, and (g)-(h) 90° to *c*-axis. ADMR was plotted in MR Ratio and change of resistivity.

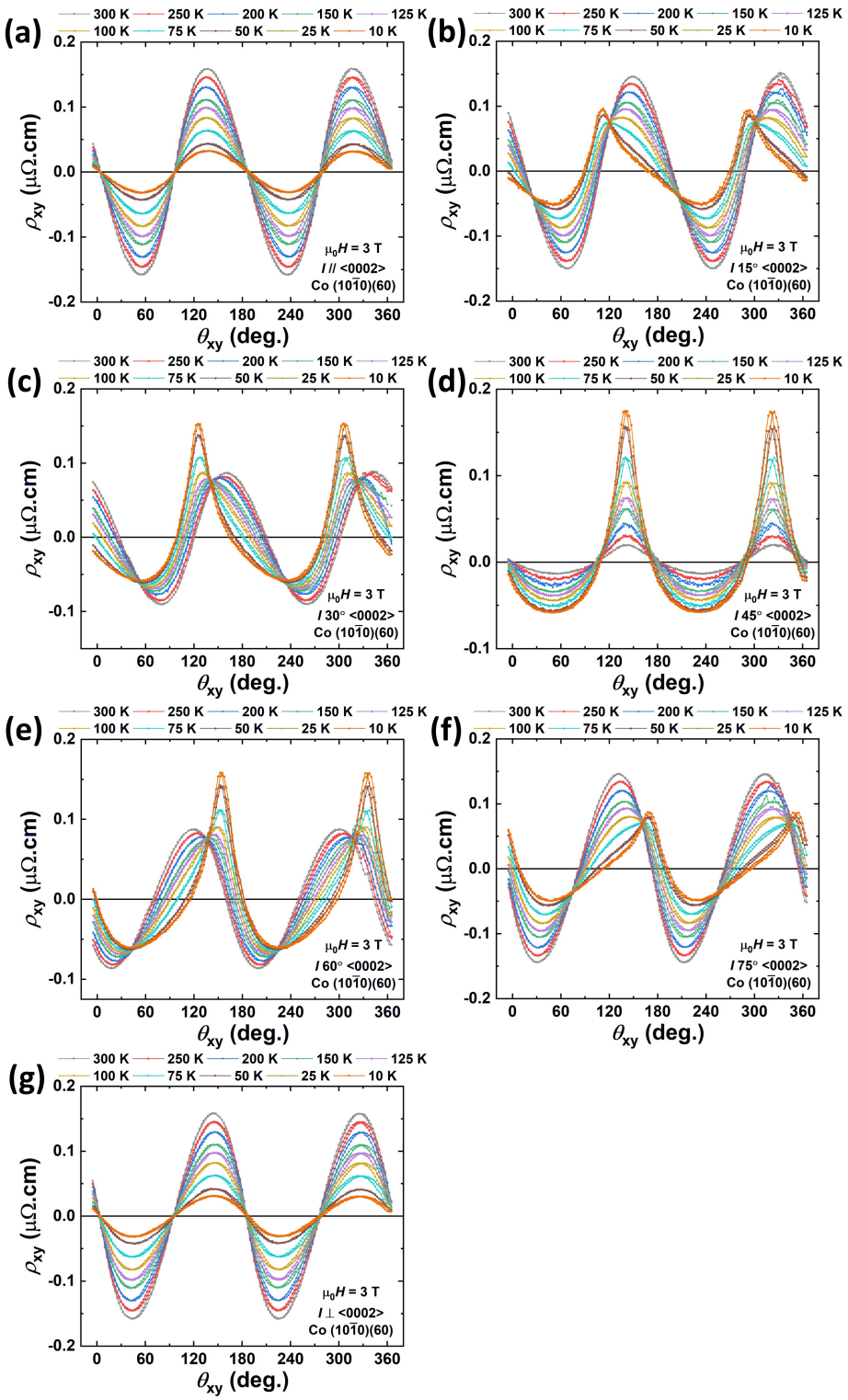

Figure 6.34. Temperature dependent PHE measured on patterned Co $(10\bar{1}0)$ with current (a) along *c*-axis, (b) 15° to *c*-axis, (c) 30° to *c*-axis, (d) 45° to *c*-axis, (e) 60° to *c*-axis, (f) 75° to *c*-axis, and (g) 90° to *c*-axis.

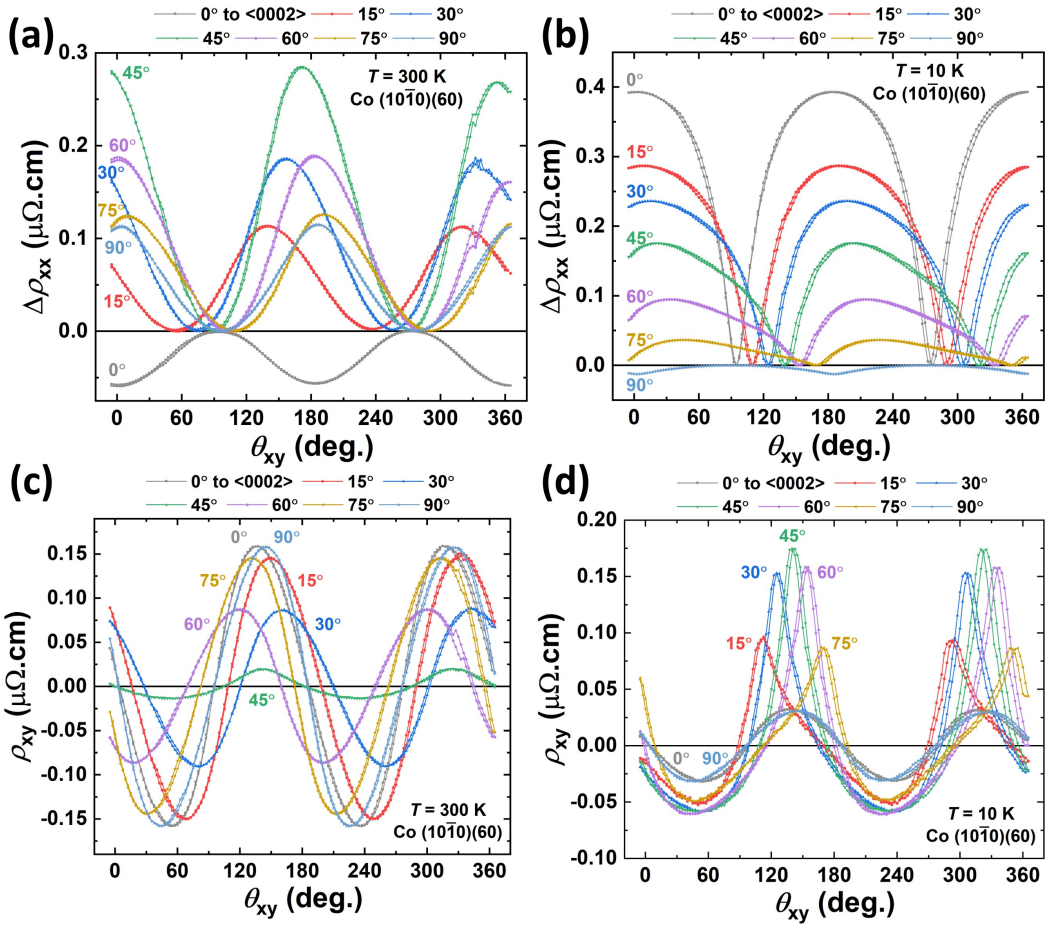

Figure 6.35. Compilation of ADMR curves measured on Co $(10\bar{1}0)$ with current along all angles to *c*-axis plotted at (a) 300 K and (b) 10 K. Compilation of PHE curves measured on Co $(10\bar{1}0)$ with current along all angles to *c*-axis plotted at (a) 300 K and (b) 10 K.

term, respectively. Again, θ_I is denoted as the phase correction to the angle of current, which should be close to 0°. θ_c is denoted as the phase correction to the angle relative to c-axis. For example, when I is 45° to c-axis, the fitted θ_c should be around 45. Intuitively, when I is either 0° or 90° to c-axis, the third term vanishes. Fig. 6.36 summarize the temperature-dependent MR Ratio and fitting parameters as a function of angle to c-axis. At low temperatures (below 100 K), the MR Ratio increases monotonically as angle to c-axis decreases to 0°. At high temperatures, MR Ratio decreases as the angle to c-axis moves away from 45°. Among the three fitting parameters, C_1 holds the highest value. C_1 and C_2 are major contributors to the MR Ratio, suggesting in a plane with uniaxial anisotropy, both the magnetization relative to the current and the magnetization relative to the easy axis play an important role in ADMR.

Similarly, the modified PHE expression is:

$$\rho_{xy} = C_1^{'}\sin(\theta-\theta_I)\cos(\theta-\theta_I) + C_2^{'}|\cos(\theta-\theta_c)| + C_3^{'}\cos^2(\theta-\theta_c) + offset \qquad (6.11)$$

where $C_1^{'}$, $C_2^{'}$, and $C_3^{'}$ are the amplitude fitting parameter of the first term, second term, and third term, respectively. Again, θ_I is denoted as the phase correction to the angle of current, which should be close to 0°. θ_c is denoted as the phase correction to the angle relative to c-axis. Importantly, when I is either 0° or 90° to c-axis, we still apply the classical PHE expression, which is the same as the PHE fitting equation uses on Co (0002) (Eq. 6.9). The classical PHE term (first term, $C_1^{'}$) and the classical ADMR-like term (third term, $C_3^{'}$) play more important role when I is 45° to c-axis. The sharp 2-fold peak in PHE data is mainly contributed by the ADMR-like high order term (third term, $C_3^{'}$).

6.6 The Sign of ADMR

We also discuss the sign of ADMR, unlike the simplest case of positive ADMR of polycrystalline Py in chapter 1, the physical origin of the sign of ADMR has multiple aspects. Mott, Campbell and Fert proposed that spin up (↑, majority) and spin down (↓, minority)

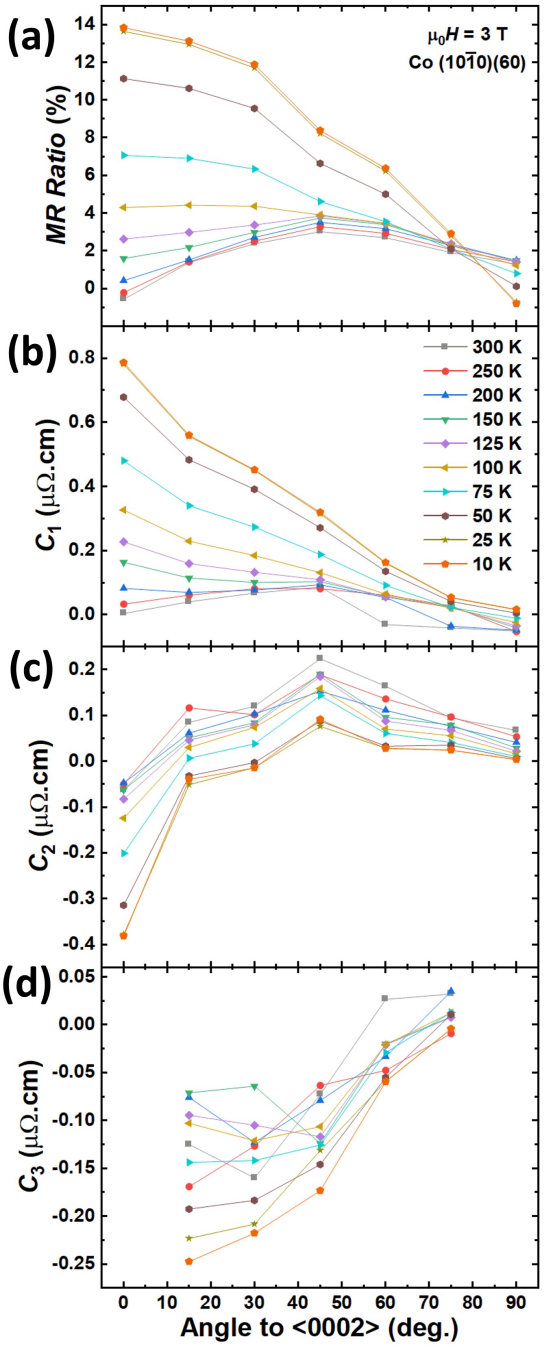

Figure 6.36. (a) Temperature-dependent MR Ratio measured on Co $(10\bar{1}0)$ plotted as a function of angle to *c*-axis. (b)-(d) Temperature-dependent ADMR fitting parameters plotted as a function of angle to *c*-axis.

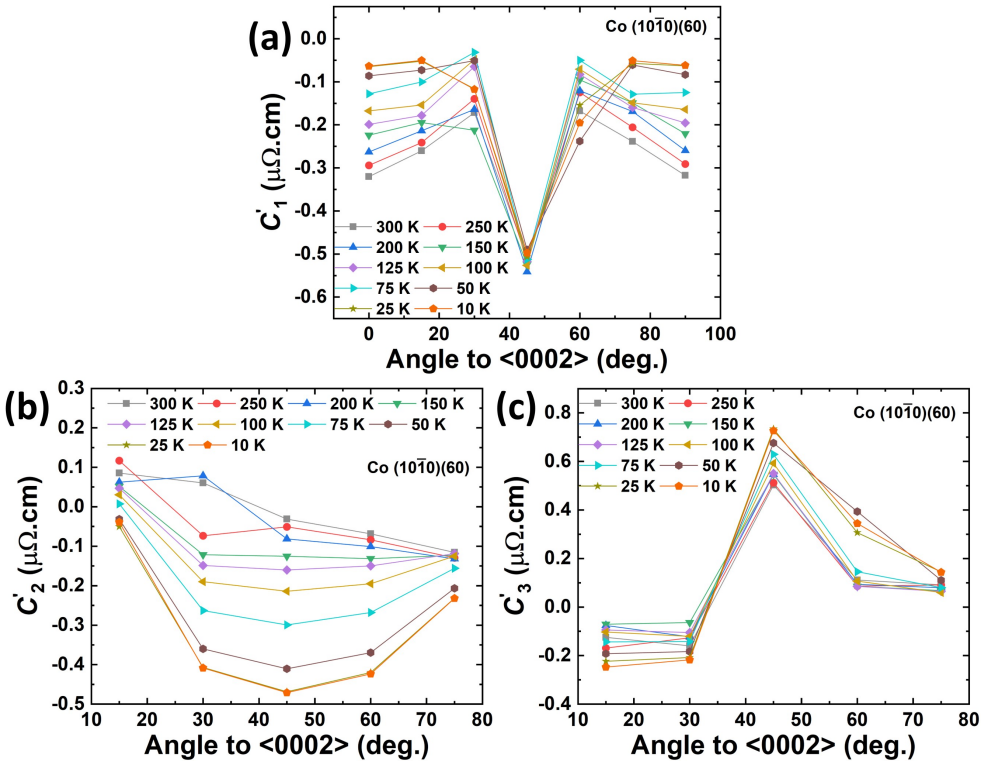

Figure 6.37. (a)-(c) Temperature-dependent PHE fitting parameters plotted as a function of angle to *c*-axis.

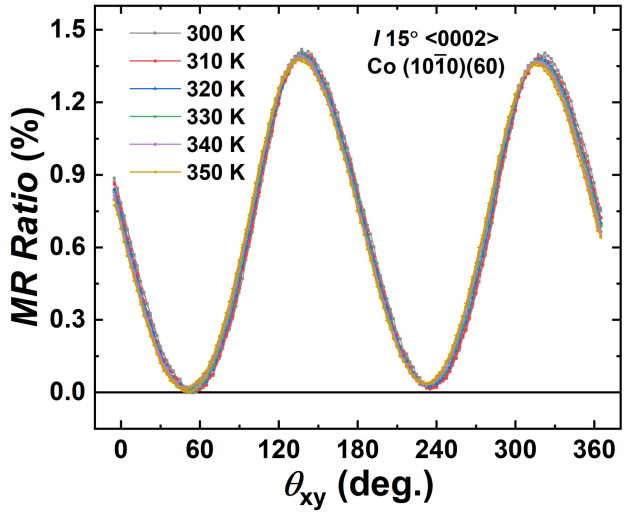

Figure 6.38. ADMR measured above 300 K on Co $(10\bar{1}0)$ with current 15° to *c*-axis

electrons can be the current carrier in parallel with different conductivities in a ferromagnet, namely two-current model [207, 4, 208]. On the basis of two-current model, the sign of AMR can be determined by the $\rho_{\uparrow}/\rho_{\downarrow}$. Because, for spin up electrons, a higher resistance state occurs when I and M are colinear. For the spin down electrons, a lower resistance state occurs when I and M are colinear. Hence, when the sign of AMR changes from positive to negative, it refers to dominant current changes from spin up to spin down [209]. Since the spin up and spin down electrons can be further manipulated by the spin Seebeck effect [210], and the Joule heating from the electrical current can thermally excite magnons via the spin Seebeck effect [211], we acknowledge the thermal effect when measuring ADMR in $CrPt_3$ and hcp Co, which is excluded. ADMR above 300 K is shown in Fig. 6.38. The MR ratio remains unchanged up to 350 K. Hence, the Joule heating effect cannot be influential to the MR Ratio measured at 300 K.

Kokado *et al*. further improved the two-current model by modeling the s–d scattering dependence of sign of the AMR: if the dominant s–d scattering process is s↑ scattered into d↑ or s↓ scattered into d↓, the AMR owns negative sign (nLMR). While the dominant s–d scattering process is s↑ scattered into d↓ or s↓ scattered into d↑, positive AMR can exhibit [212]. However, even with the same s-d scattering event, the sign of ADMR can be thickness dependent in the same material due to interfacial scattering or geometric size effect, which is reported by varying Co thickness in Pt/Co/Pt trilayer [213] or Pt/Co bilayer [214], respectively.

Moreover, the origin of nLMR topological semimetals is indeed complicated. For example, the nLMR in TaAs [215], $ZrTe_{5-\delta}$ [216] and Cd_3As_2 [217] are ascribed to chiral anomaly [218]. However, debate continues, nLMR due to Fermi energy instead of chiral anomaly was theoretically discussed [219]. nLMR due to negative off-diagonal effective mass without topological effects or chiral anomaly was predicted recently [220]. The physical origin of nLMR in $CrPt_3$ remains cloudy, both experimental (such as angle-resolved photoemission spectroscopy (ARPES)) and theoretical work shall be needed.

Apart from the factors discussed above to the ADMR sign, it is worth noting that SHE can play a role in the sign when measuring ADMR in a material with potential SHE. Remember

the spin current generation by bulk SHE which is transverse to charge current direction, spin up electron and spin down electron are deflected to opposition directions (a 90° right or left turn) when they collide with a scatter site (extrinsic scattering mechanism). Afterward, a second scatter site would cause the electron to be deflected again, making another 90° right or left turn. That means these two consecutive scatterings lead to an electron backflow [221], that is, a high resistance state. When M is colinear with I, this scattering by SHE is absent, leading to a low resistivity state. Therefore, the SHE in magnetic material can give a rise to nLMR, which can also contribute to the negative sign in $CrPt_3$ due to its strong AHE.

6.7 Acknowledgement

Chapter 6, in part, is currently being prepared for submission for publication of the material "Y. Xiao, Y. Kim, M. J. Gilbert, E. E. Fullerton, *Giant Easy-axis Dependent Transport in Epitaxial hcp Co,*" The dissertation author was one of the primary investigators and author of this material.

Chapter 7

Conclusion

In this dissertation, spin transport and magnetotransport were investigated over various epitaxial materials. The first part of this dissertation demonstrated a tunable SHE in epitaxial heavy metal (Pt) by utilizing the anisotropic resistivity along a specific crystallographic orientation. By far, most works on the spin source focused on polycrystalline and amorphous materials. Our work can hint the future work on enhanced SHE arising from crystalline orientation dependence, not only in single epitaxial materials but also in epitaxial superlattices by interfacial engineering.

Learning from the demonstration in epitaxial Pt, such tunable SHE has great potential in energy-efficient magnetization manipulation, which is the key for the iteration of future computing, such as neuromorphic computing. Artificial neurons are emulated with magnetic nano-oscillators, and the coupling between these oscillators can mimics synapses. Therefore, neuromorphic computing calls for tunable spin source materials that can drive the nano-oscillators in an energy-efficient way. Apart from well-studied heavy metals like Pt, many new materials were proposed. Nevertheless, ”old materials” is worthwhile being revisited, leading to studying the XPt_3 alloy and revisiting the rare earth material (Ho) and traditional element ferromagnet (Co). The strong AHE in ferrimagnetic $CrPt_3$ and highly anisotropic AHE in hcp Co could favor developing spintronic devices by utilizing magnetocrystalline anisotropy. The magnetic phase transition in $FePt_3$ and Ho makes them good candidates for tunable SHE or AHE that

could be promising for low temperature applications. Current work is ongoing to probe the temperature-dependent SHE in $FePt_3$ and Ho.

Apart from spin transportation, the magnetotransport unpacked fundamental understanding of magnetic epitaxial materials. The perturbation study in $FePt_3$ highlighted the field and rotation sensitivity in AFM that is nontrivial in the growing AFM memory application. The discovery of six-fold ADMR and step-like PHE in Ho improved the AMR theory on materials with strong magnetostriction. An improved understanding of ferromagnet with in-plane uniaxial magnetic anisotropy was achieved by a comprehensive picture of anisotropic AHE and magnetoresistance in hcp Co, which is somewhat absent in the literature.

Such exploration all started with the epitaxial materials.

Bibliography

[1] B. D. Cullity and C. D. Graham, *Introduction to Magnetic Materials*. John Wiley & Sons, 2011.

[2] R. C. O'handley, *Modern Magnetic Materials: Principles and Applications*. Wiley, 2000.

[3] J. Smit, "Magnetoresistance of ferromagnetic metals and alloys at low temperatures," *Physica*, vol. 17, no. 6, pp. 612–627, 1951.

[4] I. Campbell, A. Fert, and O. Jaoul, "The spontaneous resistivity anisotropy in ni-based alloys," *Journal of Physics C: Solid State Physics*, vol. 3, no. 1S, p. S95, 1970.

[5] R. I. Potter, "Magnetoresistance anisotropy in ferromagnetic NiCu alloys," *Physical review B*, vol. 10, no. 11, p. 4626, 1974.

[6] E. E. Fullerton and J. R. Childress, "Spintronics, magnetoresistive heads, and the emergence of the digital world," *Proceedings of the IEEE*, vol. 104, no. 10, pp. 1787–1795, 2016.

[7] H. Tang, R. Kawakami, D. Awschalom, and M. Roukes, "Giant planar Hall effect in epitaxial (Ga, Mn)As devices," *Physical review letters*, vol. 90, no. 10, p. 107201, 2003.

[8] L. Ejsing, M. F. Hansen, A. K. Menon, H. Ferreira, D. Graham, and P. Freitas, "Planar Hall effect sensor for magnetic micro-and nanobead detection," *Applied Physics Letters*, vol. 84, no. 23, pp. 4729–4731, 2004.

[9] J. Coey and S. S. Parkin, *Handbook of Magnetism and Magnetic Materials*. Springer, 2020.

[10] N. F. Mott, "The electrical conductivity of transition metals," *Proceedings of the Royal Society of London. Series A-Mathematical and Physical Sciences*, vol. 153, no. 880, pp. 699–717, 1936.

[11] J. C. Slonczewski, "Current-driven excitation of magnetic multilayers," *Journal of Magnetism and Magnetic Materials*, vol. 159, no. 1-2, pp. L1–L7, 1996.

[12] A. Bakun, B. Zakharchenya, A. Rogachev, M. Tkachuk, and V. Fleisher, "Observation of a surface photocurrent caused by optical orientation of electrons in a semiconductor," *Jetp Lett*, vol. 40, no. 11, 1984.

[13] J. Hirsch, "Spin Hall effect," *Physical review letters*, vol. 83, no. 9, p. 1834, 1999.

[14] W. Han, Y. Otani, and S. Maekawa, "Quantum materials for spin and charge conversion," *npj Quantum Materials*, vol. 3, no. 1, pp. 1–16, 2018.

[15] E. H. Hall, "On the "Rotational Coefficient" in nickel and cobalt," *The London, Edinburgh, and Dublin Philosophical Magazine and Journal of Science*, vol. 12, no. 74, pp. 157–172, 1881.

[16] N. Nagaosa, J. Sinova, S. Onoda, A. H. MacDonald, and N. P. Ong, "Anomalous Hall effect," *Reviews of modern physics*, vol. 82, no. 2, p. 1539, 2010.

[17] G. Vignale, "Ten years of spin Hall effect," *Journal of superconductivity and novel magnetism*, vol. 23, no. 1, pp. 3–10, 2010.

[18] A. Hoffmann, "Spin Hall effects in metals," *IEEE transactions on magnetics*, vol. 49, no. 10, pp. 5172–5193, 2013.

[19] J. Sinova, S. O. Valenzuela, J. Wunderlich, C. Back, and T. Jungwirth, "Spin hall effects," *Reviews of modern physics*, vol. 87, no. 4, p. 1213, 2015.

[20] L. Liu, C.-F. Pai, Y. Li, H. Tseng, D. Ralph, and R. Buhrman, "Spin-torque switching with the giant spin Hall effect of tantalum," *Science*, vol. 336, no. 6081, pp. 555–558, 2012.

[21] S. Bhatti, R. Sbiaa, A. Hirohata, H. Ohno, S. Fukami, and S. Piramanayagam, "Spintronics based random access memory: a review," *Materials Today*, vol. 20, no. 9, pp. 530–548, 2017.

[22] L. Landau and E. Lifshitz, "On the theory of the dispersion of magnetic permeability in ferromagnetic bodies," *Phys. Z. Sowjetunion*, vol. 8, pp. 153–164, 1935.

[23] T. Gilbert, "Lagrangian formulation of the gyromagnetic equation of the magnetic field," *Physical Review*, vol. 100, no. 4, p. 1243, 1955.

[24] K. Iwashita, T. Oguchi, and T. Jo, "Orbital and spin magnetic moments of TPt_3 (T = V, Cr, Mn, Fe, and Co)," *Physical Review B*, vol. 54, no. 2, p. 1159, 1996.

[25] R. Jesser, A. Bieber, and R. Kuentzler, "Magnetic properties of the ordered VPt_3 alloy. I.—ferromagnetic behaviour," *Journal de Physique*, vol. 42, no. 8, pp. 1157–1166, 1981.

[26] S. Pickart and R. Nathans, "Neutron diffraction investigation of Pt-based alloys of the first transition series," *Journal of Applied Physics*, vol. 34, no. 4, pp. 1203–1204, 1963.

[27] K. W. Wierman and R. D. Kirby, "Long-range order and magnetic properties of Mn_xPt_{1-x} thin films," *Journal of magnetism and magnetic materials*, vol. 154, no. 1, pp. 12–16, 1996.

[28] P. Rooney, A. Shapiro, M. Tran, and F. Hellman, "Evidence of a surface-mediated magnetically induced miscibility gap in Co-Pt alloy thin films," *Physical review letters*, vol. 75, no. 9, p. 1843, 1995.

[29] G. Bacon and J. Crangle, "Chemical and magnetic order in platinum-rich Pt + Fe alloys," *Proceedings of the Royal Society of London. Series A. Mathematical and Physical Sciences*, vol. 272, no. 1350, pp. 387–405, 1963.

[30] P. Oppeneer, V. Antonov, T. Kraft, H. Eschrig, A. Yaresko, and A. Y. Perlov, "Calculated magneto-optical Kerr spectra of compounds (X = V, Cr, Mn, Fe and Co)," *Journal of Physics: Condensed Matter*, vol. 8, no. 31, p. 5769, 1996.

[31] T. Leonhardt, Y. Chen, M. Rao, D. Laughlin, D. Lambeth, and M. Kryder, "$CrPt_3$ thin film media for perpendicular or magneto-optical recording," *Journal of applied physics*, vol. 85, no. 8, pp. 4307–4309, 1999.

[32] J. Cho, M. Park, H.-S. Kim, T. Kato, S. Iwata, and S. Tsunashima, "Large Kerr rotation in ordered $CrPt_3$ films," *Journal of applied physics*, vol. 86, no. 6, pp. 3149–3151, 1999.

[33] M. Broschwitz, S. Knetsch, A. Borgschulte, L. Bizdoaca, and J. Schoenes, "Size effects of optical and magneto-optical properties of epitaxial $CrPt_3$ films," *Journal of applied physics*, vol. 93, no. 5, pp. 2458–2463, 2003.

[34] O. Hellwig, D. Weller, A. Kellock, J. Baglin, and E. E. Fullerton, "Magnetic patterning of chemically-ordered $CrPt_3$ films," *Applied Physics Letters*, vol. 79, no. 8, pp. 1151–1153, 2001.

[35] S. Maat, A. Kellock, D. Weller, J. Baglin, and E. E. Fullerton, "Ferromagnetism of $FePt_3$ films induced by ion-beam irradiation," *Journal of magnetism and magnetic materials*, vol. 265, no. 1, pp. 1–6, 2003.

[36] A. Markou, J. Gayles, E. Derunova, P. Swekis, J. Noky, L. Zhang, M. N. Ali, Y. Sun, and C. Felser, "Hard magnet topological semimetals in XPt_3 compounds with the harmony of Berry curvature," *Communications Physics*, vol. 4, no. 1, pp. 1–7, 2021.

[37] K. S. Novoselov, A. K. Geim, S. V. Morozov, D.-e. Jiang, Y. Zhang, S. V. Dubonos, I. V. Grigorieva, and A. A. Firsov, "Electric field effect in atomically thin carbon films," *science*, vol. 306, no. 5696, pp. 666–669, 2004.

[38] H. B. Nielsen and M. Ninomiya, "Absence of neutrinos on a lattice: (I). proof by homotopy theory," *Nuclear Physics B*, vol. 185, no. 1, pp. 20–40, 1981.

[39] H. B. Nielsen and M. Ninomiya, "Absence of neutrinos on a lattice: (II). intuitive topological proof," *Nuclear Physics B*, vol. 193, no. 1, pp. 173–194, 1981.

[40] B. Yan and C. Felser, "Topological materials: Weyl semimetals," *Annual Review of Condensed Matter Physics*, vol. 8, pp. 337–354, 2017.

[41] A. Bernevig, H. Weng, Z. Fang, and X. Dai, "Recent progress in the study of topological semimetals," *Journal of the Physical Society of Japan*, vol. 87, no. 4, p. 041001, 2018.

[42] L. Yang, Z. Liu, Y. Sun, H. Peng, H. Yang, T. Zhang, B. Zhou, Y. Zhang, Y. Guo, M. Rahn, D. Prabhakaran, Z. Hussain, S.-K. Mo, C. Felser, B. Yan, and Y. L. Chen, "Weyl semimetal phase in the non-centrosymmetric compound TaAs," *Nature physics*, vol. 11, no. 9, pp. 728–732, 2015.

[43] H. Gao, J. W. Venderbos, Y. Kim, and A. M. Rappe, "Topological semimetals from first principles," *Annual Review of Materials Research*, vol. 49, pp. 153–183, 2019.

[44] M. Qadir, Y. Li, and C. Wen, "Ion-substituted calcium phosphate coatings by physical vapor deposition magnetron sputtering for biomedical applications: A review," *Acta biomaterialia*, vol. 89, pp. 14–32, 2019.

[45] E. E. Fullerton, I. K. Schuller, H. Vanderstraeten, and Y. Bruynseraede, "Structural refinement of superlattices from X-ray diffraction," *Physical Review B*, vol. 45, no. 16, p. 9292, 1992.

[46] P. Miceli, D. Neumann, and H. Zabel, "X-ray refractive index: a tool to determine the average composition in multilayer structures," *Applied physics letters*, vol. 48, no. 1, pp. 24–26, 1986.

[47] Y. Wang, R. Ramaswamy, and H. Yang, "FMR-related phenomena in spintronic devices," *Journal of Physics D: Applied Physics*, vol. 51, no. 27, p. 273002, 2018.

[48] I. M. Miron, K. Garello, G. Gaudin, P.-J. Zermatten, M. V. Costache, S. Auffret, S. Bandiera, B. Rodmacq, A. Schuhl, and P. Gambardella, "Perpendicular switching of a single ferromagnetic layer induced by in-plane current injection," *Nature*, vol. 476, no. 7359, pp. 189–193, 2011.

[49] I. M. Miron, T. Moore, H. Szambolics, L. D. Buda-Prejbeanu, S. Auffret, B. Rodmacq, S. Pizzini, J. Vogel, M. Bonfim, A. Schuhl, and G. Gaudin, "Fast current-induced domain-wall motion controlled by the Rashba effect," *Nature materials*, vol. 10, no. 6, pp. 419–423, 2011.

[50] L. Liu, O. Lee, T. Gudmundsen, D. Ralph, and R. Buhrman, "Current-induced switching of perpendicularly magnetized magnetic layers using spin torque from the spin Hall effect," *Physical review letters*, vol. 109, no. 9, p. 096602, 2012.

[51] J. Han, A. Richardella, S. A. Siddiqui, J. Finley, N. Samarth, and L. Liu, "Room-temperature spin-orbit torque switching induced by a topological insulator," *Physical review letters*, vol. 119, no. 7, p. 077702, 2017.

[52] M. Jiang, H. Asahara, S. Sato, T. Kanaki, H. Yamasaki, S. Ohya, and M. Tanaka, "Efficient full spin-orbit torque switching in a single layer of a perpendicularly magnetized single-crystalline ferromagnet," *Nature Communications*, vol. 10, no. 1, pp. 1–6, 2019.

[53] T. Tanaka, H. Kontani, M. Naito, T. Naito, D. S. Hirashima, K. Yamada, and J. Inoue, "Intrinsic spin Hall effect and orbital Hall effect in 4d and 5d transition metals," *Physical Review B*, vol. 77, no. 16, p. 165117, 2008.

[54] E. Rashba, "Properties of semiconductors with an extremum loop. I. cyclotron and combinational resonance in a magnetic field perpendicular to the plane of the loop," *Sov. Phys.-Solid State*, vol. 2, p. 1109, 1960.

[55] Y. A. Bychkov and E. I. Rashba, "Oscillatory effects and the magnetic susceptibility of carriers in inversion layers," *Journal of physics C: Solid state physics*, vol. 17, no. 33, p. 6039, 1984.

[56] V. M. Edelstein, "Spin polarization of conduction electrons induced by electric current in two-dimensional asymmetric electron systems," *Solid State Communications*, vol. 73, no. 3, pp. 233–235, 1990.

[57] Y.-C. Lau, D. Betto, K. Rode, J. Coey, and P. Stamenov, "Spin-orbit torque switching without an external field using interlayer exchange coupling," *Nature nanotechnology*, vol. 11, no. 9, pp. 758–762, 2016.

[58] A. Khitun, M. Bao, and K. L. Wang, "Magnonic logic circuits," *Journal of Physics D: Applied Physics*, vol. 43, no. 26, p. 264005, 2010.

[59] J. Grollier, D. Querlioz, K. Camsari, K. Everschor-Sitte, S. Fukami, and M. D. Stiles, "Neuromorphic spintronics," *Nature electronics*, vol. 3, no. 7, pp. 360–370, 2020.

[60] L. Liu, T. Moriyama, D. Ralph, and R. Buhrman, "Spin-torque ferromagnetic resonance induced by the spin Hall effect," *Physical review letters*, vol. 106, no. 3, p. 036601, 2011.

[61] G. Mihajlović, J. Pearson, M. Garcia, S. Bader, and A. Hoffmann, "Negative nonlocal resistance in mesoscopic gold Hall bars: absence of the giant spin Hall effect," *Physical review letters*, vol. 103, no. 16, p. 166601, 2009.

[62] M. S. El Hadri, J. Gibbons, Y. Xiao, H. Ren, H. Arava, Y. Liu, Z. Liu, A. Petford-Long, A. Hoffmann, and E. E. Fullerton, "Large spin-to-charge conversion in ultrathin gold-silicon multilayers," *Physical Review Materials*, vol. 5, no. 6, p. 064410, 2021.

[63] C.-F. Pai, L. Liu, Y. Li, H. Tseng, D. Ralph, and R. Buhrman, "Spin transfer torque devices utilizing the giant spin Hall effect of tungsten," *Applied Physics Letters*, vol. 101, no. 12, p. 122404, 2012.

[64] H. Ren, S.-Y. Wu, J. Z. Sun, and E. E. Fullerton, "Ion beam etching dependence of spin-orbit torque memory devices with switching current densities reduced by Hf interlayers," *APL Materials*, vol. 9, no. 9, p. 091101, 2021.

[65] J. Kim, J. Sinha, M. Hayashi, M. Yamanouchi, S. Fukami, T. Suzuki, S. Mitani, and H. Ohno, "Layer thickness dependence of the current-induced effective field vector in Ta/CoFeB/MgO," *Nature materials*, vol. 12, no. 3, pp. 240–245, 2013.

[66] T.-Y. Chen, C.-T. Wu, H.-W. Yen, and C.-F. Pai, "Tunable spin-orbit torque in Cu-Ta binary alloy heterostructures," *Physical Review B*, vol. 96, no. 10, p. 104434, 2017.

[67] Y. Ou, D. Ralph, and R. Buhrman, "Strong enhancement of the spin Hall effect by spin fluctuations near the Curie point of Fe_xPt_{1-x} alloys," *Physical Review Letters*, vol. 120, no. 9, p. 097203, 2018.

[68] W. Zhang, M. B. Jungfleisch, F. Freimuth, W. Jiang, J. Sklenar, J. E. Pearson, J. B. Ketterson, Y. Mokrousov, and A. Hoffmann, "All-electrical manipulation of magnetization dynamics in a ferromagnet by antiferromagnets with anisotropic spin Hall effects," *Physical Review B*, vol. 92, no. 14, p. 144405, 2015.

[69] J. Ryu, C. O. Avci, S. Karube, M. Kohda, G. S. Beach, and J. Nitta, "Crystal orientation dependence of spin-orbit torques in Co/Pt bilayers," *Applied Physics Letters*, vol. 114, no. 14, p. 142402, 2019.

[70] H. Wang, K.-Y. Meng, P. Zhang, J. T. Hou, J. Finley, J. Han, F. Yang, and L. Liu, "Large spin-orbit torque observed in epitaxial $SrIrO_3$ thin films," *Applied Physics Letters*, vol. 114, no. 23, p. 232406, 2019.

[71] T. Seki, S. Iihama, T. Taniguchi, and K. Takanashi, "Large spin anomalous Hall effect in $L1_0$-FePt: Symmetry and magnetization switching," *Physical Review B*, vol. 100, no. 14, p. 144427, 2019.

[72] H. Li, G. Wang, D. Li, P. Hu, W. Zhou, X. Ma, S. Dang, S. Kang, T. Dai, F. Yu, X. Zhou, S. Wu, and S. Li, "Spin-orbit torque-induced magnetization switching in epitaxial Au/Fe_4N bilayer films," *Applied Physics Letters*, vol. 114, no. 9, p. 092402, 2019.

[73] M. Gabor, T. Petrisor Jr, M. Nasui, M. Nsibi, J. Nath, and I. Miron, "Spin-orbit torques and magnetization switching in perpendicularly magnetized epitaxial Pd/Co_2FeAl/MgO structures," *Physical Review Applied*, vol. 13, no. 5, p. 054039, 2020.

[74] R. Thompson, J. Ryu, Y. Du, S. Karube, M. Kohda, and J. Nitta, "Current direction dependent spin Hall magnetoresistance in epitaxial Pt/Co bilayers on MgO (110)," *Physical Review B*, vol. 101, no. 21, p. 214415, 2020.

[75] R. Thompson, J. Ryu, G. Choi, S. Karube, M. Kohda, J. Nitta, and B.-G. Park, "Anisotropic spin-orbit torque through crystal-orientation engineering in epitaxial Pt," *Physical Review Applied*, vol. 15, no. 1, p. 014055, 2021.

[76] J. Ryu, M. Kohda, and J. Nitta, "Observation of the D'yakonov-Perel'spin relaxation in single-crystalline Pt thin films," *Physical review letters*, vol. 116, no. 25, p. 256802, 2016.

[77] H. Gamou, Y. Du, M. Kohda, and J. Nitta, "Enhancement of spin current generation in epitaxial α-Ta/CoFeB bilayer," *Physical Review B*, vol. 99, no. 18, p. 184408, 2019.

[78] D. Hong, N. Anand, C. Liu, H. Liu, I. Arslan, J. E. Pearson, A. Bhattacharya, and J. Jiang, "Large anomalous nernst and inverse spin-Hall effects in epitaxial thin films of kagome semimetal Mn_3Ge," *Physical Review Materials*, vol. 4, no. 9, p. 094201, 2020.

[79] N. H. D. Khang, Y. Ueda, and P. N. Hai, "A conductive topological insulator with large spin Hall effect for ultralow power spin-orbit torque switching," *Nature materials*, vol. 17, no. 9, pp. 808–813, 2018.

[80] M. Jamali, J. S. Lee, J. S. Jeong, F. Mahfouzi, Y. Lv, Z. Zhao, B. K. Nikolic, K. A. Mkhoyan, N. Samarth, and J.-P. Wang, "Giant spin pumping and inverse spin Hall effect in the presence of surface and bulk spin-orbit coupling of topological insulator Bi_2Se_3," *Nano letters*, vol. 15, no. 10, pp. 7126–7132, 2015.

[81] W. Zhang, W. Han, S.-H. Yang, Y. Sun, Y. Zhang, B. Yan, and S. S. Parkin, "Giant facet-dependent spin-orbit torque and spin Hall conductivity in the triangular antiferromagnet $IrMn_3$," *Science advances*, vol. 2, no. 9, p. e1600759, 2016.

[82] B. N. Engel, C. D. England, R. A. Van Leeuwen, M. H. Wiedmann, and C. M. Falco, "Interface magnetic anisotropy in epitaxial superlattices," *Physical review letters*, vol. 67, no. 14, p. 1910, 1991.

[83] I. Dzyaloshinsky, "A thermodynamic theory of "weak" ferromagnetism of antiferromagnetics," *Journal of Physics and Chemistry of Solids*, vol. 4, no. 4, pp. 241–255, 1958.

[84] T. Moriya, "Anisotropic superexchange interaction and weak ferromagnetism," *Physical review*, vol. 120, no. 1, p. 91, 1960.

[85] H. T. Nembach, J. M. Shaw, M. Weiler, E. Jué, and T. J. Silva, "Linear relation between Heisenberg exchange and interfacial Dzyaloshinskii-Moriya interaction in metal films," *Nature Physics*, vol. 11, no. 10, pp. 825–829, 2015.

[86] M. Hoffmann, B. Zimmermann, G. P. Müller, D. Schürhoff, N. S. Kiselev, C. Melcher, and S. Blügel, "Antiskyrmions stabilized at interfaces by anisotropic Dzyaloshinskii-Moriya interactions," *Nature communications*, vol. 8, no. 1, pp. 1–9, 2017.

[87] L. Camosi, S. Rohart, O. Fruchart, S. Pizzini, M. Belmeguenai, Y. Roussigné, A. Stashkevich, S. M. Cherif, L. Ranno, M. De Santis, and V. J., "Anisotropic Dzyaloshinskii-Moriya interaction in ultrathin epitaxial Au/Co/W (110)," *Physical Review B*, vol. 95, no. 21, p. 214422, 2017.

[88] A. Raeliarijaona, R. Nepal, and A. A. Kovalev, "Boundary twists, instabilities, and creation of skyrmions and antiskyrmions," *Physical Review Materials*, vol. 2, no. 12, p. 124401, 2018.

[89] S. Tsurkan and K. Zakeri, "Giant Dzyaloshinskii-Moriya interaction in epitaxial Co/Fe bilayers with C_{2v} symmetry," *Physical Review B*, vol. 102, no. 6, p. 060406, 2020.

[90] Y. Fan, P. Upadhyaya, X. Kou, M. Lang, S. Takei, Z. Wang, J. Tang, L. He, L.-T. Chang, M. Montazeri, G. Yu, W. Jiang, T. Nie, R. Schwartz, Y. Tserkovnyak, and K. Wang, "Magnetization switching through giant spin-orbit torque in a magnetically doped topological insulator heterostructure," *Nature materials*, vol. 13, no. 7, pp. 699–704, 2014.

[91] Y. Wang, P. Deorani, X. Qiu, J. H. Kwon, and H. Yang, "Determination of intrinsic spin Hall angle in Pt," *Applied Physics Letters*, vol. 105, no. 15, p. 152412, 2014.

[92] A. Mellnik, J. Lee, A. Richardella, J. Grab, P. Mintun, M. H. Fischer, A. Vaezi, A. Manchon, E.-A. Kim, N. Samarth, and D. C. Ralph, "Spin-transfer torque generated by a topological insulator," *Nature*, vol. 511, no. 7510, pp. 449–451, 2014.

[93] T. Nan, S. Emori, C. T. Boone, X. Wang, T. M. Oxholm, J. G. Jones, B. M. Howe, G. J. Brown, and N. X. Sun, "Comparison of spin-orbit torques and spin pumping across NiFe/Pt and NiFe/Cu/Pt interfaces," *Physical Review B*, vol. 91, no. 21, p. 214416, 2015.

[94] J.-W. Xu and A. D. Kent, "Charge-to-spin conversion efficiency in ferromagnetic nanowires by spin torque ferromagnetic resonance: reconciling lineshape and linewidth analysis methods," *Physical Review Applied*, vol. 14, no. 1, p. 014012, 2020.

[95] M. Müller, L. Liensberger, L. Flacke, H. Huebl, A. Kamra, W. Belzig, R. Gross, M. Weiler, and M. Althammer, "Temperature-dependent spin transport and current-induced torques in superconductor-ferromagnet heterostructures," *Physical Review Letters*, vol. 126, no. 8, p. 087201, 2021.

[96] G. Daalderop, P. Kelly, and F. Den Broeder, "Prediction and confirmation of perpendicular magnetic anisotropy in Co/Ni multilayers," *Physical review letters*, vol. 68, no. 5, p. 682, 1992.

[97] J. A. Brock, S. A. Montoya, M.-Y. Im, and E. E. Fullerton, "Energy-efficient generation of skyrmion phases in Co/Ni/Pt-based multilayers using Joule heating," *Physical Review Materials*, vol. 4, no. 10, p. 104409, 2020.

[98] R. McMichael, D. Twisselmann, and A. Kunz, "Localized ferromagnetic resonance in inhomogeneous thin films," *Physical review letters*, vol. 90, no. 22, p. 227601, 2003.

[99] L. Zhu, D. C. Ralph, and R. A. Buhrman, "Effective spin-mixing conductance of heavy-metal-ferromagnet interfaces," *Physical Review Letters*, vol. 123, no. 5, p. 057203, 2019.

[100] B. Lairson, M. Visokay, R. Sinclair, S. Hagstrom, and B. Clemens, "Epitaxial Pt (001), Pt (110), and Pt (111) films on MgO (001), MgO (110), MgO (111), and Al_2O_3 (0001)," *Applied physics letters*, vol. 61, no. 12, pp. 1390–1392, 1992.

[101] J. Sankey, P. Braganca, A. Garcia, I. Krivorotov, R. Buhrman, and D. Ralph, "Spin-transfer-driven ferromagnetic resonance of individual nanomagnets," *Physical review letters*, vol. 96, no. 22, p. 227601, 2006.

[102] J. C. Sankey, Y.-T. Cui, J. Z. Sun, J. C. Slonczewski, R. A. Buhrman, and D. C. Ralph, "Measurement of the spin-transfer-torque vector in magnetic tunnel junctions," *Nature Physics*, vol. 4, no. 1, pp. 67–71, 2008.

[103] C. Kittel, "On the theory of ferromagnetic resonance absorption," *Physical review*, vol. 73, no. 2, p. 155, 1948.

[104] B. Heinrich, J. Cochran, and R. Hasegawa, "Fmr linebroadening in metals due to two-magnon scattering," *Journal of Applied Physics*, vol. 57, no. 8, pp. 3690–3692, 1985.

[105] S. Petit, C. Baraduc, C. Thirion, U. Ebels, Y. Liu, M. Li, P. Wang, and B. Dieny, "Spin-torque influence on the high-frequency magnetization fluctuations in magnetic tunnel junctions," *Physical review letters*, vol. 98, no. 7, p. 077203, 2007.

[106] C. Guillemard, S. Petit-Watelot, S. Andrieu, and J.-C. Rojas-Sánchez, "Charge-spin current conversion in high quality epitaxial Fe/Pt systems: Isotropic spin Hall angle along different in-plane crystalline directions," *Applied Physics Letters*, vol. 113, no. 26, p. 262404, 2018.

[107] C. Song, R. Zhang, L. Liao, Y. Zhou, X. Zhou, R. Chen, Y. You, X. Chen, and F. Pan, "Spin-orbit torques: Materials, mechanisms, performances, and potential applications," *Progress in Materials Science*, vol. 118, p. 100761, 2021.

[108] C. Ciccarelli, L. Anderson, V. Tshitoyan, A. Ferguson, F. Gerhard, C. Gould, L. Molenkamp, J. Gayles, J. Železnỳ, L. Šmejkal, Y. Z., J. Sinova, F. Freimuth, and T. Jungwirth, "Room-temperature spin-orbit torque in NiMnSb," *Nature physics*, vol. 12, no. 9, pp. 855–860, 2016.

[109] E. Simon, A. Szilva, B. Ujfalussy, B. Lazarovits, G. Zarand, and L. Szunyogh, "Anisotropic Rashba splitting of surface states from the admixture of bulk states: Relativistic *ab initio* calculations and $k{\cdot}p$ perturbation theory," *Physical Review B*, vol. 81, no. 23, p. 235438, 2010.

[110] M. Hayashi, J. Kim, M. Yamanouchi, and H. Ohno, "Quantitative characterization of the spin-orbit torque using harmonic Hall voltage measurements," *Physical Review B*, vol. 89, no. 14, p. 144425, 2014.

[111] K. Garello, I. M. Miron, C. O. Avci, F. Freimuth, Y. Mokrousov, S. Blügel, S. Auffret, O. Boulle, G. Gaudin, and P. Gambardella, "Symmetry and magnitude of spin-orbit torques in ferromagnetic heterostructures," *Nature nanotechnology*, vol. 8, no. 8, pp. 587–593, 2013.

[112] Z. Zheng, Y. Zhang, X. Feng, K. Zhang, J. Nan, Z. Zhang, G. Wang, J. Wang, N. Lei, D. Liu, Y. Zhang, and W. Zhao, "Enhanced spin-orbit torque and multilevel current-induced switching in W/Co-Tb/Pt heterostructure," *Physical Review Applied*, vol. 12, no. 4, p. 044032, 2019.

[113] C.-F. Pai, M. Mann, A. J. Tan, and G. S. Beach, "Determination of spin torque efficiencies in heterostructures with perpendicular magnetic anisotropy," *Physical Review B*, vol. 93, no. 14, p. 144409, 2016.

[114] W. Seung Ham, S. Kim, D.-H. Kim, K.-J. Kim, T. Okuno, H. Yoshikawa, A. Tsukamoto, T. Moriyama, and T. Ono, "Temperature dependence of spin-orbit effective fields in Pt/GdFeCo bilayers," *Applied Physics Letters*, vol. 110, no. 24, p. 242405, 2017.

[115] M. Isasa, E. Villamor, L. E. Hueso, M. Gradhand, and F. Casanova, "Temperature dependence of spin diffusion length and spin Hall angle in Au and Pt," *Physical Review B*, vol. 91, no. 2, p. 024402, 2015.

[116] P. Petroff, T. Sheng, A. Sinha, G. Rozgonyi, and F. Alexander, "Microstructure, growth, resistivity, and stresses in thin tungsten films deposited by rf sputtering," *Journal of Applied Physics*, vol. 44, no. 6, pp. 2545–2554, 1973.

[117] F. Vüllers and R. Spolenak, "Alpha-vs. beta-W nanocrystalline thin films: A comprehensive study of sputter parameters and resulting materials' properties," *Thin Solid Films*, vol. 577, pp. 26–34, 2015.

[118] A. MacDonald and M. Tsoi, "Antiferromagnetic metal spintronics," *Philosophical Transactions of the Royal Society A: Mathematical, Physical and Engineering Sciences*, vol. 369, no. 1948, pp. 3098–3114, 2011.

[119] X. Marti, I. Fina, C. Frontera, J. Liu, P. Wadley, Q. He, R. Paull, J. Clarkson, J. Kudrnovskỳ, I. Turek, J. Kuneš, D. Yi, J.-H. Chu, C. Nelson, L. You, E. Arenholz, S. Salahuddin, J. Fontcuberta, T. Jungwirth, and R. Ramesh, "Room-temperature antiferromagnetic memory resistor," *Nature materials*, vol. 13, no. 4, pp. 367–374, 2014.

[120] X. Martí, I. Fina, and T. Jungwirth, "Prospect for antiferromagnetic spintronics," *IEEE transactions on magnetics*, vol. 51, no. 4, pp. 1–4, 2015.

[121] T. Jungwirth, X. Marti, P. Wadley, and J. Wunderlich, "Antiferromagnetic spintronics," *Nature nanotechnology*, vol. 11, no. 3, pp. 231–241, 2016.

[122] V. Baltz, A. Manchon, M. Tsoi, T. Moriyama, T. Ono, and Y. Tserkovnyak, "Antiferromagnetic spintronics," *Reviews of Modern Physics*, vol. 90, no. 1, p. 015005, 2018.

[123] M. B. Jungfleisch, W. Zhang, and A. Hoffmann, "Perspectives of antiferromagnetic spintronics," *Physics Letters A*, vol. 382, no. 13, pp. 865–871, 2018.

[124] T. Kosub, M. Kopte, R. Hühne, P. Appel, B. Shields, P. Maletinsky, R. Hübner, M. O. Liedke, J. Fassbender, O. G. Schmidt, and D. Makarov, "Purely antiferromagnetic magnetoelectric random access memory," *Nature communications*, vol. 8, no. 1, pp. 1–7, 2017.

[125] C. Song, Y. You, X. Chen, X. Zhou, Y. Wang, and F. Pan, "How to manipulate magnetic states of antiferromagnets," *Nanotechnology*, vol. 29, no. 11, p. 112001, 2018.

[126] B. G. Park, J. Wunderlich, X. Martí, V. Holỳ, Y. Kurosaki, M. Yamada, H. Yamamoto, A. Nishide, J. Hayakawa, H. Takahashi, A. Shick, and T. Jungwirth, "A spin-valve-like magnetoresistance of an antiferromagnet-based tunnel junction," *Nature materials*, vol. 10, no. 5, pp. 347–351, 2011.

[127] Y. Wang, C. Song, B. Cui, G. Wang, F. Zeng, and F. Pan, "Room-temperature perpendicular exchange coupling and tunneling anisotropic magnetoresistance in an antiferromagnet-based tunnel junction," *Physical review letters*, vol. 109, no. 13, p. 137201, 2012.

[128] N. P. Duong, T. Satoh, and M. Fiebig, "Ultrafast manipulation of antiferromagnetism of NiO," *Physical review letters*, vol. 93, no. 11, p. 117402, 2004.

[129] A. Kimel, A. Kirilyuk, P. Usachev, R. Pisarev, A. Balbashov, and T. Rasing, "Ultrafast non-thermal control of magnetization by instantaneous photomagnetic pulses," *Nature*, vol. 435, no. 7042, pp. 655–657, 2005.

[130] P. Wadley, B. Howells, J. Železnỳ, C. Andrews, V. Hills, R. P. Campion, V. Novák, K. Olejník, F. Maccherozzi, S. Dhesi, S. Martin, T. Wagner, J. Wunderlich, F. Freimuth, Y. Mokrousov, J. Kuneš, J. Chauhan, M. J. Grzybowski, A. W. Rushforth, K. W. Edmonds, B. L. Gallagher, and T. Jungwirth, "Electrical switching of an antiferromagnet," *Science*, vol. 351, no. 6273, pp. 587–590, 2016.

[131] Y. Cheng, S. Yu, M. Zhu, J. Hwang, and F. Yang, "Electrical switching of tristate antiferromagnetic Néel order in α-Fe_2O_3 epitaxial films," *Physical Review Letters*, vol. 124, no. 2, p. 027202, 2020.

[132] R. Cherifi, V. Ivanovskaya, L. Phillips, A. Zobelli, I. Infante, E. Jacquet, V. Garcia, S. Fusil, P. Briddon, N. Guiblin, A. Mougin, A. Ünal, F. Kronast, S. Valencia, B. Dkhil, A. Barthélémy, and M. Bibes, "Electric-field control of magnetic order above room temperature," *Nature materials*, vol. 13, no. 4, pp. 345–351, 2014.

[133] Z. Liu, H. Chen, J. Wang, J. Liu, K. Wang, Z. Feng, H. Yan, X. Wang, C. Jiang, J. Coey, and A. MacDonald, "Electrical switching of the topological anomalous Hall effect in a non-collinear antiferromagnet above room temperature," *Nature Electronics*, vol. 1, no. 3, pp. 172–177, 2018.

[134] T. Nan, Y. Lee, S. Zhuang, Z. Hu, J. D. Clarkson, X. Wang, C. Ko, H. Choe, Z. Chen, D. Budil, J. Wu, S. Salahuddin, J. Hu, R. Ramesh, and N. Sun, "Electric-field control of spin dynamics during magnetic phase transitions," *Science advances*, vol. 6, no. 40, p. eabd2613, 2020.

[135] D. Kriegner, K. Vỳbornỳ, K. Olejník, H. Reichlová, V. Novák, X. Marti, J. Gazquez, V. Saidl, P. Němec, V. Volobuev, G. Springholz, V. Holý, and T. Jungwirth, "Multiple-stable anisotropic magnetoresistance memory in antiferromagnetic MnTe," *Nature communications*, vol. 7, no. 1, pp. 1–7, 2016.

[136] S. Maat, O. Hellwig, G. Zeltzer, E. E. Fullerton, G. Mankey, M. Crow, and J. Robertson, "Antiferromagnetic structure of $FePt_3$ films studied by neutron scattering," *Physical review B*, vol. 63, no. 13, p. 134426, 2001.

[137] V. Krishnamurthy, I. Zoto, G. Mankey, J. Robertson, S. Maat, E. E. Fullerton, I. Nwagwu, and J. Akujieze, "Antiferromagnetic phase transitions in an ordered Pt_3Fe (111) film studied by neutron diffraction," *Physical Review B*, vol. 70, no. 2, p. 024424, 2004.

[138] D. Palaith, C. Kimball, R. Preston, and J. Crangle, "Magnetic behavior of the Pt+Fe system near Pt_3Fe," *Physical Review*, vol. 178, no. 2, p. 795, 1969.

[139] R. Compton, M. J. Pechan, S. Maat, and E. E. Fullerton, "Probing the magnetic transitions in exchange-biased $FePt_3$/Fe bilayers," *Physical review B*, vol. 66, no. 5, p. 054411, 2002.

[140] B. Dieny, V. S. Speriosu, S. S. Parkin, B. A. Gurney, D. R. Wilhoit, and D. Mauri, "Giant magnetoresistive in soft ferromagnetic multilayers," *Physical Review B*, vol. 43, no. 1, p. 1297, 1991.

[141] A. Berkowitz and K. Takano, "Exchange anisotropy—a review," *Journal of Magnetism and Magnetic materials*, vol. 200, no. 1-3, pp. 552–570, 1999.

[142] J. Nogués and I. K. Schuller, "Exchange bias," *Journal of Magnetism and Magnetic Materials*, vol. 192, no. 2, pp. 203–232, 1999.

[143] A. Rushforth, K. Vỳbornỳ, C. King, K. Edmonds, R. Campion, C. Foxon, J. Wunderlich, A. Irvine, P. Vašek, V. Novák, K. Olejník, J. Sinova, T. Jungwirth, and B. Gallagher, "Anisotropic magnetoresistance components in (Ga, Mn)As," *Physical review letters*, vol. 99, no. 14, p. 147207, 2007.

[144] I. Fina, X. Marti, D. Yi, J. Liu, J. Chu, C. Rayan-Serrao, S. Suresha, A. Shick, J. Železnỳ, T. Jungwirth, J. Fontcuberta, and R. Ramesh, "Anisotropic magnetoresistance in an antiferromagnetic semiconductor," *Nature communications*, vol. 5, no. 1, pp. 1–7, 2014.

[145] S. Liang, J. Lin, S. Kushwaha, J. Xing, N. Ni, R. J. Cava, and N. P. Ong, "Experimental tests of the chiral anomaly magnetoresistance in the Dirac-Weyl semimetals Na_3Bi and GdPtBi," *Physical Review X*, vol. 8, no. 3, p. 031002, 2018.

[146] K. Ahadi, X. Lu, S. Salmani-Rezaie, P. B. Marshall, J. M. Rondinelli, and S. Stemmer, "Anisotropic magnetoresistance in the itinerant antiferromagnetic $EuTiO_3$," *Physical Review B*, vol. 99, no. 4, p. 041106, 2019.

[147] O. Pavlosiuk, D. Kaczorowski, and P. Wiśniewski, "Negative longitudinal magnetoresistance as a sign of a possible chiral magnetic anomaly in the half-Heusler antiferromagnet DyPdBi," *Physical Review B*, vol. 99, no. 12, p. 125142, 2019.

[148] J. Cui, M. Shi, H. Wang, F. Yu, T. Wu, X. Luo, J. Ying, and X. Chen, "Transport properties of thin flakes of the antiferromagnetic topological insulator $MnBi_2Te_4$," *Physical Review B*, vol. 99, no. 15, p. 155125, 2019.

[149] H. Wang, C. Lu, J. Chen, Y. Liu, S. Yuan, S.-W. Cheong, S. Dong, and J.-M. Liu, "Giant anisotropic magnetoresistance and nonvolatile memory in canted antiferromagnet Sr_2IrO_4," *Nature communications*, vol. 10, no. 1, pp. 1–7, 2019.

[150] S. Y. Bodnar, Y. Skourski, O. Gomonay, J. Sinova, M. Kläui, and M. Jourdan, "Magnetoresistance effects in the metallic antiferromagnet Mn_2Au," *Physical Review Applied*, vol. 14, no. 1, p. 014004, 2020.

[151] J. Wu, M. H. Karigerasi, D. P. Shoemaker, V. O. Lorenz, and D. G. Cahill, "Temperature dependence of the anisotropic magnetoresistance of the metallic antiferromagnet Fe_2As," *Physical Review Applied*, vol. 15, no. 5, p. 054038, 2021.

[152] S. Y. Bodnar, L. Šmejkal, I. Turek, T. Jungwirth, O. Gomonay, J. Sinova, A. Sapozhnik, H.-J. Elmers, M. Kläui, and M. Jourdan, "Writing and reading antiferromagnetic Mn_2Au by néel spin-orbit torques and large anisotropic magnetoresistance," *Nature communications*, vol. 9, no. 1, pp. 1–7, 2018.

[153] J. Godinho, H. Reichlová, D. Kriegner, V. Novák, K. Olejník, Z. Kašpar, Z. Šobáň, P. Wadley, R. Campion, R. Otxoa, P. Roy, J. Železný, T. Jungwirth, and J. Wunderlich, "Electrically induced and detected néel vector reversal in a collinear antiferromagnet," *Nature communications*, vol. 9, no. 1, pp. 1–8, 2018.

[154] J. Hubbell, "Photon mass attenuation and energy-absorption coefficients," *The International Journal of Applied Radiation and Isotopes*, vol. 33, no. 11, pp. 1269–1290, 1982.

[155] C. Everhart and J. MacChesney, "Anisotropy in the electrical resistivity of vanadium dioxide single crystals," *Journal of Applied Physics*, vol. 39, no. 6, pp. 2872–2874, 1968.

[156] N. Ni, S. Bud'ko, A. Kreyssig, S. Nandi, G. Rustan, A. Goldman, S. Gupta, J. Corbett, A. Kracher, and P. Canfield, "Anisotropic thermodynamic and transport properties of single-crystalline $Ba_{1-x}K_xFe_2As_2$ (x= 0 and 0.45)," *Physical Review B*, vol. 78, no. 1, p. 014507, 2008.

[157] X. Wang, T. Wu, G. Wu, H. Chen, Y. Xie, J. Ying, Y. Yan, R. Liu, and X. Chen, "Anisotropy in the electrical resistivity and susceptibility of superconducting $BaFe_2As_2$ single crystals," *Physical review letters*, vol. 102, no. 11, p. 117005, 2009.

[158] W. R. Meier, T. Kong, U. S. Kaluarachchi, V. Taufour, N. H. Jo, G. Drachuck, A. Böhmer, S. Saunders, A. Sapkota, M. Kreyssig, A andTanatar, R. Prozorov, A. I. Goldman, F. Balakirev, A. Gurevich, S. Bud'ko, and P. Canfield, "Anisotropic thermodynamic and transport properties of single-crystalline $CaKFe_4As_4$," *Physical Review B*, vol. 94, no. 6, p. 064501, 2016.

[159] Y. Xiang, Q. Li, Y. Li, W. Xie, H. Yang, Z. Wang, Y. Yao, and H.-H. Wen, "Twofold symmetry of *c*-axis resistivity in topological kagome superconductor CsV_3Sb_5 with in-plane rotating magnetic field," *Nature communications*, vol. 12, no. 1, pp. 1–8, 2021.

[160] Y. Xiao, H. Wang, and E. E. Fullerton, "Crystalline orientation-dependent spin Hall effect in epitaxial platinum," *Frontiers in Physics*, p. 785, 2022.

[161] P. Zheng and D. Gall, "The anisotropic size effect of the electrical resistivity of metal thin films: Tungsten," *Journal of Applied Physics*, vol. 122, no. 13, p. 135301, 2017.

[162] S. H. Lee, Y. Zhu, Y. Wang, L. Miao, T. Pillsbury, H. Yi, S. Kempinger, J. Hu, C. A. Heikes, P. Quarterman, W. Ratcliff, J. Borchers, H. Zhang, X. Ke, N. Graf, D.and Alem, C.-Z. Chang, N. Samarth, and Z. Mao, "Spin scattering and noncollinear spin structure-induced intrinsic anomalous Hall effect in antiferromagnetic topological insulator $MnBi_2Te_4$," *Physical Review Research*, vol. 1, no. 1, p. 012011, 2019.

[163] D. Belanger, J. Wang, Z. Slanič, S. Han, R. Nicklow, M. Lui, C. Ramos, and D. Lederman, "Magnetic order in the random-field Ising film $Fe_{0.52}Zn_{0.48}F_2$," *Physical Review B*, vol. 54, no. 5, p. 3420, 1996.

[164] S. D. Wilson, Z. Yamani, C. Rotundu, B. Freelon, E. Bourret-Courchesne, and R. Birgeneau, "Neutron diffraction study of the magnetic and structural phase transitions in $BaFe_2As_2$," *Physical Review B*, vol. 79, no. 18, p. 184519, 2009.

[165] M. D. Stiles and R. D. McMichael, "Temperature dependence of exchange bias in polycrystalline ferromagnet-antiferromagnet bilayers," *Physical Review B*, vol. 60, no. 18, p. 12950, 1999.

[166] M. Wang, C. Andrews, S. Reimers, O. Amin, P. Wadley, R. Campion, S. Poole, J. Felton, K. Edmonds, B. Gallagher, A. W. Rushforth, O. Makarovsky, K. Gas, M. Sawicki, D. Kriegner, J. Zubáč, K. Olejník, V. Novák, T. Jungwirth, M. Shahrokhvand, U. Zeitler, S. Dhesi, and F. Maccherozzi, "Spin flop and crystalline anisotropic magnetoresistance in CuMnAs," *Physical Review B*, vol. 101, no. 9, p. 094429, 2020.

[167] C. Pfleiderer, J. Bœuf, and H. v. Löhneysen, "Stability of antiferromagnetism at high magnetic fields in Mn_3Si," *Phys. Rev. B*, vol. 65, p. 172404, Apr 2002.

[168] T. Moriya and K. Ueda, "Antiferromagnetic spin fluctuation and superconductivity," *Reports on Progress in Physics*, vol. 66, no. 8, p. 1299, 2003.

[169] E. Mendive-Tapia and J. B. Staunton, "Theory of magnetic ordering in the heavy rare earths: *Ab initio* electronic origin of pair-and four-spin interactions," *Physical Review Letters*, vol. 118, no. 19, p. 197202, 2017.

[170] R. J. Elliott, "Magnetic Properties of Rare Earth Metals," no. 9, p. 425, 1972.

[171] L. E. Spanel, *Magnetoresistance of some hexagonal close-packed metals*. PhD thesis, Iowa State University, Ames, Iowa, 1964.

[172] B. Rhodes, S. Legvold, and F. Spedding, "Magnetic properties of holmium and thulium metals," *Physical Review*, vol. 109, no. 5, p. 1547, 1958.

[173] S. Legvold, J. Alstad, and J. Rhyne, "Giant magnetostriction in dysprosium and holmium single crystals," *Physical Review Letters*, vol. 10, no. 12, p. 509, 1963.

[174] R. Cowley and S. Bates, "The magnetic structure of holmium. I," *Journal of Physics C: Solid State Physics*, vol. 21, no. 22, p. 4113, 1988.

[175] D. Tindall, M. Steinitz, M. Kahrizi, D. Noakes, and N. Ali, "Investigation of the helimagnetic phases of holmium in a *c*-axis magnetic field," *Journal of Applied Physics*, vol. 69, no. 8, pp. 5691–5693, 1991.

[176] C. Tang, W. Stirling, D. Jones, C. Wilson, P. Haycock, A. Rollason, A. Thomas, and D. Fort, "Magnetic X-ray and neutron scattering from holmium and terbium," *Journal of magnetism and magnetic materials*, vol. 103, no. 1-2, pp. 86–96, 1992.

[177] D. Jehan, D. McMorrow, R. Cowley, and G. McIntyre, "The magnetic structure of holmium in an easy-axis magnetic field," *EPL (Europhysics Letters)*, vol. 17, no. 6, p. 553, 1992.

[178] J. Jensen and A. Mackintosh, "Novel magnetic phases in holmium," *Journal of Magnetism and Magnetic Materials*, vol. 104, pp. 1481–1484, 1992.

[179] J. R. Gebhardt and N. Ali, "Magnetic phase diagrams of holmium determined from magnetoresistance measurements," *Journal of applied physics*, vol. 83, no. 11, pp. 6299–6301, 1998.

[180] R. Cowley, P. Gehring, D. Gibbs, J. Goff, B. Lake, C. Majkrzak, A. Vigliante, R. Ward, and M. Wells, "The magnetic phase transition of a lattice-matched holmium thin film," *Journal of Physics: Condensed Matter*, vol. 10, no. 30, p. 6803, 1998.

[181] T. Kosugi, S. Kawano, N. Achiwa, A. Onodera, Y. Nakai, and N. Yamamoto, "Direct evidence of helifan structures in holmium by single crystal neutron diffraction," *Physica B: Condensed Matter*, vol. 334, no. 3-4, pp. 365–368, 2003.

[182] P. Spencer, S. Wilkins, P. Hatton, S. Brown, T. Hase, J. Purton, and D. Fort, "Soft X-ray diffraction study of magnetic ordering in holmium," *Journal of Physics: Condensed Matter*, vol. 17, no. 10, p. 1725, 2005.

[183] I. Usman, K. Yates, J. Moore, K. Morrison, V. Pecharsky, K. Gschneidner, T. Verhagen, J. Aarts, V. Zverev, J. Robinson, J. D. S. Witt, M. G. Blamire, and L. Cohen, "Evidence for spin mixing in holmium thin film and crystal samples," *Physical Review B*, vol. 83, no. 14, p. 144518, 2011.

[184] T. Miyamachi, T. Schuh, T. Märkl, C. Bresch, T. Balashov, A. Stöhr, C. Karlewski, S. André, M. Marthaler, M. Hoffmann, M. Geilhufe, S. Ostanin, W. Hergert, I. Mertig, G. Schön, A. Ernst, and W. Wulfhekel, "Stabilizing the magnetic moment of single holmium atoms by symmetry," *Nature*, vol. 503, no. 7475, pp. 242–246, 2013.

[185] M. Steinitz, M. Kahrizi, D. Tindall, and N. Ali, "New magnetic phases of holmium in a magnetic field," *Physical Review B*, vol. 40, no. 1, p. 763, 1989.

[186] J. Mukherjee, T. S. Suraj, H. Basumatary, K. Sethupathi, and K. V. Raman, "Sign reversal of anomalous Hall conductivity and magnetoresistance in cubic noncollinear antiferromagnet Mn_3Pt thin films," *Phys. Rev. Materials*, vol. 5, p. 014201, Jan 2021.

[187] J. Meng, H. Xue, M. Liu, W. Jiang, Z. Zhang, J. Ling, L. He, R. Dou, C. Xiong, and J. Nie, "Planar Hall effect induced by anisotropic orbital magnetoresistance in type-II Dirac semimetal $PdTe_2$," *Journal of Physics: Condensed Matter*, vol. 32, no. 1, p. 015702, 2019.

[188] A. N. A. Nakamura and M. F. M. Futamoto, "Epitaxial growth of Co/Cr bilayer films on MgO single crystal substrates," *Japanese journal of applied physics*, vol. 32, no. 10A, p. L1410, 1993.

[189] J. Mattson, E. E. Fullerton, C. Sowers, and S. Bader, "Epitaxial growth of body-centered-cubic transition metal films and superlattices onto MgO (111), (011), and (001) substrates," *Journal of Vacuum Science & Technology A: Vacuum, Surfaces, and Films*, vol. 13, no. 2, pp. 276–281, 1995.

[190] J. Huang, Y. Liou, Y. Yao, W. Yang, C. Chang, S. Liao, and Y. Hu, "Large crystalline-induced magnetic anisotropy and field-direction-dependent magnetoresistance in Co $(1\bar{1}00)$/Cr (211) superlattices," *Physical Review B*, vol. 52, no. 18, p. R13110, 1995.

[191] M. Grimsditch, E. E. Fullerton, and R. Stamps, "Exchange and anisotropy effects on spin waves in epitaxial Co films," *Physical Review B*, vol. 56, no. 5, p. 2617, 1997.

[192] J. Brandenburg, R. Hühne, L. Schultz, and V. Neu, "Domain structure of epitaxial Co films with perpendicular anisotropy," *Physical Review B*, vol. 79, no. 5, p. 054429, 2009.

[193] Y. Barnier, R. Pauthener, and G. Rimet, "Thermomagnetic study of a hexagonal cobalt single crystal," in *Cobalt*, vol. 15, pp. 1–7, Centre d'Information du Cobalt Brussels, 1962.

[194] X. Liu, M. Steiner, R. Sooryakumar, G. Prinz, R. Farrow, and G. Harp, "Exchange stiffness, magnetization, and spin waves in cubic and hexagonal phases of cobalt," *Physical Review B*, vol. 53, no. 18, p. 12166, 1996.

[195] N. Volkenshtein, G. Fedorov, and V. Shirokovskii, "The anisotropy of the Hall effect in ferromagnetic materials," *Fiz. Metal. Metalloved*, vol. 11, no. 1, pp. 152–154, 1961.

[196] J. Kötzler and W. Gil, "Anomalous Hall resistivity of cobalt films: Evidence for the intrinsic spin-orbit effect," *Physical Review B*, vol. 72, no. 6, p. 060412, 2005.

[197] D. Hou, Y. Li, D. Wei, D. Tian, L. Wu, and X. Jin, "The anomalous Hall effect in epitaxial face-centered-cubic cobalt films," *Journal of Physics: Condensed Matter*, vol. 24, no. 48, p. 482001, 2012.

[198] J.-C. Tung, H.-R. Fuh, and G.-Y. Guo, "Anomalous and spin Hall effects in hcp cobalt from GGA+U calculations," *Physical Review B*, vol. 86, no. 2, p. 024435, 2012.

[199] V. P. Amin, J. Li, M. D. Stiles, and P. M. Haney, "Intrinsic spin currents in ferromagnets," *Physical Review B*, vol. 99, no. 22, p. 220405, 2019.

[200] T. Miyasato, N. Abe, T. Fujii, A. Asamitsu, S. Onoda, Y. Onose, N. Nagaosa, and Y. Tokura, "Crossover behavior of the anomalous Hall effect and anomalous Nernst effect in itinerant ferromagnets," *Physical review letters*, vol. 99, no. 8, p. 086602, 2007.

[201] K. Manna, L. Muechler, T.-H. Kao, R. Stinshoff, Y. Zhang, J. Gooth, N. Kumar, G. Kreiner, K. Koepernik, R. Car, J. Kübler, G. Fecher, C. Shekhar, Y. Sun, and C. Felser, "From colossal to zero: controlling the anomalous Hall effect in magnetic Heusler compounds via Berry curvature design," *Physical Review X*, vol. 8, no. 4, p. 041045, 2018.

[202] M. N. Ali, J. Xiong, S. Flynn, J. Tao, Q. D. Gibson, L. M. Schoop, T. Liang, N. Haldolaarachchige, M. Hirschberger, N. P. Ong, and R. Cava, "Large, non-saturating magnetoresistance in WTe_2," *Nature*, vol. 514, no. 7521, pp. 205–208, 2014.

[203] C. Shekhar, A. K. Nayak, Y. Sun, M. Schmidt, M. Nicklas, I. Leermakers, U. Zeitler, Y. Skourski, J. Wosnitza, Z. Liu, Y. Chen, W. Schnelle, H. Borrmann, Y. Grin, C. Felser, and B. Yan, "Extremely large magnetoresistance and ultrahigh mobility in the topological Weyl semimetal candidate NbP," *Nature Physics*, vol. 11, no. 8, pp. 645–649, 2015.

[204] J. Juraszek, L. Bochenek, A. Rudenko, M. Hosen, M. Daszkiewicz, Z. Wang, J. Wosnitza, Z. Henkie, M. Samsel-Czekała, M. Neupane, *et al.*, "Nonsaturating extreme magnetoresistance and large electronic magnetostriction in LuAs," *Physical Review Research*, vol. 1, no. 3, p. 032016, 2019.

[205] D. J. Groenendijk, N. Manca, J. de Bruijckere, A. M. R. Monteiro, R. Gaudenzi, H. S. van der Zant, and A. D. Caviglia, "Anisotropic magnetoresistance in spin-orbit semimetal $SrIrO_3$," *The European physical journal plus*, vol. 135, no. 8, pp. 1–7, 2020.

[206] R. Bozorth, "Magnetostriction and crystal anisotropy of single crystals of hexagonal cobalt," *Physical Review*, vol. 96, no. 2, p. 311, 1954.

[207] N. F. Mott, "The basis of the electron theory of metals, with special reference to the transition metals," *Proceedings of the Physical Society. Section A*, vol. 62, no. 7, p. 416, 1949.

[208] A. Fert and I. Campbell, "Two-current conduction in nickel," *Physical Review Letters*, vol. 21, no. 16, p. 1190, 1968.

[209] T. McGuire, J. Aboaf, and E. Klokholm, "Negative anisotropic magnetoresistance in 3d metals and alloys containing iridium," *IEEE Transactions on Magnetics*, vol. 20, no. 5, pp. 972–974, 1984.

[210] K. Uchida, S. Takahashi, K. Harii, J. Ieda, W. Koshibae, K. Ando, S. Maekawa, and E. Saitoh, "Observation of the spin Seebeck effect," *Nature*, vol. 455, no. 7214, pp. 778–781, 2008.

[211] J. Shan, L. J. Cornelissen, N. Vlietstra, J. B. Youssef, T. Kuschel, R. A. Duine, and B. J. Van Wees, "Influence of yttrium iron garnet thickness and heater opacity on the nonlocal transport of electrically and thermally excited magnons," *Physical Review B*, vol. 94, no. 17, p. 174437, 2016.

[212] S. Kokado, M. Tsunoda, K. Harigaya, and A. Sakuma, "Anisotropic magnetoresistance effects in Fe, Co, Ni, Fe_4N, and half-metallic ferromagnet: A systematic analysis," *Journal of the Physical Society of Japan*, vol. 81, no. 2, p. 024705, 2012.

[213] A. Kobs, S. Hesse, G. Winkler, H. P. Oepen, W. Kreuzpaintner, D. Lott, and A. Schreyer, "Anisotropic interface magnetoresistance in Co/Pt," *Verhandlungen der Deutschen Physikalischen Gesellschaft*, 2011.

[214] X. Xiao, J. Li, Z. Ding, J. Liang, L. Sun, and Y. Wu, "Unusual angular dependent magnetoresistance in single-crystalline Co/Pt bilayers," *Applied Physics Letters*, vol. 108, no. 22, p. 222402, 2016.

[215] X. Huang, L. Zhao, Y. Long, P. Wang, D. Chen, Z. Yang, H. Liang, M. Xue, H. Weng, Z. Fang, X. Dai, and G. Chen, "Observation of the chiral-anomaly-induced negative magnetoresistance in 3D Weyl semimetal TaAs," *Physical Review X*, vol. 5, no. 3, p. 031023, 2015.

[216] P. Li, C. Zhang, J. Zhang, Y. Wen, and X. Zhang, "Giant planar Hall effect in the Dirac semimetal $ZrTe_{5-\delta}$," *Physical Review B*, vol. 98, no. 12, p. 121108, 2018.

[217] M. Wu, G. Zheng, W. Chu, Y. Liu, W. Gao, H. Zhang, J. Lu, Y. Han, J. Zhou, W. Ning, and M. Tian, "Probing the chiral anomaly by planar Hall effect in Dirac semimetal Cd_3As_2 nanoplates," *Physical Review B*, vol. 98, no. 16, p. 161110, 2018.

[218] N. Ong and S. Liang, "Experimental signatures of the chiral anomaly in Dirac-Weyl semimetals," *Nature Reviews Physics*, vol. 3, no. 6, pp. 394–404, 2021.

[219] X. Dai, Z. Du, and H.-Z. Lu, "Negative magnetoresistance without chiral anomaly in topological insulators," *Physical review letters*, vol. 119, no. 16, p. 166601, 2017.

[220] A. Yamada and Y. Fuseya, "Negative magnetoresistance and sign change of the planar Hall effect due to negative off-diagonal effective mass in Weyl semimetals," *Physical Review B*, vol. 105, no. 20, p. 205207, 2022.

[221] S. S.-L. Zhang and S. Zhang, "Angular dependence of anisotropic magnetoresistance in magnetic systems," *Journal of Applied Physics*, vol. 115, no. 17, p. 17C703, 2014.